Data Consistency Conditions in 3D Tomography and Scanner Calibration using Analytic Approaches

Minh Hung Nguyen

To cite this version:

Minh Hung Nguyen. Data Consistency Conditions in 3D Tomography and Scanner Calibration using Analytic Approaches. Image Processing [eess.IV]. Université Grenoble Alpes [2020-..], 2021. English. NNT : 2021GRALM026 . tel-03476571

HAL Id: tel-03476571
https://theses.hal.science/tel-03476571

Submitted on 13 Dec 2021

THÈSE

Pour obtenir le grade de

DOCTEUR DE L'UNIVERSITÉ GRENOBLE ALPES

Spécialité : Mathématiques Appliquées

Arrêté ministériel : 25 mai 2016

Présentée par

MINH HUNG NGUYEN

Thèse dirigée par **Laurent DESBAT**,Pr, Université Grenoble Alpes
et codirigée par **Rolf CLACKDOYLE**,DR2, CNRS

préparée au sein du **Laboratoire Translational Innovation in Medicine and Complexity**
dans **l'École Doctorale Mathématiques, Sciences et technologies de l'information, Informatique**

Conditions de cohérence des données en tomographie 3D et calibration de scanners avec des approches analytiques

Data Consistency Conditions in 3D Tomography and Scanner Calibration using Analytic Approaches

Thèse soutenue publiquement le **23 juillet 2021**,
devant le jury composé de :

Monsieur MICHEL DEFRISE
PROFESSEUR EMERITE, University Hospital AZVUB, Rapporteur
Monsieur XIAOCHUAN PAN
PROFESSEUR, University of Chicago, Rapporteur
Madame VALERIE PERRIER
PROFESSEUR DES UNIVERSITES, GRENOBLE INP, Présidente
Madame FRANÇOISE PEYRIN
DIRECTEUR DE RECHERCHE, INSERM DELEGATION AUVERGNE-RHONE-ALPES, Examinatrice
Monsieur CHARLES SOUSSEN
PROFESSEUR DES UNIVERSITES, CENTRALESUPELEC, Examinateur
Monsieur YANNICK GRONDIN
INGENIEUR DOCTEUR, SURGIQUAL INSTITUTE, Examinateur

Data Consistency Conditions in 3D Tomography and Scanner Calibration using Analytic Approaches

Hung Nguyen
supervised by Laurent Desbat and Rolf Clackdoyle

October 19, 2021

Acknowledgements

First, I would like to thank the two reviewers: prof. Michel Defrise and prof. Xiaochuan Pan, who made the effort to read the manuscript and write the report for me in such a short time.

Second, I would like to deeply thank Rolf and Laurent, who guided me from the very first steps in Medical Imaging, taught me so many things from the theoretical stuff to the programming techniques to the scientific writing skills, even some important things on research ethics and some language stuff (French, but mainly English). Thanks Rolf and Laurent for literally always waiting for me, because I am almost always late (for paperwork, for email-replying, for internal deadlines, ...), and I took so long long time to get in better shape at re-search work.

Finally, I would like to thank my family for always loving me, cheering me and not leaving me alone in any cases. The past few years are not perfect, but they are good enough for me to mature in my work and personality, as well as leave many interesting memories to remember.

This work was supported by the "Fonds unique interministériel" (FUI) and the European Union FEDER in Auvergne Rhône Alpes (3D4Carm project) and by the ANR (ROIdoré project ANR-17-CE19-0006-01).

Abstract

Ce travail concerne les conditions de cohérence des données et leurs applications dans l'auto-calibrage géométrique des systèmes de tomographie. En imagerie médicale radiologique, un objet est projeté à travers un système mécanique et les projections correspondantes doivent satisfaire certaines conditions si le système est cohérent. Ces conditions sont appelées conditions de cohérence des données (DCC pour "data consistency conditions"). Dans la situation où l'objet est supposé inconnu, les DCC jouent un rôle important pour calibrer les paramètres géométriques du système uniquement à partir des données de projection. Notre travail consiste, d'une part, à dériver de nouvelles DCC dans différents contextes géométriques et, d'autre part, à essayer de les appliquer de manière appropriée à certains problèmes de calibrage géométrique correspondants. Nous étudions trois contextes géométriques : géométrie parallèle 3D, géométrie à faisceau conique avec trajectoire linéaire de la source et géométrie à faisceau conique générale. Dans le cas de la géométrie parallèle 3D, nous présentons des DCC par paires. Nous obtenons alors une formule analytique pour calibrer la direction de la projection dans le cas général, et une technique de conversion du problème de calibrage 3D en de nombreux problèmes de calibrage 2D différents dans un cas particulier dégénéré. Dans la géométrie conique avec une trajectoire linéaire de la source, nous réutilisons la technique ci-dessus et obtenons une méthode pour calibrer la position de la source de la projection correspondante, basée sur la condition de cohérence de la géométrie de faisceau en éventail. Pour la dernière contribution dans le contexte de la géométrie générale du faisceau conique, nous dérivons de nouvelles DCC avec une trajectoire de source générale et nous les appliquons à un problème de calibrage du faisceau conique avec une trajectoire circulaire de la source, où la position de la source sur la trajectoire circulaire est le paramètre à calibrer.

Mots clés : conditions de cohérence des données, conditions sur l'image des opérateurs, calibration géométrique, géométrie conique, tomographie

This work concerns the data consistency conditions and their applications in geometric self-calibration. In Medical Imaging, an object is projected through a mechanical system and the corresponding projections must satisfy certain conditions if the system is consistent. These conditions are called data consistency conditions (DCC). In the situation that the object is assumed to be unknown, DCC play an important role to calibrate the geometric parameters of the system only from the projection data. Our work on one hand is to derive new DCC in different geometry contexts, and on the other hand is to try to appropriately apply them into some corresponding geometric calibration problems. We investigate three geometry contexts: 3D parallel geometry, cone-beam geometry with linear sources and general cone-beam geometry. With 3D parallel geometry, we present a pair-wise DCC leading to an analytic formula to calibrate the projection's viewing direction in general case, and a technique of converting the 3D calibration problem into many different 2D calibration problems in a particular degenerate case. In the cone-beam geometry with linear sources, we reuse the above technique and give a method to calibrate the corresponding source position of the projection based on fan-beam consistency condition. For the last contribution with general cone-beam geometry, we derive new DCC with general source trajectory and apply them into a cone-beam calibration problem with circular source trajectory, where the source position on the circular trajectory is the parameter being calibrated.

Keywords: data consistency conditions, range conditions, geometric calibration, cone-beam geometry, tomography

Contents

Acknowledgements **i**

Abstract **iii**

1 Introduction **3**
- 1.1 2D parallel geometry . . . 5
  - 1.1.1 2D Radon transform and 2D parallel projections . . . 5
  - 1.1.2 Helgason-Ludwig consistency conditions (HLCC) . . . 6
  - 1.1.3 Fourier slice theorem and Filtered Backprojection (FBP) method . . . 6
- 1.2 3D parallel geometry . . . 7
- 1.3 Divergent geometry . . . 7

2 DCCs for 3D parallel projections and applications **11**
- 2.1 Introduction . . . 12
- 2.2 3D coordinate system and 3D parallel projections . . . 14
- 2.3 Relation between 3D X-ray transform and 3D Radon transform . . . 15
- 2.4 Pair-wise DCCs of the 2D parallel projections . . . 17
- 2.5 Geometric calibration problem and solving strategy . . . 18
  - 2.5.1 Geometric calibration problem in 3D parallel geometry . . . 18
  - 2.5.2 Solving strategy . . . 19
- 2.6 Row-matching algorithm . . . 21
- 2.7 Numerical simulations . . . 22
- 2.8 ϕ-sample refinement . . . 24
- 2.9 Particular degenerate case . . . 25
  - 2.9.1 In-plane moments . . . 25
  - 2.9.2 In-plane DCC . . . 26
  - 2.9.3 Solving algorithm in the particular degenerate case . . . 27
  - 2.9.4 Numerical simulations of the particular degenerate case . . . 29
- 2.10 Global comments . . . 29
- 2.11 Simulation images . . . 32

3 DCCs for fan-beam projections and applications **39**
- 3.1 Introduction . . . 41
- 3.2 Fan-beam consistency condition (FBCC) . . . 43
  - 3.2.1 Fan-beam projections . . . 43
  - 3.2.2 Moment of the weighted fan-beam projections and the 2D FBCC . . . 44
  - 3.2.3 Center-of-mass (COM) result . . . 45
  - 3.2.4 Numerical simulations of the FBCC . . . 47
- 3.3 2D fan-beam geometric calibration . . . 48
- 3.4 Cone-beam projections . . . 53
- 3.5 3D cone-beam geometric calibration with linear sources . . . 55
  - 3.5.1 Method of calibration . . . 55
  - 3.5.2 Numerical experiments in 3D . . . 58

4 Cone-beam Consistency Conditions 63
4.1 Introduction . . . 65
4.2 *CBCC16Converted* . . . 67
    4.2.1 Summary of *CBCC16* . . . 67
    4.2.2 Geometry of *CBCC16Converted* and the weighted cone-beam projection on the horizontal detector . . . 68
    4.2.3 Relationship between the weighted cone-beam projections on the vertical and horizontal detectors (*CBCC16* and *CBCC16Converted* geometry contexts) . . . 68
    4.2.4 Moment of the weighted cone-beam projections on the horizontal detector and DCC16Converted 70
    4.2.5 Direct proof of *CBCC16Converted* without using *CBCC16* . . . 71
    4.2.6 Numerical simulations of *CBCC16* and *CBCC16Converted* . . . 72
    4.2.7 Recalling *CBCC13* . . . 76
    4.2.8 Relationship between *CBCC16Converted* and *CBCC13* . . . 77
    4.2.9 Nonhomogeneous-polynomial CBCC . . . 78
    4.2.10 Playing with *CBCC13* . . . 81
4.3 *CBCC13Converted* . . . 89
    4.3.1 *CBCC13Converted* geometric context and the weighted cone-beam projection on the vertical detector . . . 89
    4.3.2 Relationship between the weighted cone-beam projections on the horizontal and vertical detectors (*CBCC13* and *CBCC13Converted* geometry contexts) . . . 90
    4.3.3 Moment of the weighted cone-beam projections on the vertical detector and *CBCC13Converted* 91
    4.3.4 Direct proof of the necessary direction of *CBCC13Converted* . . . 93
    4.3.5 *CBCC13Converted* in some special cases . . . 96
    4.3.6 The conventional cone-beam projections and their CBCC . . . 101
    4.3.7 Comments on the position of the 3D object . . . 109
    4.3.8 Generalization of *CBCC16* . . . 117
    4.3.9 Calibration in 3D cone-beam geometry with circular source trajectory . . . 123

Conclusions 127

A Proceedings paper in 2018 NSS/MIC 129
A.1 2D radar geometry and 2D radar projections . . . 129
A.2 DCCs for the 2D radar projections . . . 130

B Proceedings paper in SPIE Medical Imaging 2020 137

C Proceedings paper in CT Meeting 2020 149

Chapter 1

Introduction

French introduction

Nous commençons par un modèle classique en imagerie médicale. Une source radiologique émet des faisceaux de rayons X qui traversent un objet 3D. L'intensité des faisceaux de rayons X avant et après le passage de l'objet 3D est différente. En fait, selon le livre [Natterer, 2001], à la page 1, l'intensité des rayons X a été atténuée après avoir traversé l'objet, selon l'équation suivante (nous copions l'équation du livre de Natterer avec un petit changement dans les notations):

$$\frac{I_1}{I_0} = \exp\left(-\int_L F\left(\vec{x}\right) d\vec{x}\right), \quad \vec{x} = (x_1, x_2, x_3) \in \mathbb{R}^3.$$

Ici, I_0 désigne l'intensité initiale des faisceaux de rayons X et I_1 désigne l'intensité des faisceaux de rayons X après avoir traversé l'objet 3D; $F(\vec{x})$ est la représentation mathématique de l'objet 3D, et $\int_L F\left(\vec{x}\right) d\vec{x}$ désigne l'intégrale de F le long de la droite L. En pratique, l'intensité initiale des faisceaux de rayons X I_0 est connue, l'intensité des faisceaux de rayons X après avoir traversé l'objet 3D I_1 peut être mesurée, grâce à un système de radiologie. On obtient ainsi les données de l'intégrale de droite. Ces données peuvent être collectées sur un détecteur, qui se trouve de l'autre côté de l'objet 3D, par rapport à la position de la source de rayons X. Les données sur le détecteur peuvent être considérées comme une image 2D, ou plus exactement comme la projection de l'objet 3D. Prenons quelques exemples simples: la radiographie du poumon, le scanner du cerveau, etc. Ce qui est collecté sur le système de mesure est une image ou une succession d'images (projections en 3D) ou une courbe ou une succession de courbes (projections en 2D) d'un certain objet en 3D, alors que l'objet est composé de parties internes du corps humain qui ne peuvent être vus à l'œil nu. En général, on suppose que l'objet 3D est totalement inconnu. L'objectif principal de l'imagerie médicale est de reconstruire l'objet 3D inconnu à partir des données des projections 2D. Ce travail est appelé "reconstruction d'image".

Outre la reconstruction d'image, de nombreux autres aspects et problèmes doivent être pris en compte en imagerie médicale. Par exemple, dans le problème de la région d'intérêt (ROI), pour une raison quelconque, nous aimerions reconstruire seulement une certaine région à l'intérieur de l'objet, l'article [Noo et al., 2004] donne une méthode pour traiter ce problème, qui peut même fonctionner avec des projections tronquées; ou parfois nous devons synthétiser la projection inconnue à partir des données de projection déjà données, voir [Patch, 2002a, Patch, 2002b, Patch, 2004, Levine et al., 2010, Carlsson et al., 1994]. Dans notre situation, nous étudions les conditions de cohérence des données. Dans le modèle direct, où l'objet 3D est connu, si les projections sont bien définies dans un modèle géométrique et si le système est cohérent, les données de projection doivent satisfaire certaines conditions, appelées conditions de cohérence des données (CCD ou DCC Data Consistency Conditions), même s'il existe des erreurs ou des bruits dans le processus de mesure. Les DCC peuvent être des équations, des relations ou des propriétés spéciales sur les données de projection. Dans le problème sur lequel nous travaillons, qui est un modèle inverse ou un problème inverse, où l'objet 3D est inconnu, les DCC jouent un rôle crucial, car à partir de ces DCC sur les données de projection, nous pouvons calibrer les paramètres géométriques correspondants du système d'acquisition. Il s'agit d'une étape importante car nous devons savoir comment les projections que nous avons acquises sont disposées les unes par rapport aux autres ou comment elles s'alignent, avant d'effectuer l'étape de reconstruction de l'image. Selon le contexte géométrique considéré, nous disposons de différents ensembles de paramètres qui doivent être calibrés.

Le travail de notre thèse est d'étudier chaque contexte géométrique particulier pour dériver de nouvelles DCC, et ensuite essayer de les appliquer pour calibrer les paramètres géométriques correspondants. Plutôt que des méthodes d'optimisation, notre but est de donner des méthodes analytiques ou des formules, pour estimer les paramètres de calibration géométrique rapidement et correctement. Le manuscrit présente les connaissances en imagerie médicale du point de vue des DCC, ce qui signifie qu'il montre les DCC et les résultats associés dans chaque contexte géométrique, du plus basique, la géométrie parallèle 2D, au plus intéressant aujourd'hui, la géométrie à faisceau conique 3D.

Le chapitre 1 se contente d'introduire le matériel de base (définitions, propriétés connues) pour rappel au lecteur; les résultats sont énumérés sans preuves, car ils peuvent être trouvés dans d'autres sources. Les chapitres 2, 3 et 4 présentent nos contributions en détail. Le chapitre 2 présente les DCC pour les projections parallèles 3D et leurs applications dans la calibration de la géométrie parallèle 3D. Le chapitre 3 présente les DCC pour les projections en éventail, puis les applique à l'étalonnage par faisceau conique avec des sources linéaires. Enfin, le chapitre 4 présente plusieurs nouvelles DCC pour la géométrie conique dans deux contextes géométriques principaux. Enfin, les dernières DCC sont dérivées pour traiter le problème de calibration dans la géométrie conique avec trajectoire circulaire.

English introduction

We start with a classical model in Medical Imaging. There exists an x-ray source, which emits x-ray beams passing through some 3D object. The intensity of the x-ray beams before and after passing through the 3D object are different. In fact, according to the book [Natterer, 2001] on page 1, the intensity of the x-ray beams have been reduced after passing through the object, following the below equation (we are copying the equation from the book of Natterer with a tiny change in the notations):

$$\frac{I_1(L)}{I_0(L)} = \exp\left(-\int_L F(\vec{x})\, d\vec{x}\right), \quad \vec{x} = (x_1, x_2, x_3) \in \mathbb{R}^3.$$

Here $I_0(L)$ denotes the initial intensity of the x-ray beam L and I_1 denotes its intensity, which has been reduced, after passing through the 3D object. The notation $F(\vec{x})$ is the attenuation coefficient of the 3D object at $\vec{x}$, the information of $F(\vec{x})$ gives us the illustration of the 3D object. And $\int_L F(\vec{x})\, d\vec{x}$ means the line integral of F along the beam L. In practice, the initial intensity of the x-ray beams is known, the intensity of the x-ray beams after passing through the 3D object can be measured, thus from the mechanical system after the measuring process, we obtain the line-integral data. These data is recorded and collected on a detector, which is on the other side of the 3D object, in comparison to the x-ray source position. The data on the detector can be considered as a 2D image, or we properly call it the projection of the 3D object. We can take a few simple examples: in the X-ray scan of the lung, the CT scan of the brain, etc, what we receive is a 2D image or projection of a certain 3D object, while the objects are the inner parts of our bodies and cannot be seen with the naked eye. Usually, the 3D object is assumed to be completely unknown. And the main objective in Medical Imaging is to reconstruct the unknown 3D object based on the 2D projection data. This work is called Image Reconstruction.

Besides Image Reconstruction, there are also many other aspects and problems need to be considered in Medical Imaging. For instance, in the problem of region-of-interest (ROI), for some reason we would like to only reconstruct a certain region inside the object, the paper [Noo et al., 2004] gives a method to deal with it, that can even work with truncated projections; or sometimes we need to synthesize the unknown projection from the already given projection data, see [Patch, 2002a, Patch, 2002b, Patch, 2004, Levine et al., 2010, Carlsson et al., 1994]. In our situation, we study the Data Consistency Conditions. In the forward model, where the 3D object is known, if the projections are well-defined in a geometry model, and the system is consistent, then the projection data must satisfy certain conditions, which are called Data Consistency Conditions (DCCs). DCCs can be equations, relations or special properties on the projection data. In the problem we are working on, which is a backward model or an inverse problem, where the 3D object is unknown, DCCs play a crucial role, since from these DCCs on the projection data, we can calibrate the corresponding geometric parameters of the system. This is an important step because we need to know how the projections we are having relate to each other or how they align, in prior to perform the image reconstruction step. Depending on the considering geometry context, we have different set of parameters that need to be calibrated.

The work of our thesis is to study each particular geometry context to derive new DCCs, and then try to apply them to calibrate the corresponding geometric parameters. Instead of the optimization methods, our aim is to give analytic methods or formulae, to calibrate the parameters fast and correctly. The manuscript presents the Medical Imaging knowledge in the DCC point of view, which means it shows the DCCs and related results in every geometry context, from the most basic one: 2D parallel geometry, to the most interested nowadays: cone-beam geometry. Because of the length of the manuscript, chapter 1 just shows the basic materials to remind the viewers, in the spirit that the results are listed with no proofs, because they might be found in some other sources. Chapter 2, 3 and 4 will show our contributions in details. Chapter 2 shows the DCCs for 3D parallel projections and their applications in 3D parallel calibration. Chapter 3 shows the DCCs for fan-beam projections, then applying them into cone-beam calibration with linear sources. Finally, chapter 4 shows several new DCCs for cone-beam geometry in two main geometry contexts, then a final DCC is derived to deal with the calibration problem in circular cone-beam geometry. At the end, we also have an Appendix section, where our three proceedings papers are provided. The proceedings paper [Clackdoyle et al., 2018] in the 2018 IEEE Nuclear Science Symposium and Medical Imaging Conference is given in appendix A. Appendix B provides the proceedings paper [Nguyen et al., 2020a] in the SPIE Medical Imaging 2020 conference, which is the basis of chapter 2. Similarly, appendix C provides the proceedings paper [Nguyen et al., 2020b] in the 6th International Conference on Image Formation in X-Ray Computed Tomography, which is the basis of chapter 3.

Small convention on the notations

- Throughout the manuscript, we use the single integral notation, without any further mention about the bounds, to refer to the integral over the whole real line $\mathbb{R}$. And the same thing respectively apply on the double or triple integral over $\mathbb{R}^2$ and $\mathbb{R}^3$: $\int f(x)\,dx$ means $\int_{\mathbb{R}} f(x)\,dx$, $\iint f(x)\,dx$ means $\iint_{\mathbb{R}^2} f(x)\,dx$, $\iiint f(x)\,dx$ means $\iiint_{\mathbb{R}^3} f(x)\,dx$.

- Also, we use the notation $\mathscr{R}^2$ and $\mathscr{R}^3$ to mention the 2D and 3D Radon transform, respectively.

1.1 2D parallel geometry

In this section, we describe the 2D parallel geometry and show the definition of the 2D parallel projections (section 1.1.1); we also show the Helgason-Ludwig consistency conditions (section 1.1.2) and some related results (section 1.1.3).

1.1.1 2D Radon transform and 2D parallel projections

We start with the 2D plane, where (x_1, x_2) is the standard coordinate system. On this plane, we are having a 2D object f, which is assumed to be a real-valued function with compact support. A set of many x-ray sources emit many parallel beams passing through the 2D object f. The detector line is on the other side of the object, in comparison to the x-ray sources. It is perpendicular to the direction of the x-ray beams. Figure 1.1 gives us an illustration. Here we are using the 2D unit vector $\vec{\alpha}_\phi$ to show the positive direction of the detector line, where ϕ is the angle between the direction of the detector line and the x_1-axis. $\vec{\beta}_\phi$ is another 2D unit vector, which can be obtained by rotating $\vec{\alpha}_\phi$ 90° counter-clockwise. By the construction of the geometry, $\vec{\beta}_\phi$ is then showing the directions of the parallel beams. For each value of the angle ϕ, we obtain a parallel projection, which records the line integral data of the 2D object f along the x-ray beams in the $\vec{\beta}_\phi$ direction. It is a single-variable function of s, where $|s|$ is the distance from the origin to the considering x-ray beam, over whom we are computing the corresponding line integral. The 2D parallel projections are defined through the 2D Radon transform $\mathscr{R}^2$, which maps the 2D function f to the set of its line integrals:

$$\mathscr{R}^2 f(\phi, s) = \int f\left(s\vec{\alpha}_\phi + t\vec{\beta}_\phi\right) dt, \quad \forall \phi \in [0, 2\pi), \forall s \in \mathbb{R}, \tag{1.1}$$

where:

$$\vec{\alpha}_\phi = \begin{bmatrix} \cos\phi \\ \sin\phi \end{bmatrix} \quad \text{and} \quad \vec{\beta}_\phi = \begin{bmatrix} -\sin\phi \\ \cos\phi \end{bmatrix} \tag{1.2}$$

The 2D parallel projection computed at angle ϕ is then defined as:

$$p_\phi(s) = p(\phi, s) = \mathscr{R}^2 f(\phi, s) \quad \forall s \in \mathbb{R}. \tag{1.3}$$

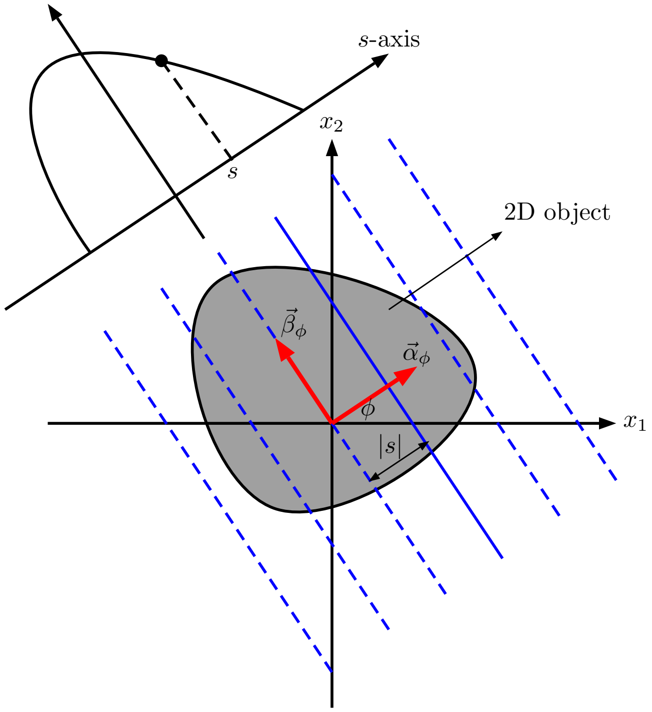

Figure 1.1: 2D parallel geometry: for each value of ϕ, the 2D parallel projection is a single-variable function of s, where $|s|$ being the distance from the origin to a certain line in the parallel beam emitted from the x-ray sources; the value being measured and recorded by the projection is the integral over the considering line.

1.1.2 Helgason-Ludwig consistency conditions (HLCC)

If p is in the range of $\mathscr{R}^2$: $p = \mathscr{R}^2 f$ for some compactly supported function f, then the moment of order n defined as follows:

$$M_n^{2D,\ parallel}(\phi) = \int p_\phi(s)\, s^n ds, \tag{1.4}$$

becomes a homogeneous polynomial in $\cos\phi$ and $\sin\phi$ of degree (at most) n (n is a non-negative integer).

We can see this result in the book [Helgason, 1980]. We can also prove it by simply use the above definition of the moment, the definition of the 2D parallel projections and a change of variables. This is our most inspired condition, since it significantly affects to our ideas of deriving new DCCs. It can be seen in our contributions that almost every new DCC is the polynomial-type condition.

1.1.3 Fourier slice theorem and Filtered Backprojection (FBP) method

With the 2D parallel projections defined in equation (1.3), we have the following relationship:

$$\widehat{p}_\phi(\sigma) = \widehat{f}(\sigma\cos\phi, \sigma\sin\phi), \tag{1.5}$$

where $\widehat{p}_\phi$ and $\widehat{f}$ are the 1D and 2D Fourier transforms of p_ϕ and f, respectively:

$$\widehat{p}_\phi(\sigma) = \int p_\phi(s)\, e^{-2i\pi\sigma s} ds, \tag{1.6}$$

$$\widehat{f}(X_1, X_2) = \iint f(x_1, x_2)\, e^{-2i\pi(X_1x_1 + X_2x_2)} dx_1 dx_2. \tag{1.7}$$

This result can also be proved by using the definitions and the technique of changing variables. It connects the Radon transform and the Fourier transform. Moreover, it is the main tool to construct one of the basic reconstruct method: the Filtered Backprojection (FBP):

If p is in the range of $\mathscr{R}^2$: $p = \mathscr{R}^2 f$ for some compactly supported function f, then:

$$f(x_1, x_2) = \int_0^{\pi} \int |\sigma| \, \widehat{p}_{\phi}(\sigma) \, e^{2i\pi[x_1(\sigma\cos\phi)+x_2(\sigma\sin\phi)]} d\sigma d\phi. \tag{1.8}$$

This theorem can be proved by applying the Fourier slice theorem, the definition of the inverse Fourier transform, with a suitable change of variables.

1.2 3D parallel geometry

As a preparation for chapter 3, we study the 3D parallel geometry. This model is the 3D version of the 2D parallel geometry. We are working in the 3D space, with (x_1, x_2, x_3) as our standard coordinate system. The considered 3D object f is assumed to have compact support. The x-ray sources emit parallel beams going through the 3D object. We recall that in 2D parallel geometry, in order to defined the 2D parallel projections, we need the 2D radon transform $\mathscr{R}^2$. We also need to set up two variables: the angular variable ϕ which characterizes the direction of the parallel beam (or the integrating direction), and the linear variable s which defines the certain line in the parallel beam that being considered for integration. In 3D parallel geometry, everything is similar. We need the 3D Radon transform $\mathscr{R}^3$, and also two variables: a 3D unit vector $\vec{\xi}$ to characterize the integrating direction, and a linear variable s. Now the 3D Radon transform $\mathscr{R}^3$ is an operator maps the 3D function f to the set of its plane integrals; which precisely help us compute the integral over the plane being perpendicular to $\vec{\xi}$ and at distance $|s|$ away from the origin $(0, 0, 0)$:

$$\mathscr{R}^3 f\left(\vec{\xi}, s\right) = \int_{\vec{\xi}^{\perp}} f\left(s\vec{\xi} + \vec{z}\right) d\vec{z}, \quad \forall\vec{\xi} \in \mathbb{S}^2, \forall s \in \mathbb{R}. \tag{1.9}$$

Here the integral $\int_{\vec{\xi}^{\perp}} d\vec{z}$ means that we are integrating over the plane which is perpendicular to $\vec{\xi}$. For a certain 3D unit vector $\vec{\xi}$, the 3D parallel projections is a single variable function, which is defined through the 3D Radon transform $\mathscr{R}^3$:

$$\mathbf{p}_{\vec{\xi}}(s) = \mathbf{p}\left(\vec{\xi}, s\right) = \mathscr{R}^3 f\left(\vec{\xi}, s\right), \quad \forall s \in \mathbb{R}. \tag{1.10}$$

1.3 Divergent geometry

In the divergent geometry in $\mathbb{R}^n$, we take more care of the two particular cases: $n = 2$ (fan-beam geometry) and $n = 3$ (cone-beam geometry). Anyway, in both cases, the divergent projections can be simply defined from a vector $\vec{s} \in \mathbb{R}^n$ showing the source position and a unit vector $\vec{\gamma} \in \mathbb{S}^{n-1}$ showing the integrating direction. There is an object f, which has compact support. The x-ray source emits the divergent beam passing through the object. Then for an arbitrary source position $\vec{s}$, the divergent projection of f computed along the direction $\vec{\gamma}$ is the following:

$$g_{\vec{s}}(\vec{\gamma}) = g(\vec{s}, \vec{\gamma}) = \mathscr{D}f(\vec{s}, \vec{\gamma}) = \int_0^{\infty} f(\vec{s} + t\vec{\gamma}) \, dt, \quad \forall\vec{\gamma} \in \mathbb{S}^{n-1}. \tag{1.11}$$

For $n = 2, 3$, the above definition respectively becomes the definitions of the so-called conventional fan-beam and cone-beam projections. Depending on each considering geometry context, many DCCs can be suitably constructed for the divergent projections.

We are just stopping right here without giving any DCCs for the 3D parallel geometry and the divergent geometry for two reasons. The first one is that we would like to save them for the presentations of the following chapters. In each chapter of the contributions, we discuss in details the corresponding DCCs in each geometry context and their applications in the suitable geometric self-calibration problems. The other obvious reason is the length of the manuscript.

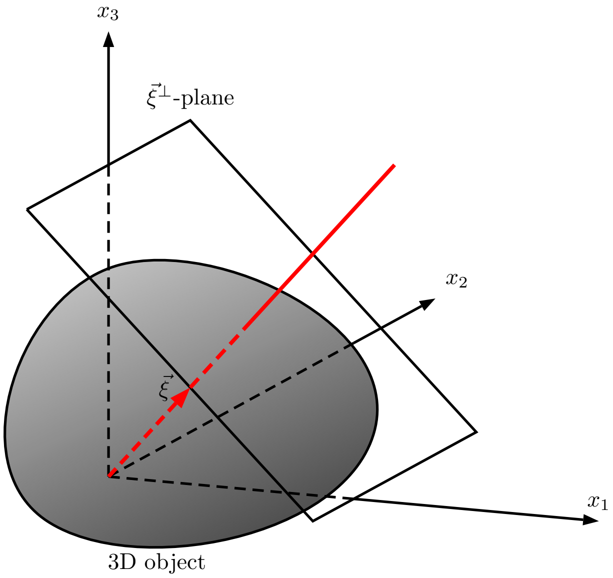

Figure 1.2: 3D parallel geometry: for each 3D unit vector $\vec{\xi}$, the 3D parallel projection is a single-variable function of s; it records the integral over the plane, which is perpendicular to $\vec{\xi}$ and at distance $|s|$ from the origin $(0,0,0)$.

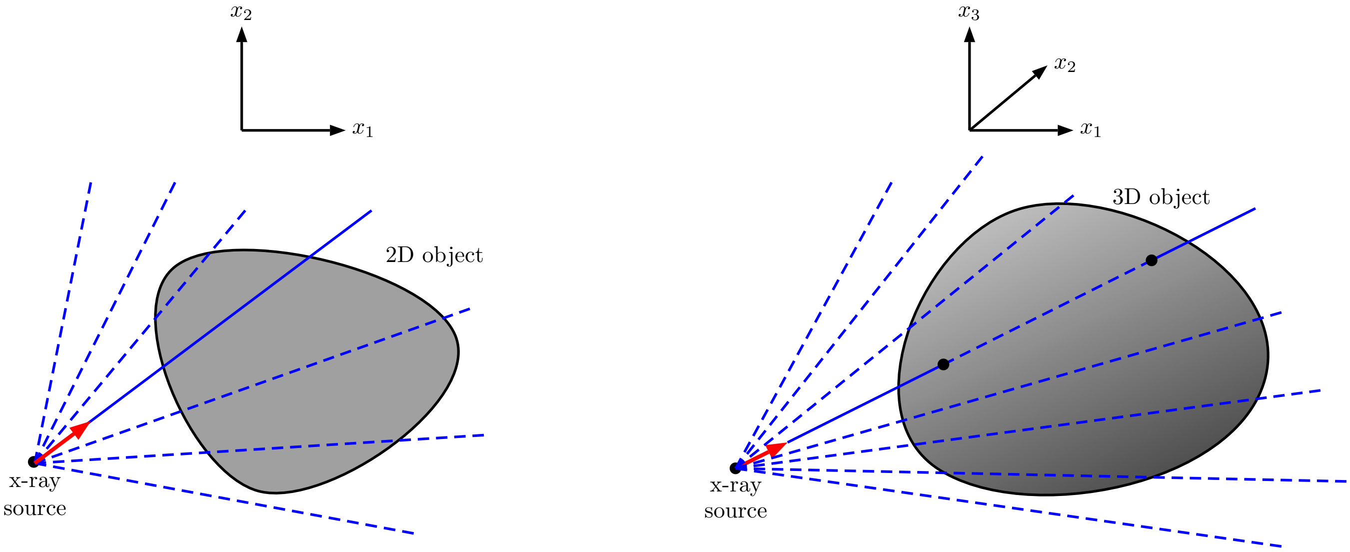

Figure 1.3: Divergent geometry: fan-beam geometry (left) and cone-beam geometry (right); in both cases, the x-ray source emits a divergent beam going through the object; the unit vector going from the x-ray source (in 2D and 3D respectively) characterizes the integrating direction, leading to the corresponding conventional divergent projection.

Thus as mentioned, we are now going to visit each particular geometry context, the corresponding DCCs will be presented in details, and we also try to apply them into some geometric calibration problems, to find analytic methods, which can estimate the geometric parameters fast and correctly.

Chapter 2

DCCs for 3D parallel projections and applications

French summary of the content

Dans ce chapitre, nous étudions les DCC en géométrie parallèle 3D, c'est à dire de la transformée en rayon-X qui modélise la projection radiographique parallèle d'un objet f. Notre objectif principal est d'appliquer ces DCC à l'auto-calibration géométrique de l'acquisition d'une succession de projections radiographiques parallèles.

En 2D, Basu et Bresler [Basu and Bresler, 2000a] ont montré, que pour presque tout objet mesuré, à partir de 9 projections parallèles (transformée de Radon), les angles des projections peuvent être identifiés à partir des DCC d'ordre 0, 1, 2. L'identification est bien sûr à une classe d'équivalence près incluant des transformations de l'objet initial (et de manière équivalente du système de mesure) par rotation, symétrie et translation (par exemple, l'angle de projection est nécessairement relatif à l'objet et a priori, on ne connaît pas l'orientation de l'objet. Autrement dit, si l'objet tourne d'un angle ϕ et que le système de mesure tourne aussi du même angle ϕ, les projections seront identiques).

En 3D, les travaux de [Van Heel, 1987] et [Van Heel et al., 1997] poursuivis dans [Shkolnisky and Singer, 2012], [Singer and Shkolnisky, 2011], utilisent le "Fourier Slice Theorem" ou "théorème de coupe-projection", pour l'auto détermination des directions de projection. Soit la projection dans la direction $\vec{\gamma}$ d'un objet f, définie à l'équation (2.1), la transformée de Fourier 2D du plan de projection est la coupe perpendiculaire à $\vec{\gamma}$ de la transformée de Fourier de f (c'est le "théorème de coupe projection" donné ici par l'équation (2.2e)). Ainsi, si on dispose de deux projections du même objet, respectivement dans les directions $\vec{\gamma_1}$ et $\vec{\gamma}$, les deux plans respectivement perpendiculaires à $\vec{\gamma_1}$ et $\vec{\gamma}$ de la transformée de Fourier de f, issus du théorème de coupe-projection, ont à leur intersection une droite commune, dans la direction $\vec{\eta_1}$ perpendiculaire à $\vec{\gamma_1}$ et $\vec{\gamma}$. Si on dispose d'une projection dans la direction $\vec{\gamma_2}$ alors on pourra construire de la même manière une direction $\vec{\eta_2}$ perpendiculaire à $\vec{\gamma_2}$ et $\vec{\gamma}$. On peut ainsi, dans les cas non dégénérés, déterminer la direction $\vec{\gamma}$ comme le produit vectoriel des vecteurs $\vec{\eta_1}$ et $\vec{\eta_2}$, donc d'une troisième direction de projection à partir de trois projections dont deux directions sont connues.

Notre approche est similaire à celle de van Heel. Nous supposons que deux directions indépendantes sont connues et nous déterminons une troisième direction de projection à partir des projections associées à ces trois directions. Pour cela, nous appliquons la transformée de Radon 2D et trouvons les paires de lignes qui sont égales dans chacune des deux paires de la transformée de Radon 2D.

Dans la section 2.2, nous introduisons les projections 3D parallèles. Nous définissons la transformée en rayons-X 3D, équation (2.4). Dans la section 2.3, nous établissons un lien avec la transformée de Radon 3D, équation (2.7) et dans 2.4 nous construisons les résultats théoriques (équation (2.13)) basés sur des DCCs afin de résoudre le problème de calibration géométrique. Dans la section 2.5 nous développons une stratégie pour identifier les paramètres de calibration géométrique : dans 2.5.1 et 2.5.2 nous identifions la direction de projection $\vec{\gamma}$ à partir des données de projection $p_{\vec{\gamma}}$ et des projections du même objet suivant $\vec{e}_2$ et $\vec{e}_3$. Dans la section 2.6 nous présentons notre algorithme de correspondance de lignes "row-matching algorithm" qui est une étape nécessaire à notre méthode de calibration géométrique. Dans la section 2.7 and 2.8 nous présentons des expérimentations numériques. Dans la section 2.9 nous traitons les cas "dégénérés". Dans section section 2.10 nous proposons quelques commentaires, en particulier l'identification des translations de détecteurs ("shifts") grâce à la propriété bien connue : la projection parallèle du centre de masse de l'objet est le centre de masse de la projection parallèle de l'objet. Et enfin, la section 2.11 regroupe toutes les images issues des simulations numériques.

2.1 Introduction

Most of the content of this chapter is a presentation of our proceedings paper [Nguyen et al., 2020a] in the SPIE Medical Imaging 2020 conference. There are some new results added after the proceedings were published, which were obtained at a later stage of the thesis.

In this chapter, we are working in 3D parallel geometry. Our aim is to find some data consistency conditions (DCCs) on the parallel projections and to apply them to solve the corresponding geometric calibration problem. It is the problem to estimate the geometric parameters of each projection, where the projection data is given in advance and the 3D object is assumed to be unknown. In general, the final objective in Medical Imaging is to reconstruct the unknown 3D object from given 2D projections. However, it is necessary to align all the projections together first, and this step requires the geometric parameters of the projections to be known. In 3D parallel geometry, the crucial parameters in each projection are the viewing direction, the unknown shift and the in-plane angle. More precisely, in our context, there is an unknown 3D object, we know some of its 2D parallel projections and we want to estimate the corresponding viewing directions, unknown shifts and in-plane angles of these projections.

The 2D version of this calibration problem was considered by Basu and Bresler in [Basu and Bresler, 2000b] and [Basu and Bresler, 2000a]. We identify the most important result in their work, which can be re-stated as: *In 2D, if we have a sufficient number of parallel projections, then the viewing angle of each projection can be uniquely determined (in 2D, the viewing direction is characterized only by the viewing angle), for almost any 2D object.* The uniqueness mentioned here has to be understood in the sense of equivalent classes. In fact, we can never obtain the unique solution of the viewing directions (or viewing angles in 2D) of the projections if we know nothing about the initial orientation of the object. For instance, in 2D, let $\mathcal{S}$ be our object, which is at somewhere near the world origin. We compute the parallel projections of $\mathcal{S}$ (by taking the 2D Radon transform) at angles $\phi = 30°, 40°, 90°, 120°$ and obtain our first set of four parallel projections. Now if we rotate the object $\mathcal{S}$ $70°$ counter-clockwise, and take the parallel projections of this rotated object at angles $\phi = 100°, 110°, 160°, 190°$, we will obtain a second set of four projections, which is exactly the same as the first one. Or even if we take the original $\mathcal{S}$ and reflect it over the x_2-axis, and take the parallel projections of this reflected object at angles $\phi = 150°, 140°, 90°, 60°$, we once again obtain a third set of four projections which perfectly match the first set. We use this example to show that the same set of projections of the object can be obtained from many different sets of viewing angles if the initial orientation of the object is changed. Thus, in our inverse problem, with only the projection data and without knowing anything about the object (which means we do not know its initial orientation either), we can point out such many sets of suitable corresponding viewing angles that these projections have probably been taken at, since we ourselves do not know the initial orientation of the object. However, all these sets of viewing-angle solutions link together, and they are clearly defined to be in the same equivalent class in the paper [Basu and Bresler, 2000b]. That is the reason why we only obtain the uniqueness of the solutions of the viewing directions (or viewing angles) in the sense of equivalent classes. The significant thing is that Basu and Bresler prove for almost any 2D objects, the viewing directions (in the sense of equivalent classes) can be uniquely and stably resolved, directly and only from the projection data using the moment conditions (or the DCCs) of order $0, 1, 2, 3$, if we have sufficient parallel projections, through constructing a lot of theoretical results, with the main cornerstone being the Bezout's theorem.

Before the work of Basu and Bresler, the 3D version of this geometric calibration problem was of interest in the field of Electron Microscopy. With the similar final goal to reconstruct the 3D structure from many given 2D parallel projections, the step of calibrating the geometric parameters of each projection is necessary. In order to obtain this information, van Heel introduced the *angular reconstitution* method in his papers [Van Heel, 1987] and [Van Heel et al., 1997]. In his work, van Heel claimed that at least three projections are required as the data, we are now calling them projections 1, 2 and 3. One similar detail to what we have just seen above is the fact that we cannot exactly obtain the unique solution to the direction of each projection, if we only have the projection data, without any knowledge about the initial orientation of the 3D object. Thus, in order to determine the viewing directions of the parallel projections, van Heel assumed that the direction of projection 1 is $\pm(1, 0, 0)$ (the unit vector being parallel to the x_1-axis); and the direction of projection 2 is in the plane $x_3 = 0$. Under these assumptions, he can clearly determine the directions of projections 2 and 3. We can see that van Heel's assumptions did affect the initial orientation of the 3D object (it is now not arbitrary or naively and completely unknown). In other words, from the knowledge of Basu and Bresler's articles, the way van Heel did is equivalent to choosing an initial orientation of the 3D object, and the result he obtained thus can be understood as a member of the equivalent class of the solutions to the viewing directions of the projections. Concerning the details of the *angular reconstitution* method, from the data of three parallel projections, van Heel applied the 2D Radon transform to obtain the corresponding sinograms. He compared the sinograms pair-wise to find which row in one sinogram matched some row in the other sinogram. Each of these matching rows related to the common line of two slices through the 3D Fourier transform of the 3D object (we will explain about these common lines in the next paragraph, but the crucial information of the common lines is that it is enough to compute the viewing directions of the projections). Although with this construction, van Heel could not immediately find the common lines after the step of finding the matching rows, he was still able to determine the angles between the common lines. With those angles and the assumptions on the directions of the first and second projections, he could determine the three corresponding common lines. From that, the three directions of three parallel projections can be computed by taking the suitable cross products of the directions of the common lines, with the meaning that the obtained set of solutions is one member of the class.

The key in van Heel's construction is the Fourier-slice theorem. Singer and Shkolnisky also used this idea to build their own method to deal with the same 3D geometric calibration problem, see [Shkolnisky and Singer, 2012], [Singer and Shkolnisky, 2011]. We recall the Fourier-slice theorem to understand about the mentioned common lines. Let $\left(\vec{\alpha}, \vec{\beta}, \vec{\gamma}\right)$ be a set of three pair-wise perpendicular unit vectors in 3D, and let the 3D object be represented by f, which is a real-valued function with compact support. The 2D parallel projection of f taken in the direction $\vec{\gamma}$ can be defined as:

$$p_{\vec{\gamma}}\left(u, v\right) = \int f\left(u\vec{\alpha} + v\vec{\beta} + t\vec{\gamma}\right) dt. \tag{2.1}$$

Then the 2D Fourier transform of an arbitrary parallel projection can be computed as follows:

$$\begin{aligned}
P_{\vec{\gamma}}\left(U, V\right) &= \iint p_{\vec{\gamma}}\left(u, v\right) e^{-2i\pi(Uu+Vv)} dudv && \text{(2.2a)}\\
&= \iiint f\left(u\vec{\alpha} + v\vec{\beta} + t\vec{\gamma}\right) e^{-2i\pi(Uu+Vv)} dtdudv && \text{(2.2b)}\\
&= \iiint f\left(\vec{x}\right) e^{-2i\pi\left[U(\vec{x}\cdot\vec{\alpha})+V\left(\vec{x}\cdot\vec{\beta}\right)\right]} d\vec{x} && \text{(2.2c)}\\
&= \iiint f\left(\vec{x}\right) e^{-2i\pi\left[\vec{x}\cdot\left(U\vec{\alpha}+V\vec{\beta}\right)\right]} d\vec{x} && \text{(2.2d)}\\
&= F\left(U\vec{\alpha} + V\vec{\beta}\right), && \text{(2.2e)}
\end{aligned}$$

here we use the capital letters P and F to denote the corresponding functions after applying the Fourier transform of the 2D projection p and to the 3D object function f. We can see that $\left(U\vec{\alpha} + V\vec{\beta}\right)$ is the plane going through the world origin $(0, 0, 0)$ and perpendicular to $\vec{\gamma}$, so $F\left(U\vec{\alpha} + V\vec{\beta}\right)$ is the slice of this plane through the 3D Fourier transform of the object. In short, we can state the Fourier-slice theorem as follows: the 2D Fourier transform of an arbitrary parallel projection is the slice through the 3D Fourier transform of the object, caused by the plane going through the world origin and being perpendicular to the viewing direction of the considered projection. Thus if we have two distinct parallel projections, their 2D Fourier transforms will correspond to two planes, each of which slices through the 3D Fourier transform of the same object. These two planes have one point in common, which is the world origin $(0, 0, 0)$, so there must exist a line of intersection of the two planes. That line of intersection is called the common line. As shown in the Fourier-slice theorem above, the corresponding plane is perpendicular to the direction of the considered parallel projection. This leads to the fact that the common line, which is on both corresponding planes, will thus be perpendicular to both directions of the two considering projections. So, if we have three distinct parallel projections 1, 2 and 3, the common line built from projections 1 and 2 and the common line built from projections 1 and 3, both will be perpendicular to the direction of projection 1. The same thing happens to the directions of projections 2 and 3. Hence, knowing the common lines leads to the determination of the directions of the projections, by simply taking the cross product of the directions of the corresponding common lines. While van Heel found the angles between the common lines, and made the assumptions on the directions of projections 1 and 2, in order to completely determine the directions of the three projections, Singer and Shkolnisky rewrote the definition of parallel projections matrix form, used the Fourier-slice theorem, then converted the calibration problem into an optimization problem, see [Singer and Shkolnisky, 2011], or used the algebraic tools to deal with the problem, see [Shkolnisky and Singer, 2012]. In the paper [Singer et al., 2010], Singer *et al* present a voting algorithm to determine the common lines, to handle the extremely small and noisy projection images in Cryo-electron Microscopy.

Our approach is quite similar to that of van Heel. We assume that we have three parallel projections, and we know the viewing directions of two of them, so the result of the unknown direction we obtain is perfectly unique (but the whole set of viewing directions of three projections is just one member of the equivalent class of the solutions, if there is no direction known in advance). Our method is to directly apply the 2D Radon transform to the given parallel projections and to then find the matching rows in those sinograms. By doing this, we obtain a pair-wise

DCC on the parallel projections. We build the common unit vectors from the information of these matching rows. These common unit vectors are perpendicular to the corresponding directions of the projections, which means they geometrically have the same directions as the common lines in the papers of van Heel, Singer and Shkolnisky. Therefore, as van Heel did, we simply take the suitable cross product of the common unit vectors to obtain the result of the unknown viewing direction. So by a different approach rather than using the Fourier-slice theorem, our method can produce an analytic formula of the unique solution to the unknown viewing direction, and the formula is rapid to compute. The unknown shifts and the in-plane angles are also be handled. Additionally, we provide a method to work with the particular degenerate case of the problem. Our method can also work if we have more than three parallel projections. As long as we know the directions of two projections, we can calibrate all of the remaining unknown directions, one at a time, repeating the same procedure dealing with a triplet of projections (two known directions and one unknown).

The structure of this chapter is as the following: section 2.2 formally defines the 3D parallel projections, section 2.3 and 2.4 build the main theory and the DCC to solve the calibration problem, section 2.5 gives the problem statement and the solving strategy, section 2.6 presents our row-matching algorithm, section 2.7 and 2.8 present the numerical experiments, section 2.9 gives us the method to deal with the particular degenerate case of the problem, section 2.10 gives some discussions and comments, and finally all of the simulation images are shown in section 2.11.

2.2 3D coordinate system and 3D parallel projections

Our aim in this section is to define 3D parallel projections more specifically. We work in the 3D parallel geometry, with (x_1, x_2, x_3) as our standard coordinate system. Given a 3D unit vector $\overline{\gamma} = (\gamma_1, \gamma_2, \gamma_3)$, we firstly define two other 3D unit vectors $\overline{\alpha}_\gamma$ and $\overline{\beta}_\gamma$, depending on $\overline{\gamma}$, as follows:

- If $\gamma_3 \neq 0$ and $|\gamma_3| \neq 1$ (so $\gamma_1^2 + \gamma_2^2 \neq 0$), then we define:

$$\begin{cases} \overline{\alpha}_\gamma = \dfrac{\operatorname{sgn}(\gamma_3)}{\sqrt{\gamma_1^2+\gamma_2^2}} \left(-\gamma_2, \gamma_1, 0\right), \\ \overline{\beta}_\gamma = \dfrac{1}{\sqrt{\gamma_1^2+\gamma_2^2}} \left(-\gamma_1\gamma_3, -\gamma_2\gamma_3, \gamma_1^2+\gamma_2^2\right). \end{cases} \tag{2.3}$$

- If $\gamma_3 = 0$ and $\gamma_2 \neq 0$, then $\overline{\gamma} = (\gamma_1, \gamma_2, 0)$ and we define: $\overline{\alpha}_\gamma = \operatorname{sgn}(\gamma_2)(-\gamma_2, \gamma_1, 0)$ and $\overline{\beta}_\gamma = (0, 0, 1)$.
- If $\gamma_3 = 0$ and $\gamma_2 = 0$, then $\overline{\gamma} = \pm(1, 0, 0)$ and we define: $\overline{\alpha}_\gamma = (0, 1, 0)$ and $\overline{\beta}_\gamma = (1, 0, 0)$.
- If $|\gamma_3| = 1$ (so $\gamma_1 = \gamma_2 = 0$), this means $\overline{\gamma} = \pm(0, 0, 1)$, then we define: $\overline{\alpha}_\gamma = (-1, 0, 0)$ and $\overline{\beta}_\gamma = (0, -1, 0)$.

Under these definitions, it can easily be verified that $\left(\overline{\alpha}_\gamma, \overline{\beta}_\gamma, \overline{\gamma}\right)$ form a set of three pair-wise perpendicular vectors.

We assume that there exists a 3D object, which is mathematically a real function f with compact support, being somewhere near the world origin $(0, 0, 0)$. The x-ray source emits a parallel beam going through the 3D object and hitting a flat detector. The direction of this parallel beam is $\overline{\gamma}$ and the detector is a perpendicular plane to $\overline{\gamma}$. On this 2D detector, the origin is the parallel projection of the world origin and the two standard coordinate axes are the u and v axes, which have the same directions as $\overline{\alpha}_\gamma$ and $\overline{\beta}_\gamma$ respectively. Figure 2.1 gives an illustration. From this construction of $\left(\overline{\alpha}_\gamma, \overline{\beta}_\gamma, \overline{\gamma}\right)$, we can define the parallel projection computed in the direction $\overline{\gamma}$, which is denoted as $p_{\overline{\gamma}}$, by the 3D X-ray transform.

Given a 3D compactly-supported real-valued function f, the parallel projection $p_{\overline{\gamma}} = \mathscr{X}^3_{\overline{\gamma}} f$ is defined as follows:

$$p_{\overline{\gamma}}(u, v) = \mathscr{X}^3_{\overline{\gamma}} f(u, v) = \int f\left(u\overline{\alpha}_\gamma + v\overline{\beta}_\gamma + t\overline{\gamma}\right) dt, \tag{2.4}$$

where $\mathscr{X}^3_{\overline{\gamma}}$ is the 3D X-ray transform.

Comments

- We can note from this construction of $\left(\overline{\alpha}_\gamma, \overline{\beta}_\gamma, \overline{\gamma}\right)$, that $\overline{\alpha}_\gamma$ is always on the plane $x_3 = 0$. The unit vector $\overline{\alpha}_\gamma$ can be visualized by projecting $\overline{\gamma}$ onto the plane $x_3 = 0$ and then rotating it a 90^0 angle counter-clockwise or clockwise, depending on the direction of $\overline{\gamma}$.

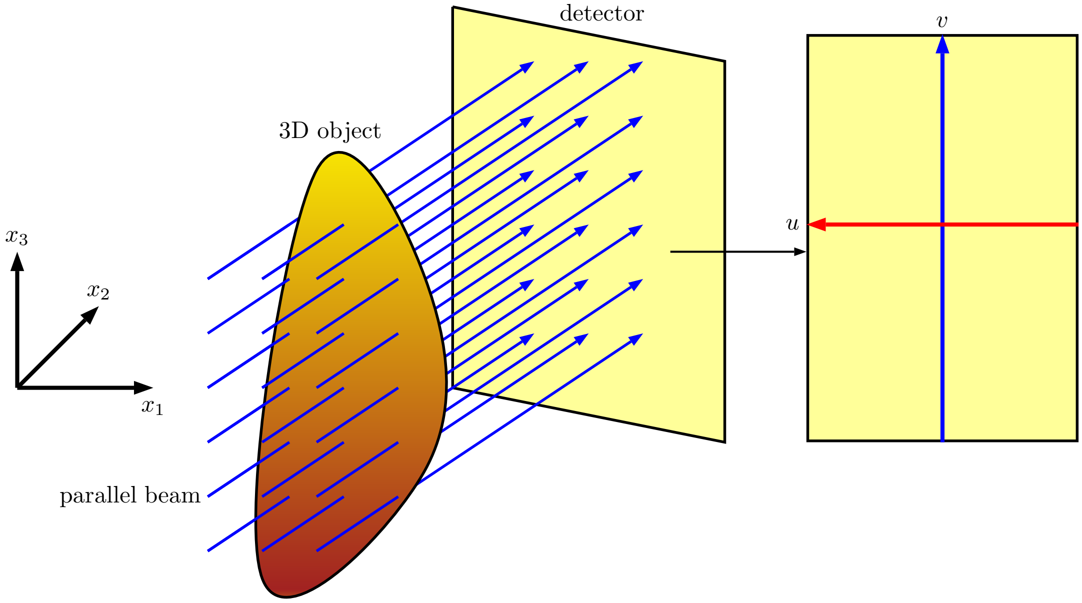

Figure 2.1: The model of 3D parallel geometry

- Our detailed definitions of $\left(\overline{\alpha}_\gamma, \overline{\beta}_\gamma, \overline{\gamma}\right)$ are motivated by the fact that for a certain coordinate (u,v) on the 2D detector, the parallel projection computed along directions $\overline{\gamma}$ and $-\overline{\gamma}$ have to be exactly the same. Mathematically, we need:

$$p_{\overline{\gamma}}\left(u,v\right) = p_{-\overline{\gamma}}\left(u,v\right), \ \forall \left(u,v\right) \in \mathbb{R}^2. \tag{2.5}$$

  And here, the definition of $\left(\overline{\alpha}_\gamma, \overline{\beta}_\gamma, \overline{\gamma}\right)$ leaves $\overline{\alpha}_\gamma$ and $\overline{\beta}_\gamma$ unchanged when $\overline{\gamma}$ changes to $-\overline{\gamma}$ (we can easily check this fact by just replacing $(\gamma_1, \gamma_2, \gamma_3)$ by $(-\gamma_1, -\gamma_2, -\gamma_3)$ in the definitions of $\overline{\alpha}_\gamma$ and $\overline{\beta}_\gamma$). Besides, by a simple change of variables, we can see that:

$$p_{-\overline{\gamma}}\left(u,v\right) = \int f\left(u\overline{\alpha}_{-\gamma} + v\overline{\beta}_{-\gamma} + t\left(-\overline{\gamma}\right)\right) dt = \int f\left(u\overline{\alpha}_\gamma + v\overline{\beta}_\gamma - t\overline{\gamma}\right) dt = \int f\left(u\overline{\alpha}_\gamma + v\overline{\beta}_\gamma + t\overline{\gamma}\right) dt = p_{\overline{\gamma}}\left(u,v\right), \tag{2.6a}$$

  and this property is what we expect in the definition of parallel projections. The mathematical requirement of equation (2.4) forces the $\left(\overline{\alpha}_\gamma, \overline{\beta}_\gamma, \overline{\gamma}\right)$ system to sometimes be right-handed, and sometimes left-handed, depending on the direction of $\overline{\gamma}$.

2.3 Relation between 3D X-ray transform and 3D Radon transform

In this section, we seek the relationship between the 3D X-ray transform and the 3D Radon transform, because it is the main material to build the pair-wise DCCs applying on two arbitrary 3D parallel projections.

Given a 3D object f, which has compact support, and given any $\overline{\gamma} \in \mathbb{S}^2$; if $p_{\overline{\gamma}} = \mathscr{X}^3_{\overline{\gamma}} f$, then for any angle $\theta \in [0, 2\pi)$, we have:

$$\mathscr{R}^2_\theta p_{\overline{\gamma}}\left(s\right) = \mathscr{R}^3_{\overline{\zeta}} f\left(s\right), \ \forall s \in \mathbb{R}, \tag{2.7}$$

where $\overline{\zeta} = \cos\theta \overline{\alpha}_\gamma + \sin\theta \overline{\beta}_\gamma$.

Mathematically, we can quickly prove this result by using the definition (2.4), in conjunction with the definitions

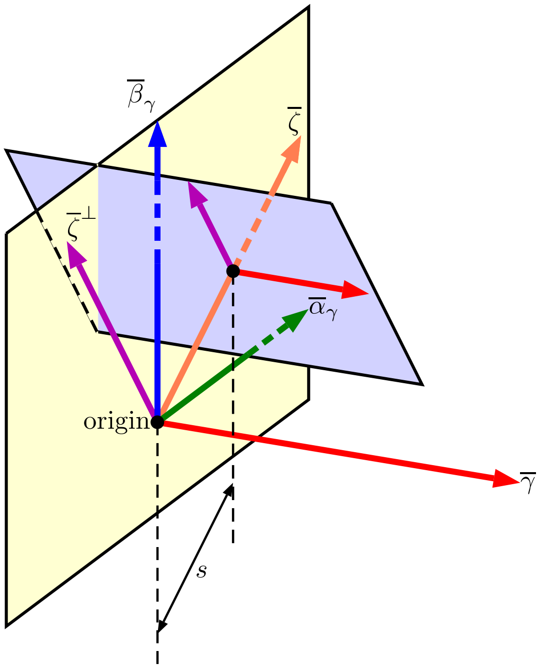

Figure 2.2: Illustration of the vectors system, the corresponding result shows that for all real values s, $\mathscr{R}^2_\theta p_{\overline{\gamma}}(s)$ and $\mathscr{R}^3_{\overline{\zeta}} f(s)$ coincide, because they both compute the same integral of the object f over the light-violet plane.

of the 2D and 3D Radon transform. For all $s \in \mathbb{R}$, we can see that:

$$\mathscr{R}^2_\theta p_{\overline{\gamma}}(s) = \int p_{\overline{\gamma}}(s\cos\theta - t'\sin\theta, s\sin\theta + t'\cos\theta)\,dt' \tag{2.8a}$$

$$= \iint f\left((s\cos\theta - t'\sin\theta)\,\overline{\alpha}_\gamma + (s\sin\theta + t'\cos\theta)\,\overline{\beta}_\gamma + t\overline{\gamma}\right) dtdt' \tag{2.8b}$$

$$= \iint f\left(s\left(\cos\theta\overline{\alpha}_\gamma + \sin\theta\overline{\beta}_\gamma\right) + t'\left(-\sin\theta\overline{\alpha}_\gamma + \cos\theta\overline{\beta}_\gamma\right) + t\overline{\gamma}\right) dtdt' \tag{2.8c}$$

$$= \iint f\left(s\overline{\zeta} + t'\overline{\zeta}^\perp + t\overline{\gamma}\right) dtdt'. \tag{2.8d}$$

Here we set $\overline{\zeta} = \cos\theta\overline{\alpha}_\gamma + \sin\theta\overline{\beta}_\gamma$ and $\overline{\zeta}^\perp = -\sin\theta\overline{\alpha}_\gamma + \cos\theta\overline{\beta}_\gamma$. The two vectors $\left(\overline{\zeta}, \overline{\zeta}^\perp\right)$ are both in the plane spanned by $\overline{\alpha}_\gamma$ and $\overline{\beta}_\gamma$ and can be obtained by rotating $\left(\overline{\alpha}_\gamma, \overline{\beta}_\gamma\right)$ counter-clockwise by angle θ. The three vectors $\left(\overline{\gamma}, \overline{\zeta}, \overline{\zeta}^\perp\right)$ are pair-wise perpendicular, so the above integral $\iint f\left(s\overline{\zeta} + t'\overline{\zeta}^\perp + t\overline{\gamma}\right) dtdt'$ equals $\mathscr{R}^3_{\overline{\zeta}} f(s)$. Hence, we obtain the result.

We can also understand this result geometrically by considering figure (2.2). For a certain value of s, the 3D Radon transform $\mathscr{R}^3_{\overline{\zeta}} f(s)$ computes the integral of f over the plane, which is at distance s from the origin and perpendicular to $\overline{\zeta}$ direction: the light-violet plane in the diagram. Two unit vectors that are parallel to this plane and perpendicular to each other are $\overline{\gamma}$ and $\overline{\zeta}^\perp$, because of the above construction of $\left(\overline{\gamma}, \overline{\zeta}, \overline{\zeta}^\perp\right)$. So another way to obtain this plane-integration value, is to integrate the 2D slice of the 3D object f on the light-violet plane, firstly along the $\overline{\gamma}$ direction (red direction) and then along the $\overline{\zeta}^\perp$ direction (purple direction). Equivalently, we can take the X-ray transform along $\overline{\gamma}$ direction, to obtain a 2D parallel projection on the detector, which is perpendicular to $\overline{\gamma}$ direction or parallel to the $\left(\overline{\alpha}_\gamma, \overline{\beta}_\gamma\right)$ plane (light-yellow plane). Then we continue by taking the 2D Radon transform of the obtained parallel projection along the line that is at distance s from the detector's origin, and is parallel direction to the $\overline{\zeta}^\perp$ direction. This geometrical description coincides with equation (2.8d) and thus illustrates the result, equation (2.7).

2.4 Pair-wise DCCs of the 2D parallel projections

From the crucial result (2.7) in the previous section on the relationship between the parallel projection and the corresponding 3D Radon transform, we can build a pair-wise DCC, which is applied to two parallel projections. Given two arbitrary unit directions $\overline{\gamma}, \overline{\gamma}' \in \mathbb{S}^2$ and two angles θ and θ' in $[0, 2\pi)$, then according to the result (2.7):

$$\begin{cases} \mathscr{R}^2_{\theta} p_{\overline{\gamma}}\left(s\right) = \mathscr{R}^3_{\overline{\zeta}} f\left(s\right), \ \forall s \in \mathbb{R}^2 \\ \mathscr{R}^2_{\theta'} p_{\overline{\gamma}'}\left(s\right) = \mathscr{R}^3_{\overline{\zeta}'} f\left(s\right), \ \forall s \in \mathbb{R}^2 \end{cases}, \tag{2.9}$$

where

$$\begin{cases} \overline{\zeta} = \cos\theta \ \overline{\alpha}_{\gamma} \ + \sin\theta \ \overline{\beta}_{\gamma} \\ \overline{\zeta}' = \cos\theta' \overline{\alpha}_{\gamma'} + \sin\theta' \overline{\beta}_{\gamma'} \end{cases}, \tag{2.10}$$

and where $\left(\overline{\alpha}_{\gamma}, \overline{\beta}_{\gamma}\right)$, $\left(\overline{\alpha}_{\gamma'}, \overline{\beta}_{\gamma'}\right)$ are computed based on $\overline{\gamma}$, $\overline{\gamma}'$ respectively. If we can find two suitable angles θ and θ' such that:

$$\cos\theta \overline{\alpha}_{\gamma} + \sin\theta \overline{\beta}_{\gamma} = \cos\theta' \overline{\alpha}_{\gamma'} + \sin\theta' \overline{\beta}_{\gamma'}, \tag{2.11}$$

then $\overline{\zeta} = \overline{\zeta}'$, and this leads $\mathscr{R}^2_{\theta} p_{\overline{\gamma}}\left(s\right)$ and $\mathscr{R}^2_{\theta'} p_{\overline{\gamma}'}\left(s\right)$ to coincide each other. From this, we can state the pair-wise DCC as the following:

Given two parallel projections taken along two arbitrary directions $\overline{\gamma}, \overline{\gamma}' \in \mathbb{S}^2$, if we can find a pair of suitable angles $\left(\theta, \theta'\right) \in [0, 2\pi)^2$ such that:

$$\cos\theta \overline{\alpha}_{\gamma} + \sin\theta \overline{\beta}_{\gamma} = \cos\theta' \overline{\alpha}_{\gamma'} + \sin\theta' \overline{\beta}_{\gamma'}, \tag{2.12}$$

then for all $s \in \mathbb{R}$:

$$\mathscr{R}^2_{\theta} p_{\overline{\gamma}}\left(s\right) = \mathscr{R}^2_{\theta'} p_{\overline{\gamma}'}\left(s\right). \tag{2.13}$$

Comment

We can see that for any two given unit directions $\overline{\gamma}$ and $\overline{\gamma}'$, there always exist two angles θ and $\theta' \in [0, 2\pi)$ satisfying the conditions (2.12) and (2.13). The reason is as follows:

- If $\overline{\gamma} = \overline{\gamma}'$, then $\left(\overline{\alpha}_{\gamma}, \overline{\beta}_{\gamma}\right)$ coincides with $\left(\overline{\alpha}_{\gamma'}, \overline{\beta}_{\gamma'}\right)$, $p_{\overline{\gamma}}$ coincides with $p_{\overline{\gamma}'}$, then we can freely choose $\theta = \theta' = \theta_0$; for any choices of θ_0 in $[0, 2\pi)$, the conditions (2.12) and (2.13) always hold.

- If $\overline{\gamma} = -\overline{\gamma}'$, then:

  $$\begin{cases} \overline{\alpha}_{\gamma} = \overline{\alpha}_{-\gamma'} = \overline{\alpha}_{\gamma'} \\ \overline{\beta}_{\gamma} = \overline{\beta}_{-\gamma'} = \overline{\beta}_{\gamma'} \\ p_{\overline{\gamma}}\left(u, v\right) = p_{-\overline{\gamma}'}\left(u, v\right) = p_{\overline{\gamma}'}\left(u, v\right), \forall \left(u, v\right) \in \mathbb{R}^2 \end{cases}, \tag{2.14}$$

  because the definitions of $\overline{\alpha}_{\gamma'}$, $\overline{\beta}_{\gamma'}$ and $p_{\overline{\gamma}'}$ remain the same as $\overline{\alpha}_{-\gamma'}$, $\overline{\beta}_{-\gamma'}$ and $p_{-\overline{\gamma}'}$, when $-\overline{\gamma}'$ becomes $\overline{\gamma}'$, as explained in section 2.2. Thus this case is exactly the same as the above case.

- If $\overline{\gamma} \neq \pm\overline{\gamma}'$, meaning $\overline{\gamma}$ and $\overline{\gamma}'$ are not collinear, then even though θ and θ' are unknown, if they exist and satisfy the condition (2.12), then $\overline{\zeta} = \cos\theta \overline{\alpha}_{\gamma} + \sin\theta \overline{\beta}_{\gamma} = \cos\theta' \overline{\alpha}_{\gamma'} + \sin\theta' \overline{\beta}_{\gamma'}$ is the vector that is on the line of intersection of two planes $\left(\overline{\alpha}_{\gamma}, \overline{\beta}_{\gamma}\right)$ and $\left(\overline{\alpha}_{\gamma'}, \overline{\beta}_{\gamma'}\right)$, and thus is perpendicular to both $\overline{\gamma}$ and $\overline{\gamma}'$. Conversely, for any two given directions $\overline{\gamma}$ and $\overline{\gamma}'$, we can choose:

  $$\overline{\psi} = \frac{\overline{\gamma} \times \overline{\gamma}'}{\|\overline{\gamma} \times \overline{\gamma}'\|}, \tag{2.15}$$

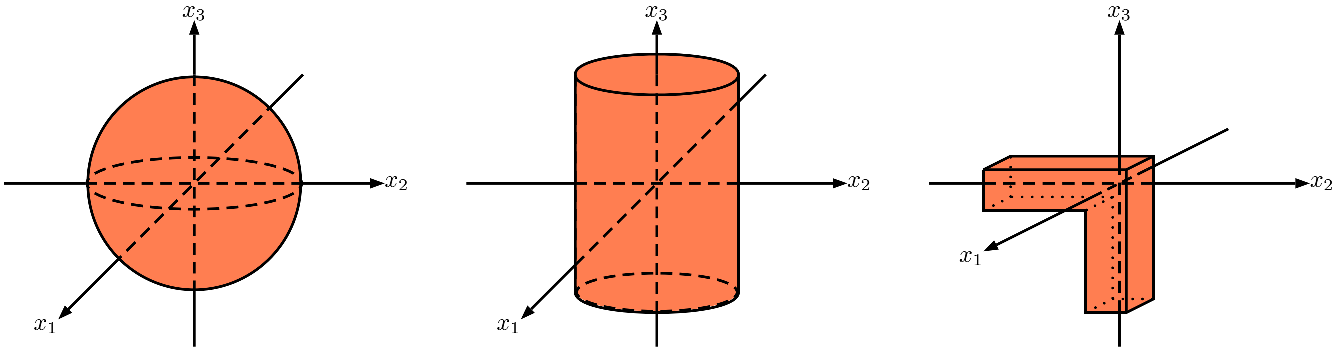

Figure 2.3: Examples of some 3D objects that do not satisfy the theoretical assumption: a ball (left), a vertical cylinder (middle) and an L-shape (right) with uniform density and the centers-of-mass at the origin; the L-shape has two cuboid branches of equal length.

which is a unit vector perpendicular to $\overline{\gamma}$ and $\overline{\gamma}'$. The vector $\overline{\psi}$ always exists, because $\|\overline{\gamma} \times \overline{\gamma}'\| \neq 0$, when $\overline{\gamma}$ and $\overline{\gamma}'$ are not collinear. Now θ and θ' can be found by the following formulae:

$$\begin{cases} \cos\theta = \overline{\psi} \cdot \overline{\alpha}_\gamma \\ \sin\theta = \overline{\psi} \cdot \overline{\beta}_\gamma \end{cases}, \qquad \begin{cases} \cos\theta' = \overline{\psi} \cdot \overline{\alpha}_{\gamma'} \\ \sin\theta' = \overline{\psi} \cdot \overline{\beta}_{\gamma'} \end{cases}. \tag{2.16}$$

This pair of angles (θ, θ') will satisfy the condition (2.12):

$$\cos\theta\overline{\alpha}_\gamma + \sin\theta\overline{\beta}_\gamma = \left(\overline{\psi} \cdot \overline{\alpha}_\gamma\right)\overline{\alpha}_\gamma + \left(\overline{\psi} \cdot \overline{\beta}_\gamma\right)\overline{\beta}_\gamma = \overline{\psi} = \left(\overline{\psi} \cdot \overline{\alpha}_{\gamma'}\right)\overline{\alpha}_{\gamma'} + \left(\overline{\psi} \cdot \overline{\beta}_{\gamma'}\right)\overline{\beta}_{\gamma'} = \cos\theta'\overline{\alpha}_{\gamma'} + \sin\theta'\overline{\beta}_{\gamma'}. \tag{2.17}$$

The two angles θ and $\theta' \in [0, 2\pi)$ will always exist, because of the existence of $\overline{\psi}$.

2.5 Geometric calibration problem and solving strategy

In this section, we define the geometric calibration problem in 3D parallel geometry, in section 2.5.1 and apply the pair-wise DCC to solve it, in section 2.5.2.

2.5.1 Geometric calibration problem in 3D parallel geometry

We will start with the simplest context, so let's say we have an unknown 3D object f with compact support, and we are given three 2D parallel projections. Two of them are computed along the directions $\overline{e}_2 = (0, 1, 0)$ and $\overline{e}_3 = (0, 0, 1)$, and the other is computed along an unknown direction $\overline{\gamma}$. We assume that there is no in-plane angle or in-plane shift in each of these three projections, which means all projections have been center-corrected by the center-of-mass result (see section 2.10); now each projection has its own center-of-mass located at the corresponding detector's origin. The crucial condition on the 3D object is that, for any two distinct unit directions $\overline{\gamma}$ and $\overline{\gamma}' \in \mathbb{S}^2$, there has to exist at least a value $s_0 \in \mathbb{R}$ such that:

$$\mathscr{R}^3_{\overline{\gamma}} f\left(s_0\right) \neq \mathscr{R}^3_{\overline{\gamma}'} f\left(s_0\right). \tag{2.18}$$

We will explain the role of this assumption later in section 2.5.2. The form of the assumption (2.18) is not natural and a bit too theoretical. It still needs to be improved and studied more. Here we stop at this point with no further clues yet. But we can show some examples of those objects which violate the above assumption, in figure 2.3.

- For the object f being a ball with uniform density and center at the origin, we can take any two distinct unit directions $\overline{\gamma}$ and $\overline{\gamma}'$, then $\mathscr{R}^3_{\overline{\gamma}} f\left(s\right) = \mathscr{R}^3_{\overline{\gamma}'} f\left(s\right), \forall s \in \mathbb{R}$, which fails the condition (2.18).

- For the object f being a vertical cylinder with uniform density and center-of-mass at the origin, we can take any two unit directions such that $\overline{\gamma} = -\overline{\gamma}'$, then we can also have $\mathscr{R}^3_{\overline{\gamma}} f\left(s\right) = \mathscr{R}^3_{\overline{\gamma}'} f\left(s\right), \forall s \in \mathbb{R}$ violating the condition (2.18).

- For the object f being an L-shape, which has two cuboid branches of equal length, with uniform density and center-of-mass at the origin, as in figure 2.3, we can consider $\gamma = (0,-1,0)$ and $\overline{\gamma}' = (0,0,-1)$, then we always have $\mathscr{R}^3_{\overline{\gamma}} f(s) = \mathscr{R}^3_{\overline{\gamma}'} f(s), \forall s \in \mathbb{R}$, violating the condition (2.18).

For simplicity, we have said that the object needs to be completely general, meaning it has no symmetry, in our paper [Nguyen et al., 2020a], but this description is a little bit weak, and does not describe the whole idea of the condition (2.18). In the next section, we will firstly explain the solving strategy of the above geometric calibration problem, then from that, we will see why the condition (2.18) is crucial.

2.5.2 Solving strategy

Now we are having in hands three projections $p_{\overline{\gamma}}$, $p_{\overline{e}_2}$, $p_{\overline{e}_3}$, with $\overline{e}_2$ and $\overline{e}_3$ are known. We will apply the pair-wise DCC to deal with the geometric calibration problem. Due to the fact that $p_{\overline{\gamma}}(u,v) = p_{-\overline{\gamma}}(u,v), \forall (u,v) \in \mathbb{R}^2$, if $\overline{\gamma}_0$ is a solution to this geometric calibration problem, then $(-\overline{\gamma}_0)$ is also a solution. Thus we will accept if the obtained solution is a pair of two opposite unit directions. Now we describe the solving strategy, following the below steps:

1. We start with $p_{\overline{\gamma}}$ and $p_{\overline{e}_2}$. From these two distinct parallel projections, we apply the 2D Radon transform to obtain the corresponding sinograms. According to the comment in section 2.4, there always exist two angles $\theta_2, \phi_2 \in [0, 2\pi)$ such that the pair-wise DCC (2.13) holds:

$$\mathscr{R}^2_{\theta_2} p_{\overline{\gamma}}(s) = \mathscr{R}^2_{\phi_2} p_{\overline{e}_2}(s), \forall s \in \mathbb{R}. \tag{2.19}$$

   The two angles $\theta_2, \phi_2 \in [0, 2\pi)$ can be found by a row-matching procedure, which we will demonstrate more precisely in the next section 2.6. For now, we assume that we have already found the two above angles θ_2, ϕ_2.

2. From $\overline{\gamma}$ and $\overline{e}_2$, we can also compute two corresponding sets of unit vectors $\left(\overline{\alpha}_\gamma, \overline{\beta}_\gamma, \overline{\gamma}\right)$ and $\left(\overline{\alpha}_{e_2}, \overline{\beta}_{e_2}, \overline{e}_2\right)$ respectively from equation (2.3) in section 2.2. Now under the object condition (2.18), we claim that the two angles $\theta_2, \phi_2 \in [0, 2\pi)$, satisfying the pair-wise DCC (2.13), will also satisfy the condition (2.12):

$$\cos\theta_2 \overline{\alpha}_\gamma + \sin\theta_2 \overline{\beta}_\gamma = \cos\phi_2 \overline{\alpha}_{e_2} + \sin\phi_2 \overline{\beta}_{e_2}. \tag{2.20}$$

   We can prove this by contradiction. Assuming that there exist two angles $\theta_0, \phi_0 \in [0, 2\pi)$ such that:

$$\mathscr{R}^2_{\theta_0} p_{\overline{\gamma}}(s) = \mathscr{R}^2_{\phi_0} p_{\overline{e}_2}(s), \forall s \in \mathbb{R}, \tag{2.21}$$

   but $\cos\theta_0 \overline{\alpha}_\gamma + \sin\theta_0 \overline{\beta}_\gamma \neq \cos\phi_0 \overline{\alpha}_{e_2} + \sin\phi_0 \overline{\beta}_{e_2}$. For simplicity, we rename these vectors as the following:

$$\begin{cases} \overline{\eta}_\gamma = \cos\theta_0 \overline{\alpha}_\gamma + \sin\theta_0 \overline{\beta}_\gamma \\ \overline{\eta}_{e_2} = \cos\phi_0 \overline{\alpha}_{e_2} + \sin\phi_0 \overline{\beta}_{e_2} \end{cases}, \tag{2.22}$$

   then by the result (2.7), we can say that:

$$\begin{cases} \mathscr{R}^2_{\theta_0} p_{\overline{\gamma}}(s) = \mathscr{R}^3_{\overline{\eta}_\gamma} f(s) \\ \mathscr{R}^2_{\phi_0} p_{\overline{e}_2}(s) = \mathscr{R}^3_{\overline{\eta}_{e_2}} f(s) \end{cases}. \tag{2.23}$$

   And the above assumption can be rewritten as: there exist two angles $\theta_0, \phi_0 \in [0, 2\pi)$ such that $\mathscr{R}^3_{\overline{\eta}_\gamma} f(s) = \mathscr{R}^3_{\overline{\eta}_{e_2}} f(s), \forall s \in \mathbb{R}$, but $\overline{\eta}_\gamma \neq \overline{\eta}_{e_2}$. This contradicts the object condition (2.18)! Then the initial assumption of the contradiction is false. And thus, if we can find the two suitable angles $\theta_2, \phi_2 \in [0, 2\pi)$ satisfying the pair-wise DCC (2.13), they also satisfy the condition (2.12). Here we realize the role of the object condition (2.18). Thus we can find two angles θ_2 and $\phi_2 \in [0, 2\pi)$ simultaneously satisfying the following conditions:

$$\begin{cases} \mathscr{R}^2_{\theta_2} p_{\overline{\gamma}}(s) = \mathscr{R}^2_{\phi_2} p_{\overline{e}_2}(s) \\ \cos\theta_2 \overline{\alpha}_\gamma + \sin\theta_2 \overline{\beta}_\gamma = \cos\phi_2 \overline{\alpha}_{e_2} + \sin\phi_2 \overline{\beta}_{e_2} \end{cases}. \tag{2.24}$$

   Now we set $\overline{\psi}_2 = \cos\phi_2 \overline{\alpha}_{e_2} + \sin\phi_2 \overline{\beta}_{e_2}$, $\overline{\psi}_2$ is clearly computed because $\left(\overline{\alpha}_{e_2}, \overline{\beta}_{e_2}\right)$ can be calculated from $\overline{e}_2 = (0,1,0)$ and ϕ_2 has just been found from the above row-matching procedure. By the result (2.24), we also know that $\overline{\psi}_2 = \cos\phi_2 \overline{\alpha}_{e_2} + \sin\phi_2 \overline{\beta}_{e_2} = \cos\theta_2 \overline{\alpha}_\gamma + \sin\theta_2 \overline{\beta}_\gamma$, and this leads to the fact that $\overline{\psi}_2$ is on the $\left(\overline{\alpha}_\gamma, \overline{\beta}_\gamma\right)$ plane, and thus is perpendicular to $\overline{\gamma}$.

3. Completely similar to the previous steps, we can also find $\theta_3, \phi_3 \in [0, 2\pi)$ such that

$$\begin{cases} \mathscr{R}^2_{\theta_3} p_{\overline{\gamma}}(s) = \mathscr{R}^2_{\phi_3} p_{\overline{e}_3}(s) \\ \cos\theta_3 \overline{\alpha}_\gamma + \sin\theta_3 \overline{\beta}_\gamma = \cos\phi_3 \overline{\alpha}_{e_3} + \sin\phi_3 \overline{\beta}_{e_3} \end{cases}. \tag{2.25}$$

   Then we can precisely compute $\overline{\psi}_3 = \cos\phi_3 \overline{\alpha}_{e_3} + \sin\phi_3 \overline{\beta}_{e_3}$, and know that $\overline{\psi}_3$ is perpendicular to $\overline{\gamma}$.

4. From the second and the third step, we obtain $\overline{\gamma}$ as the unit vector, which is perpendicular to both $\overline{\psi}_2$ and $\overline{\psi}_3$, thus $\overline{\gamma}$ can be computed by the following formula:

$$\overline{\gamma} = \pm \frac{\overline{\psi}_2 \times \overline{\psi}_3}{\|\overline{\psi}_2 \times \overline{\psi}_3\|} \tag{2.26}$$

   We thus obtain a pair of two acceptable opposite solutions.

5. However, from the formula (2.26) of solution to $\overline{\gamma}$, we can see that this method will fail if $\|\overline{\psi}_2 \times \overline{\psi}_3\| = 0$, and this happens when $\overline{\psi}_2$ and $\overline{\psi}_3$ are collinear. In this case, we will only know that $\overline{\gamma}$ is on the plane, which is perpendicular to the line containing both $\overline{\psi}_2$ and $\overline{\psi}_3$. Moreover, this plane has to contain $\overline{e}_2$ and $\overline{e}_3$ respectively, because by the construction, $\overline{\psi}_2 = \left(\cos\phi_2 \overline{\alpha}_{e_2} + \sin\phi_2 \overline{\beta}_{e_2}\right) \perp \overline{e}_2$ and $\overline{\psi}_3 = \left(\cos\phi_3 \overline{\alpha}_{e_3} + \sin\phi_3 \overline{\beta}_{e_3}\right) \perp \overline{e}_3$. Then we can say that the above method fails if $\overline{\gamma}$ is on the $(\overline{e}_2, \overline{e}_3)$ plane.

In conclusion, if $\overline{\gamma}$ is not on the $(\overline{e}_2, \overline{e}_3)$ plane, then $\overline{\gamma}$ is found by the analytic formula (2.26); and if $\overline{\gamma}$ is on $(\overline{e}_2, \overline{e}_3)$ plane, then we need another strategy to deal with this case, which we call the *degenerate case* of the problem, presented in section 2.9.

Particularly, in the case where $\overline{e}_2 = (0, 1, 0)$ and $\overline{e}_3 = (0, 0, 1)$, let us compute everything precisely to see the detailed formula of the solution to $\overline{\gamma}$. Firstly,

$$\begin{cases} \overline{\alpha}_{e_2} = (-1, 0, 0) \\ \overline{\beta}_{e_2} = (0, 0, 1) \end{cases}, \qquad \begin{cases} \overline{\alpha}_{e_3} = (-1, 0, 0) \\ \overline{\beta}_{e_3} = (0, -1, 0) \end{cases}. \tag{2.27}$$

Then we can compute $\overline{\psi}_2$ and $\overline{\psi}_3$ respectively:

$$\begin{cases} \overline{\psi}_2 = \cos\phi_2 \overline{\alpha}_{e_2} + \sin\phi_2 \overline{\beta}_{e_2} = \cos\phi_2 (-1, 0, 0) + \sin\phi_2 (0, 0, 1) \quad = (-\cos\phi_2, 0, \sin\phi_2) \\ \overline{\psi}_3 = \cos\phi_3 \overline{\alpha}_{e_3} + \sin\phi_3 \overline{\beta}_{e_3} = \cos\phi_3 (-1, 0, 0) + \sin\phi_3 (0, -1, 0) = (-\cos\phi_3, -\sin\phi_3, 0) \end{cases}. \tag{2.28}$$

We can continue to compute:

$$\overline{\psi}_2 \times \overline{\psi}_3 = (\sin\phi_2 \sin\phi_3, -\sin\phi_2 \cos\phi_3, \cos\phi_2 \sin\phi_3), \tag{2.29a}$$

$$\|\overline{\psi}_2 \times \overline{\psi}_3\| = \sqrt{\sin^2\phi_2 \sin^2\phi_3 + \sin^2\phi_2 \cos^2\phi_3 + \cos^2\phi_2 \sin^2\phi_3} \tag{2.29b}$$

$$= \sqrt{\sin^2\phi_2 + \cos^2\phi_2 \sin^2\phi_3} \tag{2.29c}$$

$$= \sqrt{1 - \cos^2\phi_2 + \cos^2\phi_2 (1 - \cos^2\phi_3)} \tag{2.29d}$$

$$= \sqrt{1 - \cos^2\phi_2 \cos^2\phi_3}. \tag{2.29e}$$

Finally, the analytic formula of the solution to $\overline{\gamma}$ is the following:

$$\overline{\gamma} = \frac{\overline{\psi}_2 \times \overline{\psi}_3}{\|\overline{\psi}_2 \times \overline{\psi}_3\|} = \frac{(\sin\phi_2 \sin\phi_3, -\sin\phi_2 \cos\phi_3, \cos\phi_2 \sin\phi_3)}{\sqrt{1 - \cos^2\phi_2 \cos^2\phi_3}}. \tag{2.30}$$

And the above formula will fail if:

$$\sqrt{1 - \cos^2\phi_2 \cos^2\phi_3} = 0 \Longleftrightarrow \begin{cases} \cos\phi_2 = \pm 1 \\ \cos\phi_3 = \pm 1 \end{cases} \text{ and } \begin{cases} \sin\phi_2 = 0 \\ \sin\phi_3 = 0 \end{cases}. \tag{2.31}$$

From the system (2.28), this means $\overline{\psi}_2 = \pm(1, 0, 0)$ and $\overline{\psi}_3 = \pm(1, 0, 0)$, and $\overline{\gamma}$ is perpendicular to both of these vectors, leading to the fact that $\overline{\gamma}$ is in the plane of $(\overline{e}_2, \overline{e}_3)$, where $\overline{e}_2 = (0, 1, 0)$ and $\overline{e}_3 = (0, 0, 1)$.

2.6 Row-matching algorithm

As mentioned in the previous section 2.5.2, the aim of this algorithm is from two sinograms of two given parallel projections, let's say $p_{\overline{\gamma}}$ and $p_{\overline{\gamma}'}$, to find two suitable angles $\Phi_0, {\Phi_0}' \in [0, 2\pi)$ such that:

$$\mathscr{R}^2_{\Phi_0} p_{\overline{\gamma}}(s) = \mathscr{R}^2_{{\Phi_0}'} p_{\overline{\gamma}'}(s), \forall s \in \mathbb{R}. \tag{2.32}$$

A sinogram is a function of two variables ϕ and s, here we consider it as an image with the horizontal axis is for s and the vertical axis is for ϕ. In numerical analysis, this sinogram image is in fact a matrix with the columns are the discretization of s, and the rows are the discretization of ϕ from 0 to 2π (the row 2π is not included). Precisely, the two sinograms of $p_{\overline{\gamma}}$ and $p_{\overline{\gamma}'}$ are two matrices of the same size, let's call them S and S' of the same dimensions $N_\phi \times Ns$. Finding two angles Φ_0 and ${\Phi_0}'$ satisfying equation (2.32) means finding two rows, one in each sinogram, that perfectly match each other. This leads us to find two rows in the two matrices, one in S and one in S', such that all values on the row in S respectively match all values on the row in S' (that's why we name it the row-matching algorithm). As explained in the previous sections, these two rows have to exist. We find these two rows (of two matrices) by the following algorithm:

Row-matching algorithm:

1. *We take the first row of S' and duplicate it $(N_\phi - 1)$ times to make a new matrix S'' of dimension $N_\phi \times Ns$, where all the rows are copied from the first row of S'.*
2. *We compute $H = S - S''$, and take the Euclidean norm of every row of H, then we obtain a column vector $(N_\phi \times 1)$ and we save this column as the first column of the norm-of-difference (NoD) matrix.*
3. *Similarly, we take the second row of S', repeat the two above steps and obtain the second column of the NoD matrix. Then we continue to repeat the procedure of step 1 and 2 until we finish taking all the rows of S'. We thus obtain the NoD matrix of dimension $N_\phi \times N_\phi$.*
4. *In theory, there have to be 0-values in the NoD matrix, where the specific rows in S and S' match together. We know that there always exist two 0-values in the NoD matrix, and either of these two corresponds to the matching rows, which lead to the true solution of the unknown viewing direction (we explain in the remarks section below). In practice, we might not have the perfect 0-values, thus the idea is to find the smallest value among all values in the NoD matrix and its corresponding position in the NoD matrix. The row and the column of the smallest value link to the rows of S and S' respectively, that match together. Firstly from the theory, there must exist two elements in the NoD matrix share the same smallest value and either of these two leads to the true solution of the unknown viewing direction. In the case that the NoD matrix happens to have more elements (than two) which hold that same smallest value, we cannot choose which element among those to be the suitable one, thus more works need to be done with this last step of the algorithm.*

After the above final step, we will know which row of S matching which row of S'. Below are some remarks.

Remarks

- From the definition of the 2D Radon transform, we know that, for all $\Phi \in [0, 2\pi)$ and for all $s \in \mathbb{R}$:

$$\begin{aligned}
\mathscr{R}^2_{\Phi+\pi} p_{\overline{\gamma}}(s) &= \int p_{\overline{\gamma}}\left(s\cos(\Phi+\pi) - t\sin(\Phi+\pi), s\sin(\Phi+\pi) + t\cos(\Phi+\pi)\right) dt && (2.33)\\
&= \int p_{\overline{\gamma}}\left(-s\cos\phi_0 + t\sin\phi_0, -s\sin\phi_0 - t\cos\phi_0\right) dt && (2.34)\\
&= \int p_{\overline{\gamma}}\left(-s\cos\phi_0 - t'\sin\phi_0, -s\sin\phi_0 + t'\cos\phi_0\right) dt' && (2.35)\\
&= \mathscr{R}^2_{\Phi} p_{\overline{\gamma}}(-s). && (2.36)
\end{aligned}$$

This means if Φ_0 and ${\Phi_0}'$ are two suitable angles satisfying $\mathscr{R}^2_{\Phi_0} p_{\overline{\gamma}}(s) = \mathscr{R}^2_{{\Phi_0}'} p_{\overline{\gamma}'}(s), \forall s \in \mathbb{R}$, then:

$$\mathscr{R}^2_{\Phi_0+\pi} p_{\overline{\gamma}}(s) = \mathscr{R}^2_{\Phi_0} p_{\overline{\gamma}}(-s) = \mathscr{R}^2_{{\Phi_0}'} p_{\overline{\gamma}'}(-s) = \mathscr{R}^2_{{\Phi_0}'+\pi} p_{\overline{\gamma}'}(s), \forall s \in \mathbb{R}. \tag{2.37}$$

In other words, we can claim in a more proper way as follows:

+ If Φ_0 and ${\Phi_0}'$ are the pair of angles satisfying equation (2.32), and $\Phi_0, {\Phi_0}' \in [0,\pi)$, then $(\Phi_0+\pi)$ and $\left({\Phi_0}'+\pi\right)$ are also.
+ If Φ_0 and ${\Phi_0}'$ are the pair of angles satisfying equation (2.32), and $\Phi_0, {\Phi_0}' \in [\pi,2\pi)$, then $(\Phi_0-\pi)$ and $\left({\Phi_0}'-\pi\right)$ are also.
+ If Φ_0 and ${\Phi_0}'$ are the pair of angles satisfying equation (2.32), and $\Phi_0 \in [0,\pi)$, ${\Phi_0}' \in [\pi,2\pi)$, then $(\Phi_0+\pi)$ and $\left({\Phi_0}'-\pi\right)$ are also.
+ If Φ_0 and ${\Phi_0}'$ are the pair of angles satisfying equation (2.32), and $\Phi_0 \in [\pi,2\pi)$, ${\Phi_0}' \in [0,\pi)$, then $(\Phi_0-\pi)$ and $\left({\Phi_0}'+\pi\right)$ are also.

For simplicity, we can say that in any two given sinograms, we can find at least two pairs of matching rows (because if $\overline{\gamma} = \pm\overline{\gamma}'$ then $p_{\overline{\gamma}}(u,v) = p_{\overline{\gamma}'}(u,v), \forall (u,v) \in \mathbb{R}^2$, so we will definitely have more than just two pairs of matching rows in the two sinograms).

- In theory and in general, if the two parallel projections are computed along two directions which are not collinear and if the data is consistent, then after performing the row-matching algorithm, we should receive only two suitable pairs of angles $\left(\Phi_1, {\Phi_1}'\right)$ and $\left(\Phi_2, {\Phi_2}'\right)$ characterizing two pairs of matching rows, where:

$$\begin{cases} \Phi_2 \ = \Phi_1 + \pi, & \text{or} \quad \Phi_2 \ = \Phi_1 - \pi \\ {\Phi_2}' = {\Phi_1}' + \pi, & \text{or} \quad {\Phi_2}' = {\Phi_1}' - \pi \end{cases}. \tag{2.38}$$

Or we can say that:

$$\begin{cases} \cos\Phi_2 = -\cos\Phi_1 \\ \sin\Phi_2 = -\sin\Phi_1 \end{cases}, \quad \text{and} \quad \begin{cases} \cos{\Phi_2}' = -\cos{\Phi_1}' \\ \sin{\Phi_2}' = -\sin{\Phi_1}' \end{cases}. \tag{2.39}$$

Now coming back with our solving strategy 2.5.2, the aim of the first step is to use the row-matching algorithm to find two suitable angles $\theta_2, \phi_2 \in [0,2\pi)$ such that the pair-wise DCC (2.13) holds. However, as we have just explained, the row-matching algorithm gives us two pairs of suitable angles $(\theta_{2,1}, \phi_{2,1})$ and $(\theta_{2,2}, \phi_{2,2})$, where:

$$\begin{cases} \cos\theta_{2,2} = -\cos\theta_{2,1} \\ \sin\theta_{2,2} = -\sin\theta_{2,1} \end{cases}, \quad \text{and} \quad \begin{cases} \cos\phi_{2,2} = -\cos\phi_{2,1} \\ \sin\phi_{2,2} = -\sin\phi_{2,1} \end{cases}. \tag{2.40}$$

After that, at the final of the second step in the solving strategy 2.5.2, we will compute $\overline{\psi}_2 = \cos\phi_2\overline{\alpha}_{e_2} + \sin\phi_2\overline{\beta}_{e_2}$. Here with two different values of ϕ_2: $\phi_{2,1}$ and $\phi_{2,2}$, we will obtain two different vectors: $\overline{\psi}_{2,1}$ and $\overline{\psi}_{2,2}$, but we also know that:

$$\overline{\psi}_{2,2} = \cos\phi_{2,2}\overline{\alpha}_{e_2} + \sin\phi_{2,2}\overline{\beta}_{e_2} = -\cos\phi_{2,1}\overline{\alpha}_{e_2} - \sin\phi_{2,1}\overline{\beta}_{e_2} = -\overline{\psi}_{2,1}. \tag{2.41}$$

Similarly, when applying the row-matching algorithm to $p_{\overline{\gamma}}$ and $p_{\overline{e}_3}$, we will also obtain two different vectors such that $\overline{\psi}_{3,2} = -\overline{\psi}_{3,1}$. And by step 4 of the solving strategy 2.5.2, we know that the solution of $\overline{\gamma}$ is produced from one of the following four pairs of vectors $\left\{\overline{\psi}_{2,1}, \overline{\psi}_{3,1}\right\}$, $\left\{\overline{\psi}_{2,1}, \overline{\psi}_{3,2}\right\}$, $\left\{\overline{\psi}_{2,2}, \overline{\psi}_{3,1}\right\}$ and $\left\{\overline{\psi}_{2,2}, \overline{\psi}_{3,2}\right\}$. We can also notice that:

$$\frac{\overline{\psi}_{2,1} \times \overline{\psi}_{3,1}}{\left\|\overline{\psi}_{2,1} \times \overline{\psi}_{3,1}\right\|} = -\frac{\overline{\psi}_{2,1} \times \overline{\psi}_{3,2}}{\left\|\overline{\psi}_{2,1} \times \overline{\psi}_{3,2}\right\|} = -\frac{\overline{\psi}_{2,2} \times \overline{\psi}_{3,1}}{\left\|\overline{\psi}_{2,2} \times \overline{\psi}_{3,1}\right\|} = \frac{\overline{\psi}_{2,2} \times \overline{\psi}_{3,2}}{\left\|\overline{\psi}_{2,2} \times \overline{\psi}_{3,2}\right\|}. \tag{2.42}$$

This means we are safe, because the solution that we finally receive is only $\overline{\gamma}$ or $-\overline{\gamma}$, regardless the chosen pairs of matching rows after performing two times of the row-matching procedure

2.7 Numerical simulations

We consider a slightly simplified version of the MRI 3D Shepp-Logan phantom as our object (the details of the MRI 3D Shepp-Logan phantom can be found in [Gach et al., 2008]), to test the method. This object consists of

Table 2.1: Details of 15 ellipsoids of the considering 3D object

Ellisoid	Centers $(\times 10^2)$			Semi-axes $(\times 10^2)$			Gray level $(\times 10)$
i	$c_1(i)\times 10^2$	$c_2(i)\times 10^2$	$c_3(i)\times 10^2$	$r_1(i)\times 10^2$	$r_2(i)\times 10^2$	$r_3(i)\times 10^2$	$v(i)\times 10$
1	00.00	00.00	00.00	72.00	95.00	93.00	08.00
2	00.00	00.00	00.00	69.00	92.00	90.00	-06.80
3	00.00	-01.84	00.00	66.24	87.40	88.00	08.60
4	00.00	-01.84	00.00	65.24	86.40	87.00	-02.35
5	-22.00	00.00	-25.00	16.00	41.00	21.00	02.35
6	22.00	00.00	-25.00	11.00	31.00	22.00	02.35
7	00.00	35.00	-25.00	21.00	25.00	35.00	-01.28
8	00.00	10.00	-25.00	04.60	04.60	04.60	02.05
9	-08.00	-60.50	-25.00	04.60	02.30	02.00	02.05
10	06.00	-60.50	-25.00	02.30	04.60	02.00	02.05
11	00.00	-10.00	-25.00	04.60	04.60	04.60	02.05
12	00.00	-60.50	-25.00	02.30	02.30	02.30	02.05
13	06.00	-10.50	06.25	04.00	05.60	10.00	01.85
14	00.00	10.00	62.50	05.60	05.60	10.00	02.35
15	47.00	-40.00	-25.00	03.00	20.00	10.00	01.05

15 ellipsoids, and none of them is tilted. Mathematically, our object is the following three-variable real function: $f=\sum_{i=1}^{15} f_i$, where:

$$f_i\left(x_1,x_2,x_3\right)=\begin{cases} v\left(i\right), & \text{if} \quad \left(\dfrac{x_1-c_1\left(i\right)}{r_1\left(i\right)}\right)^2+\left(\dfrac{x_2-c_2\left(i\right)}{r_2\left(i\right)}\right)^2+\left(\dfrac{x_3-c_3\left(i\right)}{r_3\left(i\right)}\right)^2\leq 1 \\ 0, & \text{otherwise}\end{cases}, \tag{2.43}$$

with $c\left(i\right)=\left(c_1\left(i\right),c_2\left(i\right),c_3\left(i\right)\right)$, $r\left(i\right)=\left(r_1\left(i\right),r_2\left(i\right),r_3\left(i\right)\right)$ and $v\left(i\right)$ are the center coordinate, the semi-axes and the gray level of the i-th ellipsoid, respectively. The details of $c\left(i\right)$, $r\left(i\right)$ and $v\left(i\right)$ are shown in table 2.1. We have developed three programs, called *projection-simulator*, *sinogram-generator* and *solver*. *Projection-simulator* received the information of the 3D object, the three given directions $\overline{\gamma}$, $\overline{e}_2$, $\overline{e}_3$ and simulated the corresponding 2D parallel projections: $p_{\overline{\gamma}}$, $p_{\overline{e}_2}$, $p_{\overline{e}_3}$. Then *sinogram-generator* received the three simulated projections and generated the corresponding sinograms. Finally, $\overline{\gamma}$ was supposed to be the unknown direction, *solver* took the information of the three generated sinograms, with the information of $\overline{e}_2$ and $\overline{e}_3$, performed the row-matching procedures and then estimated the solutions to $\overline{\gamma}$. Here we are going to show the results of three tests.

Test 1

In this test, we choose $\overline{\gamma}=\left(\dfrac{1}{3},-\dfrac{2}{3},\dfrac{2}{3}\right)$, $\overline{\Gamma}=\left(\dfrac{1}{2},\dfrac{1}{2},\dfrac{1}{\sqrt{2}}\right)$, $\overline{e}_2=(0,1,0)$, $\overline{e}_3=(0,0,1)$. We treat $\overline{e}_2$ and $\overline{e}_3$ as our known directions and $\overline{\gamma}$ and $\overline{\Gamma}$ as the unknowns that need to be estimated. After following the method, we respectively obtain the following estimated solutions to $\overline{\gamma}$ and $\overline{\Gamma}$:

$$\overline{\gamma}_{\text{est}}\approx\pm\left(0.3260,-0.6685,0.6685\right), \tag{2.44}$$

$$\overline{\Gamma}_{\text{est}}\approx\pm\left(0.4975,0.4975,0.7106\right). \tag{2.45}$$

Figure 2.4 shows us the images of the projections $p_{\overline{e}_2}$, $p_{\overline{e}_3}$, and figure 2.5 shows the images of $p_{\overline{\gamma}}$, $p_{\overline{\Gamma}}$. Here the intervals $[-1,1]$ on the two standard axes u and v of each projection image have been discretized as 1001-equidistant samples, which makes each projection be an image at 1001×1001 pixels. Figure 2.6 shows the four corresponding sinograms of $p_{\overline{e}_2}$, $p_{\overline{e}_3}$, $p_{\overline{\gamma}}$ and $p_{\overline{\Gamma}}$. In each sinogram image, the considered angles are from 0° to 359° with the sampling step 1° (we use this notation to describe the angles: $\phi=0^\circ:1^\circ:359^\circ$), and s is a 1001-equidistant sample of $[-2,2]$. Figure 2.7 shows the projections computed along two estimated directions: $p_{\overline{\gamma}_{\text{est}}}$ and $p_{\overline{\Gamma}_{\text{est}}}$. For convenience of reading the text, we will separate the simulation images and present them all at once in section 2.11. Here we have repeated our method two times to estimate respectively $\overline{\gamma}_{\text{est}}$ and $\overline{\Gamma}_{\text{est}}$. We perform this test and show the results of $\overline{\gamma}_{\text{est}}$ and $\overline{\Gamma}_{\text{est}}$ at the same time to say that: we only need to know the projection data and two unit vectors in advance, all of the unknown unit vectors can be calibrated independently of each other, repeating the same process.

Test 2

We choose $\overline{e}_2 = \left(\frac{1}{2}, \frac{1}{3}, -\frac{\sqrt{23}}{6}\right)$, $\overline{e}_3 = \left(-\frac{2}{3}, -\frac{1}{4}, -\frac{\sqrt{71}}{12}\right)$ to be the two known directions and $\overline{\gamma} = \left(-\frac{1}{4}, \frac{1}{4}, \frac{\sqrt{14}}{4}\right)$ to be the unknown. After following the method presented in section 2.5.2, from three 2D parallel projections and two known directions $\overline{e}_2$ and $\overline{e}_3$, we obtain the estimated solution to $\overline{\gamma}$ as the following:

$$\overline{\gamma}_{\text{est}} \approx \pm\left(-0.2427, 0.2550, 0.9360\right). \tag{2.46}$$

Figure 2.8 shows us the projections and their corresponding sinograms, and figure 2.9 shows the projection at the estimated direction. We can notice that in test 1, $\overline{e}_2 = (0,1,0)$ and $\overline{e}_3 = (0,0,1)$, which are perpendicular to each other. The aim of this test is to show an example that our method also works if the two known directions are not perpendicular to each other. In short, we can conclude again that, the two known directions can be any two unit vectors that are not collinear to each other. The estimated solution $\overline{\gamma}_{\text{est}}$ can be analytically computed by the formula (2.26). In the particular case that the two known directions are $\overline{e}_2 = (0,1,0)$ and $\overline{e}_3 = (0,0,1)$, we can even more quickly compute $\overline{\gamma}_{\text{est}}$ by the formula (2.30).

2.8 ϕ-sample refinement

After performing the above experiments, we obtain the estimated solutions $\overline{\gamma}_{\text{est}}$ approximating $\overline{\Gamma}_{\text{est}}$.

- In the first test:
  + $\overline{\gamma}_{\text{est}} \approx \pm\left(0.3260, -0.6685, 0.6685\right)$ approximates $\overline{\gamma} = \left(\frac{1}{3}, -\frac{2}{3}, \frac{2}{3}\right) \approx (0.3333, -0.6667, 0.6667)$,
  + $\overline{\Gamma}_{\text{est}} \approx \pm\left(0.4975, 0.4975, 0.7106\right)$ approximates $\overline{\Gamma} = \left(\frac{1}{2}, \frac{1}{2}, \frac{1}{\sqrt{2}}\right) \approx (0.5, 0.5, 0.7071)$.
- And in the second test:
  + $\overline{\gamma}_{\text{est}} \approx \pm\left(-0.2427, 0.2550, 0.9360\right)$ approximates $\overline{\gamma} = \left(-\frac{1}{4}, \frac{1}{4}, \frac{\sqrt{14}}{4}\right) \approx (-0.25, 0.25, 0.9354)$.

In fact, looking into these results, the approximations are not good, comparing to the fact that all the data we are working on is the simulated data, not the real data. Now we are going to explain about the errors and then improve the approximations. We consider the first example of the first test: calibrating $\overline{\gamma} = \left(\frac{1}{3}, -\frac{2}{3}, \frac{2}{3}\right)$. The two other examples are similar.

In the first example, $\overline{e}_2 = (0,1,0)$, $\overline{e}_3 = (0,0,1)$ and $\overline{\gamma} = \left(\frac{1}{3}, -\frac{2}{3}, \frac{2}{3}\right)$. From the formula (2.26), the estimated solution is computed from $\overline{\psi}_2$ and $\overline{\psi}_3$. Theoretically, in the third statement in the comment in section 2.4, if $\overline{\gamma}$ is supposed to be known in advance, then $\overline{\psi}_2$ is computed as follows:

$$\overline{\psi}_2 = \pm\frac{\overline{\gamma} \times \overline{e}_2}{\|\overline{\gamma} \times \overline{e}_2\|} = \pm\frac{\left(\frac{1}{3}, -\frac{2}{3}, \frac{2}{3}\right) \times (0,1,0)}{\left\|\left(\frac{1}{3}, -\frac{2}{3}, \frac{2}{3}\right) \times (0,1,0)\right\|} = \pm\frac{\left(-\frac{2}{3}, 0, \frac{1}{3}\right)}{\left\|\left(-\frac{2}{3}, 0, \frac{1}{3}\right)\right\|} = \pm\left(-\frac{2}{\sqrt{5}}, 0, \frac{1}{\sqrt{5}}\right). \tag{2.47}$$

Then also following the idea in the comment, if θ_2 and $\phi_2 \in [0, 2\pi)$ are the two suitable angles characterizing two matching rows (one in each sinogram), then theoretically, they satisfy:

$$\begin{cases} \cos\theta_2 = \overline{\psi}_2 \cdot \overline{\alpha}_\gamma \\ \sin\theta_2 = \overline{\psi}_2 \cdot \overline{\beta}_\gamma \end{cases}, \qquad \begin{cases} \cos\phi_2 = \overline{\psi}_2 \cdot \overline{\alpha}_{e_2} \\ \sin\phi_2 = \overline{\psi}_2 \cdot \overline{\beta}_{e_2} \end{cases}. \tag{2.48}$$

From this, θ_2 and ϕ_2 satisfy the following equations:

$$\begin{cases} \cos\theta_2 = -\frac{4}{5} \\ \sin\theta_2 = \frac{3}{5} \end{cases} \text{ and } \begin{cases} \cos\phi_2 = \frac{2}{\sqrt{5}} \\ \sin\phi_2 = \frac{1}{\sqrt{5}} \end{cases}, \quad \text{or} \quad \begin{cases} \cos\theta_2 = \frac{4}{5} \\ \sin\theta_2 = -\frac{3}{5} \end{cases} \text{ and } \begin{cases} \cos\phi_2 = -\frac{2}{\sqrt{5}} \\ \sin\phi_2 = -\frac{1}{\sqrt{5}} \end{cases}. \tag{2.49}$$

Thus in theory, the two suitable pairs of angles are $(\theta_{2,\text{theory}}, \phi_{2,\text{theory}}) \approx (143.13^\circ, 26.57^\circ)$ or $(\theta_{2,\text{theory}}, \phi_{2,\text{theory}}) \approx (323.13^\circ, 206.57^\circ)$. Similarly, the two suitable pairs of angles when we compare the corresponding sinograms of $p_{\overline{\gamma}}$ and $p_{\overline{e}_3}$ should be $(\theta_{3,\text{theory}}, \phi_{3,\text{theory}}) \approx (180^\circ, 26.57^\circ)$ or $(\theta_{3,\text{theory}}, \phi_{3,\text{theory}}) \approx (0^\circ, 206.57^\circ)$. In our program, the ϕ-variable in each sinogram has been discretized as the sample: $0^\circ : 1^\circ : 359^\circ$, which gives us the result $\phi_2 = \phi_3 = 26^\circ$. Comparing to the suitable angles in theory, which should be 26.57°, and because of the effect of the discretization, these ϕ_2 and ϕ_3 are reasonable. Moreover, due to this reason, we can conclude that: in order to obtain a better approximation for the estimated solution, we decided to perform a refinement step on ϕ. In fact, the work is to zoom in the two considering sinograms with two corresponding finer discretization of ϕ. For instance, now instead of comparing respectively the sinograms of $p_{\overline{\gamma}}$ with $p_{\overline{e}_2}$, and $p_{\overline{\gamma}}$ with $p_{\overline{e}_3}$, where $\phi = 0^\circ : 1^\circ : 359^\circ$ in both sinograms, we consider:

- $p_{\overline{\gamma}}$ with $\phi = 143^\circ : 0.01^\circ : 144^\circ$ and $p_{\overline{e}_2}$ with $\phi = 26^\circ : 0.01^\circ : 27^\circ$ in the first comparison,
- $p_{\overline{\gamma}}$ with $\phi = 179.5^\circ : 0.01^\circ : 180.5^\circ$ and $p_{\overline{e}_3}$ with $\phi = 26^\circ : 0.01^\circ : 27^\circ$ in the second comparison.

This leads exactly to the result $\phi_2 = \phi_3 = 26.57^\circ$ and the refined-estimated solution to $\overline{\gamma}$:

$$\overline{\gamma}_{\text{est, refined}} = \pm (0.3334, -0.6667, 0.6667) . \tag{2.50}$$

Similarly, we also apply this refinement step to the second example of test 1 and test 2.

- Second example of test 1: the suitable pairs of angles in theory are $(\theta_{2,\text{theory}}, \phi_{2,\text{theory}}) \approx (54.74^\circ, 35.26^\circ)$ or $(\theta_{2,\text{theory}}, \phi_{2,\text{theory}}) \approx (234.74^\circ, 215.26^\circ)$; and $(\theta_{3,\text{theory}}, \phi_{3,\text{theory}}) = (180^\circ, 135^\circ)$ or $(\theta_{3,\text{theory}}, \phi_{3,\text{theory}}) = (0^\circ, 315^\circ)$. Before the refinement step, we have $\phi_2 = 215^\circ$ and $\phi_3 = 315^\circ$. After the refinement step, we have $\phi_2 = 215.27^\circ$ and $\phi_3 = 315^\circ$. And this gives us the refined-estimated solution:

$$\overline{\Gamma}_{\text{est, refined}} = \pm (0.5001, 0.5001, 0.7070) , \text{ approximating } \overline{\Gamma} = \left(\frac{1}{2}, \frac{1}{2}, \frac{1}{\sqrt{2}} \right) \approx (0.5, 0.5, 0.7071) . \tag{2.51}$$

- Test 2: the suitable pairs of angles should be $(\theta_{2,\text{theory}}, \phi_{2,\text{theory}}) \approx (106.30^\circ, 34.38^\circ)$ or $(\theta_{2,\text{theory}}, \phi_{2,\text{theory}}) \approx (286.30^\circ, 214.38^\circ)$; and $(\theta_{3,\text{theory}}, \phi_{3,\text{theory}}) = (51.06^\circ, 157.28^\circ)$ or $(\theta_{3,\text{theory}}, \phi_{3,\text{theory}}) = (231.06^\circ, 337.28^\circ)$. Before the refinement step, we have $\phi_2 = 214^\circ$ and $\phi_3 = 157^\circ$. After the refinement step, we have $\phi_2 = 214.35^\circ$ and $\phi_3 = 157.31^\circ$. And this gives us the refined-estimated solution:

$$\overline{\gamma}_{\text{est, refined}} = \pm (-0.2499, 0.2496, 0.9356) , \text{ approximating } \overline{\gamma} = \left(-\frac{1}{4}, \frac{1}{4}, \frac{\sqrt{14}}{4} \right) \approx (-0.25, 0.25, 0.9354) . \tag{2.52}$$

Figure 2.10 shows all the corresponding projections computed at the refined-estimated directions.

2.9 Particular degenerate case

As shown at the final of section 2.5.2, the method of using the row-matching procedure will fail if the unknown direction is on the same plane as the two known directions; and we call this the *degenerate case*. However, so far we are only able to solve the particular degenerate case, where the two known directions are $\overline{e}_2 = (0, 1, 0)$ and $\overline{e}_3 = (0, 0, 1)$. The work is to define the so-called in-plane moments and derive a new in-plane DCC, which are presented in section 2.9.1 and 2.9.2.

2.9.1 In-plane moments

The unit vector $\overline{\gamma}$ is in the $(\overline{e}_2, \overline{e}_3)$ plane, where $\overline{e}_2 = (0, 1, 0)$ and $\overline{e}_3 = (0, 0, 1)$. This means $\overline{\gamma}$ is in the plane $x_1 = 0$, then $\overline{\gamma}$ has the form $\overline{\gamma} = (0, \gamma_2, \gamma_3)$. With the assuption that any two of the three vectors are not collinear, then $\overline{\gamma} \neq \pm\overline{e}_2$ and $\overline{\gamma} \neq \pm\overline{e}_3$, thus $\gamma_2, \gamma_3 \neq 0$ satisfying $\gamma_2^2 + \gamma_3^2 = 1$ (because $\overline{\gamma}$ is a unit vector). By the definition in section 2.2, we have:

$$\overline{\alpha}_{\gamma} = \frac{\operatorname{sgn}(\gamma_3)}{\sqrt{\gamma_2^2}} (-\gamma_2, 0, 0) = -\frac{\operatorname{sgn}(\gamma_3)\, \gamma_2}{|\gamma_2|} (1, 0, 0) = -\frac{\gamma_2 \gamma_3}{|\gamma_2 \gamma_3|} (1, 0, 0) , \tag{2.53a}$$

$$\overline{\beta}_{\gamma} = \frac{1}{\sqrt{\gamma_2^2}} \left(0, -\gamma_2\gamma_3, \gamma_2^2\right) = \frac{1}{|\gamma_2|} \left(0, -\gamma_2\gamma_3, \gamma_2^2\right) = \left(0, -\frac{\gamma_2\gamma_3}{|\gamma_2|}, |\gamma_2|\right) . \tag{2.53b}$$

With this coordinate system $\left(\overline{\alpha}_\gamma, \overline{\beta}_\gamma, \overline{\gamma}\right)$, we defined the same 2D parallel projection as in equation (2.4). The in-plane moment of the parallel projection computed along $\overline{\gamma}$ direction will then be defined as follows:

$$P_{\overline{\gamma}}^{n}(u) = \int p_{\overline{\gamma}}(u,v)\, v^n dv. \tag{2.54}$$

2.9.2 In-plane DCC

From the above definition of the in-plane moment, we will construct our in-plane DCC, with the technique of the changing variables. Using the definition (2.4) and the definition of the above coordinate system $\left(\overline{\alpha}_\gamma, \overline{\beta}_\gamma, \overline{\gamma}\right)$, we can see that:

$$\begin{aligned}
P_{\overline{\gamma}}^{n}(u) &= \int p_{\overline{\gamma}}(u,v)\, v^n dv && (2.55a)\\
&= \iint f\left(u\overline{\alpha}_\gamma + v\overline{\beta}_\gamma + t\overline{\gamma}\right) v^n dtdv && (2.55b)\\
&= \iint f\left(-\frac{\gamma_2\gamma_3}{|\gamma_2\gamma_3|}u\,(1,0,0) + v\left(0, -\frac{\gamma_2\gamma_3}{|\gamma_2|}, |\gamma_2|\right) + t\,(0,\gamma_2,\gamma_3)\right) v^n dtdv && (2.55c)\\
&= \iint f\left(-\frac{\gamma_2\gamma_3}{|\gamma_2\gamma_3|}u, -\frac{\gamma_2\gamma_3}{|\gamma_2|}v + \gamma_2 t, |\gamma_2|\, v + \gamma_3 t\right) v^n dtdv. && (2.55d)
\end{aligned}$$

We change the variables: $y = -\frac{\gamma_2\gamma_3}{|\gamma_2|}v + \gamma_2 t$ and $z = |\gamma_2|\, v + \gamma_3 t$, then we can quickly compute the Jacobian matrix as the followings:

$$\begin{aligned}
J &= \begin{bmatrix} \dfrac{\partial y}{\partial v} & \dfrac{\partial y}{\partial t} \\[2ex] \dfrac{\partial z}{\partial v} & \dfrac{\partial z}{\partial t} \end{bmatrix} = \begin{bmatrix} -\dfrac{\gamma_2\gamma_3}{|\gamma_2|} & \gamma_2 \\[2ex] |\gamma_2| & \gamma_3 \end{bmatrix}, && (2.56a)\\
\det J &= -\frac{\gamma_2\gamma_3^2}{|\gamma_2|} - \gamma_2\,|\gamma_2| = -\frac{\gamma_2\gamma_3^2}{|\gamma_2|} - \frac{\gamma_2\gamma_2^2}{|\gamma_2|} = -\frac{\gamma_2}{|\gamma_2|}\left(\gamma_2^2+\gamma_3^2\right) = -\frac{\gamma_2}{|\gamma_2|}, && (2.56b)\\
|\det J| &= 1. && (2.56c)
\end{aligned}$$

This leads $dydz = dtdv$. Moreover, we can also compute:

$$\begin{aligned}
-\frac{\gamma_2\gamma_3}{|\gamma_2|}y + |\gamma_2|\, z &= -\frac{\gamma_2\gamma_3}{|\gamma_2|}\left(-\frac{\gamma_2\gamma_3}{|\gamma_2|}v + \gamma_2 t\right) + |\gamma_2|\left(|\gamma_2|\, v + \gamma_3 t\right) && (2.57a)\\
&= \gamma_3^2 v - |\gamma_2|\,\gamma_3 t + \gamma_2^2 v + |\gamma_2|\,\gamma_3 t && (2.57b)\\
&= \left(\gamma_2^2+\gamma_3^2\right) v && (2.57c)\\
&= v. && (2.57d)
\end{aligned}$$

Then after changing the variables, the above integral becomes:

$$\begin{aligned}
P_{\overline{\gamma}}^{n}(u) &= \iint f\left(-\frac{\gamma_2\gamma_3}{|\gamma_2\gamma_3|}u, -\frac{\gamma_2\gamma_3}{|\gamma_2|}v + \gamma_2 t, |\gamma_2|\, v + \gamma_3 t\right) v^n dtdv && (2.58)\\
&= \iint f\left(-\frac{\gamma_2\gamma_3}{|\gamma_2\gamma_3|}u, y, z\right)\left(-\frac{\gamma_2\gamma_3}{|\gamma_2|}y + |\gamma_2|\, z\right)^n dydz. && (2.59)
\end{aligned}$$

With $n = 1$, the above result can be rewritten as:

$$P_{\overline{\gamma}}^{1}(u) = \iint f\left(-\frac{\gamma_2\gamma_3}{|\gamma_2\gamma_3|}u, y, z\right)\left(-\frac{\gamma_2\gamma_3}{|\gamma_2|}y + |\gamma_2|\, z\right) dydz. \tag{2.60}$$

Our next aim is from the above equality to make $P_{\overline{e}_2}$ and $P_{\overline{e}_3}$ appear on the right-hand-side, to obtain a link between different first-order in-plane moments. Using the definition of the in-plane moments, changing the order of integrating, and changing the variables, we thus obtain the following first-order in-plane DCC in moment form:

The relationship between three different first-order in-plane moments:

$$P^1_{\overline{\gamma}}(u) = \frac{\gamma_2\gamma_3}{|\gamma_2|} P^1_{\overline{e}_3}\left(\frac{\gamma_2\gamma_3}{|\gamma_2\gamma_3|}u\right) + |\gamma_2|\, P^1_{\overline{e}_2}\left(\frac{\gamma_2\gamma_3}{|\gamma_2\gamma_3|}u\right), \forall u \in \mathbb{R}. \tag{2.61}$$

2.9.3 Solving algorithm in the particular degenerate case

We will use this first-order in-plane DCC to calibrate $\overline{\gamma}$ in this particular degenerate case. In the above equation (2.61), we can notice that: if $(\widehat{\gamma}_2, \widehat{\gamma}_3)$ is a solution, then $(-\widehat{\gamma}_2, -\widehat{\gamma}_3)$ is also. Then without loss of generality, we assume that $\gamma_2 > 0$, and then solve for (γ_2, γ_3). If we obtain the solution $(\widehat{\gamma}_2, \widehat{\gamma}_3)$ with $\widehat{\gamma}_2 > 0$, then we will also take $(-\widehat{\gamma}_2, -\widehat{\gamma}_3)$ as our solution. With this assumption, equation (2.61) can be rewritten as:

$$P^1_{\overline{\gamma}}(u) = \gamma_3 P^1_{\overline{e}_3}\left(\frac{\gamma_3}{|\gamma_3|}u\right) + \gamma_2 P^1_{\overline{e}_2}\left(\frac{\gamma_3}{|\gamma_3|}u\right), \forall u \in \mathbb{R}. \tag{2.62}$$

And the above equation is equivalent to the following system:

$$\begin{cases} P^1_{\overline{\gamma}}(u) = \gamma_3 P^1_{\overline{e}_3}(u) \quad + \gamma_2 P^1_{\overline{e}_2}(u), \quad \forall u \in \mathbb{R} \quad \text{if} \quad \gamma_3 > 0, \\ P^1_{\overline{\gamma}}(u) = \gamma_3 P^1_{\overline{e}_3}(-u) + \gamma_2 P^1_{\overline{e}_2}(-u), \forall u \in \mathbb{R} \quad \text{if} \quad \gamma_3 < 0. \end{cases} \tag{2.63}$$

2.9.3.1 Case 1: $\gamma_2, \gamma_3 > 0$

With $\gamma_2, \gamma_3 > 0$, we combine the first equation of the system (2.63) with the fact that $\overline{\gamma}$ is a unit vector to obtain a system of equations in γ_2 and γ_3. For each value $u_0 \in \mathbb{R}$, we have:

$$\begin{cases} \gamma_3 P^1_{\overline{e}_3}(u_0) + \gamma_2 P^1_{\overline{e}_2}(u_0) = P^1_{\overline{\gamma}}(u_0) \\ \gamma_2^2 + \gamma_3^2 = 1 \end{cases}. \tag{2.64}$$

This system (2.64) leads to the second-order equations as follows:

$$\left(P^1_{\overline{\gamma}}(u_0) - P^1_{\overline{e}_3}(u_0)\gamma_3\right)^2 + \left(P^1_{\overline{e}_2}(u_0)\gamma_3\right)^2 = \left(P^1_{\overline{e}_2}(u_0)\right)^2, \tag{2.65}$$

or it can be rewritten as:

$$\left[\left(P^1_{\overline{e}_2}(u_0)\right)^2 + \left(P^1_{\overline{e}_3}(u_0)\right)^2\right]\gamma_3^2 - 2P^1_{\overline{\gamma}}(u_0)\, P^1_{\overline{e}_3}(u_0)\,\gamma_3 + \left[\left(P^1_{\overline{\gamma}}(u_0)\right)^2 - \left(P^1_{\overline{e}_2}(u_0)\right)^2\right] = 0. \tag{2.66}$$

This second-order equation gives us at most two solutions:

$$\gamma_3(u_0) = \frac{P^1_{\overline{\gamma}}(u_0)\, P_{\overline{e}_3}(u_0) \pm |P_{\overline{e}_2}(u_0)| \sqrt{\left(P^1_{\overline{e}_2}(u_0)\right)^2 + \left(P^1_{\overline{e}_3}(u_0)\right)^2 - \left(P^1_{\overline{\gamma}}(u_0)\right)^2}}{\left(P^1_{\overline{e}_2}(u_0)\right)^2 + \left(P^1_{\overline{e}_3}(u_0)\right)^2}. \tag{2.67}$$

We can see that we have a similar system of equations as the system (2.64) for each value of $u \in \mathbb{R}$. In fact, solving each of these systems is equivalent to considering a plane $x_1 = u$, which intersects the 3D object and solving the 2D calibration problem on that plane containing the 2D slice of the object. From this point of view, we have many parallel planes slicing through the 3D object and solving each 2D calibration problem gives us at most two solutions on each plane. Here we neither claim that there always exists solution nor confirm the number of solutions on each plane. But if $(0, \widetilde{\gamma}_2, \widetilde{\gamma}_3)$ is the true solution to $\overline{\gamma}$, then yes, there must always exists solution on every plane, and among the solutions on each plane, there must exist one solution, which equals to $\widetilde{\gamma}_3$. We mention this fact because it is the crucial trick that we used to solve this particular degenerate case. Moreover, this technique of considering a 3D calibration problem as a series of many 2D calibration problems, solving each 2D problem and choosing the common solution among them is also used in chapter 3, to solve the calibration problem in 3D cone-beam geometry with linear sources. We now leave it here to finish the details for case 2 first, and will come back to demonstrate the solution-determining step. After obtaining the solution to γ_3, we can compute γ_2 by using the first equation of the system (2.63):

$$\gamma_2 = \frac{P^1_{\overline{\gamma}}(u) - \gamma_3 P^1_{\overline{e}_3}(u)}{P^1_{\overline{e}_2}(u)} \tag{2.68a}$$

$$= \frac{\left|P^1_{\overline{e}_2}(u)\right|}{P^1_{\overline{e}_2}(u)} \frac{P^1_{\overline{\gamma}}(u)\left|P^1_{\overline{e}_2}(u)\right| \mp P^1_{\overline{e}_3}(u)\sqrt{\left(P^1_{\overline{e}_2}(u)\right)^2 + \left(P^1_{\overline{e}_3}(u)\right)^2 - \left(P^1_{\overline{\gamma}}(u)\right)^2}}{\left(P^1_{\overline{e}_2}(u)\right)^2 + \left(P^1_{\overline{e}_3}(u)\right)^2}, \ \forall u \in \mathbb{R}. \tag{2.68b}$$

2.9.3.2 Case 2: $\gamma_2 > 0$ and $\gamma_3 < 0$

In this case, we look for the solution $(0, \gamma_2, \gamma_3)$ with $\gamma_2 > 0$ and $\gamma_3 < 0$. Completely similar to case 1, for each value $u_0 \in \mathbb{R}$, we need to solve the following system of equations:

$$\begin{cases} \gamma_3 P^1_{\overline{e}_3}(-u_0) + \gamma_2 P^1_{\overline{e}_2}(-u_0) = P^1_{\overline{\gamma}}(u_0) \\ \gamma_2^2 + \gamma_3^2 = 1 \end{cases}, \tag{2.69}$$

to obtain the solutions to γ_3 for each value of u_0 (on each parallel plane):

$$\gamma_3(u_0) = \frac{P^1_{\overline{\gamma}}(u_0) P_{\overline{e}_3}(-u_0) \pm \left|P_{\overline{e}_2}(-u_0)\right| \sqrt{\left(P^1_{\overline{e}_2}(-u_0)\right)^2 + \left(P^1_{\overline{e}_3}(-u_0)\right)^2 - \left(P^1_{\overline{\gamma}}(u_0)\right)^2}}{\left(P^1_{\overline{e}_2}(-u_0)\right)^2 + \left(P^1_{\overline{e}_3}(-u_0)\right)^2}. \tag{2.70}$$

As mentioned in case 1, after deciding the solution to γ_3, we continue using the second equation of system (2.63) to solve for γ_2 as follows:

$$\gamma_2 = \frac{\left|P^1_{\overline{e}_2}(-u)\right|}{P^1_{\overline{e}_2}(-u)} \frac{P^1_{\overline{\gamma}}(u)\left|P^1_{\overline{e}_2}(-u)\right| \mp P^1_{\overline{e}_3}(-u)\sqrt{\left(P^1_{\overline{e}_2}(-u)\right)^2 + \left(P^1_{\overline{e}_3}(-u)\right)^2 - \left(P^1_{\overline{\gamma}}(u)\right)^2}}{\left(P^1_{\overline{e}_2}(-u)\right)^2 + \left(P^1_{\overline{e}_3}(-u)\right)^2}, \ \forall u \in \mathbb{R}. \tag{2.71}$$

2.9.3.3 Remarks on the solution-determining step

As presented in the previous section, in both cases, in order to solve for γ_3, we need to solve many second-order equations (each equation is obtained on one parallel plane), to obtain many (pairs of) solutions of γ_3. We make two following necessary remarks:

- In theory, the true solution can only appear in one of the two cases, because the two cases are independent of each other. More precisely, our two cases are: $(\gamma_2 > 0, \gamma_3 > 0)$ and $(\gamma_2 > 0, \gamma_3 < 0)$, which are not $(\gamma_2 > 0, \gamma_3 > 0)$ and $(\gamma_2 < 0, \gamma_3 < 0)$, or $(\gamma_2 < 0, \gamma_3 > 0)$ and $(\gamma_2 > 0, \gamma_3 < 0)$, they do not link to each other, there has to be no possibility that the true solution appear in both cases under the form of $\overline{\gamma}$ and $-\overline{\gamma}$.

- In order to determine the good approximation of the true solution of γ_3, we suggest plotting all the obtained solutions in case 1 in a figure, and all solutions in case 2 in another figure. Since the solution of γ_3 we obtained are the functions of u in both cases, the horizontal axes in both figures are for u and the vertical axes are showing the potential values of the solutions. Now if $\widetilde{\gamma}_3$ is the true solution and if $\widetilde{\gamma}_3 > 0$, then in the figure of case 1, there must appear a horizontal line, which is made up of many collinear solution-points. This comes from the fact that the solutions exist for all values of u and for each value of u, there has to exist one solution which equals to the constant value $\widetilde{\gamma}_3$. The same thing happens with the figure of case 2 if $\widetilde{\gamma}_3 < 0$. And from the above remark, this horizontal line will appear in only one of the two figures. Visually, we can determine the approximation of the true solution of γ_3. And using the corresponding formula (2.68) or (2.71), we can find the approximation of γ_2.

- We will use this last remark to explain the idea of the method of determining a good approximation of γ_3. It will not be precisely presented here, because it would be better to be shown in details in chapter 3, where it plays such an important and central role of solving the calibration problem in 3D cone-beam geometry with linear sources. Now the idea of the method is after plotting all the solutions in the two corresponding figures, the horizontal line of collinear solutions will appear in one of the two figures. We will focus on this figure. Because of the existence of the (true) solutions, we can see that for every value of u, we will plot two corresponding points of solutions. Now we find the biggest solution $\gamma_3^{\max}$ among all and its corresponding u_1 value, then we find the smallest solution $\gamma_3^{\min}$ among the solutions that correspond to other values $u \neq u_1$ and we also find the value u_2 which links to $\gamma_3^{\min}$. We can see that $\gamma_3^{\max}$ (corresponding to u_1) and $\gamma_3^{\min}$ (corresponding to u_2) will be significantly different from each other. However, because of the existence of the true solution, there must exist two solutions respectively corresponding to u_1 and u_2, being approximately the same. We can easily find these two solutions and compute the average value of them $\gamma_3^{\text{average}}$. Then, for each value of u, we will find the solution that approximates $\gamma_3^{\text{average}}$. Finally, we again compute the average value over the just-found solutions, which gives us the good approximation of γ_3. Here, we choose u_1 and u_2, which respectively correspond to $\gamma_3^{\max}$ and $\gamma_3^{\min}$, rather than two arbitrary values of u, because it will be easier for the next task to detect the two solutions which corresponds to u_1 and u_2 and are approximately the same.

2.9.4 Numerical simulations of the particular degenerate case

We perform one more test with $\overline{\gamma}$ is on the same plane as $\overline{e}_2 = (0,1,0)$ and $\overline{e}_3 = (0,0,1)$, which is the particular degenerate case. Here we continue to use the same object as section 2.7 - the modified 3D Shepp-Logan phantom. In this test, we choose $\overline{\gamma} = \left(0, \frac{1}{2}, -\frac{\sqrt{3}}{2}\right)$ and $\overline{\Gamma} = \left(0, -\frac{2\sqrt{2}}{3}, \frac{1}{3}\right)$. We will see once again that the unknown directions can be calibrated independently of each other repeating the same process. We do not show again the images of the two projections $p_{\overline{e}_2}$ and $p_{\overline{e}_3}$ (they are already there in figure 2.4).

- For $\overline{\gamma} = \left(0, \frac{1}{2}, -\frac{\sqrt{3}}{2}\right)$, after performing the method presented in the previous section, we obtain the potential solutions of γ_3 as in figure 2.11. By the solution-determining step, we obtain the approximate solution of γ_3: $\overline{\gamma}_{3,\text{approx}} = -0.8663$. From this we can compute $\overline{\gamma}_{2,\text{approx}} = 0.4996$, which leads to the approximate solution of $\overline{\gamma}$ as follows:

$$\overline{\gamma}_{\text{approx}} = (0, 0.4996, -0.8663) \text{ approximates } \overline{\gamma} = \left(0, \frac{1}{2}, -\frac{\sqrt{3}}{2}\right) \approx (0, 0.5, -0.8660)\,. \tag{2.72}$$

- For $\overline{\Gamma} = \left(0, -\frac{2\sqrt{2}}{3}, \frac{1}{3}\right)$, we repeat the whole process and obtain all the potential solutions of γ_3 shown in figure 2.13. Here we want to explain why the true solution of γ_3 should be $\frac{1}{3}$, while we can visually see that the horizontal line of collinear solutions is pointing to some negative value (in figure 2.13 on the right). The reason is that the true solution $\overline{\gamma}$ that we expect has $\gamma_2 < 0$, while the algorithm given in the theory assumes $\gamma_2 > 0$ and only solves for this case, thus in this situation, the result of the algorithm will be an approximation of $-\overline{\Gamma} = \left(0, \frac{2\sqrt{2}}{3}, -\frac{1}{3}\right)$. And yes, after finish all the steps, the result of $\overline{\Gamma}_{\text{approx}}$ turns out to be:

$$\overline{\Gamma}_{\text{approx}} = (0, 0.942814, -0.333319) \text{ approximates } -\overline{\Gamma} = \left(0, \frac{2\sqrt{2}}{3}, -\frac{1}{3}\right) \approx (0, 0.942809, -0.333333)\,. \tag{2.73}$$

  In this example, we use six digits after the decimal points, since four digits show no differences when comparing the approximate solution to the true solution.

After that, we confirm the final estimated solutions by also taking the corresponding opposite directions of the approximate solutions that we just obtain:

$$\overline{\gamma}_{\text{est}} = \pm(0, 0.4996, -0.8663) \quad \text{and} \quad \overline{\Gamma}_{\text{est}} = \pm(0, 0.942814, -0.333319)\,. \tag{2.74}$$

Figure 2.12 and 2.14 respectively show the images of the projections taken at the two final estimated directions.

2.10 Global comments

- Our method was designed for a 3D object, which is fixed at a certain position. In reality, the object may have some small movements during the measuring or scanning process to obtain the projection images. For instance, when a person needs to take a CT scan, he or she will be asked to stay still in a period of time. But in fact the person may have some small movements during the scanning process. Let's say these movements are made up only from some translations (not rotations), then that leads to the existence of the unknown and random shift amount in every 2D parallel projection. Thus we will need to correct these random shifts in the parallel projections, prior to performing our method of calibrating. We base on the well-known center-of-mass result: *"the center-of-mass (COM) of a 2D parallel projection is the projection of the center-of-mass of the 3D object"*, which means all of the COMs of the parallel projections link together because they are all the projections of the COM of the 3D object along different directions. Now for each raw parallel projection, we shift to make its own COM locate at the origin of the detector. After all the COMs of the projections locate at their own detectors' origins, then because each detector's origin is in fact the projection of the world origin along the corresponding direction, it is equivalent to say that the object is now fixed at the position that the COM of the object locates at the world origin (the origin of the 3D coordinate system). Then we are ready to perform the calibration process.

- We also allow each projection image to have an unknown in-plane angle, which may be caused by an unexpected random in-plane rotation of the detector during the measuring process. By using the same row-matching method, we can even calibrate these in-plane angles. We use the word "measurements" to refer to the projections which contain the unknown in-plane angles, and to distinguish them from the projections that we have considered so far. Mathematically, each measurement $m_{\overline{\gamma},\lambda}\left(u,v\right)$ $(\lambda \in [0,2\pi))$ is defined as:

$$m_{\overline{\gamma},\lambda}\left(u,v\right) = \int f\left(u\overline{\alpha}_{\gamma}^{\lambda} + v\overline{\beta}_{\gamma}^{\lambda} + t\overline{\gamma}\right)dt, \tag{2.75}$$

where $\left(\overline{\alpha}_{\gamma}^{\lambda}, \overline{\beta}_{\gamma}^{\lambda}\right)$ is obtained by rotating $\left(\overline{\alpha}_{\gamma}, \overline{\beta}_{\gamma}\right)$ an angle λ counter-clockwise:

$$\overline{\alpha}_{\gamma}^{\lambda} = \cos\lambda\overline{\alpha}_{\gamma} + \sin\lambda\overline{\beta}_{\gamma}, \qquad \overline{\beta}_{\gamma}^{\lambda} = -\sin\lambda\overline{\alpha}_{\gamma} + \cos\lambda\overline{\beta}_{\gamma}. \tag{2.76}$$

The definition of $m_{\overline{\gamma},\lambda}$ is in fact the 2D parallel projection taken along the same direction $\overline{\gamma}$ as $p_{\overline{\gamma}}$, except the fact that the detector's coordinate system $\left(\overline{\alpha}_{\gamma}, \overline{\beta}_{\gamma}\right)$ is rotated to be $\left(\overline{\alpha}_{\gamma}^{\lambda}, \overline{\beta}_{\gamma}^{\lambda}\right)$; this is what we have just explained above about the unexpected in-plane rotation of the detector. Now the problem is that: assuming we have three (shift-corrected) measurements $m_{\overline{\gamma},\lambda}$, $m_{\overline{e}_2,\lambda_2}$, $m_{\overline{e}_3,\lambda_3}$ and we know $\overline{e}_2$, $\overline{e}_3$, we claim that by the same method of using the row-matching procedure, we can calibrate three unknown in-plane angles, and the unknown direction $\overline{\gamma}$. By the definition of the measurement and the projection, we can see the relation:

$$\begin{aligned} m_{\overline{\gamma},\lambda}\left(u,v\right) &= \int f\left(u\overline{\alpha}_{\gamma}^{\lambda} + v\overline{\beta}_{\gamma}^{\lambda} + t\overline{\gamma}\right)dt & (2.77a)\\ &= \int f\left(u\left(\cos\lambda\overline{\alpha}_{\gamma} + \sin\lambda\overline{\beta}_{\gamma}\right) + v\left(-\sin\lambda\overline{\alpha}_{\gamma} + \cos\lambda\overline{\beta}_{\gamma}\right) + t\overline{\gamma}\right)dt & (2.77b)\\ &= \int f\left(\left(u\cos\lambda - v\sin\lambda\right)\overline{\alpha}_{\gamma} + \left(u\sin\lambda + v\cos\lambda\right)\overline{\beta}_{\gamma} + t\overline{\gamma}\right)dt & (2.77c)\\ &= p_{\overline{\gamma}}\left(u\cos\lambda - v\sin\lambda, u\sin\lambda + v\cos\lambda\right). & (2.77d) \end{aligned}$$

Then for any $\theta \in [0,2\pi)$ and for all $s \in \mathbb{R}$, using this relation and applying the 2D Radon transform, we continue to obtain the following relation:

$$\begin{aligned} &\mathscr{R}_{\theta}^{2} m_{\overline{\gamma},\lambda}\left(s\right) & (2.78a)\\ &= \int m_{\overline{\gamma},\lambda}\left(s\cos\theta - t'\sin\theta, s\sin\theta + t'\cos\theta\right)dt' & (2.78b)\\ &= \int p_{\overline{\gamma}}\left(\left(s\cos\theta - t'\sin\theta\right)\cos\lambda - \left(s\sin\theta + t'\cos\theta\right)\sin\lambda, \left(s\cos\theta - t'\sin\theta\right)\sin\lambda + \left(s\sin\theta + t'\cos\theta\right)\cos\lambda\right)dt' & (2.78c)\\ &= \int p_{\overline{\gamma}}\left(s\left(\cos\theta\cos\lambda - \sin\theta\sin\lambda\right) - t'\left(\sin\theta\cos\lambda + \cos\theta\sin\lambda\right),\right.\\ &\qquad\qquad \left. s\left(\cos\theta\sin\lambda + \sin\theta\cos\lambda\right) + t'\left(\cos\theta\cos\lambda - \sin\theta\sin\lambda\right)\right)dt' & (2.78d)\\ &= \int p_{\overline{\gamma}}\left(s\cos\left(\theta+\lambda\right) - t'\sin\left(\theta+\lambda\right), s\sin\left(\theta+\lambda\right) + t'\cos\left(\theta+\lambda\right)\right)dt' & (2.78e)\\ &= \mathscr{R}_{\theta+\lambda}^{2} p_{\overline{\gamma}}\left(s\right). & (2.78f) \end{aligned}$$

By the result (2.7), we know that:

$$\mathscr{R}^2_{\theta} m_{\overline{\gamma},\lambda}\left(s\right) = \mathscr{R}^2_{\theta+\lambda} p_{\overline{\gamma}}\left(s\right) = \mathscr{R}^3_{\overline{\Psi}}\left(s\right), \forall s \in \mathbb{R}, \tag{2.79}$$

where $\overline{\Psi} = \cos\left(\theta+\lambda\right)\overline{\alpha}_{\gamma} + \sin\left(\theta+\lambda\right)\overline{\beta}_{\gamma}$. This is the general version of the relation (2.7), and from it, we derive the general pair-wise DCC for two arbitrary measurements.

Given two measurements taken along two arbitrary directions $\overline{\gamma}, \overline{\gamma}' \in \mathbb{S}^2$ with λ and λ' are two corresponding in-plane angles, if we can find a pair of suitable angles $\left(\theta, \theta'\right) \in \left[0, 2\pi\right)^2$ such that:

$$\cos\left(\theta+\lambda\right)\overline{\alpha}_{\gamma} + \sin\left(\theta+\lambda\right)\overline{\beta}_{\gamma} = \cos\left(\theta'+\lambda'\right)\overline{\alpha}_{\gamma'} + \sin\left(\theta'+\lambda'\right)\overline{\beta}_{\gamma'}, \tag{2.80}$$

then for all $s \in \mathbb{R}$:

$$\mathscr{R}^2_{\theta} m_{\overline{\gamma},\lambda}\left(s\right) = \mathscr{R}^2_{\theta'} m_{\overline{\gamma'},\lambda'}\left(s\right). \tag{2.81}$$

With this general pair-wise DCC (2.81), we (quite) similarly follow the steps in section 2.5.2.

1. Finding two in-plane angles λ_2 and λ_3: We compare two sinograms of $m_{\overline{e}_2,\lambda_2}$ and $m_{\overline{e}_3,\lambda_3}$, then perform the row-matching procedure to obtain two suitable angles $\omega_2, \omega_3 \in \left[0, 2\pi\right)$ such that:

$$\mathscr{R}^2_{\omega_2} m_{\overline{e}_2,\lambda_2}\left(s\right) = \mathscr{R}^2_{\omega_3} m_{\overline{e}_3,\lambda_3}\left(s\right), \forall s \in \mathbb{R}. \tag{2.82}$$

Then, under the condition (2.18) on the object, we also know that:

$$\cos\left(\omega_2+\lambda_2\right)\overline{\alpha}_{e_2} + \sin\left(\omega_2+\lambda_2\right)\overline{\beta}_{e_2} = \cos\left(\omega_3+\lambda_3\right)\overline{\alpha}_{e_3} + \sin\left(\omega_3+\lambda_3\right)\overline{\beta}_{e_3}. \tag{2.83}$$

We claim that from this equation, we can calculate the in-plane angles λ_2 and λ_3. Instead of using the trigonometry knowledge (which may be complicated in this case), we repeat the same trick has been used in the comment of section 2.4. Let's say both sides of the above equation equal to a vector $\overline{\xi}$, then $\overline{\xi}$ will be a unit vector, which is perpendicular to both $\overline{e}_2$ and $\overline{e}_3$:

$$\cos\left(\omega_2+\lambda_2\right)\overline{\alpha}_{e_2} + \sin\left(\omega_2+\lambda_2\right)\overline{\beta}_{e_2} = \cos\left(\omega_3+\lambda_3\right)\overline{\alpha}_{e_3} + \sin\left(\omega_3+\lambda_3\right)\overline{\beta}_{e_3} = \overline{\xi}. \tag{2.84}$$

Under the initial assumption that $\overline{e}_2 \neq \pm\overline{e}_3$, we know that there are only two possible solutions of $\overline{\xi}$:

$$\overline{\xi} = \pm\frac{\overline{e}_2 \times \overline{e}_3}{\left\|\overline{e}_2 \times \overline{e}_3\right\|}. \tag{2.85}$$

With $\overline{\xi} = \dfrac{\overline{e}_2 \times \overline{e}_3}{\left\|\overline{e}_2 \times \overline{e}_3\right\|}$, from equation (2.84), the set of solutions $\left(\widehat{\lambda}_2, \widehat{\lambda}_3\right)$ of the in-plane angles satisfying:

$$\begin{cases} \cos\left(\omega_2+\widehat{\lambda}_2\right) = \dfrac{\left(\overline{e}_2 \times \overline{e}_3\right)\cdot\overline{\alpha}_{e_2}}{\left\|\overline{e}_2 \times \overline{e}_3\right\|} \\ \sin\left(\omega_2+\widehat{\lambda}_2\right) = \dfrac{\left(\overline{e}_2 \times \overline{e}_3\right)\cdot\overline{\beta}_{e_2}}{\left\|\overline{e}_2 \times \overline{e}_3\right\|} \end{cases} \text{and} \quad \begin{cases} \cos\left(\omega_3+\widehat{\lambda}_3\right) = \dfrac{\left(\overline{e}_2 \times \overline{e}_3\right)\cdot\overline{\alpha}_{e_3}}{\left\|\overline{e}_2 \times \overline{e}_3\right\|} \\ \sin\left(\omega_3+\widehat{\lambda}_3\right) = \dfrac{\left(\overline{e}_2 \times \overline{e}_3\right)\cdot\overline{\beta}_{e_3}}{\left\|\overline{e}_2 \times \overline{e}_3\right\|} \end{cases}. \tag{2.86}$$

Since ω_2 and ω_3 have just been found, the solutions $\left(\widehat{\lambda}_2, \widehat{\lambda}_3\right)$ of the in-plane angles are clearly defined by the above systems of equations. Similarly, with $\overline{\xi} = -\dfrac{\overline{e}_2 \times \overline{e}_3}{\left\|\overline{e}_2 \times \overline{e}_3\right\|}$, we obtain another set of solutions $\left(\widetilde{\lambda}_2, \widetilde{\lambda}_3\right)$ of the in-plane angles satisfying:

$$\begin{cases} \cos\left(\omega_2+\widetilde{\lambda}_2\right) = -\dfrac{\left(\overline{e}_2 \times \overline{e}_3\right)\cdot\overline{\alpha}_{e_2}}{\left\|\overline{e}_2 \times \overline{e}_3\right\|} \\ \sin\left(\omega_2+\widetilde{\lambda}_2\right) = -\dfrac{\left(\overline{e}_2 \times \overline{e}_3\right)\cdot\overline{\beta}_{e_2}}{\left\|\overline{e}_2 \times \overline{e}_3\right\|} \end{cases} \text{and} \quad \begin{cases} \cos\left(\omega_3+\widetilde{\lambda}_3\right) = -\dfrac{\left(\overline{e}_2 \times \overline{e}_3\right)\cdot\overline{\alpha}_{e_3}}{\left\|\overline{e}_2 \times \overline{e}_3\right\|} \\ \sin\left(\omega_3+\widetilde{\lambda}_3\right) = -\dfrac{\left(\overline{e}_2 \times \overline{e}_3\right)\cdot\overline{\beta}_{e_3}}{\left\|\overline{e}_2 \times \overline{e}_3\right\|} \end{cases}. \tag{2.87}$$

From the above system of equations, we can also see that these two sets of solutions link to each other:

$$\left|\widehat{\lambda}_2 - \widetilde{\lambda}_2\right| = \pi, \tag{2.88a}$$

$$\left|\widehat{\lambda}_3 - \widetilde{\lambda}_3\right| = \pi. \tag{2.88b}$$

2. Finding the unknown direction $\overline{\gamma}$: After the two in-plane angles λ_2 and λ_3 being found, we continue to apply the row-matching procedure to the sinograms of $m_{\overline{\gamma},\lambda}$ and $m_{\overline{e}_2,\lambda_2}$, then we can find two suitable angles $\mu_2, \nu_2 \in [0, 2\pi)$ such that:

$$\begin{cases} \mathscr{R}^2_{\mu_2} m_{\overline{\gamma},\lambda}(s) = \mathscr{R}^2_{\nu_2} m_{\overline{e}_2,\lambda_2}(s), \forall s \in \mathbb{R} \\ \cos(\mu_2+\lambda)\,\overline{\alpha}_\gamma + \sin(\mu_2+\lambda)\,\overline{\beta}_\gamma = \cos(\nu_2+\lambda_2)\,\overline{\alpha}_{e_2} + \sin(\nu_2+\lambda_2)\,\overline{\beta}_{e_2} \end{cases}. \tag{2.89}$$

Similarly, comparing the sinograms of $m_{\overline{\gamma},\lambda}$ and $m_{\overline{e}_3,\lambda_3}$, we can also obtain two suitable angles $\mu_3, \nu_3 \in [0, 2\pi)$ such that:

$$\begin{cases} \mathscr{R}^2_{\mu_3} m_{\overline{\gamma},\lambda}(s) = \mathscr{R}^2_{\nu_3} m_{\overline{e}_3,\lambda_3}(s), \forall s \in \mathbb{R} \\ \cos(\mu_3+\lambda)\,\overline{\alpha}_\gamma + \sin(\mu_3+\lambda)\,\overline{\beta}_\gamma = \cos(\nu_3+\lambda_3)\,\overline{\alpha}_{e_3} + \sin(\nu_3+\lambda_3)\,\overline{\beta}_{e_3} \end{cases}. \tag{2.90}$$

Since $\nu_2, \lambda_2, \nu_3, \lambda_3$ and $\overline{\alpha}_{e_2}, \overline{\beta}_{e_2}, \overline{\alpha}_{e_3}, \overline{\beta}_{e_3}$ are all known, we can set the two following vectors which are already known:

$$\begin{cases} \overline{\Psi}_2 = \cos(\nu_2+\lambda_2)\,\overline{\alpha}_{e_2} + \sin(\nu_2+\lambda_2)\,\overline{\beta}_{e_2} \\ \overline{\Psi}_3 = \cos(\nu_3+\lambda_3)\,\overline{\alpha}_{e_3} + \sin(\nu_3+\lambda_3)\,\overline{\beta}_{e_3} \end{cases}, \tag{2.91}$$

then the estimated solution to $\overline{\gamma}$ can be obtained as in equation (2.26):

$$\overline{\gamma} = \pm \frac{\overline{\Psi}_2 \times \overline{\Psi}_3}{\left\|\overline{\Psi}_2 \times \overline{\Psi}_3\right\|}. \tag{2.92}$$

Since the two sets $\left(\widehat{\lambda}_2, \widehat{\lambda}_3\right)$ and $\left(\widetilde{\lambda}_2, \widetilde{\lambda}_3\right)$ are π-different from each other, thus they do not affect to the solution of $\overline{\gamma}$.

3. Find the final in-plane angle: From the second equation in system (2.89), since the angles μ_2, ν_2, λ_2 and the unit vectors $\overline{\alpha}_\gamma, \overline{\beta}_\gamma, \overline{\alpha}_{e_2}, \overline{\beta}_{e_2}$ are already known, we can calculate λ using the same trick as presented in step 1. We will also obtain two possible solutions $\widehat{\lambda}$ and $\widetilde{\lambda}$, which respectively correspond $\left(\widehat{\lambda}_2, \widehat{\lambda}_3\right)$ and $\left(\widetilde{\lambda}_2, \widetilde{\lambda}_3\right)$ (substituting $\widehat{\lambda}_2$ or $\widetilde{\lambda}_2$ into to the equation respectively leads to the solution $\widehat{\lambda}$ or $\widetilde{\lambda}$).

In conclusion, by the same method as in section 2.5.2 with some extra works, we can calibrate the unknown direction and the three correponding in-plane angles. Here we obtain two possible sets of solutions of the in-plane angles: $\left(\widehat{\lambda}, \widehat{\lambda}_2, \widehat{\lambda}_3\right)$ and $\left(\widetilde{\lambda}, \widetilde{\lambda}_2, \widetilde{\lambda}_3\right)$, which are π-different from each other, with no further clues, some more studies need to be done.

- Again, we repeat that the degenerate case that has been done here is just a particular case, when the two known directions are $(0,1,0)$ and $(0,0,1)$. Further studies need to be done to completely solve the general degenerate case. One hidden but important thing that we need to mention here is that the solution of the particular degenerate case depends on solving many 2D calibration problems on the parallel planes and it can only be solved if there are at least two parallel planes giving different information about the slices of the 3D object. Otherwise, if all parallel planes give the same information about the slices, in general we end up obtaining a pair of solutions repeating multiple times and we will not know which of them is the true solution that needs to be chosen. Thus the structure of the 3D object has to be general enough, and once again the object condition (2.18) contributes a crucial part even in this degenerate case.
- In order to obtain a fully automatic calibration method to this problem, we need to get rid of the assumption of knowing the viewing directions of two projections in advance. Following the idea of Basu and Bresler of defining the equivalent classes is a possible path to start (see [Basu and Bresler, 2000b, Basu and Bresler, 2000a]).
- We keep repeating this, but the trick of consider a 3D calibration problem as a series of many 2D calibration problems, and related topics are the main and central part of chapter 3. So they will be shown and explained in details in the next chapter.

2.11 Simulation images

As mentioned before, this section contains all of the simulation images in the order that they appear in the text.

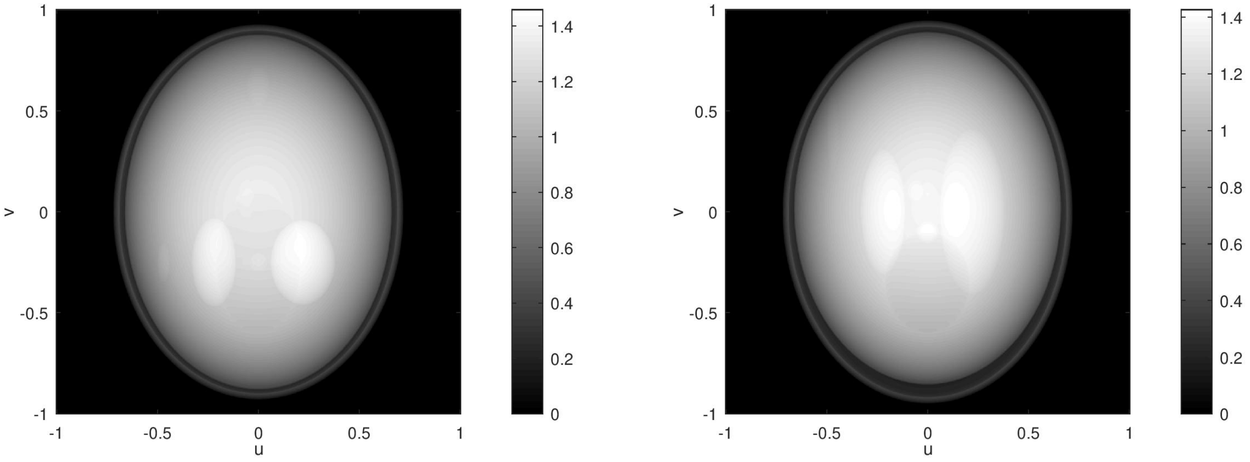

Figure 2.4: Projection images $p_{\overline{e}_2}(u,v)$ (left) and $p_{\overline{e}_3}(u,v)$ (right), where $\overline{e}_2 = (0,1,0)$ and $\overline{e}_3 = (0,0,1)$

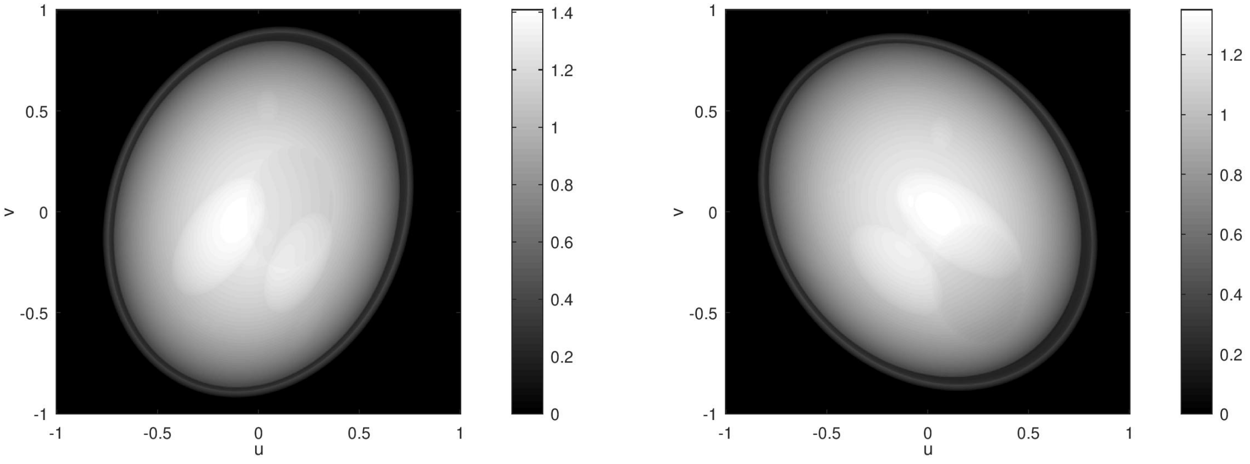

Figure 2.5: Projection images $p_{\overline{\gamma}}(u,v)$ (left) and $p_{\overline{\Gamma}}(u,v)$ (right), where $\overline{\gamma} = \left(\frac{1}{3}, -\frac{2}{3}, \frac{2}{3}\right)$ and $\Gamma = \left(\frac{1}{2}, \frac{1}{2}, \frac{1}{\sqrt{2}}\right)$

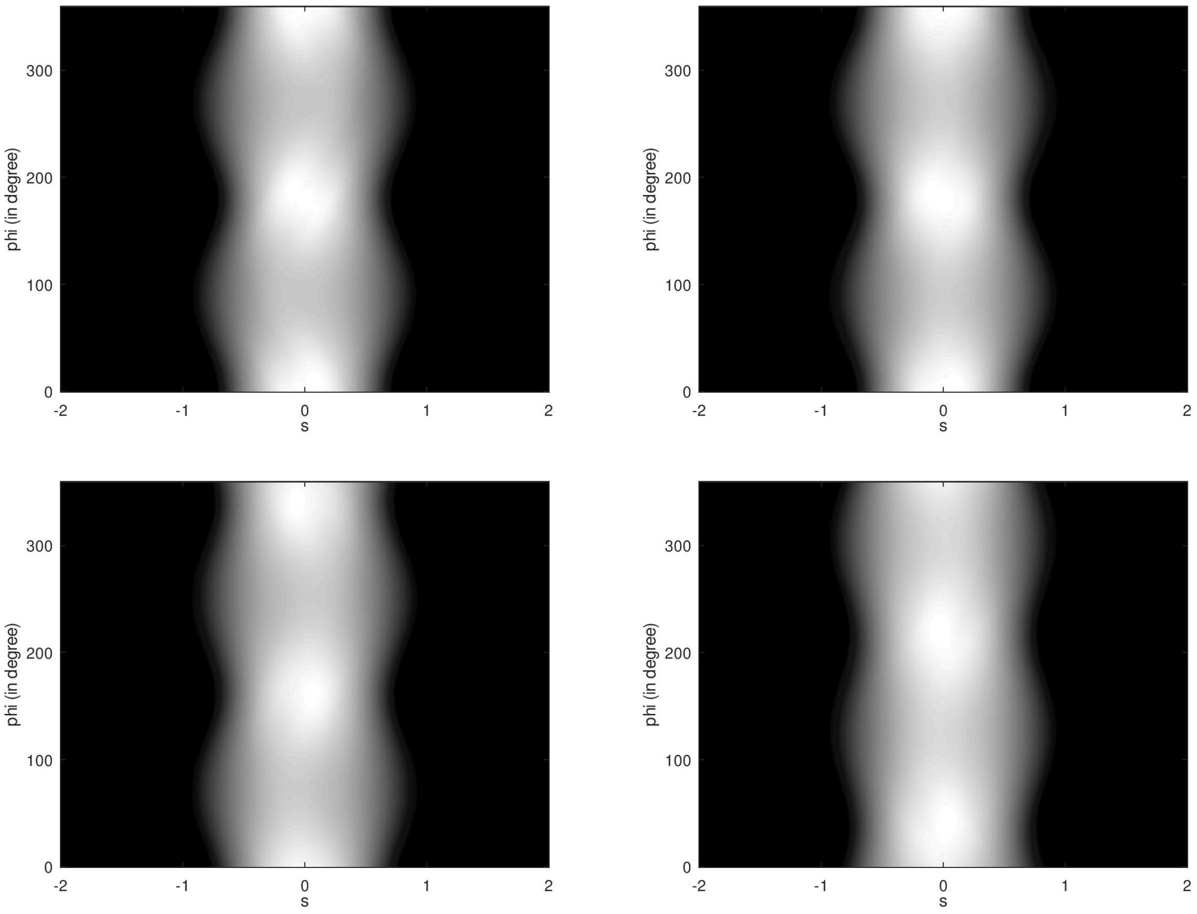

Figure 2.6: Sinograms which correspond to $p_{\overline{e}_2}$ (top-left), $p_{\overline{e}_3}$ (top-right), $p_{\overline{\gamma}}$ (bottom-left) and $p_{\overline{\Gamma}}$ (bottom-right)

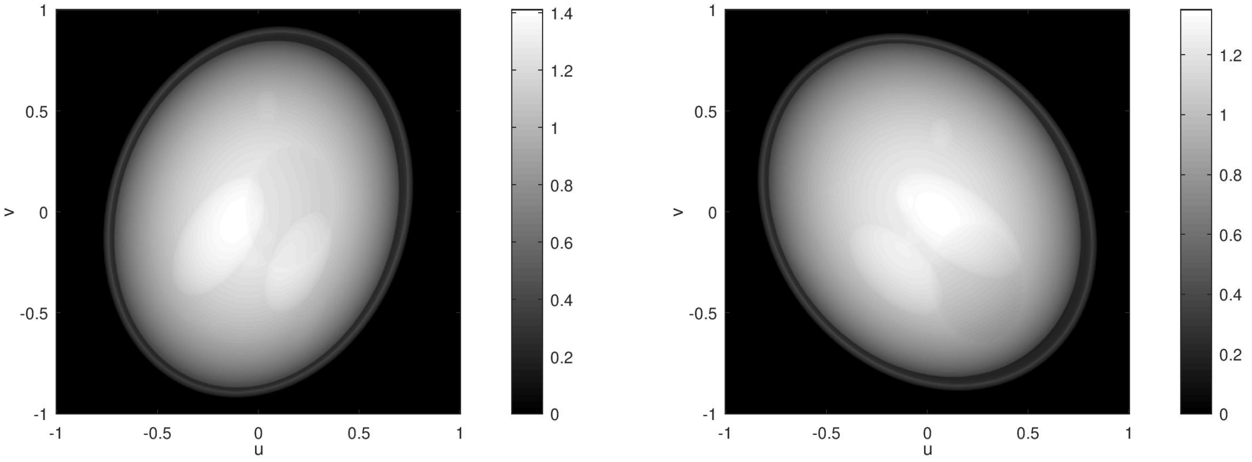

Figure 2.7: Projection images along two respective estimated directions of $\overline{\gamma}$ and $\overline{\Gamma}$: $p_{\overline{\gamma}_{\text{est}}}$ and $p_{\overline{\Gamma}_{\text{est}}}$, where $\overline{\gamma}_{\text{est}} \approx (0.3260, -0.6685, 0.6685)$ and $\overline{\Gamma}_{\text{est}} \approx (0.4975, 0.4975, 0.7106)$

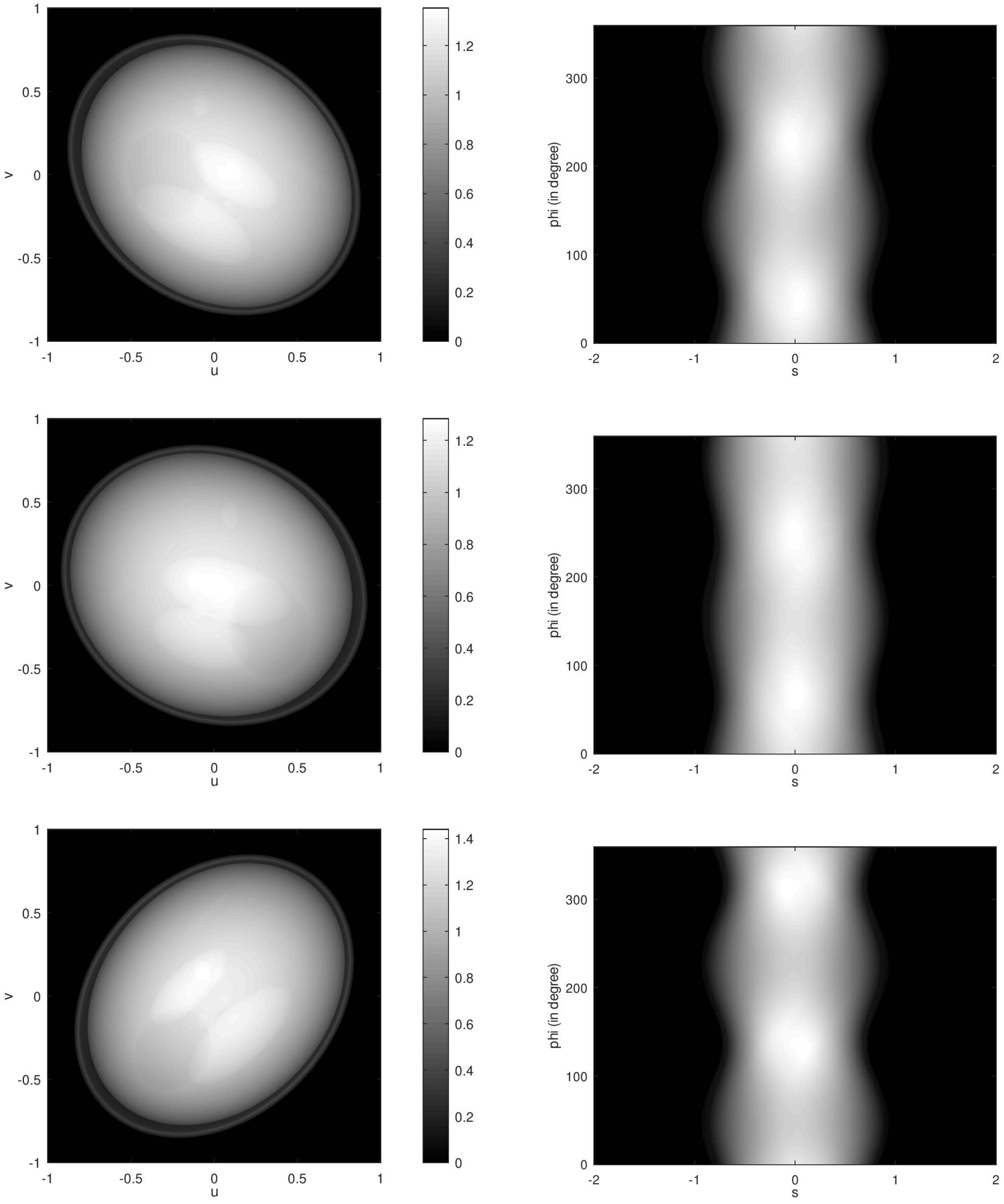

Figure 2.8: Projection images (left column) and their corresponding sinograms (right column) of $p_{\overline{e}_2}(u,v)$ (top row), $p_{\overline{e}_3}(u,v)$ (middle row) and $p_{\overline{\gamma}}(u,v)$ (bottom row), where $\overline{e}_2 = \left(\frac{1}{2}, \frac{1}{3}, -\frac{\sqrt{23}}{6}\right)$, $\overline{e}_3 = \left(-\frac{2}{3}, -\frac{1}{4}, -\frac{\sqrt{71}}{12}\right)$, and $\overline{\gamma} = \left(-\frac{1}{4}, \frac{1}{4}, \frac{\sqrt{14}}{4}\right)$

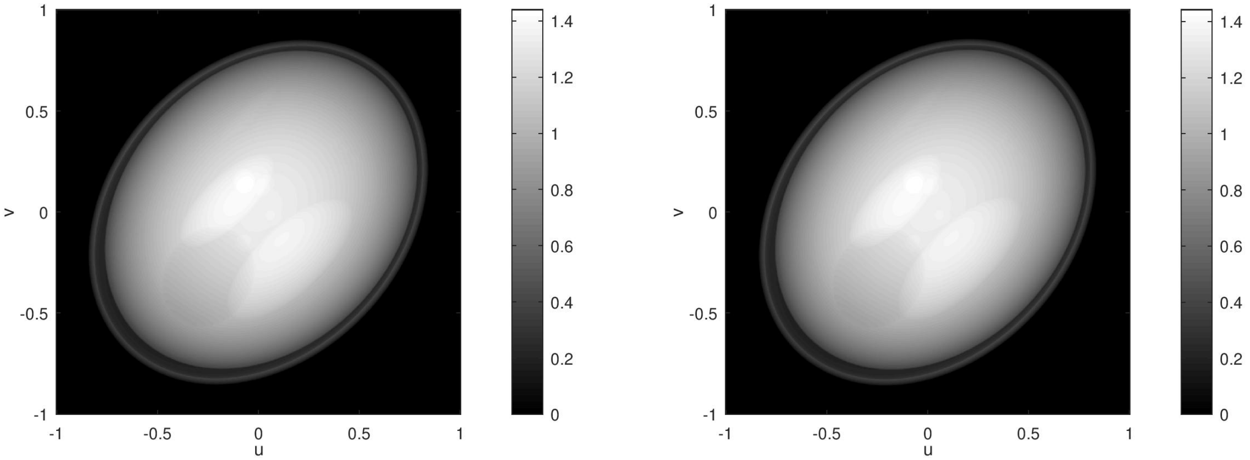

Figure 2.9: Projection images along the unknown direction $p_{\overline{\gamma}}(u,v)$ and its estimated direction $p_{\overline{\gamma}_{\text{est}}}(u,v)$, where $\overline{\gamma} = \left(-\frac{1}{4}, \frac{1}{4}, \frac{\sqrt{14}}{4}\right)$ and $\overline{\gamma}_{\text{est}} \approx (-0.2427, 0.2550, 0.9360)$

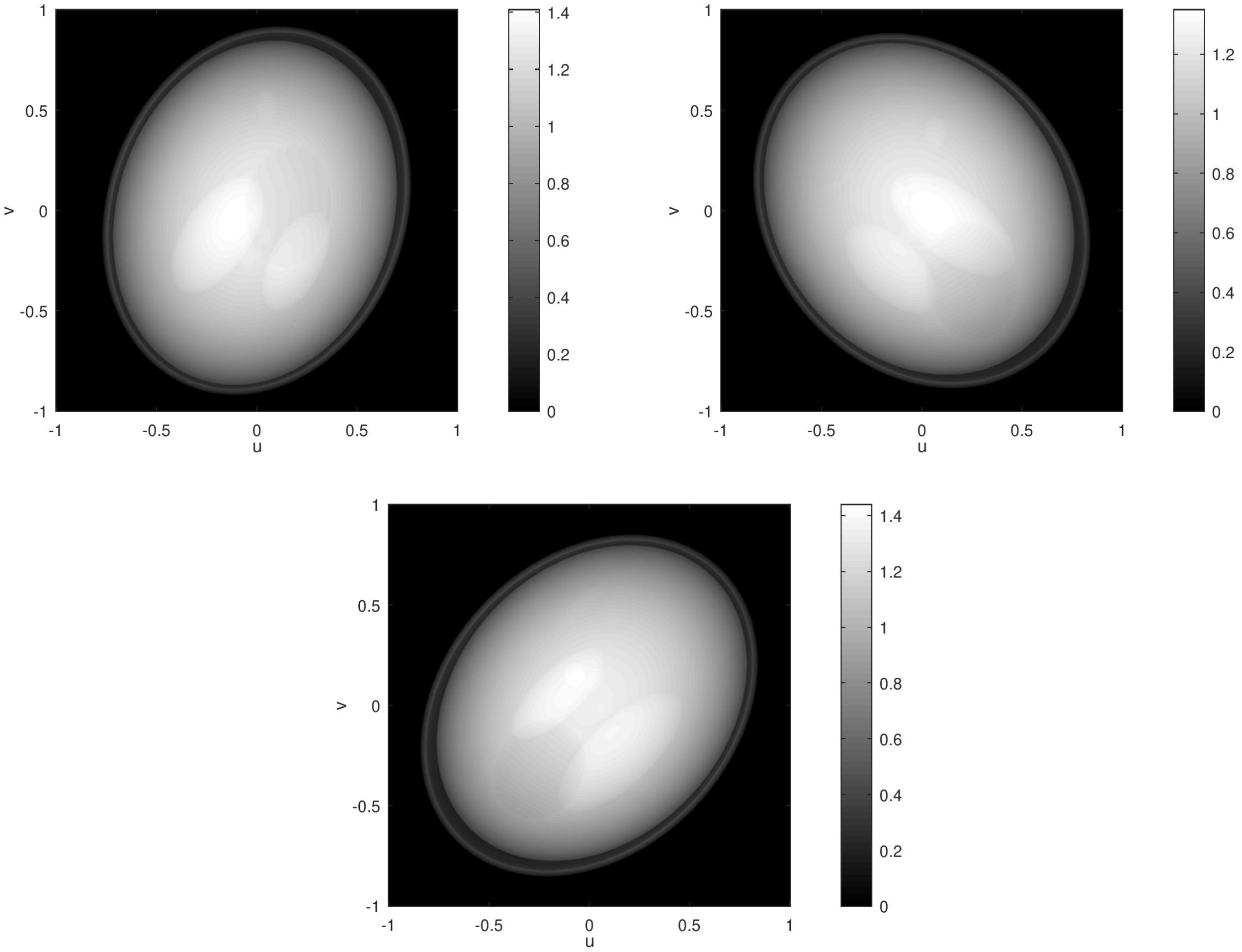

Figure 2.10: Top row: projections along refined estimated directions $\overline{\gamma}_{\text{est, refined}} = (0.3334, -0.6667, 0.6667)$ and $\overline{\Gamma}_{\text{est, refined}} = (0.5001, 0.5001, 0.7070)$ (test 1), bottom row: projection along refined estimated direction $\overline{\gamma}_{\text{est}} = (-0.2499, 0.2496, 0.9356)$ (test 2)

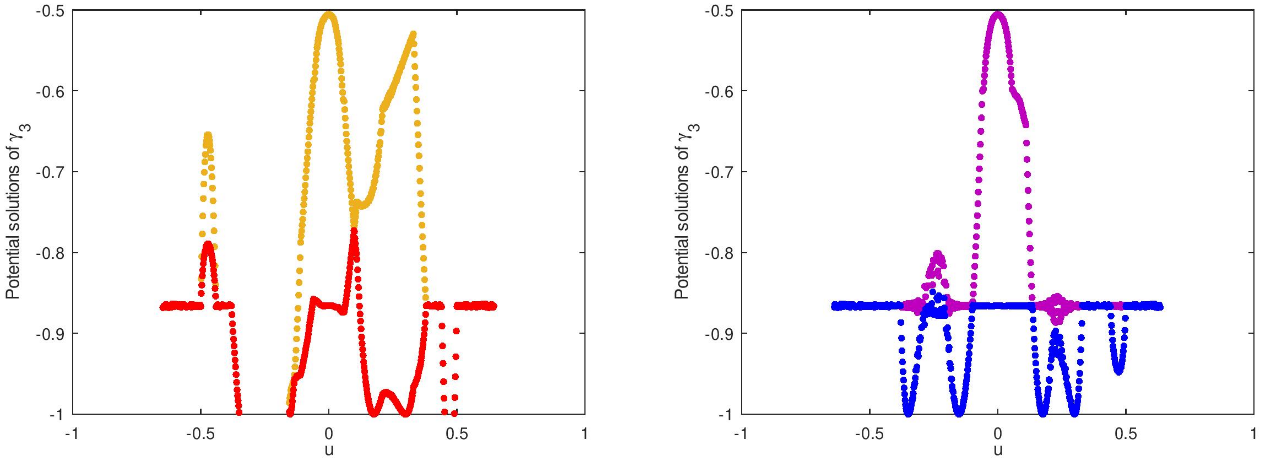

Figure 2.11: Potential solutions of γ_3 in case 1: $\gamma_2, \gamma_3 > 0$ (left) and case 2: $\gamma_2 > 0, \gamma_3 < 0$ (right)

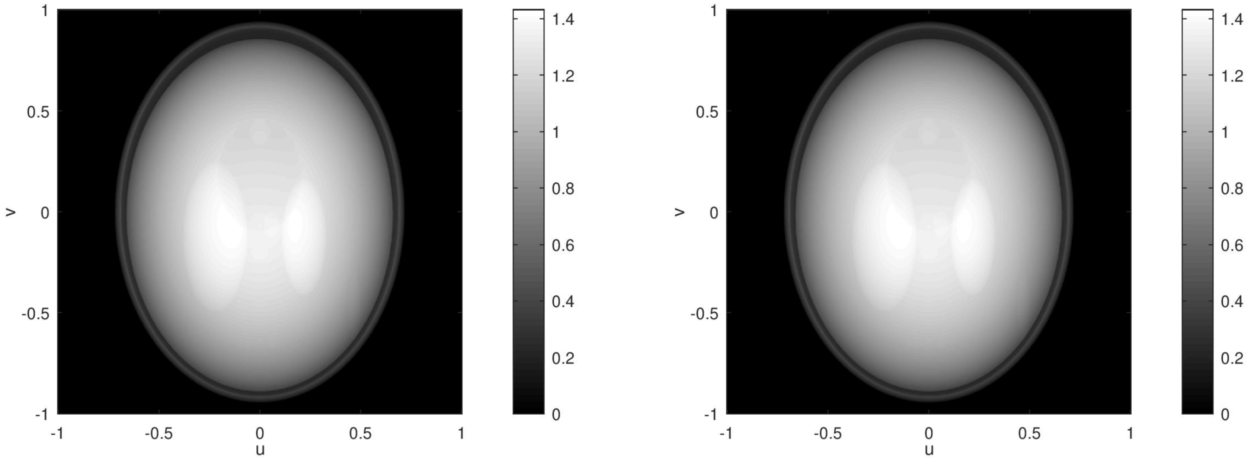

Figure 2.12: Projections along the unknown direction $\overline{\gamma} = \left(0, \frac{1}{2}, -\frac{\sqrt{3}}{2}\right)$ (left) and the approximate direction $\overline{\gamma}_{\text{approx}} = (0, 0.4996, -0.8663)$

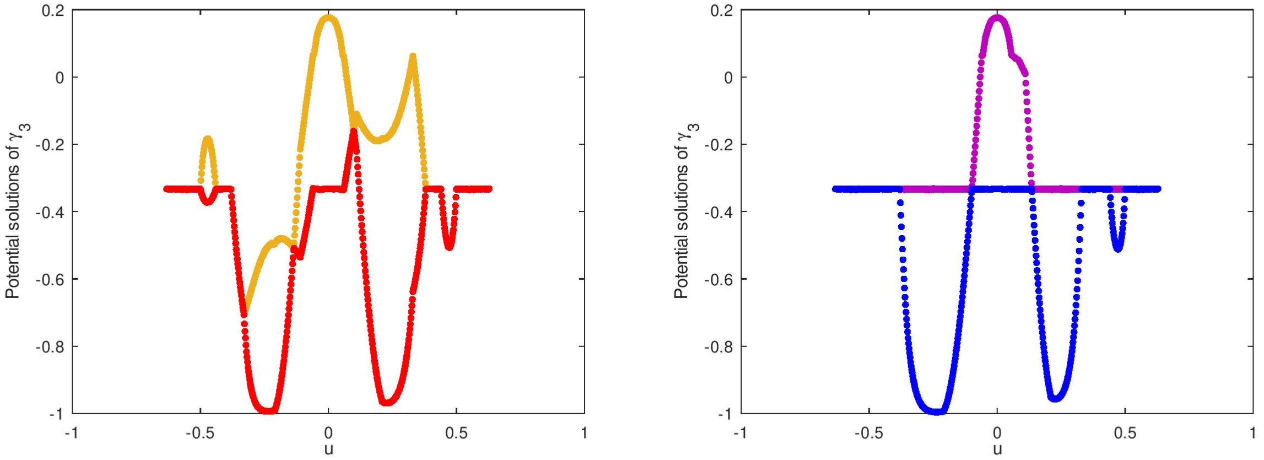

Figure 2.13: Potential solutions of γ_3 in case 1: $\gamma_2, \gamma_3 > 0$ (left) and case 2: $\gamma_2 > 0, \gamma_3 < 0$ (right)

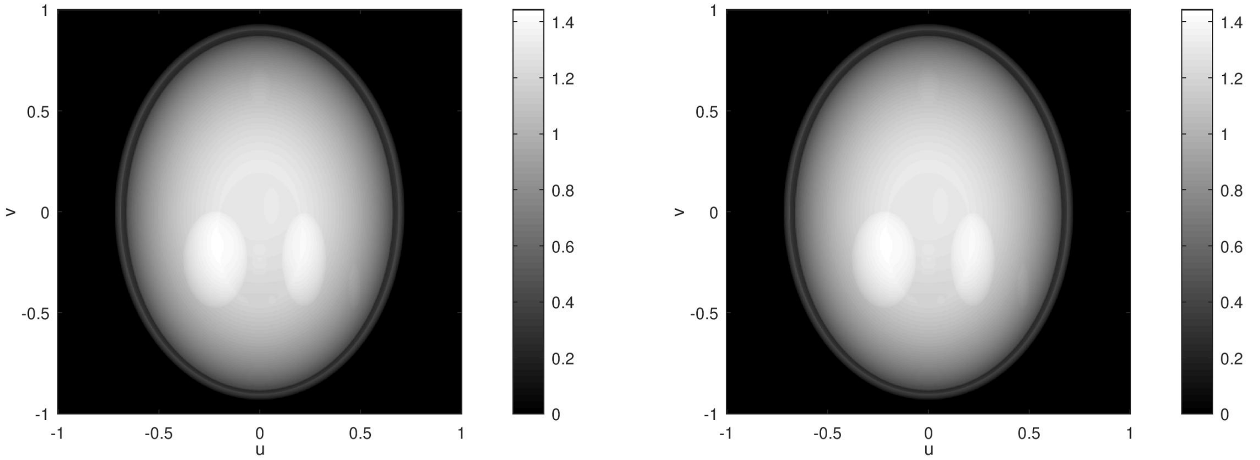

Figure 2.14: Projections along the unknown direction $\overline{\Gamma} = \left(0, -\frac{2\sqrt{2}}{3}, \frac{1}{3}\right)$ (left) and the approximate direction $\overline{\Gamma}_{\text{est}} = (0, 0.942814, -0.333319)$

Chapter 3

DCCs for fan-beam projections and applications

French summary of the content

Dans ce chapitre, nous travaillons avec la géométrie divergente, et nous étudions les conditions de cohérence des données pour les projections en éventail, ou *Fan-beam consistency conditions* (FBCC). Ce chapitre reprend notre intervention [Nguyen et al., 2020b] dans la conférence *CT Meeting 2020*. Les résultats numériques ont été améliorés après la publication de l'article, ce qui montre quelques différences par rapport à l'article original.

Une approche principale pour créer les FBCC, qui a suscité de l'intérêt pendant un certain temps, consiste à trouver la relation entre les projections parallèles 2D et les projections en éventail, afin de convertir les conditions de cohérence Helgason-Ludwig (HLCC) de la géométrie parallèle vers la géométrie en éventail, c'est à dire des variables parallèles vers les variables en éventail, voir [Hengyong Yu et al., 2006] et [Yu and Wang, 2007]. Dans ces articles, la version fan-beam des HLCC est obtenue pour les projections conventionnelles en géométrie fan-beam (ce qui signifie que les projections fan-beam sont les intégrales linéaires calculées en termes de vecteurs unitaires montrant la direction d'intégration), avec la source de rayons X se déplaçant le long d'un cercle. Les HLCC sont directement converties de la géométrie parallèle 2D standard vers la géométrie fan-beam en trajectoire circulaire de la source. Dans les articles [Clackdoyle, 2013, Clackdoyle et al., 2014, Clackdoyle, 2018], Clackdoyle et al. considèrent la géométrie du faisceau en éventail avec la source de rayons X se déplaçant le long d'une droite. Il existe deux FBCC de type polynomial. Une condition fonctionne avec les projections conventionnelles en éventail, qui sont des fonctions à variable angulaire. Le moment d'ordre n dans cette situation intègre les projections fan-beam classiques multipliées par le terme $tan^n(\phi)/cos\phi$, où ϕ est la variable angulaire. L'autre condition est établie pour les projections fan-beam collectés sur un détecteur plat qui se situe sur une ligne parallèle à la trajectoire de la source. Elle fonctionne avec des projections pondérées par des fonctions de la variable réelle u modélisant le détecteur. Le moment d'ordre n est l'intégration des projections pondérées en éventail multipliées par le terme u^n. Bien que les formules de moment soient différentes, ces deux FBCC s'impliquent mutuellement, ce qui signifie que nous pouvons obtenir une condition à partir de l'autre en changeant les variables de manière appropriée. En outre, l'article [Clackdoyle, 2018] nous montre également quelques DCC pour les projections parallèles 3D et les projections à faisceau conique, avec la source de rayons X se déplaçant sur un plan. L'article [Clackdoyle and Desbat, 2015] présente une FBCC s'appliquant sur les projections conventionnelles en éventail avec la source se déplaçant le long d'un cercle. L'article nous apprend que cette FBCC est construite sur la base du résultat suivant en géométrie parallèle 2D : étant donnée une fonction f à valeurs réelles 2D à support compact, si p est définie comme la projection parallèle modélisée par la transformée de Radon 2D :

$$p\left(\phi, s\right)=\int f\left(s\begin{bmatrix}\cos\phi\\ \sin\phi\end{bmatrix}+t\begin{bmatrix}-\sin\phi\\ \cos\phi\end{bmatrix}\right)dt, \quad \forall\phi\in\left[0,2\pi\right), \forall s\in\mathbb{R},$$

alors $B_n(x)$ défini par :

$$B_n\left(x\right)=\int_{-\pi/2}^{\pi/2}p\left(\phi, x\cos\phi+y_0\sin\phi\right)\frac{\tan^n\phi}{\cos\phi}d\phi,$$

deviendra un polynôme en x de degré au plus n, où y_0 est une valeur appropriée telle que $y=y_0$ est une ligne horizontale qui n'intersecte jamais l'enveloppe convexe du support de f. Le FBCC dans [Clackdoyle and Desbat, 2015] est la version du résultat ci-dessus en géométrie parallèle 2D convertie en géométrie fan-beam avec une trajectoire circulaire de la source. De plus, dans l'article [Clackdoyle et al., 2015], Clackdoyle et al. nous montrent la FBCC s'appliquant sur les projections classiques en éventail, avec la source se déplaçant le long d'un petit arc de cercle. L'idée pour créer cette FBCC est de considérer la corde reliant deux extrémités de l'arc, puis de "rebinner" (réorganiser) les données en recherchant la relation entre les projections réelles de faisceaux en éventail avec les sources sur l'arc considéré, et les projections virtuelles de faisceaux en éventail avec les sources sur la corde correspondante. Comme la trajectoire de la source des projections virtuelles en éventail est un segment de droite, il existe déjà la FBCC à variable angulaire pour ces projections virtuelles en éventail, voir [Clackdoyle, 2013], puis les auteurs obtiennent une nouvelle forme de cette FBCC à appliquer sur les projections en éventail avec des sources sur un arc de cercle. La formule sous cette forme est similaire à la FBCC de l'article [Clackdoyle and Desbat, 2015]. Il existe une autre approche consistant à utiliser le résultat de Levine, basé sur l'équation de John, pour obtenir une FBCC pour les projections pondérées en éventail avec des sources sur une ligne, voir [Levine et al., 2010]. Le résultat de Levine est lié à la FBCC d'ordre 0 à variable linéaire dans [Clackdoyle, 2013]. Ce fait a également été mentionné et utilisé dans [Lesaint et al., 2017].

En plus des résultats de DCC, nous apprenons également de l'article [Desbat and Clackdoyle, 2019] les résultats sur les liens entre le centre de masse (center of mass - COM) de l'objet et le COM d'une telle projection considérée, en géométrie parallèle ainsi qu'en géométrie fan-beam avec des sources sur une ligne. Dans notre travail, nous voulons présenter à nouveau la FBCC pour les projections pondérées en éventail et le résultat du COM en géométrie en éventail avec des sources linéaires, et les utiliser pour aborder un problème de calibrage géométrique 3D en faisceau conique. Dans ce problème, nous travaillons dans l'espace 3D, avec (x_1, x_2, x_3) comme système de coordonnées standard. Le modèle avec lequel nous allons travailler comprend une source de rayons X se déplaçant le long de l'axe x_1, et un détecteur plat en 2D, qui est perpendiculaire à l'axe x_2 et à une distance $T > 0$ de l'origine du référentiel de travail. Nous disposons d'une collection de projections par faisceau conique d'un objet inconnu 3D à support compact, qui ont été acquise sur un détecteur plan. Supposons que nous connaissions à l'avance trois positions de la source, pour lesquelles respectivement trois projections par faisceau conique ont été acquises. Nous pouvons alors calibrer les positions des sources de toutes les autres projections à faisceau conique, une par une et indépendamment les unes des autres. D'un point de vue physique, nous pouvons comprendre le modèle comme suit : un objet 3D se trouve sur un tapis roulant horizontal, placé entre une source de rayons X et un détecteur suffisamment grand. La source de rayons X est fixe, tandis que la bande transporteuse et le détecteur se déplacent ensemble horizontalement dans la même direction mais à des vitesses différentes, en suivant la règle selon laquelle la projection du faisceau conique de l'objet reste toujours entièrement à l'intérieur du détecteur, de sorte qu'il n'y a pas de troncature dans toutes les projections du faisceau conique, voir figure 3.1. Ce mouvement équivaut au fait que l'objet 3D est fixé à une certaine position, que le détecteur se déplace dans la même direction horizontale que ci-dessus, tandis que la source de rayons X se déplace maintenant le long d'une ligne dans la direction opposée, par rapport au détecteur, voir figure 3.2. Supposons que, pour une raison quelconque, lors de la procédure de mesure et de prise des projections de l'objet, après les trois premières projections, le système commence à perdre sa trace. Les projections sont toujours correctes, mais nous ne pouvons connaître aucune autre position de source à laquelle les projections ont été prises, à l'exception des trois premières projections. Nous cherchons donc à calibrer les positions des sources de toutes les autres projections en faisceau conique, en nous basant sur les trois positions connues des sources, leurs projections en faisceau conique et les projections correspondantes des positions inconnues des sources.

Les chapitres 2 et 3 peuvent également être considérés comme un duo de chapitres liés, puisque le chapitre 3 a le même esprit que le cas dégénéré du chapitre 2. Le chapitre 2 traite de la géométrie parallèle 3D, et la technique utilisée dans le cas dégénéré peut être comprise comme la construction de nombreux plans parallèles, qui passent par l'objet 3D, et la résolution des problèmes de calibration 2D sur chaque plan au lieu de résoudre le problème de calibration 3D, puis de choisir la solution commune à tous. Le chapitre 3 traite de la géométrie du faisceau conique 3D. Nous verrons que nous effectuons un travail similaire en construisant de nombreux plans obliques coupant l'objet 3D, et en considérant le problème de calibrage du faisceau conique 3D comme une série de nombreux problèmes de calibrage du faisceau en éventail 2D sur les plans obliques, pour les résoudre et choisir la solution commune à tous.

Ce chapitre est organisé comme suit : la section 3.2 présente les définitions des projections du faisceau en éventail, les définitions de leurs moments correspondants, la FBCC, le résultat du COM et une petite simulation pour illustrer la FBCC ; la section 3.3 montre la méthode de calibrage de la position de la source dans le problème de calibrage du faisceau en éventail 2D, avec une simulation numérique pour tester la méthode. De même, la section 3.4 présente les définitions des projections du faisceau conique. La section 3.5 donne la méthode de construction des plans obliques et de calibrage des positions de source inconnues. Un algorithme permettant de choisir la solution finale estimée pour la position de la source inconnue, ainsi que deux expériences numériques sont également présentés dans cette section.

3.1 Introduction

This chapter presents our proceedings paper [Nguyen et al., 2020b] in the conference CT Meeting 2020. The numerical results are improved after the paper being published, which shows some differences in comparison to the original published proceeding.

In this chapter, we work with the divergent geometry, and study the Data consistency conditions for the fan-beam projections, or Fan-beam consistency conditions (FBCCs). One main approach to create the FBCCs, which has been of interests for a period of time, is to find the relationship between the 2D parallel projections and the fan-beam projections, in order to convert the well-known Helgason-Ludwig consistency conditions (HLCCs) into fan-beam geometry, with fan-beam variables, see [Hengyong Yu et al., 2006] and [Yu and Wang, 2007]. In those papers, the fan-beam version of the HLCC is applied for the conventional fan-beam projections (meaning the fan-beam projections are the line integrals computed in terms of unit vectors showing the integration direction), with the x-ray source moving along a circle, since it is directly converted from the standard 2D parallel geometry, which deals with circular source trajectory. In the papers [Clackdoyle, 2013, Clackdoyle et al., 2014, Clackdoyle, 2018], Clackdoyle *et. al.* considers the fan-beam geometry with the x-ray source moving along a line. There are two polynomial-type FBCCs: one condition works with the conventional fan-beam projections, which are angular-variable functions. The moment of order n in this situation integrates the conventional fan-beam projections multiplied by the term $\tan^n(\phi)/\cos\phi$, where ϕ is the angular variable. The other condition works with the weighted fan-beam projections, which are linear-variable functions. They are assumed to be collected on a flat detector, which locates on a line being parallel and at a distance to the line of source trajectory. The moment of order n is the integration of the weighted fan-beam projections multiplied by the term u^n, where u is the linear variable. Although the moment formulae are different, these two FBCCs imply each other, meaning we can obtain one condition from the other one by changing the variables appropriately. Additionally, the paper [Clackdoyle, 2018] also shows us some DCCs for the 3D parallel projections and the cone-beam projections, with the x-ray source moving on a plane. The paper [Clackdoyle and Desbat, 2015] presents a FBCC applying on the conventional fan-beam projections with the source moving along a circle. We learn from the paper that this FBCC is constructed basing on the following result in 2D parallel geometry: given a 2D real-valued function f, with compact support, if p is defined as the parallel projection thanks to the 2D Radon transform:

$$p(\phi, s) = \int f\left(s\begin{bmatrix}\cos\phi\\ \sin\phi\end{bmatrix} + t\begin{bmatrix}-\sin\phi\\ \cos\phi\end{bmatrix}\right)dt, \quad \forall\phi\in[0,2\pi), \forall s\in\mathbb{R}, \tag{3.1}$$

then $B_n(x)$ defined as the following:

$$B_n(x) = \int_{-\pi/2}^{\pi/2} p(\phi, x\cos\phi + y_0\sin\phi)\frac{\tan^n\phi}{\cos\phi}d\phi, \tag{3.2}$$

will become a polynomial in x of degree at most n, where y_0 is a suitable value such that $y = y_0$ is a horizontal line that never intersects the convex hull of the support of f. The FBCC in [Clackdoyle and Desbat, 2015] is the converted version of the above result (in 2D parallel geometry) into fan-beam geometry with circular source trajectory. Moreover, in the paper [Clackdoyle et al., 2015], Clackdoyle *et. al.* shows us the FBCC applying on the conventional fan-beam projections, with the source moving along a small arc of a circle. The idea to create this FBCC is to consider the chord connecting two endpoints of the arc, then rebin the data by seeking the relationship between the real fan-beam projections with sources on the considering arc, and the virtual fan-beam projections with sources on the corresponding chord. Since the source trajectory of the virtual fan-beam projections is a line segment, there already exists the angular-variable FBCC for these virtual fan-beam projections as in [Clackdoyle, 2013], then the authors obtain a new form of this FBCC to apply on the fan-beam projections with sources on an arc of a circle. The formula in this form is similar to the FBCC in the paper [Clackdoyle and Desbat, 2015]. There is one more approach of using Levine's result, based on John's equation, to obtain a FBCC for the weighted fan-beam projections with sources on a line, see [Levine et al., 2010]. Levine's result links to the linear-variable FBCC in [Clackdoyle, 2013] of order 0, this fact has also be mentioned and used in [Lesaint et al., 2017].

In addition to the DCC results, we learn also from the paper [Desbat and Clackdoyle, 2019] the results on the links between the center-of-mass (COM) of the object and the COM of such a considering projection, in parallel as well as fan-beam geometry with sources on a line. In our work, we want to describe again the FBCC for the weighted fan-beam projections and the COM result in fan-beam geometry with linear sources, and make use of them to approach a 3D cone-beam geometric calibration "toy" problem. In this problem, we are working in the 3D space, with (x_1, x_2, x_3) as our standard coordinate system. The model we are going to work with include an x-ray source moving along the x_1-axis, and a 2D flat detector, which is perperdicular to the x_2-axis and at distance $T > 0$

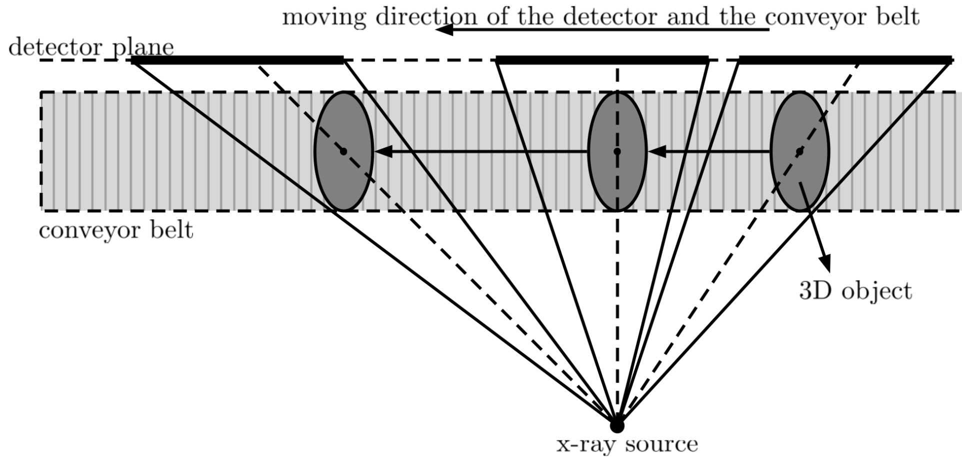

Figure 3.1: Top view of the physical model: the x-ray source is fixed, while the 3D object sitting on the conveyor belt and the detector are moving respectively together in the same direction. The speeds of the detector and the conveyor belt are unknown, and different from each other, but the cone-beam projection of the object always stay inside the detector, meaning there is no truncation in the cone-beam projections.

away from the world origin. We are having a collection of cone-beam projections of an unknown 3D object with compact support, that were taken on the flat detector. Assuming that we know in advance three source positions, that three corresponding cone-beam projections were taken at. Then we can calibrate the source positions of every other cone-beam projection, one at a time and independently of each other. Physically, we can understand the model as follows: there is a 3D object sitting on a horizontal conveyor belt, which is placed in between an x-ray source and a sufficiently large detector. The x-ray source is fixed at its own position, while the conveyor belt and the detector are moving together horizontally in the same direction but at different speeds, following the rule that the cone-beam projection of the object always remains entirely inside the detector, so there is no truncation in all the cone-beam projections, see figure 3.1. This motion is equivalent to the 3D object being fixed at a certain position, the detector is moving in the same horizontal direction as above, while the x-ray source is now moving along a line in the opposite direction, comparing to the detector. And they are moving corresponding to each other, see figure 3.2. Assuming that for some reason, in the procedure of measuring and taking the projections of the object, after the first three projections, the system start losing its track. The projections are still correct, but we cannot know any other source positions that the projections were taken at, except the first three projections. So we aim to calibrate the source positions of all other cone-beam projections, based on the three known source positions, their cone-beam projections, and the corresponding projections of the unknown source positions.

Chapter 2 and chapter 3 can also be considered as a duo of linked chapters, since this chapter has the same spirit as the *degenerate case* in chapter 2. Chapter 2 deals with the 3D parallel geometry, and the technique used in the degenerate case can be understood as constructing many parallel planes, which pass through the 3D object, and solving the 2D calibration problems on each plane instead of solving the 3D calibration problem, then choosing the common solution among all. Chapter 3 works with the 3D cone-beam geometry, we will see below that we are doing a similar job of constructing many oblique planes slicing through the 3D object, and considering the 3D cone-beam calibration problem as a series of many 2D fan-beam calibration problems on the oblique planes, to solve them and to choose the common solution among all of them.

This chapter is organized as follows: section 3.2 presents the definitions of the fan-beam projections, the definitions of their corresponding moments, the FBCC, the COM result, and a small simulation to illustrate the FBCC; section 3.3 shows the method to calibrate the source position in the 2D fan-beam calibration problem, with a numerical experiment testing the method. Similarly, section 3.4 shows the definitions of the cone-beam projections. And section 3.5 gives the method of constructing the oblique planes and calibrating the unknown source positions. An algorithm to choose the final estimated solution for the unknown source position, and two numerical experiments have also been presented in this section.

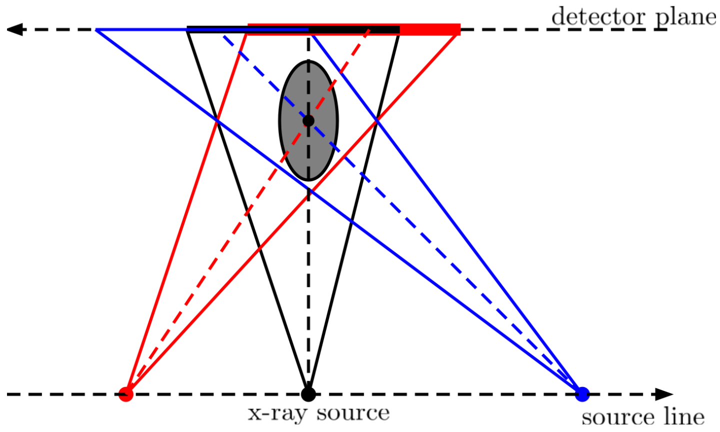

Figure 3.2: Top view of the equivelant model: the 3D object is fixed, while the x-ray source and the detector are moving respectively to each other in opposite directions.

3.2 Fan-beam consistency condition (FBCC)

We present the related materials to the FBCC. Section 3.2.1 gives the definition of the fan-beam projections, section 3.2.2 gives the definitions of the moment of the weighted fan-beam projections and presents the FBCC, section 3.2.3 shows the COM result, and section 3.2.4 shows a small numerical simulation to illustrate the FBCC.

3.2.1 Fan-beam projections

We start with the conventional fan-beam projection definition. Given a 2D compactly supported function f, for an arbitrary source location on the 2D plane $\vec{x} = (x_1, x_2)$, the conventional fan-beam projection computed at $\vec{x}$ and the integration direction $\vec{\gamma}$ is defined as follows:

$$\widehat{p}_{\vec{x}}\left(\vec{\gamma}\right) = \int_0^\infty f\left(\vec{x} + t'\vec{\gamma}\right) dt', \quad \forall \gamma \in \mathbb{S}^1. \tag{3.3}$$

Throughout this section, we use the notation $\vec{x}$ (x with the arrow above) to mention the 2D vector $\vec{x} = (x_1, x_2)$; and x (only) to imply a real number. More precisely, we use $(x, 0)$ to mention the source location on the x_1-axis. We continue to consider the following model, as shown in figure 3.3, where the x-ray source is moving along x_1-axis. We assume the detector line is $x_2 = D$, where D is a positive constant. We call the detector line the u-axis, with the origin of the detector is at $(0, D)$ and u-axis has the same direction as x_1-axis. With f being the 2D object - the 2D compactly supported function, lying in between the x_1-axis and u-axis, the weighted fan-beam projection on the detector line $x_2 = D$ (with the source moving along the x_1-axis) is defined as:

$$p_{(x,0),D}\left(u\right) = \int_0^\infty f\left((x,0) + t\left[(u,D) - (x,0)\right]\right) dt = \int_0^\infty f\left((x,0) + t\left(u-x, D\right)\right) dt = \int_0^\infty f\left(x + t\left(u-x\right), Dt\right) dt. \tag{3.4}$$

We call it the weighted fan-beam projection, since it can be computed from the conventional fan-beam projection by applying an appropriate weight. From the definition of the weighted and conventional fan-beam projections, we can see that:

$$p_{(x,0),D}\left(u\right) = \int_0^\infty f\left((x,0) + t\left(u-x, D\right)\right) dt \tag{3.5a}$$

$$= \int_0^\infty f\left((x,0) + t\sqrt{\left(u-x\right)^2 + D^2}\frac{(u-x, D)}{\sqrt{\left(u-x\right)^2 + D^2}}\right) dt \tag{3.5b}$$

$$= \int_0^\infty f\left((x,0) + t'\vec{\gamma}_{x,u}\right) dt' \frac{1}{\sqrt{\left(u-x\right)^2 + D^2}} \tag{3.5c}$$

$$= \widehat{p}_{(x,0)}\left(\vec{\gamma}_{x,u}\right) \frac{1}{\sqrt{\left(u-x\right)^2 + D^2}}, \tag{3.5d}$$

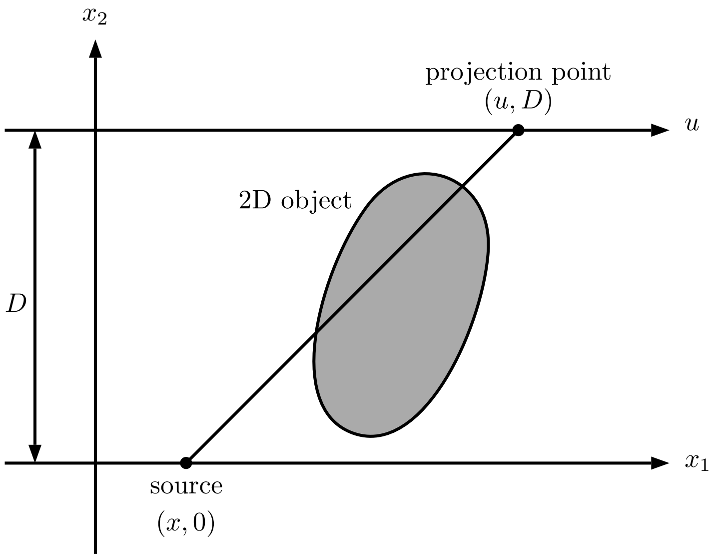

Figure 3.3: 2D model: the x-ray source is moving along the x_1-axis, and the detector line is $x_2 = D$. The detector's origin is at location $(0, D)$ and standard axis is u-axis, which has the same direction as x_1-axis.

where:

$$\vec{\gamma}_{x,u} = \frac{(u-x, D)}{\sqrt{(u-x)^2 + D^2}} \in \mathbb{S}^2. \tag{3.6}$$

Here we have changed the variables $t' = t\sqrt{(u-x)^2 + D^2}$, then $dt' = \sqrt{(u-x)^2 + D^2}\,dt$. Thus the weighted fan-beam projection relates to the conventional one by the weight $\frac{1}{\sqrt{(u-x)^2 + D^2}}$.

3.2.2 Moment of the weighted fan-beam projections and the 2D FBCC

The aim of this section is to restate the result of the FBCC, which can already be seen in the works [Clackdoyle, 2013, Clackdoyle, 2018, Lesaint, 2018]. Below is the definition of the moment of the weighted fan-beam projections:

$$M_n(x) = \int p_{(x,0),D}(u)\, u^n du. \tag{3.7}$$

From this definition (3.7) and the definition of the weighted fan-beam projection (3.4), we obtain:

$$M_n(x) = \int \left[\int_0^\infty f(x + t(u-x), Dt)\, dt\right] u^n du \tag{3.8a}$$

$$= \int \int_0^\infty f(x + t(u-x), Dt)\, u^n dt du. \tag{3.8b}$$

We continue to change the variables:

$$\begin{cases} y_1 = x + t(u-x) \\ y_2 = Dt \end{cases}. \tag{3.9}$$

Then the Jacobian matrix can be simply computed as follows:

$$J = \begin{bmatrix} \frac{\partial y_1}{\partial t} & \frac{\partial y_1}{\partial u} \\ \frac{\partial y_2}{\partial t} & \frac{\partial y_2}{\partial u} \end{bmatrix} = \begin{bmatrix} u-x & t \\ D & 0 \end{bmatrix}, \tag{3.10a}$$

$$\det J = Dt. \tag{3.10b}$$

From this, we obtain: $dy_1 dy_2 = |\det J|\, dtdu = D\,|t|\, dtdu = Dtdtdu$ (since $t > 0$). Conversely, we can also compute t and u in terms of y_1 and y_2:

$$t = \frac{y_2}{D}, \tag{3.11a}$$

$$u = x + \frac{y_1 - x}{t} = x + \frac{D\,(y_1 - x)}{y_2} = x + \frac{D\,(y_1 - x)}{y_2} = \left(1 - \frac{D}{y_2}\right) x + \frac{Dy_1}{y_2}. \tag{3.11b}$$

This leads to the computation of $dtdu$ in terms of $dy_1 dy_2$:

$$dtdu = \frac{1}{D}\frac{D}{y_2} dy_1 dy_2 = \frac{1}{y_2} dy_1 dy_2. \tag{3.12}$$

From these materials, we can rewrite the moment formula as:

$$\begin{aligned}
M_n(x) &= \int\int_0^{\infty} f\left(x + t\,(u - x), Dt\right) u^n dtdu && (3.13a)\\
&= \iint f(y_1, y_2) \left[\left(1 - \frac{D}{y_2}\right) x + \frac{Dy_1}{y_2}\right]^n \frac{1}{y_2} dy_1 dy_2 && (3.13b)\\
&= \iint f(y_1, y_2) \left[\sum_{k=0}^{n} \binom{n}{k} \left(\frac{Dy_1}{y_2}\right)^{n-k} \left(1 - \frac{D}{y_2}\right)^{k} x^k\right] \frac{1}{y_2} dy_1 dy_2 && (3.13c)\\
&= \sum_{k=0}^{n} \left[D^{n-k} \binom{n}{k} \iint f(y_1, y_2) \frac{y_1^{n-k} (y_2 - D)^k}{y_2^{n+1}} dy_1 dy_2\right] x^k && (3.13d)\\
&= \sum_{k=0}^{n} C_{k,n} x^k, && (3.13e)
\end{aligned}$$

where $C_{k,n}$ are the coefficients:

$$C_{k,n} = D^{n-k} \binom{n}{k} \iint f(y_1, y_2) \frac{y_1^{n-k} (y_2 - D)^k}{y_2^{n+1}} dy_1 dy_2. \tag{3.14}$$

These calculations are similar to those found in [Clackdoyle, 2013]. Here the double integral $\int\int_0^{\infty} dtdu$ can be changed to the double integral $\iint dy_1 dy_2$ because of the compact support of the 2D object, and because of the position of the object, which is strictly between the x_1-axis (the source line) and the u-axis (the detector line). We then obtain the FBCC, which is a simple rewording of the corresponding condition found in [Clackdoyle, 2013] (the two geometry contexts are almost the same), which can be stated as follows:

> Given a real-valued function f, which has compact support, $p_{(x,0),D}(u)$ (defined in equation (3.4)) is the weighted fan-beam projection of f on the detector line $x_2 = D$ with the source moving along the x_1-axis, then the moment of order n (defined in equation (3.7)) becomes a polynomial in x of degree n, for all non-negative integer n:
>
> $$M_n(x) = \sum_{k=0}^{n} C_{k,n} x^k, \tag{3.15}$$
>
> where:
>
> $$C_{k,n} = D^{n-k} \binom{n}{k} \iint f(y_1, y_2) \frac{y_1^{n-k} (y_2 - D)^k}{y_2^{n+1}} dy_1 dy_2. \tag{3.16}$$

3.2.3 Center-of-mass (COM) result

In this section, we show a brief application of the above moment condition (FBCC): the COM result. Although this result is not new, but we can directly and quickly obtain it after constructing the moment condition, by using the moments of orders 0 and 1 (defined in equation (3.7)). The result can be roughly stated that: *"The COM of a weighted fan-beam projection (on a detector line) is the fan-beam projection of the COM of a weighted version of the object."*

Now, for a certain source position $(x, 0)$ on the x_1-axis, we have one weighted fan-bean projection. Let's call the position of the COM of this weighted fan-beam projection on the detector line ($x_2 = D$): (u_x, D), where:

$$u_x = \frac{\displaystyle\int p_{(x,0),D}(u)\, u du}{\displaystyle\int p_{(x,0),D}(u)\, du}. \tag{3.17}$$

By the definition of the moment of the weighted fan-beam projections (see equation (3.7)), the above numerator and denominator can be rewritten as: $u_x = M_1(x)/M_0(x)$. From the FBCC (3.15), we can see that $M_0(x)$ is a constant, and $M_1(x)$ is a first-degree polynomial in x:

$$u_x = \frac{C_{1,1}x + C_{0,1}}{C_{0,0}} = \frac{C_{1,1}}{C_{0,0}}x + \frac{C_{0,1}}{C_{0,0}}, \tag{3.18}$$

where the coefficients can be computed by equation (3.16):

$$C_{1,1} = \iint f(y_1, y_2) \frac{y_2 - D}{y_2^2} dy_1 dy_2, \tag{3.19a}$$

$$= \iint f(y_1, y_2) \left(\frac{1}{y_2} - \frac{D}{y_2^2} \right) dy_1 dy_2, \tag{3.19b}$$

$$= \iint f(y_1, y_2) \frac{1}{y_2} dy_1 dy_2 - D \iint f(y_1, y_2) \frac{1}{y_2^2} dy_1 dy_2, \tag{3.19c}$$

$$C_{0,1} = D \iint f(y_1, y_2) \frac{y_1}{y_2^2} dy_1 dy_2, \tag{3.19d}$$

$$C_{0,0} = \iint f(y_1, y_2) \frac{1}{y_2} dy_1 dy_2. \tag{3.19e}$$

Then u_x can be explicitly rewritten as:

$$u_x = \frac{\displaystyle\iint f(y_1, y_2) \frac{1}{y_2} dy_1 dy_2 - D \iint f(y_1, y_2) \frac{1}{y_2^2} dy_1 dy_2}{\displaystyle\iint f(y_1, y_2) \frac{1}{y_2} dy_1 dy_2} x + \frac{\displaystyle D \iint f(y_1, y_2) \frac{y_1}{y_2^2} dy_1 dy_2}{\displaystyle\iint f(y_1, y_2) \frac{1}{y_2} dy_1 dy_2}. \tag{3.20}$$

Now we consider f_W as the weighted version of the 2D object f, where:

$$f_W(y_1, y_2) = \frac{1}{y_2^2} f(y_1, y_2). \tag{3.21}$$

Then, the formula of u_x becomes:

$$u_x = \frac{\displaystyle\iint f_W(y_1, y_2)\, y_2 dy_1 dy_2 - D \iint f_W(y_1, y_2)\, dy_1 dy_2}{\displaystyle\iint f_W(y_1, y_2)\, y_2 dy_1 dy_2} x + \frac{\displaystyle D \iint f_W(y_1, y_2)\, y_1 dy_1 dy_2}{\displaystyle\iint f_W(y_1, y_2)\, y_2 dy_1 dy_2}. \tag{3.22}$$

We divide all the numerators and denomiators by $\iint f_W(y_1, y_2)\, dy_1 dy_2$, and set:

$$c_1 = \frac{\displaystyle\iint f_W(y_1, y_2)\, y_1 dy_1 dy_2}{\displaystyle\iint f_W(y_1, y_2)\, dy_1 dy_2} \quad \text{and} \quad c_2 = \frac{\displaystyle\iint f_W(y_1, y_2)\, y_2 dy_1 dy_2}{\displaystyle\iint f_W(y_1, y_2)\, dy_1 dy_2}, \tag{3.23}$$

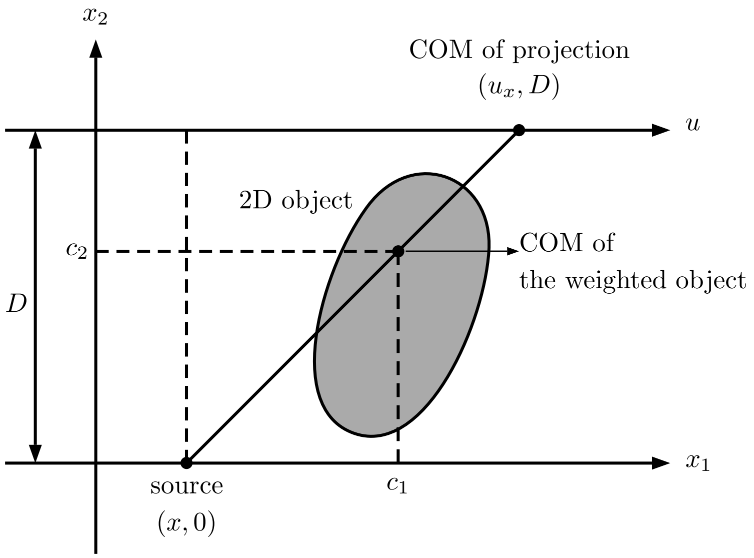

Figure 3.4: COM result: the COM of the weighted fan-beam projection is the fan-beam projection of the COM of a weighted version of the 2D object: the three points $(x, 0)$, (c_1, c_2) and (u_x, D) are collinear.

then:

$$u_x = \frac{c_2 - D}{c_2} x + D\frac{c_1}{c_2} = \left(1 - \frac{D}{c_2}\right) x + D\frac{c_1}{c_2} = x + \frac{D}{c_2}\left(c_1 - x\right). \tag{3.24}$$

And this leads to the fact that:

$$u_x - x = \frac{D}{c_2}\left(c_1 - x\right). \tag{3.25}$$

By the definition of c_1 and c_2, we know that (c_1, c_2) is the coordinate of the COM of the weighted object f_W. Moreover, the vector connecting the x-ray source $(x, 0)$ to this COM of the weighted object (c_1, c_2) is $(c_1 - x, c_2)$. And the vector connecting the x-ray source $(x, 0)$ to the COM of the weighted fan-beam projection (u_x, D) is $(u_x - x, D)$. Thus from equation (3.25), we can conclude that the three points $(x, 0)$, (c_1, c_2) and (u_x, D) are collinear, which shows that the COM of the weighted fan-beam projection (u_x, D) is the fan-beam projection of the COM (c_1, c_2) of the weighted object f_W. Figure 3.4 gives us an illustration. We can also geometrically see how equation (3.25) works through Thalès theorem or the property of the congruent triangles.

3.2.4 Numerical simulations of the FBCC

We are showing a small simulation to illustrate the result of the FBCC. In this simulation, our 2D object consists of 15 disks, which have centers and radii randomly chosen under the uniform distribution. More precisely, the centers are taken in $[-0.4, 0.4] \times [0.4, 0.6]$ and the radii are taken in the interval $[0.05, 0.19]$. The gray level are also taken randomly in the interval $[0.1, 1.1]$. The mathematical formula of the 2D object can be written as:

$$f\left(x_1, x_2\right) = \sum_{i=1}^{15} f_i\left(x_1, x_2\right), \tag{3.26}$$

where

$$f_i\left(x_1, x_2\right) = \begin{cases} gr\left(i\right), \text{ if } \left(x_1 - c_1\left(i\right)\right)^2 + \left(x_2 - c_2\left(i\right)\right)^2 \leq r^2\left(i\right) \\ \quad 0, \text{ otherwise} \end{cases}. \tag{3.27}$$

The details of $c_1(i)$, $c_2(i)$, $r(i)$ and $gr(i)$ are given in the table 3.1. Figure 3.5 gives us the image of the tested 2D object. In this test, the source is moving from $(-1, 0)$ to $(1, 0)$ on the x_1-axis. We have performed the test for $500-$equidistant source locations. Each weighted fan-beam projection is simulated on $1000-$equidistant samples of u in $[-8, 8]$. Figure 3.6 shows the weighted fan-beam projections, which were taken at several source locations:

Table 3.1: Details of the centers, radii, and gray level of 15 considering disks

Disk index	Disk centers		Disk radii	Gray level
i	$c_1(i)$	$c_2(i)$	$r(i)$	$gr(i)$
01	0.0872	0.4370	0.0885	0.1330
02	0.3968	0.4920	0.1258	0.6730
03	-0.2752	0.5502	0.1897	0.3800
04	0.1352	0.4686	0.1013	0.8330
05	-0.2960	0.4336	0.0675	0.7920
06	0.3240	0.5712	0.0565	0.3760
07	0.2840	0.4420	0.1385	0.2110
08	0.0192	0.5906	0.1712	0.8620
09	-0.3784	0.4442	0.1550	0.9910
10	0.2864	0.4820	0.1805	0.4320
11	0.0560	0.4478	0.1460	0.4530
12	0.2328	0.4308	0.0633	0.3950
13	0.3760	0.4590	0.1024	0.9430
14	-0.2104	0.5510	0.0521	0.2900
15	0.1616	0.4038	0.0821	0.9510

$x = -1,\ -0.6,\ -0.2,\ 0.2,\ 0.6,\ 1$. Based on definition (3.7), we can compute the numerical moments from these numerical weighted fan-beam projections. Figure 3.7 shows us the graphs of the moments of order 0, 1, 2, 3. In each image, we can see that the moment data approximates a suitable polynomial of the same order, where each polynomial is in x (the source location). We can compute explicitly these approximate polynomials (will be explained in chapter 4). They respectively are the following:

$$\mathcal{M}_0(x) \approx 0.8888, \tag{3.28a}$$

$$\mathcal{M}_1(x) \approx -1.0549x + 0.0388, \tag{3.28b}$$

$$\mathcal{M}_2(x) \approx 1.4071x^2 - 0.0568x + 0.3808, \tag{3.28c}$$

$$\mathcal{M}_3(x) \approx -2.0632x^3 - 0.0133x^2 - 1.5891x - 0.0395. \tag{3.28d}$$

3.3 2D fan-beam geometric calibration

In this section, we present a way to get the information of the unknown source position in the fan-beam calibration problem using FBCC. We also show a numerical experiment to test our method. Our result states that if we know three distinct source positions and their corresponding weighted fan-beam projections, then for any other weighted fan-beam projection (which is not the same as any of the three known ones), we can obtain at most two potential solutions of the source position that this projection were taken at. We do not aim to completely solve this fan-beam

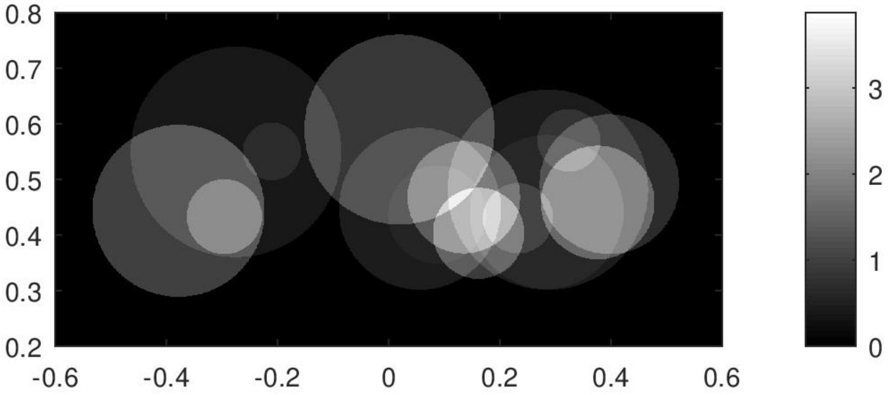

Figure 3.5: Tested 2D object is the superposition of a set of 15 random disks

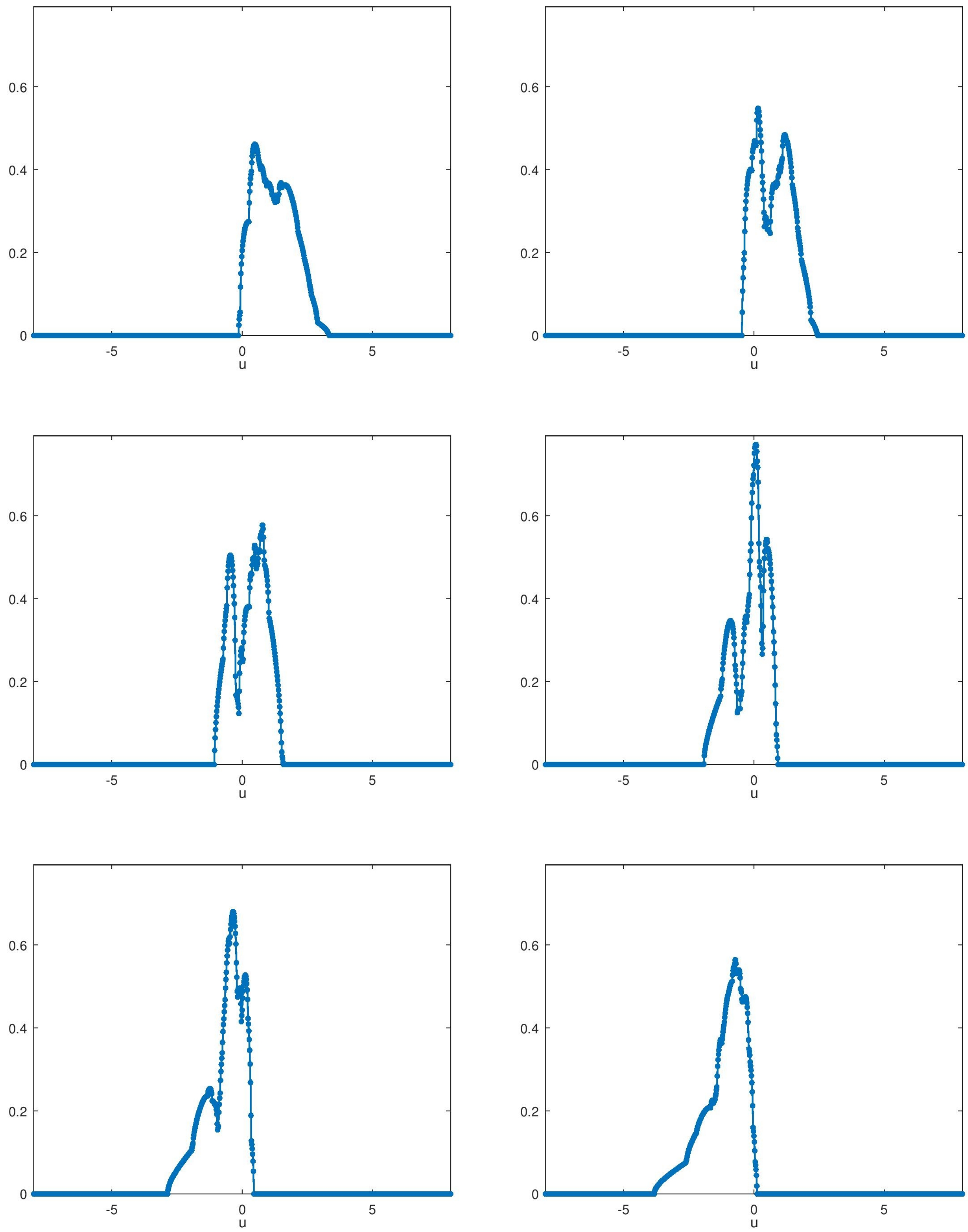

Figure 3.6: Weighted fan-beam projections taken at several source locations $(x, 0, 0)$ on the x_1-axis, where $x = -1, -0.6, -0.2, 0.2, 0.6, 1$ (respectively top-left, top-right, mid-left, mid-right, bottom-left, bottom-right)

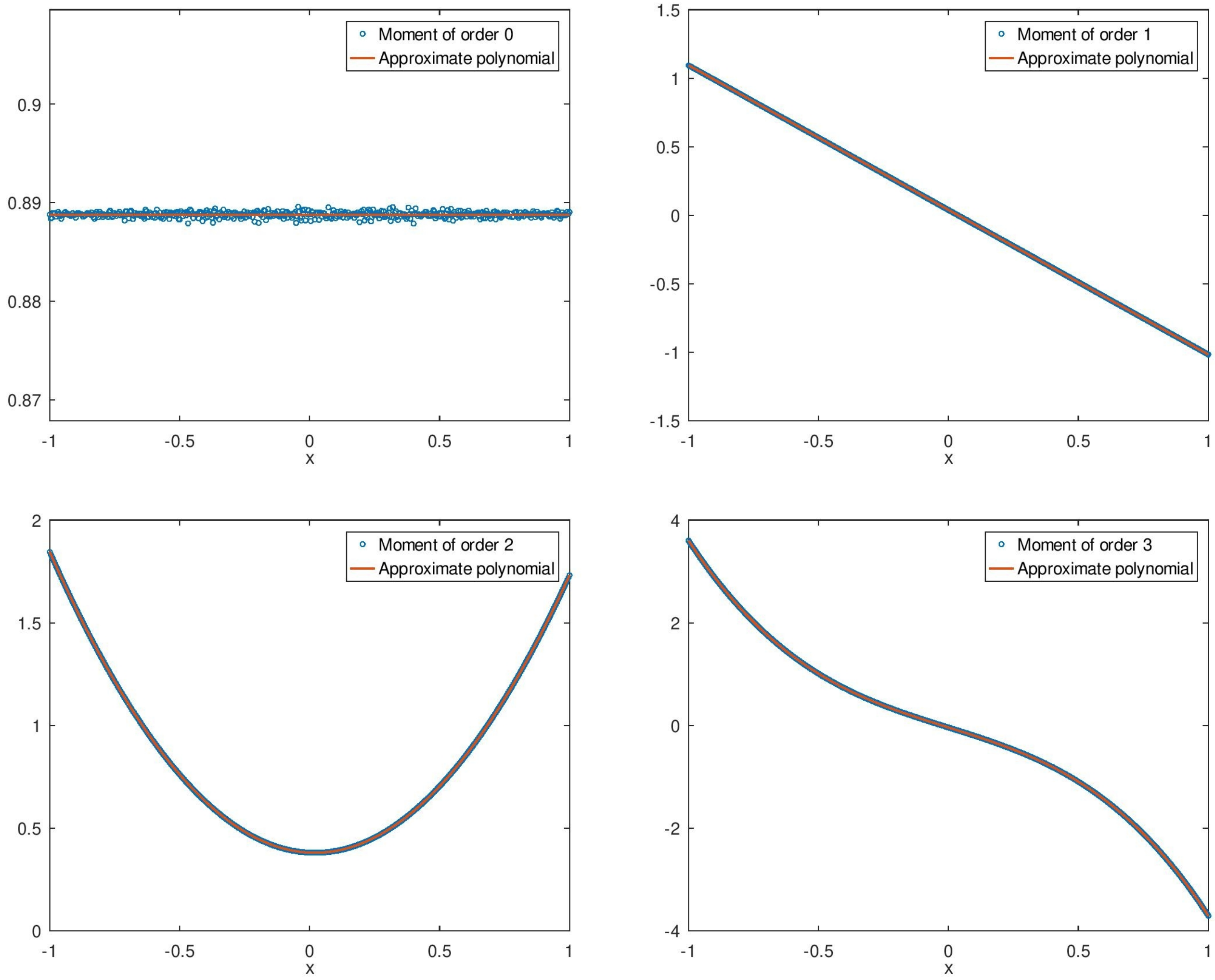

Figure 3.7: Moments of the weighted fan-beam projections of order 0 (top-left), 1 (top-right), 2 (bottom-left), 3 (bottom-right)

geometric calibration problem, but we want to use this potential information of the estimated source position to approach the 3D cone-beam calibration problem with linear sources. Mathematically, we assume x_a, x_b, x_c are the three distinct known source positions and $p_{(x_a,0),D}(u)$, $p_{(x_b,0),D}(u)$, $p_{(x_c,0),D}(u)$ are the three corresponding weighted fan-beam projections. Let's call x_d an arbitrary unknown source position, and $p_{(x_d,0),D}(u)$ is the weigted fan-beam projection computed at source location x_d. If $p_{(x_d,0),D}(u)$ is known, then we can calibrate x_d. The main tool being used is the second-order FBCC. From the theory of the FBCC (when the source moves along x_1-axis), the second-order moment will be a polynomial of second degree in the source location:

$$M_2(x) = C_0 + C_1 x + C_2 x^2. \tag{3.29}$$

We apply this equation (3.29) for $x = x_a, x_b, x_c$ and obtain:

$$\begin{cases} C_0 + C_1 x_a + C_2 x_a^2 = M_2(x_a) \\ C_0 + C_1 x_b + C_2 x_b^2 = M_2(x_b) \\ C_0 + C_1 x_c + C_2 x_c^2 = M_2(x_c) \end{cases}. \tag{3.30}$$

Since the three positions x_a, x_b, x_c are known and the three corresponding weighted fan-beam projections $p_{(x_a,0),D}(u)$, $p_{(x_b,0),D}(u)$, $p_{(x_c,0),D}(u)$ are also known, then the three corresponding moments $M_2(x_a)$, $M_2(x_b)$, $M_2(x_c)$ can be computed by the definition (3.7). Thus we can compute the three coefficients C_0, C_1, C_2 by solving the above linear system of equations. We firstly consider the matrix:

$$V = \begin{bmatrix} 1 & x_a & x_a^2 \\ 1 & x_b & x_b^2 \\ 1 & x_c & x_c^2 \end{bmatrix}. \tag{3.31}$$

Then we can simply compute the determinant of V:

$$\det V = (x_b - x_a)(x_c - x_b)(x_c - x_a). \tag{3.32}$$

From this we can see that $\det V \neq 0$ since the three known source positions x_a, x_b, x_c are two-by-two different. Thus we can compute the three coefficients C_0, C_1, C_2. Precisely, we continue considering these following matrices:

$$V_0 = \begin{bmatrix} M_2(x_a) & x_a & x_a^2 \\ M_2(x_b) & x_b & x_b^2 \\ M_2(x_c) & x_c & x_c^2 \end{bmatrix}, \quad V_1 = \begin{bmatrix} 1 & M_2(x_a) & x_a^2 \\ 1 & M_2(x_b) & x_b^2 \\ 1 & M_2(x_c) & x_c^2 \end{bmatrix}, \quad V_2 = \begin{bmatrix} 1 & x_a & M_2(x_a) \\ 1 & x_b & M_2(x_b) \\ 1 & x_c & M_2(x_c) \end{bmatrix}. \tag{3.33}$$

Then the three coefficients are computed as follows:

$$C_0 = \frac{\det V_0}{\det V}, \qquad C_1 = \frac{\det V_1}{\det V}, \qquad C_2 = \frac{\det V_2}{\det V}. \tag{3.34}$$

We can see that the key condition is the fact that the three known source positions have to be two-by-two different, in order to make $\det V \neq 0$.
Additionally, the matrix V is the transpose of a Vandermonde matrix. We can find the definition of a Vandermonde matrix in the book of L.M. Milne-Thomson, see [Milne-Thomson, 2000] on page 9. The Vandermonde matrix is defined as follows:

$$\mathfrak{V} = \begin{bmatrix} 1 & 1 & 1 & \dots & 1 \\ a_1 & a_2 & a_3 & \dots & a_N \\ a_1^2 & a_2^2 & a_3^2 & \dots & a_N^2 \\ \vdots & \vdots & \vdots & \ddots & \vdots \\ a_1^{N-1} & a_2^{N-1} & a_3^{N-1} & \dots & a_N^{N-1} \end{bmatrix}, \tag{3.35}$$

and its determinant is:

$$\det \mathfrak{V} = \prod_{1 \leq i < j \leq N} (a_j - a_i). \tag{3.36}$$

If we apply this result with $N = 3$ and the property of the determinant of a transpose matrix, we can obtain absolutely the same result as $\det V$.

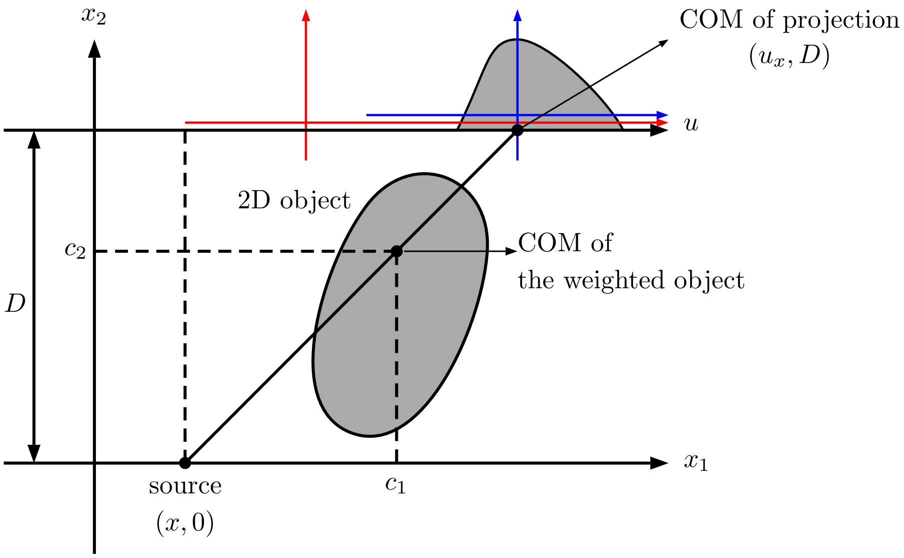

Figure 3.8: Illustration of the raw measurement, the corrected measurent and the corresponding projection in terms of u coordinate system

Coming back to our calibration problem, after computing the three coefficients C_0, C_1, C_2, we continue to apply the second-order FBCC for $x = x_d$:

$$M_2\left(x_d\right) = C_0 + C_1 x_d + C_2 x_d^2. \tag{3.37}$$

Now the weighted fan-beam projection $p_{(x_d,0),D}\left(u\right)$ is known, then $M_2\left(x_d\right)$ is also known. Thus computing x_d is in fact solving the following second-order equation:

$$C_2 x_d^2 + C_1 x_d + \left(C_0 - M_2\left(x_d\right)\right) = 0. \tag{3.38}$$

In general, we obtain two possible solutions of x_d:

$$x_d = \frac{-C_1 \pm \sqrt{C_1^2 - 4C_2\left(C_0 - M_2\left(x_d\right)\right)}}{2C_2}. \tag{3.39}$$

Comments

The method provided above assumes that the projections we have are of the form $p_{(x,0),D}\left(u\right)$ ($p_{(x_a,0),D}\left(u\right)$ for instance). These are one-variable functions in terms of u coordinate system. However in reality, instead of having these projections, we may have the one-variable functions, which are in terms of some unknown coordinate systems, that we do not know how they relate to the u coordinate system. We can see in figure 3.8, for an arbitrary projection on the detector line, the one-variable function we have may be in terms of the red coordinate system, which is unknown in the sense that we do not know how it relates to the u-axis. We call this one-variable function the raw measurement. The only difference between the raw measurement and the corresponding projection is the considering coordinate system. Now we assume that we only have the raw measurements instead of the projections in terms of u coordinate system, we still can construct the second-order FBCC using the COM result. For each raw measurement, the first step is to find its own COM, and then correct the raw measurement by translating it horizontally, such that its COM now locates at the origin. We obtain a function called the corrected measurement. And again, the graph of the raw measurement, the corrected measurement, and the corresponding projection are the same; the only difference between them is the coordinate system being considered. For illustration, the corrected measurement is the one-variable function in terms of the blue coordinate system in figure 3.8. We denote the corrected measurement as $m_{(x,0),D}\left(u\right)$, and we can simply see the relationship between the corrected measurement and the corresponding projection is the following:

$$m_{(x,0),D}\left(u\right) = p_{(x,0),D}\left(u + u_x\right), \tag{3.40}$$

where u_x is the position of the COM of the projection on the u-axis. From this, the second-order moment of the corrected measurements can be computed as:

$$\mathfrak{M}_2(x) = \int m_{(x,0),D}(u)\, u^2 du = \int p_{(x,0),D}(u + u_x)\, u^2 du. \tag{3.41}$$

Then by changing the variables: $u' = u + u_x$, we know that $du' = du$ and the above integral becomes:

$$\begin{aligned}
\mathfrak{M}_2(x) &= \int p_{(x,0),D}(u')\,(u' - u_x)^2\, du' && \text{(3.42a)}\\
&= \int p_{(x,0),D}(u')\left(u'^2 - 2u_x u' + u_x^2\right) du' && \text{(3.42b)}\\
&= \int p_{(x,0),D}(u')\, u'^2 du' - 2u_x \int p_{(x,0),D}(u')\, u' du' + u_x^2 \int p_{(x,0),D}(u')\, du' && \text{(3.42c)}\\
&= M_2(x) - 2u_x M_1(x) + u_x^2 M_0(x), && \text{(3.42d)}
\end{aligned}$$

where $M_0(x)$, $M_1(x)$, $M_2(x)$ respectively are the moments of the projections $p_{(x,0),D}(u)$ of order 0, 1, 2, see definition (3.7). By the FBCC (3.15), we know that $M_0(x)$, $M_1(x)$, $M_2(x)$ are the polynomial in x of degree 0, 1, 2, respectively. And by the COM result (3.25), we know that $u_x = x + (D/c_2)(c_1 - x)$ (where (c_1, c_2) is the coordinate of the COM of the weighted object), which also means u_x is a first-degree polynoial in x. Thus, $\mathfrak{M}_2(x)$ becomes a second-degree polynomial in x. This can be considered as a FBCC for the corrected measurements.
And from this fact, following the same spirit as the above method of calibration, we are still able to solve the 2D fan-beam calibration problem using the second-order FBCC for the corrected measurements, although we are given the raw measurements instead of the projections.

Numerical experiment in 2D

We continue the above small simulation in order to illustrate the above method. The 2D object remains the same as in the experiment in section 3.2.4. Now we assume the three known source positions are:

$$x_a = -0.182, \qquad x_b = -0.736, \qquad x_c = -0.066, \tag{3.43}$$

and the unknown source position we aim to calibrate is $x_d = -0.958$.
We have developed two separate programs, called *simulator* and *solver*. *Simulator* received all four source locations and simulated four respective weighted fan-beam projections. All the projections were simulated on $1000-$equidistant samples on the detector line. After that, *solver* received the simulated weighted fan-beam projections and only three known source positions x_a, x_b, x_c. Then from the information of four weighted fan-beam projections, *solver* computed the respective moments $M_2(x_a)$, $M_2(x_b)$, $M_2(x_c)$, $M_2(x_d)$. From the information of x_a, x_b, x_c, $M_2(x_a)$, $M_2(x_b)$, $M_2(x_c)$, it computed the three coefficients C_0, C_1, C_2 characterizing the second-degree polynomial of the FBCC. Finally, from the information of $M_2(x_d)$ and the three coefficients C_0, C_1, C_2, it computed and gave us the possible estimated solutions of x_d.
After performing this algorithm, we obtain the two estimated solutions as the following:

$$x_d^{\text{est1}} = 0.998015, \quad \text{and} \quad x_d^{\text{est2}} = -0.958009. \tag{3.44}$$

We can see that the $x_d^{\text{est2}} = -0.958009$ approximating the true solution $x_d = -0.958$ that we want to obtain.

3.4 Cone-beam projections

In this section, we are working in the 3D space with the standard coordinate system (x_1, x_2, x_3). The 3D object being considered is a 3D real-valued function F with compact support. Then, for an arbitrary 3D unit vector $\vec{\Gamma}$, the conventional cone-beam projection of F computed at source location $\vec{X} = (x_1, x_2, x_3)$ and along the direction $\vec{\Gamma}$, is defined as follows:

$$\widehat{P}_{\vec{X}}\left(\vec{\Gamma}\right) = \int_0^\infty F\left(\vec{X} + t'\vec{\Gamma}\right) dt', \quad \forall \vec{\Gamma} \in \mathbb{S}^2. \tag{3.45}$$

Similar to section 3.2, we use the notation $\vec{X}$ (capital X with the arrow above) to mention the 3D vector $\vec{X} = (x_1, x_2, x_3)$; and x only to imply a real number. In this situation, we assume the source to move along the x_1-axis,

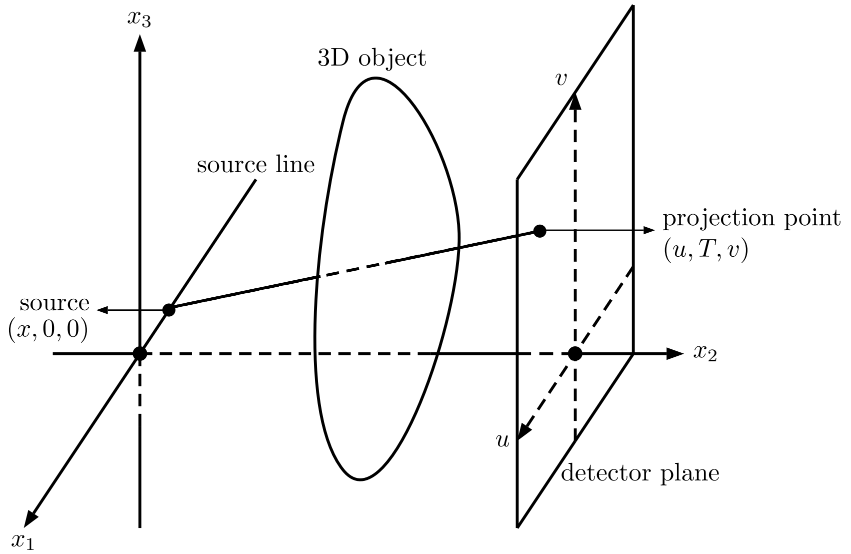

Figure 3.9: 3d model: the x-ray source is moving along the x_1-axis, the detector plane is $x_2 = T$. The detector's origin is at location $(0, T, 0)$; and two stardard axes: u and v-axes, have the same directions as x_1 and x_3-axes.

so we use the notation $(x, 0, 0)$ to show the source location.
More precisely, we are now considering the model as shown in figure 3.9. The source is moving along x_1-axis, the detector is perpendicular to x_2-axis, and at distance $T > 0$ away from the world origin $(0, 0, 0)$. The detector plane's equation is: $x_2 = T$. The detector has its own origin and coordinate system (u, v). Its origin is at location $(0, T, 0)$ in 3D space; the u and v-axes respectively have the same directions as the x_1 and x_3-axes. The 3D object F is in between the x_1-axis (the source line) and the plane $x_2 = T$ (the detector plane). Then the weighted cone-beam projection of F on the detector plane with the source moving along x_1-axis is defined as follows:

$$P_{(x,0,0),T}\left(u,v\right) = \int_0^\infty F\left((x,0,0) + t\left[(u,T,v) - (x,0,0)\right]\right) dt \tag{3.46a}$$

$$= \int_0^\infty F\left(x + t\left(u - x\right), tT, tv\right) dt. \tag{3.46b}$$

Again, by the technique of changing variables, we can find the relationship between the weighted and conventional cone-beam projections:

$$P_{(x,0,0),T}\left(u,v\right) = \int_0^\infty F\left((x,0,0) + t\left(u - x, T, v\right)\right) dt \tag{3.47a}$$

$$= \int_0^\infty F\left((x,0,0) + t\sqrt{\left(u-x\right)^2 + v^2 + T^2}\,\frac{(u-x,T,v)}{\sqrt{\left(u-x\right)^2 + v^2 + T^2}}\right) dt \tag{3.47b}$$

$$= \int_0^\infty F\left((x,0,0) + t'\vec{\Gamma}_{x,u,v}\right) dt' \frac{1}{\sqrt{\left(u-x\right)^2 + v^2 + T^2}} \tag{3.47c}$$

$$= \widehat{P}_{(x,0,0)}\left(\vec{\Gamma}_{x,u,v}\right) \frac{1}{\sqrt{\left(u-x\right)^2 + v^2 + T^2}}, \tag{3.47d}$$

where:

$$\vec{\Gamma}_{x,u,v} = \frac{(u-x,T,v)}{\sqrt{\left(u-x\right)^2 + v^2 + T^2}}. \tag{3.48}$$

Here we set $t' = t\sqrt{\left(u-x\right)^2 + v^2 + T^2}$, which implies $dt' = \sqrt{\left(u-x\right)^2 + v^2 + T^2}dt$. So the above weighted cone-beam projection can be obtained from the conventional one by applying the weight: $\frac{1}{\sqrt{\left(u-x\right)^2 + v^2 + T^2}}$.

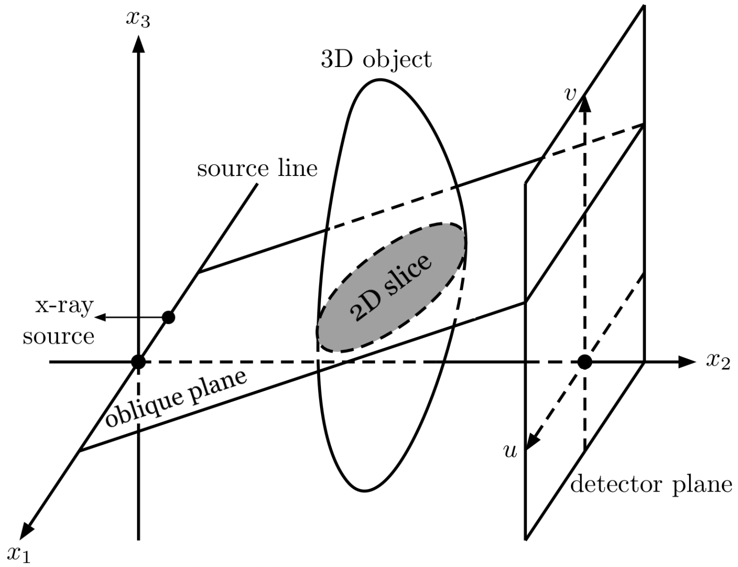

Figure 3.10: Construction of the oblique plane

3.5 3D cone-beam geometric calibration with linear sources

We state the 3D cone-beam geometric calibration problem and show a method to solve it in section 3.5.1, and we give some numerical experiments in section 3.5.2.

3.5.1 Method of calibration

Our aim in this section is to make use of the FBCC to solve the 3D cone-beam geometric calibration problem. This problem is the 3D version of the problem we have seen in section 3.3. We are given three two-by-two distinct source locations on the x_1-axis and their respective weighted cone-beam projections on the detector. Now for an arbitrary weighted cone-beam projection, which is not the same as any of the three above, we can calibrate the source location on the x_1-axis that this projection was taken at. Firstly, on the detector, we consider a line which is parallel to the x_1-axis. So on the detector, this line's equation is: $v = v_0$. And in the 3D space, it can be rewritten as the following:

$$\begin{cases} x_1 \in \mathbb{R} \\ x_2 = T \\ x_3 = v_0 \end{cases} . \tag{3.49}$$

Since this line on the detector is parallel to the x_1-axis, then there is a plane generated from it and the x_1-axis, and we call this plane the oblique plane. We have the illustration in figure 3.10. By simple calculation, we can find the equation of this oblique plane. It contains at least two vectors: $(1, 0, 0)$ and $(0, T, v_0)$, so it must be perpendicular to the vector:

$$(1, 0, 0) \times (0, T, v_0) = (0, -v_0, T). \tag{3.50}$$

Additionally, this oblique plane goes through the world origin $(0, 0, 0)$, so its equation in the 3D space is:

$$0\,(x_1 - 0) - v_0\,(x_2 - 0) + T\,(x_3 - 0) = 0 \iff -v_0 x_2 + T x_3 = 0 \iff x_3 = \frac{v_0}{T} x_2. \tag{3.51}$$

According to this equation, one arbitrary point in the 3D space (x_1, x_2, x_3) needs to satisfy $x_3 = \dfrac{v_0}{T} x_2$ to be on the oblique plane. In other words, each point on the oblique plane will have the representation $\left(x_1, x_2, \dfrac{v_0}{T} x_2\right)$ in the 3D space. The oblique plane also has its own origin and coordinate system. For simplicity, we choose its origin to be at the world origin $(0, 0, 0)$. And its two standard axes include the x_1-axis, and the other axis having the same direction as the vector $(0, T, v_0)$. Thus one such point $\left(x_1, x_2, \dfrac{v_0}{T} x_2\right)$ in the 3D space will have another

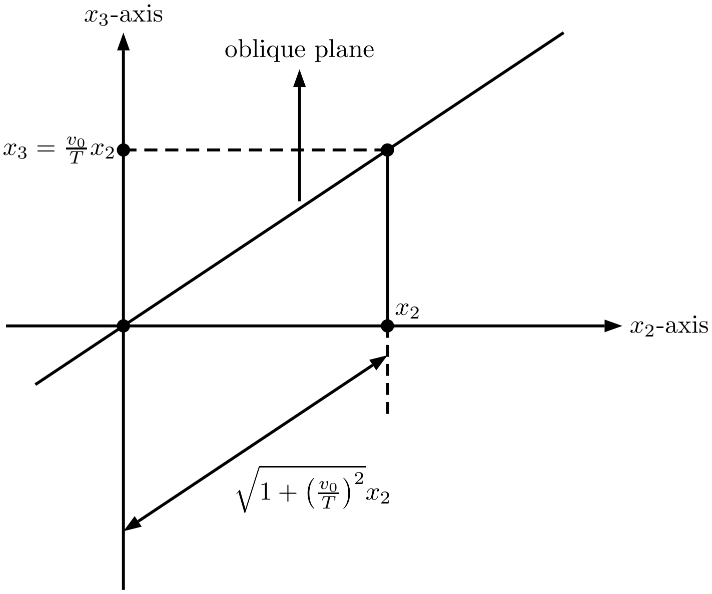

Figure 3.11: Front view of the 3D model: the oblique plane becomes a line, and its two standard axes include: x_1-axis (now becomes a point pinned at the world origin $(0,0,0)$) and the other axis having the same direction as the line that the oblique plane becomes. So the coordinate $\left(x_2, \dfrac{v_0}{T}x_2\right)$ will define a diagonal segment (on the line of the oblique plane) of the length $\sqrt{x_2^2+\left(\dfrac{v_0}{T}x_2\right)^2} = \sqrt{1+\left(\dfrac{v_0}{T}\right)^2}x_2$. Thus the point $\left(x_1, x_2, \dfrac{v_0}{T}x_2\right)$ in the 3D space will have the representation $\left(x_1, \sqrt{1+\left(\dfrac{v_0}{T}\right)^2}x_2\right)$ on the oblique plane.

representation on the oblique plane. By a simple calculation, we can see that the point $\left(x_1, x_2, \dfrac{v_0}{T}x_2\right)$ in the 3D space will have the representation $\left(x_1, \sqrt{1+\left(\dfrac{v_0}{T}\right)^2}x_2\right)$ on the oblique plane. Figure 3.11 will give us a better understanding.

The oblique plane slices through the 3D object, and then creates a slice of the object on the plane, which is a 2D real-valued function with compact support. We call this 2D function f. The relationship between the 3D object F and its 2D slice f on the oblique plane is the following:

$$F\left(x_1, x_2, \frac{v_0}{T}x_2\right) = f\left(x_1, \sqrt{1+\left(\frac{v_0}{T}\right)^2}x_2\right). \tag{3.52}$$

This relationship comes from the fact that for the same point on the oblique plane, there are two different representations: $\left(x_1, x_2, \dfrac{v_0}{T}x_2\right)$ in the 3D space and $\left(x_1, \sqrt{1+\left(\dfrac{v_0}{T}\right)^2}x_2\right)$ in the coordinate system of the oblique plane. From this relationship (3.52) and the definitions (3.4) and (3.46b) of the weighted fan-beam and cone-beam projections (with the source moving along the x_1-axis), we can see that:

$$P_{(x,0,0),T}\left(u, v_0\right) = \int_0^\infty F\left(x+t\left(u-x\right), tT, tv_0\right)dt = \int_0^\infty F\left(x+t\left(u-x\right), tT, \left(\frac{v_0}{T}\right)tT\right)dt \tag{3.53a}$$

$$= \int_0^\infty f\left(x+t\left(u-x\right), \sqrt{1+\left(\frac{v_0}{T}\right)^2}tT\right)dt = \int_0^\infty f\left(x+t\left(u-x\right), \sqrt{T^2+v_0^2}t\right)dt \tag{3.53b}$$

$$= \int_0^\infty f\left(x+t\left(u-x\right), Dt\right)dt\Big|_{D=\sqrt{T^2+v_0^2}} = p_{(x,0),\sqrt{T^2+v_0^2}}\left(u\right). \tag{3.53c}$$

This means: if we collect the weighted cone-beam projections of the 3D object F on the line $v = v_0$ on the detector plane, we obtain the same as the weighted fan-beam projections of the 2D slice f (on the oblique plane $x_3 = \dfrac{v_0}{T}x_2$)

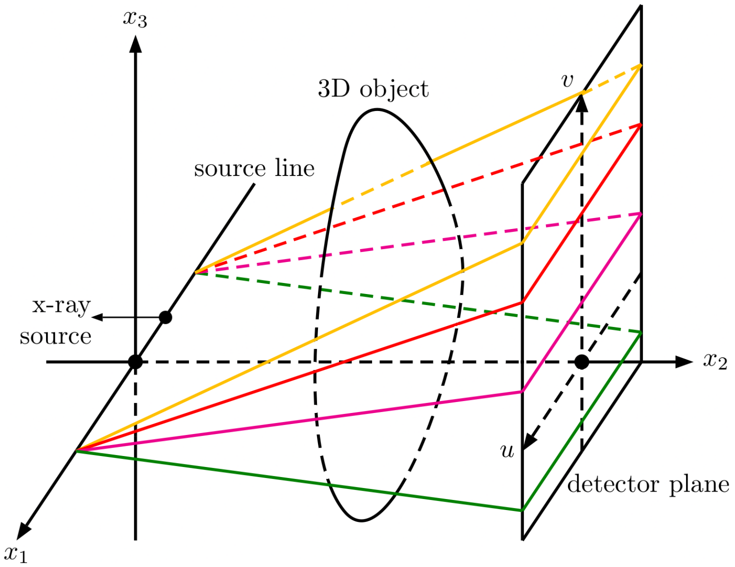

Figure 3.12: The 3D cone-beam calibration problem is broken down into many 2D fan-beam calibration problems. Solving each of these 2D fan-beam calibration problems (following the method in section 3.3) and choosing the common solution among all potential pairs of solutions leads to the result of the estimated solution to the unknown source position.

on the corresponding detector line. And the fan-beam calibration problem on this oblique plane is exactly the same as the 2D fan-beam calibration problem shown in section 3.3. Thus, instead of solving a 3D cone-beam calibration problem, we break it down into a series of many 2D fan-beam calibration problems (each on one different oblique plane), and solve all of them, once at a time, using the method presented in section 3.3. Figure 3.12 shows us this idea. More precisely, we consider many lines of the form $v = v_0$ on the detector plane (v_0 varies), and obtain many oblique planes, which go through the 3D object and create many corresponding 2D slices of the object. By section 3.3, for each 2D fan-beam calibration problem on each oblique plane, in which we are given three known distinct source positions and are asked to find the unknown source position (and these four values remain the same for all oblique planes), we will obtain at most two potential solutions to the unknown source position. So, if we have K oblique planes, then there will be at most K pairs of potential solutions. However, since the true value of the unknown source position must uniquely exist, then these K pairs of solutions must have one solution in common, which is the true solution. So in order to determine this estimated solution among those all potential solutions, after solving every considered 2D fan-beam calibration problem, we plot all the potential solutions in a figure. In this figure, we take the horizontal axis to stand for v_0 values, which is the only varied parameter to generate the oblique plane, and the vertical axis to stand for the potential solution values. In general, for each value of v_0 or for each oblique plane, we have a corresponding pair of potential solutions. After plotting all the pair of potential solutions, there must appear a horizontal line created by the collinear points, since all the pairs of solutions have one value in common. And the crucial value of those collinear solutions give us the estimated solution of the unknown source location. The important requirement we need is that the 3D object must be general and varies along the vertical direction, because the oblique plane is parameterized only by the value of v_0 on the v-axis (the vertical axis on the detector plane, see figure 3.12), so if the 3D object does not satisfy the above requirement, then we cannot have new information on the 2D slices, when jumping from this oblique plane to another one. We may continue to end up with two potential solutions, without any clues to decide which solution can approximate the true solution, as what we have obtained in the end of section 3.3.

Comment

Following the idea in the comments in section 3.3, we allow the flat detector to have an unknown horizontal shift (an unknown shift along horizontal direction) at every source position. Because this makes the 2D fan-beam projections of the 2D slices on the oblique planes become raw measurements (in the sense that has been mentiond in the comments in section 3.3), which can be handled by a correction step, a second-order moment computation, and by the FBCC for the corrected measurements. Thus with a similar method, we still can solve the 3D cone-beam calibration problem, as long as the unknown horizontal shifts of the detector do not cause any truncation in the

Table 3.2: Details of the centers, radii, and gray level of 15 considering balls

Ball index	Ball centers			Ball radii	Gray level
i	$C_1(i)$	$C_2(i)$	$C_3(i)$	$R(i)$	$Gr(i)$
01	0.1648	0.7212	0.1160	0.0912	0.8610
02	0.1672	0.5176	0.0604	0.0281	0.8650
03	-0.0924	0.7556	-0.0216	0.0757	0.9970
04	0.1416	0.7596	0.1288	0.1059	0.4800
05	0.0848	0.5724	0.0012	0.0402	0.5610
06	-0.0932	0.4732	-0.1088	0.0178	0.1850
07	-0.0536	0.4396	0.1480	0.0231	0.4680
08	-0.0044	0.6768	0.1240	0.0872	0.9520
09	0.1032	0.5912	-0.1664	0.0744	0.7110
10	0.1804	0.4744	-0.0336	0.1430	0.2830
11	0.0288	0.5368	-0.0472	0.0774	0.9890
12	0.1760	0.4332	0.1440	0.1189	1.0600
13	-0.0336	0.6480	0.0016	0.0199	0.6970
14	-0.1420	0.4752	-0.0564	0.0632	0.3400
15	-0.0660	0.7924	-0.0392	0.0936	0.8450

projections on the detector.

3.5.2 Numerical experiments in 3D

We have performed two different experiments to illustrate our method. In the first experiment, we tested our method with a 3D object, which is chosen randomly. The main aim of this experiment is to show the phenomenon that a horizontal line of collinear points will appear in the figure of all potential estimated solutions, as described in the previous section. We also give an algorithm to quickly compute the final estimated solution of the unknown source location from the potential ones. The second experiment takes into account 100 randomly chosen objects, which means the second experiment repeats the procedure of the first experiment for 100 times, each time with one new random 3D object. Our aim is to check how good the final estimated solution is, when we repeat the same experiment for 100 times.

3.5.2.1 Experiment 1

In this experiment, the 3D object being considered is the superposition of a set of 15 balls, where the centers are randomly taken in $[-0.2, 0.2] \times [0.4, 0.8] \times [-0.2, 0.2]$ and the radii are randomly taken in the interval $[0.01, 0.15]$, under the uniform distribution. Even the gray level of each ball are also randomly taken in $[0.1, 1.1]$. Mathematically, the 3D object formula can be written as the following:

$$F(x_1, x_2, x_3) = \sum_{i=1}^{15} F_i(x_1, x_2, x_3), \tag{3.54}$$

where

$$F_i(x_1, x_2, x_3) = \begin{cases} Gr(i), & \text{if } (x_1 - C_1(i))^2 + (x_2 - C_2(i))^2 + (x_3 - C_3(i))^2 \leq R^2(i) \\ 0, & \text{otherwise} \end{cases}. \tag{3.55}$$

The details of $C_1(i)$, $C_2(i)$, $C_3(i)$, $R(i)$ and $Gr(i)$ can be found in table 3.2. We perform our method by take v_0 varied from -0.3 to 0.3. More precisely, v_0 is treated as a 600-equidistant sample of $[-0.3, 0.3]$. In other words, we consider 600 oblique planes, since each value of v_0 is in charge of one oblique plane. Figure 3.13 shows several slices on the corresponding oblique planes. In this experiment, we consider the three known source position on the x_1-axis to be:

$$x_a = 0.192, \qquad x_b = -0.014, \qquad x_c = -0.628, \tag{3.56}$$

and the unknown source position to be calibrated is $x_d = 0.281$. We re-use the method presented in section 3.3 to solve each 2D calibration problem on each oblique plane. As explained in the previous section 3.5, we obtain, in

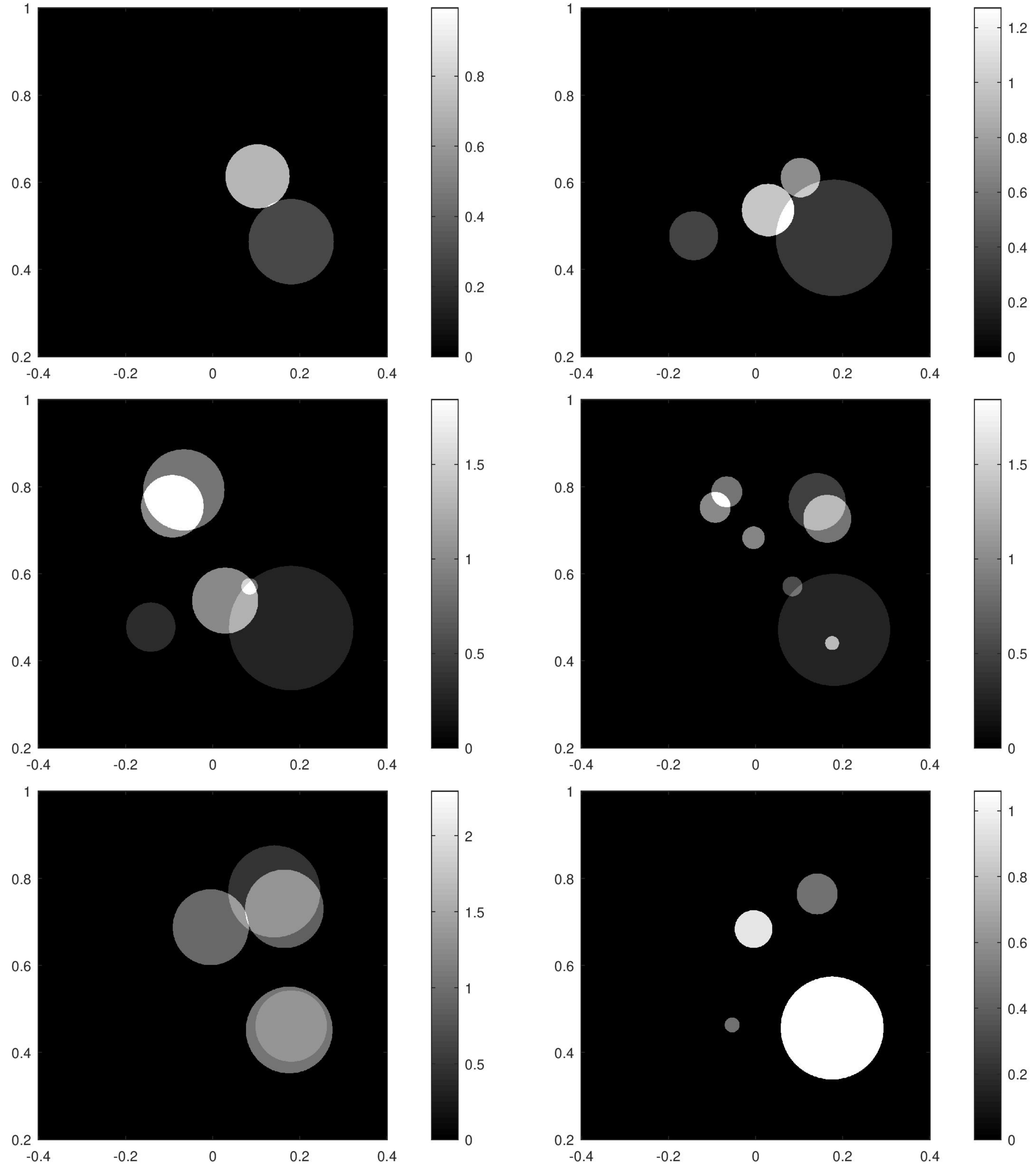

Figure 3.13: The 2D slices of the 3D object on several oblique planes: $x_3 = -0.3x_2$ (top-left), $x_3 = -0.18x_2$ (top-right), $x_3 = -0.06x_2$ (mid-left), $x_3 = 0.06x_2$ (mid-right), $x_3 = 0.18x_2$ (bottom-left), $x_3 = 0.3x_2$ (bottom-right).

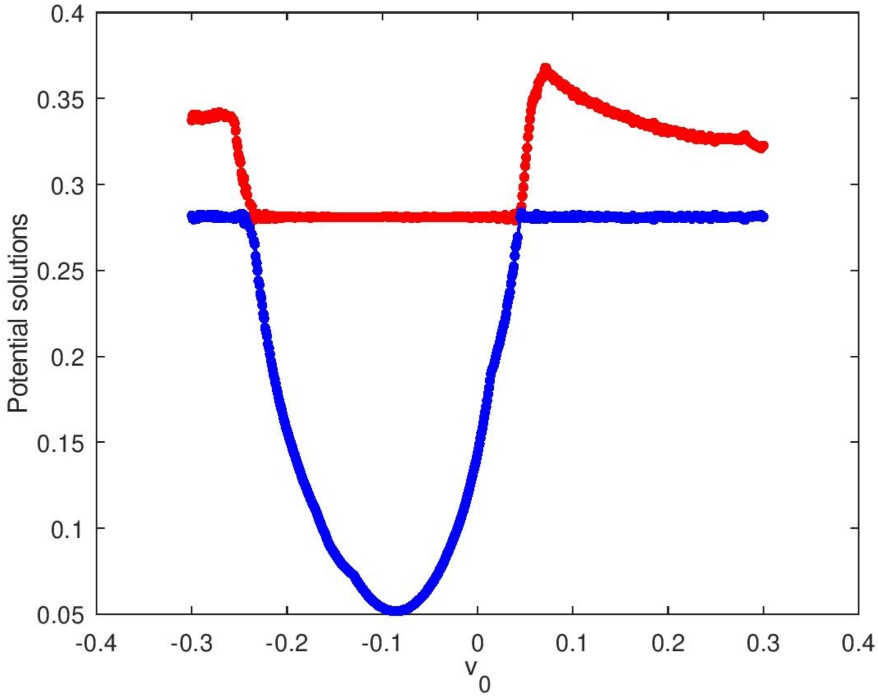

Figure 3.14: Image of all potential solutions: the horizontal axis is for v_0 values, each v_0 value parameterizes one oblique plane, and corresponds (at most) to a pair of potential solutions: bigger solution (red dot) and smaller solution (blue dot)

general, two potential solutions for each oblique plane (each v_0 value). After plotting all of the potential solutions on a same figure, we obtain the result as in figure 3.14. In this figure, we can obviously see the horizontal line of collinear points, which we expect. And the values of these collinear solutions give us the estimated value of the unknown source location x_d. Although we still can visually "see" that the collinear solutions approximating the true solution $x_d = 0.281$. However, we will give an algorithm to analytically find this crucial value from the collinear potential solutions.

Algorithm: finding final estimated solution algorithm from the potential solutions

1. From the set of all potential solutions, we find the highest potential solution $x_d^{\max}$ (highest red value in figure 3.14), and the value v_1 that corresponds to $x_d^{\max}$.

2. We ignore the value v_1 and find the lowest potential solution $x_d^{\min}$ among the other v_0 values. Then we also find the value v_2 that corresponds to $x_d^{\min}$

3. In general, for $v_0 = v_1$, we have two potential solutions: $x_d^{\max}$ and $x_d^{v_1}$. And for $v_0 = v_2$, we have two potential solutions: $x_d^{\min}$ and $x_d^{v_2}$. By theory, among these two pairs of solutions: $(x_d^{\max}, x_d^{v_1})$ and $\left(x_d^{\min}, x_d^{v_2}\right)$, there must be two solutions, one in each pair, that approximates each other. However, by the construction, we can see that $x_d^{\max}$ and $x_d^{\min}$ will be significantly different from each other, so we will only compute these following differences:

$$H_1 = \left|x_d^{v_1} - x_d^{\min}\right|, \qquad H_2 = \left|x_d^{v_2} - x_d^{\max}\right|, \qquad H_3 = \left|x_d^{v_1} - x_d^{v_2}\right|. \tag{3.57}$$

   Then we find the smallest value of $H = \min\{H_1, H_2, H_3\}$. This value of H will show us which the two solutions, that approximating each other, are.

   - If $H = H_1$, then $var = \frac{1}{2}\left(x_d^{v_1} + x_d^{\min}\right)$.
   - If $H = H_2$, then $var = \frac{1}{2}\left(x_d^{v_2} + x_d^{\max}\right)$.
   - If $H = H_3$, then $var = \frac{1}{2}\left(x_d^{v_1} + x_d^{v_2}\right)$.

   We use this *var* as a temporary variable to store the value, that we expect to approximate the true solution of the unknown source location.

4. We run a *for* loop over v_0. For each value of v_0, we have (in general) two potential solutions, then we find and choose the potential solution among them that approximates the *var* value better. After finishing that *for* loop, we obtain an array (which has the same length as the sample v_0) containing all the potential solutions that approximate the *var* value. Then we compute the mean value of this array to obtain the final estimated solution to the unknown source location.

Back to our experiment, after performing the above algorithm, we obtain the final estimated solution $x_d^{\text{est}} = 0.281030$ approximating the true solution $x_d = 0.281$.

3.5.2.2 Experiment 2

In this experiment, the three known source positions $x_a = 0.192$, $x_b = -0.014$, $x_c = -0.628$ and the unknown source position $x_d = 0.281$ that we would like to calibrate, remain the same as experiment 1. We repeat the same procedure of experiment 1 for 100 times, each time with a different object, following the same rule: each object is a superposition of a set of 15 random balls. We perform absolutely the same method and algorithm as explained in the previous sections, and we obtain the final estimated solution for each time, which are shown in details in table 3.3 The mean value of 100 final estimated solutions to the true solution $x_d = 0.281$ in 100 tests is $x_d^{avg} = 0.281122$. We also store the 100 final estimated solutions in an array, and subtract this array by the true solution x_d to obtain the so-called *Err*-array (which stores the error values). The max value of *Err* is:

$$\|Err\|_{l^\infty} = \max_{i=1,2,\ldots,100} |Err\,(i)| = 0.008222, \tag{3.58}$$

and the mean value of *Err* is:

$$\frac{1}{100}\|Err\|_{l^1} = \frac{1}{100}\sum_{i=1}^{100} |Err\,(i)| = 0.000133. \tag{3.59}$$

Table 3.3: Final estimated solutions to the unknown source location in 100 tests

Test index	Solutions	Test index	Solutions	Test index	Solutions	Test index	Solutions	Test index	Solutions
001	0.28098	021	0.28101	041	0.28101	061	0.28100	081	0.28100
002	0.28103	022	0.28095	042	0.28100	062	0.28100	082	0.28101
003	0.28099	023	0.28100	043	0.28102	063	0.28099	083	0.28099
004	0.28100	024	0.28101	044	0.28100	064	0.28100	084	0.28100
005	0.28098	025	0.28111	045	0.28100	065	0.28100	085	0.28259
006	0.28315	026	0.28100	046	0.28101	066	0.28103	086	0.28098
007	0.28098	027	0.28100	047	0.28100	067	0.28102	087	0.28096
008	0.28099	028	0.28114	048	0.28099	068	0.28100	088	0.28103
009	0.28100	029	0.28098	049	0.28101	069	0.28101	089	0.28101
010	0.28104	030	0.28100	050	0.28100	070	0.28099	090	0.28100
011	0.28101	031	0.28100	051	0.28099	071	0.28105	091	0.28099
012	0.28101	032	0.28922	052	0.28104	072	0.28097	092	0.28100
013	0.28100	033	0.28099	053	0.28100	073	0.28100	093	0.28101
014	0.28102	034	0.28099	054	0.28101	074	0.28100	094	0.28100
015	0.28099	035	0.28100	055	0.28102	075	0.28106	095	0.28098
016	0.28099	036	0.28095	056	0.28100	076	0.28100	096	0.28099
017	0.28100	037	0.28100	057	0.28100	077	0.28100	097	0.28098
018	0.28099	038	0.28101	058	0.28100	078	0.28094	098	0.28100
019	0.28100	039	0.28100	059	0.28101	079	0.28104	099	0.28102
020	0.28101	040	0.28099	060	0.28101	080	0.28099	100	0.28099

Chapter 4

Cone-beam Consistency Conditions

French summary of the content

Les conditions de cohérence des données (DCC) peuvent être des équations qui représentent les relations de dépendance entre les projections ou, plus généralement, des propriétés ou des règles que les données des projections doivent respecter pour être considérées comme vraies. Ce chapitre couvre le sujet des conditions de cohérence du faisceau conique (CBCC). Nous pouvons constater dans la littérature que, jusqu'à présent, il existe trois approches principales pour créer les CBCC : partir de l'équation de John, considérer les projections par paires ou créer les CBCC de type polynomial (comme les conditions bien connues de Helgason-Ludwig).

Nous pouvons trouver la première approche dans le travail de Patch, voir [Patch, 2002b] et [Patch, 2002a]. Elle a dérivé quelques conditions de cohérence des données en géométrie Cone Beam (Cone Beam Consistency Conditions (CBCC)) de l'équation de John pour deux contextes géométriques différents. Dans l'article [Patch, 2002b], la source de rayons X se déplace le long d'un cercle et le détecteur est parallèle au plan de la trajectoire, tandis que dans [Patch, 2002a], la source de rayons X et le détecteur sont considérés comme se déplaçant de manière correspondante sur deux trajectoires hélicoïdales, l'objet 3D étant fixe. C'est en fait le modèle du scanner car ce mouvement est équivalent à la source et au détecteur se déplaçant sur des trajectoires circulaires tandis que le lit du patient se déplace en translation vers le cercle de la trajectoire de la source (le détecteur dans ce cas est supposé être perpendiculaire au plan de la trajectoire). Son objectif final était d'établir une relation entre les projections conduisant à la prédiction de projections non mesurées à partir des données mesurées. Dans [Levine et al., 2010], Levine et al. ont suivi presque le même chemin que Patch dans [Patch, 2002b]. Ils ont obtenu une CBCC dans la géométrie où la source de rayons X se déplace le long d'une ligne et le détecteur est parallèle au plan de la trajectoire. Plus précisément, la CBCC dans cet article peut être comprise comme suit : si la source de rayons X se déplace le long d'une ligne et que le détecteur est parallèle au plan de trajectoire, nous considérons une ligne sur le détecteur, qui est parallèle à la ligne de trajectoire de la source, alors l'intégrale de la projection pondérée de l'objet 3D sur cette ligne est indépendante de l'emplacement de la source. En fait, cette condition est liée à la condition de cohérence du faisceau en éventail (FBCC - Fan Beam Consistency Condition) d'ordre 0, qui a été montrée au chapitre 3. Dans leur article [Ma et al., 2017], Ma *et. al.* ont également suivi une voie similaire à celle de Patch dans [Patch, 2002a] pour dériver des CBCC dans la géométrie où la source et le détecteur se déplacent sur des trajectoires circulaires tandis que l'objet 3D est fixé. Ainsi, ils peuvent restaurer des données de projection, qui ont été perdues dans le processus d'imagerie pour certaines raisons, à partir des données mesurées restantes. En 2005, Sidky et al. ont également développé une CBCC pour les projections pondérées de faisceaux coniques définies par la source et les points de détection correspondants, lorsqu'ils sont censés se trouver sur la même surface en 3D, voir [Sidky et al., 2005]. Cette CBCC a une forme similaire à l'équation de John.

La géométrie avec une trajectoire de source circulaire et un détecteur perpendiculaire au plan de la trajectoire a toujours suscité de l'intérêt. Une technique qui a été utilisée pour travailler avec cette géométrie est de considérer deux emplacements de source arbitraires, aux intersectionx de la droite qui les joint et du cercle de la trajectoire de la source. Ainsi, bien que les deux emplacements sont manifestement sur le cercle, nous pouvons toujours les considérer comme deux positions d'une source de rayons X sur une droite, ce qui nous permet d'appliquer certaines CBCC appropriées construites pour les projections de faisceaux coniques dont les positions de source sont sur une droite. Cette idée permet de créer les CBCC par paires. Dans [Lesaint et al., 2017], Lesaint et al. ont utilisé cette technique et ont construit la condition basée sur la FBCC (qui est également liée au résultat de [Levine et al., 2010]). Plus précisément, ils ont considéré un détecteur dit virtuel, qui est parallèle à la ligne reliant deux emplacements de source considérés, et ont généré un plan oblique à partir de cette ligne et d'une ligne parallèle sur le détecteur virtuel, puis la condition a été construite sur ce plan oblique en changeant la FBCC à la forme de variables angulaires, pour se débarrasser de la considération des variables de coordonnées des détecteurs. Une autre façon d'utiliser la technique ci-dessus est basée sur le résultat de Grangeat, qui peut être trouvé dans [Grangeat, 1991].

Dans [Lesaint et al., 2018], Lesaint et al. ont travaillé avec la source linéaire de rayons X et le détecteur parallèle à la droite, trajectoire de la source. Ils ont présenté la CBCC basée sur Grangeat, et montré la relation entre cette dernière et la FBCC. Ainsi, cet article est également lié aux articles [Lesaint et al., 2017] et [Levine et al., 2010]. Le modèle de Grangeat qui traitait du contexte géométrique avec une trajectoire de source circulaire et un détecteur perpendiculaire à la trajectoire de la source peut être trouvé dans [Abdurahman et al., 2018] et [Luo et al., 2020].

Une autre approche pour construire de nouvelles CBCC consiste à créer les CBCC de type polynomiales. Clackdoyle et Desbat dans l'article [Clackdoyle and Desbat, 2013] ont construit la CBCC complète dans la géométrie de la source de rayons X se déplaçant sur un plan et le détecteur étant parallèle à ce plan de trajectoire. Il s'agit de conditions complètes, ce qui signifie qu'elles sont à la fois des conditions nécessaires et suffisantes. De plus, ces conditions sont si générales que de nombreuses DCC dans des contextes géométriques différents peuvent en être extraites. Par exemple, la FBCC, qui est liée aux conditions de [Levine et al., 2010] et [Lesaint et al., 2017], en est un cas particulier. En 2016, Clackdoyle et al. ont également développé des CBCC de type polynomiales dans la géométrie bien connue d'une trajectoire circulaire de la source, le détecteur étant perpendiculaire au plan de la trajectoire. Lesaint et al. dans l'article [Lesaint et al., 2016] ont défini un type de moment similaire à celui de [Clackdoyle et al., 2016], qui prend en compte le filtre de rampe et le filtre dérivé. Il ont obtenu deux CBCC liées : la condition construite à partir de la fonction du filtre de rampe était la CBCC dans [Clackdoyle et al., 2016] d'ordre 0. Tous les résultats mentionnés de Lesaint peuvent être trouvés dans sa thèse de doctorat [Lesaint et al., 2018].

Comme nous venons de le voir, les CBCC existantes sont toutes connectées. Nous présentons dans l'introduction de ce chapitre un diagramme qui montre les liens et illustre de ce que nous venons d'expliquer ci-dessus.

Dans ce chapitre, afin de créer de nouvelles CBCC de type polynomial, nous étudions en profondeur les CBCC de [Clackdoyle and Desbat, 2013] et [Clackdoyle et al., 2016]. Dans [Clackdoyle and Desbat, 2013], nous appelons les CBCC *CBCC13* qui correspondent à la trajectoire planaire de la source de rayons X, le détecteur étant parallèle au plan de la trajectoire et les CBCC dans l'article [Clackdoyle et al., 2016] *CBCC16* qui correspondent à la trajectoire circulaire de la source, le détecteur étant perpendiculaire au plan de la trajectoire.

En regardant rapidement l'expression des deux moments correspondants aux deux CBCC est différente. *CBCC13* et *CBCC16* ne semblent pas tellement liées l'une à l'autre. Cependant, nous découvrons leurs relations, et à partir de ces relations, nous pouvons dériver de nouvelles CBCC. Nous obtenons des CBCC générales et complètes dans le cas de la géométrie où la source décrit une trajectoire planaire non spécifique et le détecteur est perpendiculaire à ce plan. Nous obtenons également un résultat très préliminaire de l'application ces CBCC au problème de calibration géométrique dans une géométrie 3D à faisceau conique. Afin de produire de nouvelles CBCC, notre toute première idée est de trouver la connexion entre *CBCC16* et *CBCC13*. En changeant la position du détecteur, nous obtenons la nouvelle forme de ces CBCC dans les autres contextes géométriques, que nous appelons ci-dessous les "CBCC converties". Ce sont de nouvelles CBCC, et leurs relations avec *CBCC13* et *CBCC16* nous aident également à obtenir de nombreux autres résultats intéressants.

Chaque CBCC et la géométrie correspondante seront expliquées en détail dans les sections 4.2 et 4.3. Nous informerons le contenu de chaque section à un niveau de détail plus élevé au début de chaque section.

La section 4.2 donne de brefs résumés de *CBCC16*, *CBCC13*, montre les relations entre les deux contextes géométriques, et dérive de nouvelles CBCC appelées *CBCC16Converted* sur la base de ces relations. Elles sont appliquées dans la géométrie avec la trajectoire circulaire de la source, le détecteur étant parallèle au plan de la trajectoire. Les relations entre ces nouvelles CBCC, *CBCC16Converted* et *CBCC13*, sont également prises en compte et développées. Nous montrons également les détails de *CBCC13* dans plusieurs cas particuliers. Nous pouvons obtenir de nouvelles DCC en considérant *CBCC13* dans certains contextes géométriques. Toutes les simulations numériques correspondantes se trouvent également dans cette section.

La section 4.3 explore la direction opposée par rapport à la section 4.2. Nous prenons les *CBCC13* comme base, changeons la position du détecteur, et obtenons de nouvelles CBCC (*CBCC13Converted*) avec la source générale planaire et le détecteur perpendiculaire au plan de la trajectoire. Nous suivons également la technique de l'article [Clackdoyle et al., 2016] et [Lesaint et al., 2016] pour définir le moment correspondant en utilisant le filtre de rampe pour étendre les nouvelles CBCC à une version généralisée complète de *CBCC16*. Les relations et les CBCC concernant les projections conventionnelles par faisceau conique sont également présentées. Enfin, nous essayons de définir et de résoudre le problème de calibration dans la géométrie avec trajectoire circulaire avec détecteur perpendiculaire au plan de la trajectoire, en utilisant ces nouvelles CBCC.

4.1 Introduction

Data consistency conditions (DCCs) can be equations that represent the relationships between the projections, or more generally, DCCs give us some properties or rules that the projection data must follow to be considered as true and consistent. This chapter covers the topic of Cone-beam Consistency Conditions (CBCC). We can find in the literature that so far, there are three main approaches to create CBCCs: going from John's equation, considering the projections by pairs, or creating the polynomial-type CBCCs (like the well-known Helgason-Ludwig conditions).

We can find the first approach in the work of Patch, see [Patch, 2002b] and [Patch, 2002a]. She derived some CBCCs from John's equation for two different geometry contexts: the paper [Patch, 2002b] dealt with the x-ray source moving along a circle and the detector being parallel to the trajectory plane; while in [Patch, 2002a], the x-ray source and the detector were considered to correspondingly move on two helical trajectories with the 3D object being fixed. This is in fact the model of the CT scan because this motion is equivalent to the source and detector moving along circular trajectories while the bed of patient moving towards through the circle of source trajectory (the detector in this case is supposed to be perpendicular to the trajectory plane). Her final goal was to establish a relationship between the projections leading to computation of the unmeasured projections from the measured data. In [Levine et al., 2010], Levine *et al.* went almost the same way as Patch in [Patch, 2002b], they obtained a CBCC in the geometry that the x-ray source moved along a line and the detector was parallel to the trajectory plane. More precisely, the CBCC in this paper can be understood as: if the x-ray source moves along a line and the detector is parallel to the trajectory plane, we consider a line on the detector, which is parallel to the line of source trajectory, then the integral of the weighted projection of the 3D object over this line is independent of the source location. In fact, this condition links to the fan-beam consistency condition (FBCC) of order 0, which has been shown in chapter 3. Ma *et al.* in the paper [Ma et al., 2017] also followed the similar way as Patch in [Patch, 2002a] to derive the CBCCs in the geometry that both source and detector moved on circular trajectories while the 3D object is fixed, to restore the projection data, which had been lost in the imaging process for some reasons, from the measured data. In 2005, Sidky *et al.* also developed a CBCC for weighted cone-beam projections defined by the source and the corresponding detection points, where they were supposed to be on the same surface in 3D, see [Sidky et al., 2005]. This CBCC has a similar form as John's equation.

The geometry with circular source trajectory and the detector being perpendicular to the trajectory plane has always been of interests. One technique that has been used to work with this geometry is to consider two arbitrary source locations, which must be the intersections of some line with the circle of source trajectory. Then although the two locations are obviously on the circle, we can still consider they as two positions of an x-ray source moving along a line, so we are able to apply some pre-built suitable CBCCs for the cone-beam projections taken at these two locations of the source. Following this idea helps create the pair-wise CBCCs. In [Lesaint et al., 2017], Lesaint *et al.* used this technique and build the condition based on the FBCC (which also links to the result in [Levine et al., 2010]). More precisely, in order to construct from the FBCC, they considered a so-called virtual detector, which is parallel to the line connecting two considering source locations, and generated an oblique plane from this line and a parallel line on the virtual detector, then the condition was built on this oblique plane by changing FBCC to the form of angular variables, to get rid of considering the detectors' coordinate variables. Another way to use the above technique is based on Grangeat's result, which can be found in [Grangeat, 1991]. In [Lesaint et al., 2018], Lesaint *et al.* worked with the linear x-ray source and the detector being parallel to the line of source trajectory. They presented the Grangeat-based CBCC, and shown the relationship between it and FBCC. Thus this paper also links to the papers [Lesaint et al., 2017] and [Levine et al., 2010]. The Grangeat-based which dealt with the geometry context with circular source trajectory and the detector being perpendicular to the source trajectory can be found in [Abdurahman et al., 2018] and [Luo et al., 2020].

Another approach to construct new CBCCs is to create the polynomial-type CBCCs. Clackdoyle and Desbat in the paper [Clackdoyle and Desbat, 2013] constructed the full CBCC in the geometry that the x-ray source moving on a plane and the detector being parallel to that trajectory plane. It is a full condition, which means it is both necessary and sufficient condition. Additionally, this condition is such general that many DCCs in different geometry contexts can be extracted from it. For instance, the FBCC, which links to the conditions in [Levine et al., 2010] and [Lesaint et al., 2017], is a special case of it. In 2016, Clackdoyle *et al.* also developed a polynomial-type CBCC in the well-known geometry with circular source trajectory and the detector being perpendicular to the trajectory plane. Lesaint *et al.* in the paper [Lesaint et al., 2016] defined a similar moment type as in [Clackdoyle et al., 2016], which took the ramp filter and the derivative filter into account. He obtained two corresponding CBCCs and and the condition built from the ramp filter function was the CBCC in [Clackdoyle et al., 2016] of order 0. All the mentioned results of Lesaint can be found in his Ph. D. thesis [Lesaint, 2018]. As we have just seen, the existed CBCCs are all connected, and we attach the below diagram as an illustration of what we just explained above.

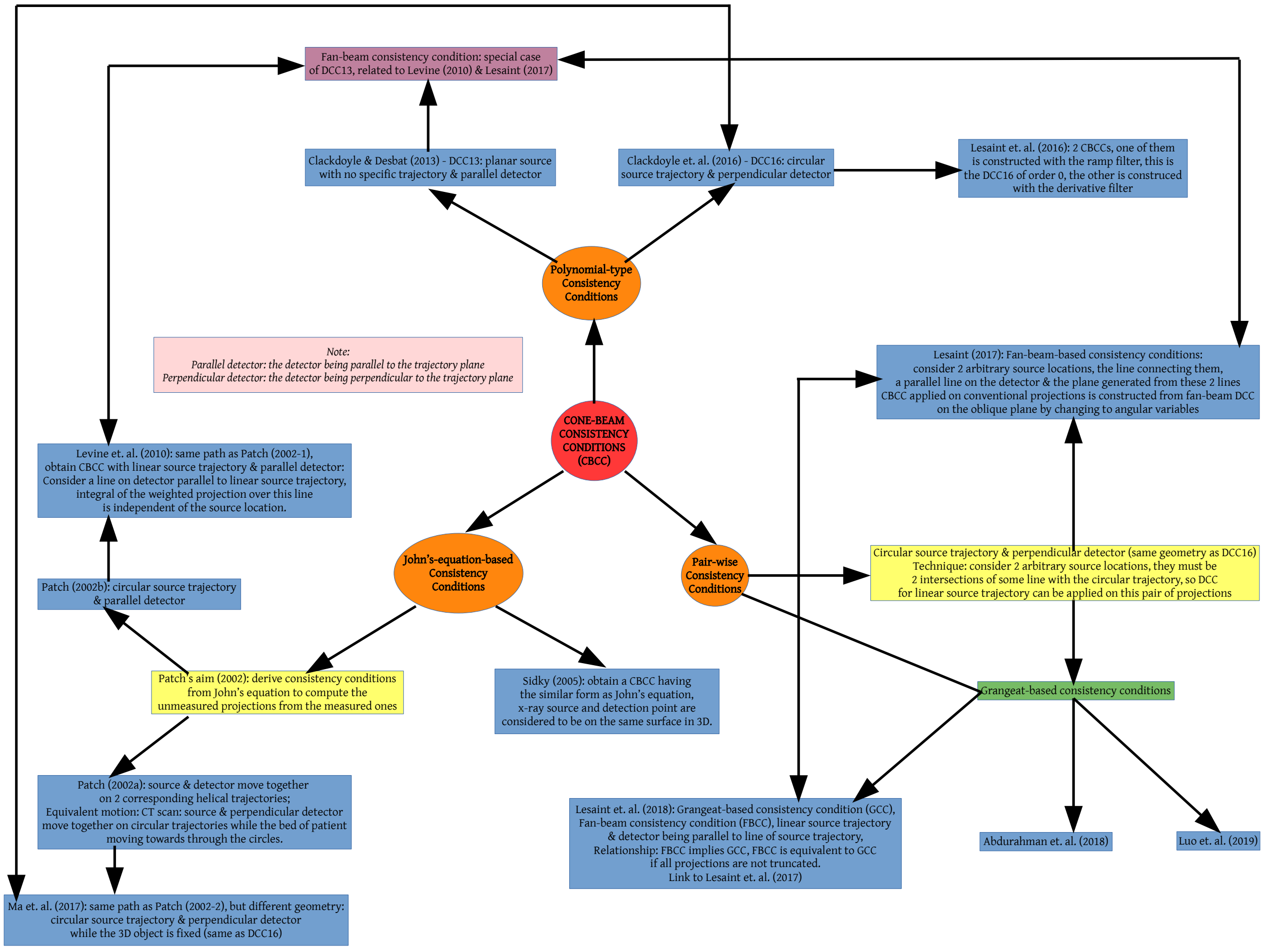

In this chapter, we investigate the CBCCs in [Clackdoyle and Desbat, 2013] and [Clackdoyle et al., 2016] deeply, to understand them and to create new polynomial-type CBCCs. We call the CBCC in [Clackdoyle and Desbat, 2013] *CBCC13* which is applied with the planar x-ray source and the detector being parallel to the trajectory plane; and the CBCC in the paper [Clackdoyle et al., 2016] *CBCC16*, which is applied when the source is moving along a circle and the detector is perpendicular to the trajectory plane. By a quick look, the form of two corresponding moments of two CBCCs are different and not so related to each other. However, we find out their relationships, and from these relationships, we can derive new CBCCs. The final one we obtain is the general and full CBCC which can be applied in the geometry that the source is on a plane with no specific trajectory and the detector is perpendicular to that plane. We also obtain a very preliminary result of the application of this CBCC in the corresponding calibration problem in 3D cone-beam geometry. In order to produce new CBCCs, our very first idea is to find the connection between *CBCC16* and *CBCC13*. By changing the position of the detector, we obtain the new form of those CBCCs in the other geometry contexts, which we call the converted CBCCs below. They are new CBCCs, and their relations to *CBCC13* and *CBCC16* also help us find many other interesting results. Each CBCC and corresponding geometry will be explained in details in the respective following sections. Section 4.2 gives the brief summaries of *CBCC16*, *CBCC13*, shows the relationships between the two geometry contexts, and derives new CBCCs called *CBCC16Converted* based on these relationships, which is applied in the geometry with the circular source trajectory and the detector being parallel to the trajectory plane. The relation between this new *CBCC16Converted* and *CBCC13* is also taken into account. We also show the details of *CBCC13* in several particular cases, that we can earn more DCCs by considering *CBCC13* in certain geometry contexts. All the corresponding numerical simulations can be found in this section also. We will inform the content of each section at a higher level of details at the beginning of each section.

Section 4.3 performs the work which is in the opposite direction in comparison to section 4.2. We take *CBCC13* as

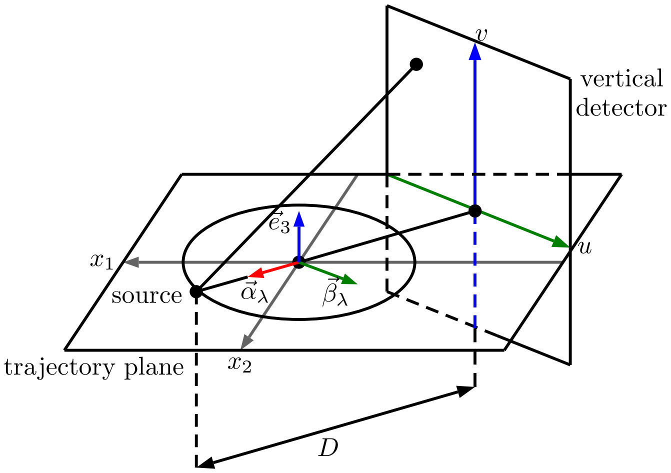

Figure 4.1: *CBCC16* geometry

our base, change the position of the detector, and obtain a new CBCC with the general planar source and the detector being perpendicular to the trajectory plane. We also follow the technique in the papers [Clackdoyle et al., 2016] and [Lesaint et al., 2016] to define the corresponding moment using the ramp filter to extend the new CBCC to a complete generalized version of *CBCC16*. The relationships and CBCCs concerning the conventional cone-beam projections have also been presented. Finally, we try to define and solve the calibration problem in the geometry with circular trajectory and perpendicular detector, using this new CBCC.

4.2 *CBCC16Converted*

In this section, we build the new *CBCC16Converted* step by step. Section 4.2.1 recalls *CBCC16* - the CBCC in [Clackdoyle et al., 2016]. Section 4.2.2 introduce the geometry with circular source trajectory and the detector being parallel to the trajectory plane, and define the weighted cone-beam projection on that detector. Section 4.2.3 shows the relation between the two definitions of the weighted cone-beam projection when we change the position of the detector. Section 4.2.4 constructs the new form the moment of the weighted cone-beam projections from the moment defined in [Clackdoyle et al., 2016] by changing the variables, and introduces the new consistency condition *CBCC16Converted*. Section 4.2.5 gives a direct proof of *CBCC16Converted*, instead of walking all the path from *CBCC16*. Section 4.2.6 performs the numerical simulations to illustrate the result of *six* and *CBCC16Converted*, we can also see the relation between them. Section 4.2.7 briefly summarize the main result in the paper [Clackdoyle and Desbat, 2013]. Section 4.2.8 shows the relationship between *CBCC16Converted* and *CBCC13*. We then realize that *CBCC16Converted* is a special case of *CBCC13*, thus we can obtain another new CBCC in section 4.2.9, whose results are the nonhomogeneous polynomial in cos and sin. Section 4.2.10 deeply dives into *CBCC13* and shows some new CBCCs in particular geometry contexts.

4.2.1 Summary of *CBCC16*

We firstly recall the crucial definitions and results of *CBCC16* [Clackdoyle et al., 2016], since they are our important bricks to build new DCCs. Now we are working in 3D with $O\,(0,0,0)$ as the world origin and (x_1,x_2,x_3) as the standard coordinate system. As mentioned above, the geometry of *CBCC16* contains an x-ray source moving along a circle and a vertical detector. We assume that this circle is on the trajectory plane $x_3=0$, whose center is at the origin and radius is R. Also, the vertical detector is supposed to be always at distance D away from the source. And the projections are assumed to have no truncation. Figure 4.1 shows us the considered geometry. In this geometry, the source location is parameterized by radius $R>0$ and angle $\lambda\in[0,2\pi)$ (the angle between x_1-axis and the ray connecting the origin to the source location), $\vec{\alpha}_\lambda$ is the unit vector pointing towards the source, $\vec{\beta}_\lambda$ is obtained by rotating $\vec{\alpha}_\lambda$ 90° counter-clockwise in the (x_1,x_2) plane. More precisely, in the coordinate system (x_1,x_2,x_3):

$$\vec{\alpha}_\lambda=(\cos\lambda,\sin\lambda,0)\,,\quad \vec{\beta}_\lambda=(-\sin\lambda,\cos\lambda,0)\,,\quad \vec{e}_3=(0,0,1)\,,\quad \vec{s}_\lambda=R\vec{\alpha}_\lambda=(R\cos\lambda,R\sin\lambda,0)\,. \tag{4.1}$$

The origin of the vertical detector is at location $(R-D)\,\vec{\alpha}_\lambda$. The u and v axes on the vertical detector have the same directions as $\vec{\beta}_\lambda$ and $\vec{e}_3$ respectively. We assume our 3D object is the three-variable real function f, which has compact support. Let $\mathcal{P}^{\mathcal{V}}$ be the projection operator applying on the object f to produce the weighted cone-beam projection on the vertical detector $p^V = \mathcal{P}^{\mathcal{V}} f$, where the x-ray source is moving along a circle with the center at the origin and the radius being R, then the projection data on the detector is:

$$p_\lambda^V(u,v) = p^V(\lambda,u,v) = \mathcal{P}^{\mathcal{V}} f(\lambda,u,v) = \int_0^\infty f\left(\vec{s}_\lambda + t\left(u\vec{\beta}_\lambda + v\vec{e}_3 - D\vec{\alpha}_\lambda\right)\right) dt. \tag{4.2}$$

We use the notation p_λ^V to emphasize that this is the weighted cone-beam projection on the vertical detector (V here stands for vertical) with the weight $\left(1/\sqrt{u^2+v^2+D^2}\right)$ in comparison to the conventional cone-beam projection. This relation will be explained explicitly in section 4.3.6.1. For now, to explain the weight, we can understand that the conventional cone-beam projection is defined in terms of unit vector in $\mathbb{S}^2$. And the weighted cone-beam projection defined by equation (4.2) is computed from the vector $\left(u\vec{\beta}_\lambda + v\vec{e}_3 - D\vec{\alpha}_\lambda\right)$ connecting the source to the detection point, which is not unit. In order to make it be unit vector, we need to divide this vector by its length $\sqrt{u^2+v^2+D^2}$ and change the variables of integration, which leads to the above weight. The moment of the weighted projections is the following:

$$M_n^V(\lambda) = \iint p_\lambda^V(u,v)\frac{u^n}{v^{n+2}} du dv. \tag{4.3}$$

CBCC16 tells us that:

> *If p^V is in the range of $\mathcal{P}^{\mathcal{V}}$: $p^V = \mathcal{P}^{\mathcal{V}} f$ for some f (which is a compactly supported real function) then $M_n^V(\lambda)$ is a homogeneous polynomial in $\cos\lambda$ and $\sin\lambda$ of degree n for all non-negative integer n.*

We can see a singularity in the definition of the moment $M_n^V(\lambda)$ when $v = 0$. In [Clackdoyle et al., 2016], this singularity has been perfectly handled by replacing the term $1/v^{n+2}$ by the generalized function $h_n(v)$, which is the inverse Fourier transform of

$$H_n(\nu) = \frac{(-2i\pi)^{n+2}}{2(n+1)!} |\nu| \nu^n. \tag{4.4}$$

This means in *CBCC16*, the support of the object is allowed to intersect the trajectory plane $x_3 = 0$. For now, we will temporarily ignore this fact and assume that the object is strictly above the plane $x_3 = 0$ and strictly inside the circular source trajectory. We change the geometry by flipping the vertical detector to obtain a horizontal detector. This leads to a new form of *CBCC16*, which can link to *CBCC13*.

4.2.2 Geometry of *CBCC16Converted* and the weighted cone-beam projection on the horizontal detector

Now we have the horizontal detector at distance T from the trajectory plane, instead of the vertical detector. More precisely, the horizontal detector is on the plane $x_3 = T$, where T is a positive constant. The origin of the horizontal detector is at location $(0,0,T)$, and its coordinate axes u, w have the same directions as $\vec{\beta}_\lambda$ and $\vec{\alpha}_\lambda$. Here we use the same notation u as the previous section because the direction of this axis remains the same as the u-axis in *CBCC16* geometry. The 3D object is strictly above the trajectory plane, and the source is still moving along the same circle. Figure 4.2 shows us the geometry. One point (u,w) on the horizontal detector can be written as $u\vec{\beta}_\lambda + w\vec{\alpha}_\lambda + T\vec{e}_3$ in 3D. The weighted cone-beam projection p_λ^H on the horizontal detector is then defined as follows: let $\mathcal{P}^{\mathcal{H}}$ be the projection operator applying on the object f to produce the weighted cone-beam projection on the horizontal detector $p^H = \mathcal{P}^{\mathcal{H}} f$, where the x-ray source is moving along a circle with the center at the origin and the radius being R, then the projection data is:

$$p_\lambda^H(u,w) = p^H(\lambda,u,w) = \mathcal{P}^{\mathcal{H}} f(\lambda,u,w) = \int_0^\infty f\left(\vec{s}_\lambda + t\left(u\vec{\beta}_\lambda + w\vec{\alpha}_\lambda + T\vec{e}_3 - \vec{s}_\lambda\right)\right) dt \tag{4.5a}$$

$$= \int_0^\infty f\left(\vec{s}_\lambda + t\left(u\vec{\beta}_\lambda + (w-R)\vec{\alpha}_\lambda + T\vec{e}_3\right)\right) dt. \tag{4.5b}$$

4.2.3 Relationship between the weighted cone-beam projections on the vertical and horizontal detectors (*CBCC16* and *CBCC16Converted* geometry contexts)

If we consider both detectors at the same time, then one point (u,v) on the vertical detector will link to a point on the horizontal detector, by taking the intersection of the horizontal detector and the line connecting the source and

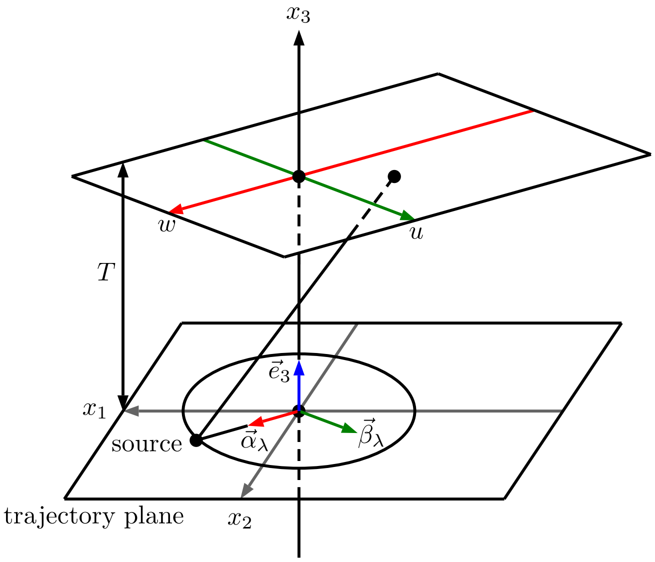

Figure 4.2: *CBCC16Converted* geometry

the point on the vertical detector. More precisely, this line passes through $(R\cos\lambda, R\sin\lambda, 0)$ and has the same direction as $u\vec{\beta}_\lambda + v\vec{e}_3 - D\vec{\alpha}_\lambda$. Its equation is the following:

$$\frac{x_1 - R\cos\lambda}{-u\sin\lambda - D\cos\lambda} = \frac{x_2 - R\sin\lambda}{u\cos\lambda - D\sin\lambda} = \frac{x_3}{v}. \tag{4.6}$$

And since the horizontal detector is on the plane $x_3 = T$ then the intersection is $(\widehat{x}_1, \widehat{x}_2, \widehat{x}_3)$ where

$$\widehat{x}_1 = R\cos\lambda - \frac{T}{v}\left(u\sin\lambda + D\cos\lambda\right), \tag{4.7a}$$

$$\widehat{x}_2 = R\sin\lambda + \frac{T}{v}\left(u\cos\lambda - D\sin\lambda\right), \tag{4.7b}$$

$$\widehat{x}_3 = T. \tag{4.7c}$$

Moreover, one such point (u, w) on the horizontal detector has the representation $u\vec{\beta}_\lambda + w\vec{\alpha}_\lambda + T\vec{e}_3$ in 3D, then the intersection (in 3D)

$$(\widehat{x}_1, \widehat{x}_2, \widehat{x}_3) = \left(R\cos\lambda - \frac{T}{v}\left(u\sin\lambda + D\cos\lambda\right), R\sin\lambda + \frac{T}{v}\left(u\cos\lambda - D\sin\lambda\right), T\right) \tag{4.8a}$$

$$= \left(\frac{Tu}{v}\left(-\sin\lambda\right) + \left(R - \frac{DT}{v}\right)\cos\lambda, \frac{Tu}{v}\cos\lambda + \left(R - \frac{DT}{v}\right)\sin\lambda, T\right) \tag{4.8b}$$

$$= \frac{Tu}{v}\vec{\beta}_\lambda + \left(R - \frac{DT}{v}\right)\vec{\alpha}_\lambda + T\vec{e}_3, \tag{4.8c}$$

will be the point $\left(\frac{Tu}{v}, R - \frac{DT}{v}\right)$ on the horizontal detector. Thus the point (u, v) on the vertical detector links to the point $\left(\frac{Tu}{v}, R - \frac{DT}{v}\right)$ on the horizontal detector. The link is in the sense that the respective weighted cone-beam projections on the vertical and horizontal detectors relate to each other, since they are both computed on the same direction from the source (the source and those two points are collinear).

This means there has to exist a formula connecting $p_\lambda^V(u, v)$ and $p_\lambda^H\left(\frac{Tu}{v}, R - \frac{DT}{v}\right)$. Using the definitions (4.5b) and (4.2), we obtain the following relationship between the two weighted cone-beam projections on the horizontal and vertical detectors:

$$p_\lambda^H\left(\frac{Tu}{v}, R-\frac{DT}{v}\right) = \int_0^\infty f\left(\vec{s}_\lambda + t\left(\frac{Tu}{v}\vec{\beta}_\lambda + \left(R - \frac{DT}{v} - R\right)\vec{\alpha}_\lambda + T\vec{e}_3\right)\right)dt \tag{4.9a}$$

$$= \int_0^\infty f\left(\vec{s}_\lambda + t\left(\frac{Tu}{v}\vec{\beta}_\lambda - \frac{DT}{v}\vec{\alpha}_\lambda + T\vec{e}_3\right)\right)dt \tag{4.9b}$$

$$= \int_0^\infty f\left(\vec{s}_\lambda + t\frac{T}{v}\left(u\vec{\beta}_\lambda + v\vec{e}_3 - D\vec{\alpha}_\lambda\right)\right)dt \tag{4.9c}$$

$$= \int_0^\infty f\left(\vec{s}_\lambda + t'\left(u\vec{\beta}_\lambda + v\vec{e}_3 - D\vec{\alpha}_\lambda\right)\right)dt'\frac{v}{T} \tag{4.9d}$$

$$= p_\lambda^V(u,v)\frac{v}{T}, \tag{4.9e}$$

here we have changed the variable $t(T/v) = t'$, then $dt' = (T/v)\,dt$.

4.2.4 Moment of the weighted cone-beam projections on the horizontal detector and DCC16Converted

From the relationship (4.9e) and the definition (4.3), the moment of projections obtained on the vertical detector will become:

$$M_n^V(\lambda) = \iint p_\lambda^V(u,v)\frac{u^n}{v^{n+2}}dudv \tag{4.10a}$$

$$= \int_\epsilon^\infty \int p_\lambda^V(u,v)\frac{u^n}{v^{n+2}}dudv \tag{4.10b}$$

$$= \int_\epsilon^\infty \int p_\lambda^H\left(\frac{Tu}{v}, R-\frac{DT}{v}\right)\frac{T}{v}\frac{u^n}{v^{n+2}}dudv \tag{4.10c}$$

$$= T\int_\epsilon^\infty \int p_\lambda^H\left(\frac{Tu}{v}, R-\frac{DT}{v}\right)\frac{u^n}{v^{n+3}}dudv. \tag{4.10d}$$

Thanks to the assumption that the support of the 3D object is strictly above the trajectory plane, then there exists $\epsilon > 0$, such that $p_\lambda^V(u,v) = 0$ if $v \leq \epsilon$, then the integral $\iint dudv$ can be changed to $\int_\epsilon^\infty \int dudv$, and there is also no confusion about the singularity when v is on the denominator. We change the variables: $y = Tu/v$ and $z = R - (DT/v)$. Since $u \in \mathbb{R}$ and $v \in [\epsilon, \infty)$ $(\epsilon > 0)$, then $y \in \mathbb{R}$ and $z \in [R - (DT/\epsilon), R)$. We can also compute:

$$v = \frac{DT}{R-z}, \quad u = \frac{yv}{T} = \frac{Dy}{R-z}. \tag{4.11}$$

Also, we have the Jacobian matrix:

$$J = \begin{bmatrix} \frac{\partial y}{\partial u} & \frac{\partial y}{\partial v} \\ \frac{\partial z}{\partial u} & \frac{\partial z}{\partial v} \end{bmatrix} = \begin{bmatrix} \frac{T}{v} & -\frac{Tu}{v^2} \\ 0 & \frac{DT}{v^2} \end{bmatrix}, \quad \det(J) = \frac{DT^2}{v^3}, \tag{4.12}$$

then $dydz = \frac{DT^2}{v^3}dudv$, or:

$$dudv = \frac{1}{DT^2}\frac{(DT)^3}{(R-z)^3}dydz = \frac{D^2T}{(R-z)^3}dydz. \tag{4.13}$$

Thus the above integral becomes:

$$M_n^V(\lambda) = T\int_{R-(DT/\epsilon)}^R \int p_\lambda^H(y,z)\frac{(Dy)^n}{(R-z)^n}\frac{(R-z)^{n+3}}{(DT)^{n+3}}\frac{D^2T}{(R-z)^3}dydz = \frac{1}{DT^{n+1}}\int_{R-(DT/\epsilon)}^R \int p_\lambda^H(y,z)\,y^n dydz. \tag{4.14}$$

- Once again, thanks to the assumption that the support of the 3D object is compact and strictly inside the circular source trajectory, then there exists $\iota < R$ such that:

$$p_\lambda^H(y,z) = 0 \quad \text{if} \quad z \geq \iota; \tag{4.15}$$

- Additionally, thanks to the fact that there exists $\epsilon > 0$ such that $p_\lambda^V(u,v) = 0$ if $v \le \epsilon$, then:

$$p_\lambda^H(y,z) = 0 \quad \text{if} \quad z \le R - \frac{DT}{\epsilon}. \tag{4.16}$$

Thus the integral $\int_{R-(DT/\epsilon)}^{R}\int dydz$ can be changed to $\iint dydz$. From this, we define the moment of the projections obtained on the horizontal detector as:

$$M_n^H(\lambda) = \iint p_\lambda^H(u,w)\,u^n dudw, \tag{4.17}$$

then we have the relationship between the two types of moments:

$$M_n^H(\lambda) = DT^{n+1}M_n^V(\lambda), \tag{4.18}$$

where D and T are respectively the distances from the source to the vertical and horizontal detectors. However, by *CBCC16*, $M^V(\lambda)$ is a homogeneous polynomial in $\cos\lambda$ and $\sin\lambda$ of degree n, then so is $M^H(\lambda)$. We thus obtain our *CBCC16Converted*:

> *If p^H is in the range of $\mathcal{P}^{\mathcal{H}}$: $p^H = \mathcal{P}^{\mathcal{H}}f$ for some f (which is a compactly supported real function) then $M^H(\lambda)$ is a homogeneous polynomial in $\cos\lambda$ and $\sin\lambda$ of degree n for all non-negative integer n.*

4.2.5 Direct proof of *CBCC16Converted* without using *CBCC16*

We can also prove *CBCC16Converted* directly without knowing *CBCC16* by simply using the technique of changing variables, however sacrificing the knowledge about *CBCC16* means paying back with a lot more computations. By definitions (4.17) and (4.5b), we can see that:

$$M_n^H(\lambda) = \iint p_\lambda^H(u,w)\,u^n dudw \tag{4.19a}$$

$$= \iint\int_0^\infty f\left(\vec{s}_\lambda + t\left(u\vec{\beta}_\lambda + (w-R)\,\vec{\alpha}_\lambda + T\vec{e}_3\right)\right)u^n dtdudw. \tag{4.19b}$$

More precisely, as defined before, in 3D coordinate system:

$$\vec{s}_\lambda + t\left(u\vec{\beta}_\lambda + (w-R)\,\vec{\alpha}_\lambda + T\vec{e}_3\right) = \begin{bmatrix} R\cos\lambda \\ R\sin\lambda \\ 0 \end{bmatrix} + t\begin{bmatrix} -u\sin\lambda + (w-R)\cos\lambda \\ u\cos\lambda + (w-R)\sin\lambda \\ T \end{bmatrix} \tag{4.20a}$$

$$= \begin{bmatrix} R\cos\lambda - tu\sin\lambda + t\,(w-R)\cos\lambda \\ R\sin\lambda + tu\cos\lambda + t\,(w-R)\sin\lambda \\ tT \end{bmatrix}. \tag{4.20b}$$

(Here we write the vectors in the column form to save spaces and to make it visually easier for reading.) Now we change the variables: $\vec{s}_\lambda + t\left(u\vec{\beta}_\lambda + (w-R)\,\vec{\alpha}_\lambda + T\vec{e}_3\right) = \vec{x}$, this means:

$$x_1 = R\cos\lambda - tu\sin\lambda + t\,(w-R)\cos\lambda, \tag{4.21a}$$

$$x_2 = R\sin\lambda + tu\cos\lambda + t\,(w-R)\sin\lambda, \tag{4.21b}$$

$$x_3 = tT. \tag{4.21c}$$

Then conversely, we also have:

$$t = \frac{x_3}{T}, \tag{4.22a}$$

$$-u\sin\lambda + (w-R)\cos\lambda = \frac{1}{t}(x_1 - R\cos\lambda) = \frac{T}{x_3}(x_1 - R\cos\lambda), \tag{4.22b}$$

$$u\cos\lambda + (w-R)\sin\lambda = \frac{1}{t}(x_2 - R\sin\lambda) = \frac{T}{x_3}(x_2 - R\sin\lambda), \tag{4.22c}$$

Thus u can also be computed in terms of (x_1, x_2, x_3) as follows:

$$u = \frac{T}{x_3}\left(-x_1 \sin\lambda + R\cos\lambda\sin\lambda\right) + \frac{T}{x_3}\left(x_2\cos\lambda - R\cos\lambda\sin\lambda\right) = \frac{T}{x_3}\left(-x_1\sin\lambda + x_2\cos\lambda\right). \tag{4.23}$$

Moreover, we have the Jacobian matrix as follows:

$$J = \begin{bmatrix} \dfrac{\partial x_1}{\partial t} & \dfrac{\partial x_1}{\partial u} & \dfrac{\partial x_1}{\partial w} \\ \dfrac{\partial x_2}{\partial t} & \dfrac{\partial x_2}{\partial u} & \dfrac{\partial x_2}{\partial w} \\ \dfrac{\partial x_3}{\partial t} & \dfrac{\partial x_3}{\partial u} & \dfrac{\partial x_3}{\partial w} \end{bmatrix} = \begin{bmatrix} -u\sin\lambda + (w-R)\cos\lambda & -t\sin\lambda & t\cos\lambda \\ u\cos\lambda + (w-R)\sin\lambda & t\cos\lambda & t\sin\lambda \\ T & 0 & 0 \end{bmatrix}, \tag{4.24a}$$

$$\det(J) = -Tt^2\sin^2\lambda - Tt^2\cos^2\lambda = -Tt^2. \tag{4.24b}$$

Then $d\vec{x} = dx_1dx_2dx_3 = Tt^2dtdudw$, or $dtdudw = \frac{1}{T}\frac{T^2}{x_3^2}d\vec{x} = \frac{T}{x_3^2}d\vec{x}$. And the above integral becomes:

$$\begin{aligned} M_n^H(\lambda) &= \iiint f(\vec{x})\left(\frac{T}{x_3}\right)^n\left(-x_1\sin\lambda + x_2\cos\lambda\right)^n\frac{T}{x_3^2}d\vec{x} && (4.25a) \\ &= T^{n+1}\iiint f(\vec{x})\left(-x_1\sin\lambda + x_2\cos\lambda\right)^n\frac{d\vec{x}}{x_3^{n+2}} && (4.25b) \\ &= T^{n+1}\iiint f(\vec{x})\left[\sum_{k=0}^{n}\binom{n}{k}\left(-x_1\right)^{n-k}x_2^k\left(\sin\lambda\right)^{n-k}\left(\cos\lambda\right)^k\right]\frac{d\vec{x}}{x_3^{n+2}} && (4.25c) \\ &= \sum_{k=0}^{n}\left[\binom{n}{k}T^{n+1}\iiint f(\vec{x})\frac{\left(-x_1\right)^{n-k}x_2^k}{x_3^{n+2}}d\vec{x}\right]\left(\sin\lambda\right)^{n-k}\left(\cos\lambda\right)^k && (4.25d) \\ &= \sum_{k=0}^{n}a_k\left(\sin\lambda\right)^{n-k}\left(\cos\lambda\right)^k, && (4.25e) \end{aligned}$$

where

$$a_k = \binom{n}{k}T^{n+1}\iiint f(\vec{x})\frac{\left(-x_1\right)^{n-k}x_2^k}{x_3^{n+2}}d\vec{x}, \tag{4.26}$$

depend only on f. The coefficients obtained from the homogeneous polynomial in [Clackdoyle et al., 2016] are:

$$A_k = \binom{n}{k}\frac{1}{D}\iiint f(\vec{x})\frac{\left(-x_1\right)^{n-k}x_2^k}{x_3^{n+2}}d\vec{x}. \tag{4.27}$$

The only difference between them are the weights: $a_k = DT^{n+1}A_k$ for all non-negative integer k, which once again show the relationship: $M_n^H(\lambda) = DT^{n+1}M_n^V(\lambda)$ (in the paper [Clackdoyle et al., 2016], we do not see the extra term $1/D$ in the coefficients; the reason is that the weighted cone-beam projection defined in that paper is $D/\sqrt{u^2+v^2+D^2}$ weighted from the conventional projection, while in this work, by our definition, the weighted projection is obtained from the conventional one with the weight $1/\sqrt{u^2+v^2+D^2}$). Therefore $M^H(\lambda)$ is a homogeneous polynomial in $\cos\lambda$ and $\sin\lambda$ of degree n. In fact, the integral $\iint\int_0^\infty dtdudw$ is equal to the triple integral $\iiint d\vec{x}$ over the whole $\mathbb{R}^3$ because the support of the 3D object f is compact, and its convex hull is strictly inside the source trajectory.

4.2.6 Numerical simulations of *CBCC16* and *CBCC16Converted*

In this section, we perform numerical experiments to illustrate the results of *CBCC16* and *CBCC16Converted*, as well as the relation between the corresponding moments. Section 4.2.6.1 introduce the details of the 3D object and the information of the detectors and the source trajectory. Section 4.2.6.2 shows the numerical simulation results.

4.2.6.1 The 3D object, the x-ray source and the detectors

We perform some experiments to test our above results. The considered 3D object is a slightly modified version of the 3D Shepp-Logan phantom. The detail of the 3D Shepp-Logan phantom can be found in [Kak and Slaney, 1988] [Noo, 1998]. Here we refer to [Noo, 1998], our 3D object also contains twelve 3D ellipsoids, with one exception that none of them has the tilted angle. More precisely, our object is $f = \sum_{i=1,2,\dots,12} f_i$, where:

$$f_i = \begin{cases} v(i), & \text{if} \quad \left(\frac{x_1 - c_1(i)}{r_1(i)}\right)^2 + \left(\frac{x_2 - c_2(i)}{r_2(i)}\right)^2 + \left(\frac{x_3 - c_3(i)}{r_3(i)}\right)^2 \le 1 \\ 0, & \text{otherwise} \end{cases}, \tag{4.28}$$

where $c(i) = (c_1(i), c_2(i), c_3(i))$, $r(i) = (r_1(i), r_2(i), r_3(i))$, $v(i)$ are respectively the center coordinate, the semi-axes, and the gray level of the ith ellipsoid. The information of each ellipsoid is shown in the following table:

Ellipsoid index	Centers $(\times 10^2)$			Semi-axes $(\times 10^2)$			Gray level $(\times 10^{-2})$
i	$c_1(i)$	$c_2(i)$	$c_3(i)$	$r_1(i)$	$r_2(i)$	$r_3(i)$	$v(i)$
1	00.00	00.00	00.00	69.00	90.00	92.00	02.00
2	00.00	00.00	-01.84	66.24	88.00	87.40	-00.98
3	-22.00	-25.00	00.00	21.00	41.00	16.00	-00.02
4	22.00	-25.00	00.00	22.00	31.00	11.00	-00.02
5	00.00	-25.00	35.00	21.00	35.00	25.00	00.01
6	00.00	-25.00	10.00	04.60	04.60	04.60	00.01
7	-08.00	-25.00	-60.50	04.60	02.00	02.30	00.01
8	06.00	-25.00	-60.50	04.60	02.00	02.30	00.01
9	06.00	06.25	-10.50	05.60	10.00	04.00	00.02
10	00.00	62.50	10.00	05.60	10.00	05.60	-00.02
11	00.00	25.00	10.00	04.60	04.60	04.60	00.01
12	00.00	-25.00	-60.50	02.30	02.30	02.30	00.01

Now, we translate this object along the vector $(0.1, 0, 2)$. This means we move the object upwards to make it strictly above the trajectory plane $x_3 = 0$, then we move it a little bit along x_1-axis towards the positive direction, so it is not perfectly at the origin. We will use this object for simulations throughout this chapter. The purpose is to perform many experiments with such an object, then we have a chance to see the relationships between the CBCCs. Regarding the x-ray source and the detectors:

- The source is assumed to move along the circle $x_1^2 + x_2^2 = (5/2)^2$ on the trajectory plane $x_3 = 0$.
- The vertical detector is always at distance $D = 4.5$ away from the source.
- The horizontal detector is on the plane $x_3 = T = 3.5$.

Throughout this chapter, the detectors in all experiments have 500 × 500 pixels and there are 360 source positions in those experiments concerning the circular and elliptic source trajectories, and 300 source positions in the cases with the linear or parabollic source trajectories. It has also been tested that the more number of pixels, the less error we obtain, meaning the data tends to be in shape of the polynomial if we increase the number of pixels. The projections are always computed by measuring the length between two intersections of the integration lines with the ellipsoids, with the corresponding densities being taken into account.

4.2.6.2 Numerical simulations

Below are the figures of the moment $M_n^V(\lambda)$ of orders $n = 0, 1, 2, 3$, which are the moments of projections on the vertical detector, see figure 4.3. They are supposed to be homogeneous polynomials in $\cos\lambda$ and $\sin\lambda$ of degrees $n = 0, 1, 2, 3$, by *CBCC16*. The red lines are the graphs of homogeneous polynomials in $\cos\lambda$ and $\sin\lambda$, which fit the data of the moments. They respectively are:

$$P_0^V(\lambda) = 17.1281, \tag{4.29a}$$

$$P_1^V(\lambda) = 0.0009\cos\lambda - 0.9919\sin\lambda, \tag{4.29b}$$

$$P_2^V(\lambda) = 0.8727\cos^2\lambda + 0.0001\cos\lambda\sin\lambda + 0.5868\sin^2\lambda, \tag{4.29c}$$

$$P_3^V(\lambda) = 0.0000\cos^3\lambda - 0.1562\cos^2\lambda\sin\lambda + 0.0001\cos\lambda\sin^2\lambda - 0.0980\cos^3\lambda. \tag{4.29d}$$

We are going to quickly present how we obtain the above polynomials. In theory, from *CBCC16*, if the projection data is in the range of the projection operator, then the moment $M_n^V(\lambda)$ must be a homogeneous polynomial in $\cos\lambda$ and $\sin\lambda$ of degree n:

$$M_n^V(\lambda) = \sum_{k=0}^{n} B_{k,n} (\cos\lambda)^k (\sin\lambda)^{n-k}. \tag{4.30}$$

Now, our job is to figure out the polynomials $P_n^V(\lambda) = \sum_{k=0}^{n} B_{k,n} (\cos\lambda)^k (\sin\lambda)^{n-k}$, and in order to do that, we need to compute the coefficients $B_{k,n}$ for each n, and for $0 \le k \le n$. For each n, the number of coefficients $B_{k,n}$ that we have to compute is $(n+1)$: $B_{0,n}$, $B_{1,n}$, …, $B_{n,n}$. Therefore a system of $(n+1)$ linear equations should be taken into account to solve for the coefficients $B_{k,n}$, for each value of n. Here we would like to find $P_n^V(\lambda)$ for $n = 0,1,2,3$ (which means n is at most 3), thus we just need to choose four specific values λ_j, $j = 1,2,3,4$, then we compute $\{M_0^V(\lambda_1)\}$, $\{M_1^V(\lambda_1), M_1^V(\lambda_2)\}$, $\{M_2^V(\lambda_1), M_2^V(\lambda_2), M_2^V(\lambda_3)\}$, $\{M_3^V(\lambda_1), M_3^V(\lambda_2), M_3^V(\lambda_3), M_3^V(\lambda_4)\}$ (we only mean that we will compute the moment data, but we put them into respective curly brackets to make it easier for the readers to look at). So from these information, subtituting back into equation (4.30), we obtain all coefficients of the four homogeneous polynomials in $\cos\lambda$ and $\sin\lambda$ of degree $n = 0,1,2,3$ as shown above. We then plot their graphs on the same corresponding figures of the moment data. All of the below similar process of finding the homogeneous polynomials, which fit the moment data, has also been done this way. Additionally, we use the term “nearest” homogeneous polynomials to mean that the polynomials are computed theoretically as shown in the above process, without any approximation approach.

Next, we check the results of *CBCC16Converted*. Figure 4.4 shows us the moments of the projections on the hori-

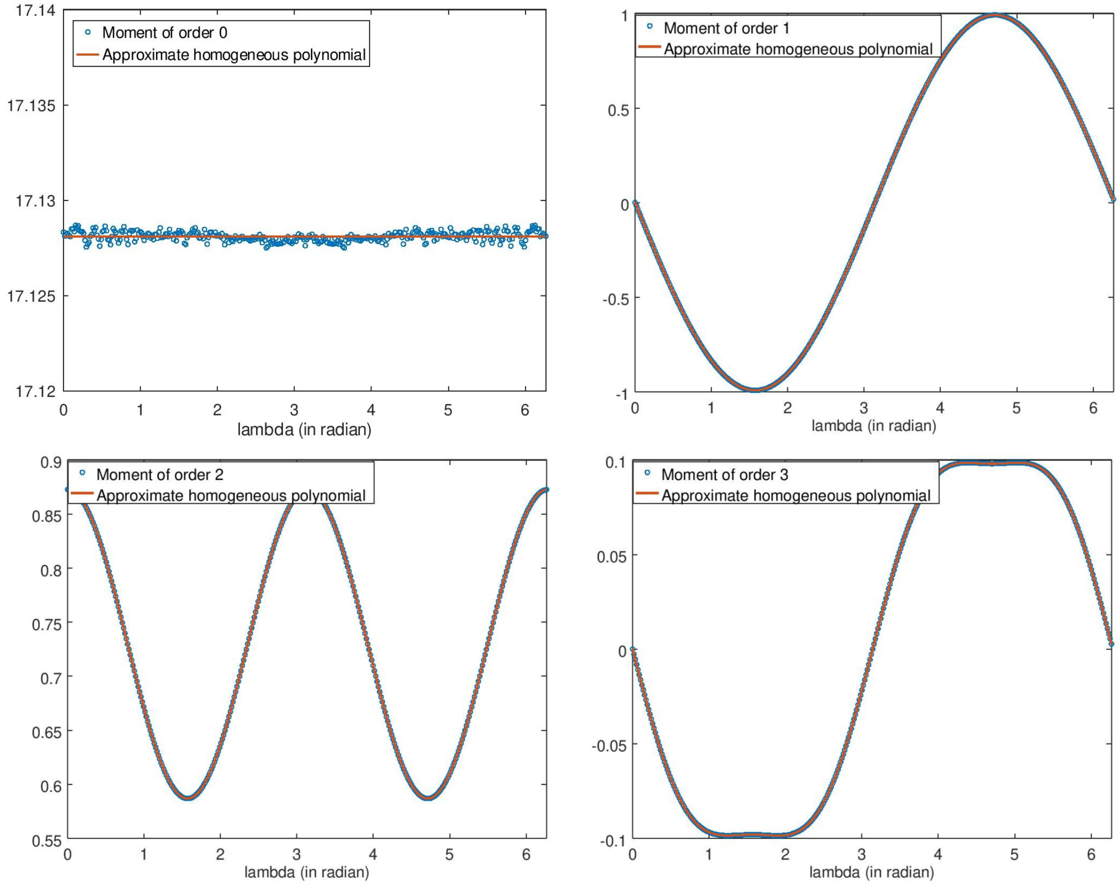

Figure 4.3: Moments $M^V(\lambda)$ of orders 0 (top-left), 1 (top-right), 2 (bottom-left), 3 (bottom-right) of the weighted cone-beam projections on the vertical detector, where the source is moving along the circle: $x_1^2 + x_2^2 = (5/2)^2$ on the trajectory plane $x_3 = 0$. The graph of the 3rd-order moment has this shape is because of the coefficients of the corresponding polynomial, there are still two bumps on the intervals $[1,2]$ and $[4,5]$ of λ although they look almost flat.

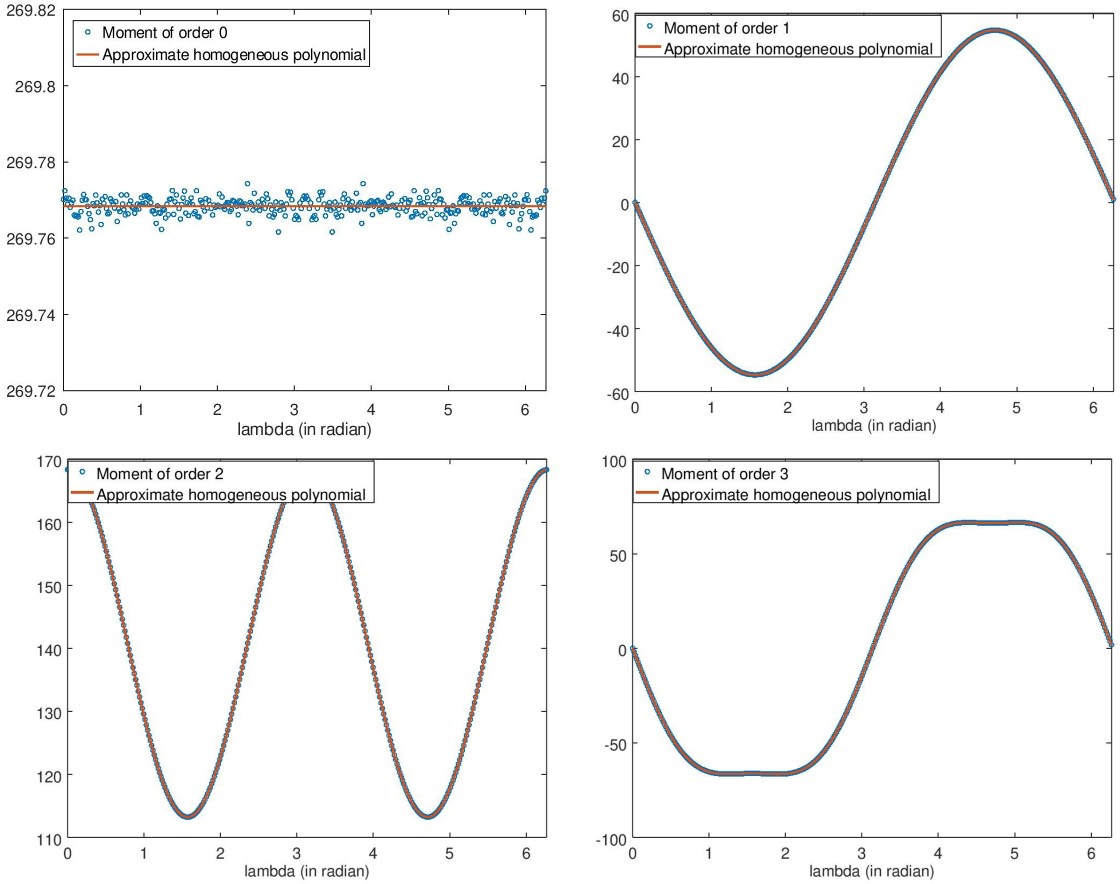

Figure 4.4: Moments $M^H(\lambda)$ of orders 0 (top-left), 1 (top-right), 2 (bottom-left), 3 (bottom-right) of the weighted cone-beam projections on the horizontal detector, where the source is moving along the circle: $x_1^2 + x_2^2 = (5/2)^2$ on the trajectory plane $x_3 = 0$.

zontal detector $M_n^H(\lambda)$ of orders $n = 0, 1, 2, 3$. By *CBCC16Converted*, they are also presumed to be homogeneous polynomials in $\cos\lambda$ and $\sin\lambda$ of degree $n = 0, 1, 2, 3$. We obtain the following homogeneous polynomials in $\cos\lambda$ and $\sin\lambda$, which fit the data of the moments:

$$P_0^H(\lambda) = 269.7684, \tag{4.31a}$$

$$P_1^H(\lambda) = 0.0480\cos\lambda - 54.6831\sin\lambda, \tag{4.31b}$$

$$P_2^H(\lambda) = 168.3633\cos^2\lambda - 0.0043\cos\lambda\sin\lambda + 113.2235\sin^2\lambda, \tag{4.31c}$$

$$P_3^H(\lambda) = 0.0233\cos^3\lambda - 105.4782\cos^2\lambda\sin\lambda + 0.0356\cos\lambda\sin^2\lambda - 66.2001\cos^3\lambda. \tag{4.31d}$$

Moreover, we stated before that there is a relationship between the two types of moments: $M_n^H(\lambda) = DT^{n+1}M_n^V(\lambda)$, see equation (4.18). Since $P_n^H(\lambda)$ and $P_n^V(\lambda)$ are the nearest homogeneous polynomials fitting the data of $M_n^H(\lambda)$ and $M_n^V(\lambda)$ respectively, and since $D = 4.5$ and $T = 3.5$, from the above numerical results, we hope that:

$$P_0^H(\lambda) \approx 15.75 P_0^V(\lambda), \tag{4.32a}$$

$$P_1^H(\lambda) \approx 55.125 P_1^V(\lambda), \tag{4.32b}$$

$$P_2^H(\lambda) \approx 192.9375 P_2^V(\lambda), \tag{4.32c}$$

$$P_3^H(\lambda) \approx 675.28125 P_3^V(\lambda). \tag{4.32d}$$

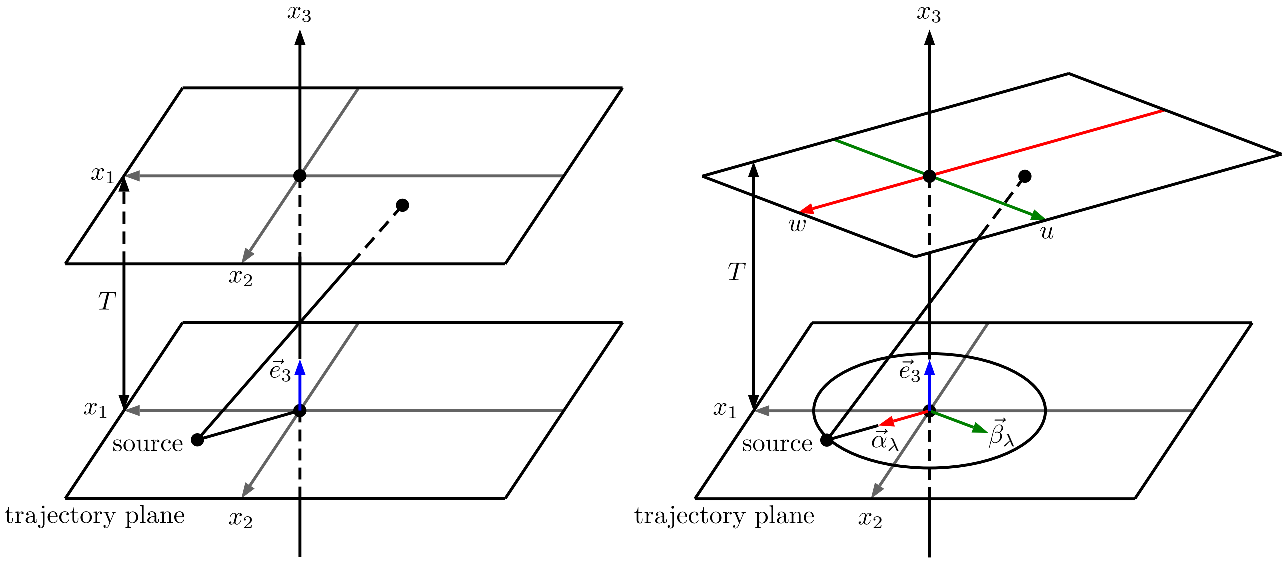

Figure 4.5: *CBCC13* geometry (left) and *CBCC16Converted* geometry (right)

For an easy comparison, from (4.29), we compute:

$$15.75 P_0^V(\lambda) = 269.7676, \tag{4.33a}$$

$$55.125 P_1^V(\lambda) = 0.0481\cos\lambda - 54.6761\sin\lambda, \tag{4.33b}$$

$$192.9375 P_2^V(\lambda) = 168.3731\cos^2\lambda + 0.0152\cos\lambda\sin\lambda + 113.2152\sin^2\lambda, \tag{4.33c}$$

$$675.28125 P_3^V(\lambda) = 0.0230\cos^3\lambda - 105.4978\cos^2\lambda\sin\lambda + 0.0371\cos\lambda\sin^2\lambda - 66.1897\sin^3\lambda. \tag{4.33d}$$

Comparing (4.31) and (4.33), we can see that (4.18) makes sense.

4.2.7 Recalling *CBCC13*

In the geometry of *CBCC13*, we also have the horizontal detector. But the only constraint of the source is that it just needs to be on the trajectory plane $x_3 = 0$, it does not need to be on any specific trajectory. One more difference when we compare this geometry to *CBCC16Converted* geometry is that the two standard axes u and w on the horizontal detector in *CBCC16Converted* geometry are computed depending on λ. This shows the fact that the horizontal detector in *CBCC16Converted* geometry is rotating around the vertical axis correspondingly to the source location (parameterized by λ if the radius R is considered as a constant), although it is not translating or tilting. In *CBCC13* geometry, the horizontal detector is completely fixed, not moving, tilting, or rotating. Figure 4.5 shows us the geometry. The two standard axes on this fixed horizontal detector have the same directions as x_1 and x_2, so we keep the notations x_1, x_2 when working with this horizontal detector of *CBCC13* geometry (then we do not get lost because of too many notations). We again follow the paper [Clackdoyle and Desbat, 2013]: let $\mathcal{G}^{\mathcal{H}}$ be the projection operator applying on the object f to produce the weighted cone-beam projection on the fixed horizontal detector ($x_3 = T$): $g^H = \mathcal{G}^{\mathcal{H}} f$, where the x-ray source is moving on the plane ($x_3 = 0$) without any specific trajectory, then the projection data is:

$$g^H(s_1, s_2, x_1, x_2) = \mathcal{G}^{\mathcal{H}} f(s_1, s_2, x_1, x_2) = \int_0^\infty f(\vec{s} + t((x_1, x_2, T) - (s_1, s_2, 0)))\, dt \tag{4.34a}$$

$$= \int_0^\infty f(\vec{s} + t(x_1 - s_1, x_2 - s_2, T))\, dt. \tag{4.34b}$$

Here the source does not move along a circle, so it cannot be parameterized by an angle λ and a radius R as the previous sections, thus we use the notation $\vec{s} = (s_1, s_2, 0)$ instead of $\vec{s}_\lambda$. The moment of the weighted projections $g^H(s_1, s_2, x_1, x_2)$ is also defined as follows:

$$J_n^H(s_1, s_2, Y_1, Y_2) = \iint g^H(s_1, s_2, x_1, x_2)(x_1 Y_1 + x_2 Y_2)^n\, dx_1 dx_2. \tag{4.35}$$

Then *CBCC13* states that:

g^H is in the range of $\mathcal{G}^{\mathcal{H}}$: $g^H = \mathcal{G}^{\mathcal{H}} f$ for some f (which is a compactly supported real function), if and only if for all $(s_1, s_2) \in \mathbb{R}^2$, $g^H(s_1, s_2, \cdot, \cdot)$ has compact support in $\mathbb{R}^2$ and:

$$J_n^H(s_1, s_2, Y_1, Y_2) = K_n^H(Y_1, Y_2, -s_1Y_1 - s_2Y_2), \quad \forall n = 0, 1, 2, \ldots, \tag{4.36}$$

where $K_n^H(Y_1, Y_2, Y_3) = \sum_{i+j+k=n} C_{i,j,k}^H Y_1^i Y_2^j Y_3^k$ is a homogeneous polynomial in three variables Y_1, Y_2, Y_3 of degree n.

This means $g^H(s_1, s_2, x_1, x_2)$ is the weighted cone-beam projection on the fixed horizontal detector, if and only if the moment $J_n^H(s_1, s_2, Y_1, Y_2)$ is the intersection when slicing the plane $Y_3 = -s_1Y_1 - s_2Y_2$ through the 3D homogeneous polynomial $K_n^H(Y_1, Y_2, Y_3)$. In the notations of g^H and J_n^H, the first two variables provides the source information, the last two varibles are the main variables of the functions.

4.2.8 Relationship between *CBCC16Converted* and *CBCC13*

We can see that the projections defined in *CBCC13* and *CBCC16Converted* geometries link to each other if we consider the source to move along a circle, since they both are the weighted cone-beam projections on the horizontal detector, the only difference is the reference frames: the fixed (x_1, x_2) and the rotating (u, w). Comparing the definitions (4.34b) and (4.5b), we obtain the relationship:

$$p_\lambda^H(u, w) = \int_0^\infty f\left(\vec{s}_\lambda + t\left(u\vec{\beta}_\lambda + w\vec{\alpha}_\lambda + T\vec{e}_3 - \vec{s}_\lambda\right)\right) dt \tag{4.37a}$$

$$= \int_0^\infty f\left(\vec{s}_\lambda + t\left((-u\sin\lambda + w\cos\lambda, u\cos\lambda + w\sin\lambda, T) - (R\cos\lambda, R\sin\lambda, 0)\right)\right) dt \tag{4.37b}$$

$$= g^H(R\cos\lambda, R\sin\lambda, -u\sin\lambda + w\cos\lambda, u\cos\lambda + w\sin\lambda). \tag{4.37c}$$

From this, we can also obtain a link between the moments $M_n^H(\lambda)$ and $J_n^H(R\cos\lambda, R\sin\lambda, Y_1, Y_2)$. Precisely, by the definition (4.17), we have:

$$M_n^H(\lambda) = \iint p_\lambda^H(u, w)\, u^n du dw \tag{4.38a}$$

$$= \iint g^H(R\cos\lambda, R\sin\lambda, -u\sin\lambda + w\cos\lambda, u\cos\lambda + w\sin\lambda)\, u^n du dw. \tag{4.38b}$$

We change the variables $-u\sin\lambda + w\cos\lambda = x_1$ and $u\cos\lambda + w\sin\lambda = x_2$, then conversely:

$$u = -x_1\sin\lambda + x_2\cos\lambda, \tag{4.39a}$$

$$w = x_1\cos\lambda + x_2\sin\lambda, \tag{4.39b}$$

and we can also simply obtain $dudw = dx_1dx_2$. Then the above integral becomes:

$$M_n^H(\lambda) = \iint g^H(R\cos\lambda, R\sin\lambda, x_1, x_2)\,(-x_1\sin\lambda + x_2\cos\lambda)^n dx_1dx_2 \tag{4.40a}$$

$$= J_n^H(R\cos\lambda, R\sin\lambda, -\sin\lambda, \cos\lambda). \tag{4.40b}$$

This follows the definition (4.35). Using *CBCC13* (4.36), the above moment becomes:

$$
\begin{aligned}
M_n^H(\lambda) &= J_n^H(R\cos\lambda, R\sin\lambda, -\sin\lambda, \cos\lambda) && \text{(4.41a)}\\
&= K_n^H(-\sin\lambda, \cos\lambda, -R\cos\lambda(-\sin\lambda) - R\sin\lambda\cos\lambda) && \text{(4.41b)}\\
&= K_n^H(-\sin\lambda, \cos\lambda, 0) && \text{(4.41c)}\\
&= \sum_{i+j+k=n} C_{i,j,k}^H(-\sin\lambda)^i(\cos\lambda)^j 0^k && \text{(4.41d)}\\
&= \sum_{\substack{k=0\\ i+j+k=n}} C_{i,j,k}^H(-\sin\lambda)^i(\cos\lambda)^j 0^k + \sum_{\substack{k>0\\ i+j+k=n}} C_{i,j,k}^H(-\sin\lambda)^i(\cos\lambda)^j 0^k && \text{(4.41e)}\\
&= \sum_{i+j=n} C_{i,j,0}^H(-\sin\lambda)^i(\cos\lambda)^j . && \text{(4.41f)}
\end{aligned}
$$

And this is a homogeneous polynomial in $\cos\lambda$ and $\sin\lambda$ of degree n. Thus we see that using *CBCC13* with $Y_1 = -\sin\lambda$ and $Y_2 = \cos\lambda$ leads exactly to *CBCC16Converted*. From this, we have the feeling that *CBCC13* is such a general CBCC, in the sense that substituting suitable values of Y_1 and Y_2 in *CBCC13* will give us many more new DCCs.

4.2.9 Nonhomogeneous-polynomial CBCC

In the previous sections, we see that the moment in the form $\iint p_\lambda^V(u,v)\left(u^n/v^{n+2}\right)dudv$ in *CBCC16* geometry has been converted to the moment in the form $\iint p_\lambda^H(u,w)\,u^n dudw$ in *CBCC16Converted* geometry. Both CBCCs lead to the homogeneous polynomials in $\cos\lambda$ and $\sin\lambda$ of degrees n. After obtaining *CBCC16Converted* with the moment form $\iint p_\lambda^H(u,w)\,u^n dudw$, we are tempted to also check the moment in the form $\overline{M}_n^H(\lambda) = \iint p_\lambda^H(u,w)\,w^n dudw$ to see if there exists some interesting DCCs. Section 4.2.8 shows us a way to get the full version of *CBCC16Converted* by linking the moment $M_n^H(\lambda)$ to the moment $J_n^H(s_1, s_2, Y_1, Y_2)$, and then using *CBCC13* with $Y_1 = -\sin\lambda$ and $Y_2 = \cos\lambda$. Now we are going to redo the same process:

$$
\begin{aligned}
\overline{M}_n^H(\lambda) &= \iint p_\lambda^H(u,w)\,w^n dudw && \text{(4.42a)}\\
&= \iint g^H(R\cos\lambda, R\sin\lambda, -u\sin\lambda + w\cos\lambda, u\cos\lambda + w\sin\lambda)\,w^n dudw && \text{(4.42b)}\\
&= \iint g^H(R\cos\lambda, R\sin\lambda, x_1, x_2)(x_1\cos\lambda + x_2\sin\lambda)^n dudw && \text{(4.42c)}\\
&= J_n^H(R\cos\lambda, R\sin\lambda, \cos\lambda, \sin\lambda). && \text{(4.42d)}
\end{aligned}
$$

Here we have used again the relationship (4.37c), the definition (4.35) and changed the variables (exactly the same as section 4.2.8): $x_1 = -u\sin\lambda + w\cos\lambda$ and $x_2 = u\cos\lambda + w\sin\lambda$. Now using *CBCC13* with $Y_1 = \cos\lambda$ and $Y_2 = \sin\lambda$, we obtain:

$$
\begin{aligned}
\overline{M}_n^H(\lambda) &= J_n^H(R\cos\lambda, R\sin\lambda, \cos\lambda, \sin\lambda) && \text{(4.43a)}\\
&= K_n^H(\cos\lambda, \sin\lambda, -R\cos\lambda(\cos\lambda) - R\sin\lambda(\sin\lambda)) && \text{(4.43b)}\\
&= K_n^H(\cos\lambda, \sin\lambda, -R) && \text{(4.43c)}\\
&= \sum_{i+j+k=n} C_{i,j,k}^H(\cos\lambda)^i(\sin\lambda)^j(-R)^k && \text{(4.43d)}\\
&= \sum_{k=0}^{n}\left[(-R)^k \sum_{i+j=n-k} C_{i,j,k}^H(\cos\lambda)^i(\sin\lambda)^j\right] && \text{(4.43e)}\\
&= \sum_{k=0}^{n}(-R)^k\,\mathfrak{T}_{n-k}(\lambda), && \text{(4.43f)}
\end{aligned}
$$

where $\mathfrak{T}_l(\lambda)$ is a homogeneous polynomial in $\cos\lambda$ and $\sin\lambda$ of degree l. We obtain the *nonhomogeneous-polynomial CBCC* as follows:

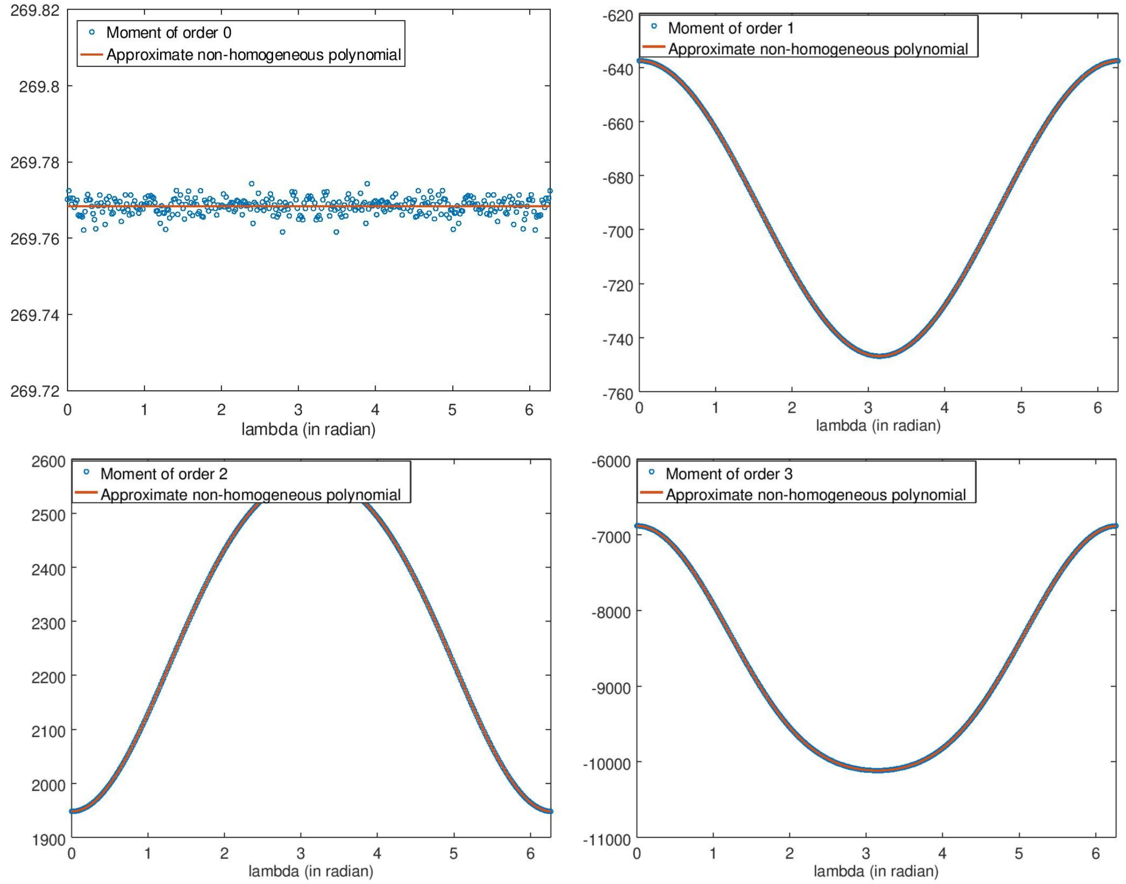

Figure 4.6: Moments $\overline{M}_n^H(\lambda)$ of orders 0 (top-left), 1 (top-right), 2 (bottom-left), 3 (bottom-right) of the weighted cone-beam projections on the horizontal detector, where the source is moving along the circle: $x_1^2 + x_2^2 = (5/2)^2$ on the trajectory plane $x_3 = 0$. These moments were supposed to be the nonhomogeneous polynomial in $\cos\lambda$ and $\sin\lambda$ of degree n.

If p^H is in the range of $\mathcal{P}^{\mathcal{H}}$: $p^H = \mathcal{P}^{\mathcal{H}} f$ for some f (which is a compactly supported real function) then $\overline{M}_n^H(\lambda)$ is a nonhomogeneous polynomial in $\cos\lambda$ and $\sin\lambda$ of degree n for all non-negative integer n:

$$\overline{M}_n^H(\lambda) = \sum_{k=0}^{n} (-R)^k \, \mathfrak{T}_{n-k}(\lambda) \,, \tag{4.44}$$

where $\mathfrak{T}_l(\lambda)$ is a homogeneous polynomial in $\cos\lambda$ and $\sin\lambda$ of degree l.

Numerical simulations of the nonhomogeneous-polynomial CBCC

For this simulation, the information of the 3D object, the source and the horizontal detector remains the same as in section 4.2.6. Figure 4.6 shows us the moments $\overline{M}_n^H(\lambda)$ of orders $n = 0, 1, 2, 3$. The nearest nonhomogeneous polynomials fitting the data of the moments are:

$$\overline{P}_0^H(\lambda) = 269.7684, \tag{4.45a}$$

$$\overline{P}_1^H(\lambda) = -692.1892 + 54.6833\cos\lambda + 0.0392\sin\lambda, \tag{4.45b}$$

$$\begin{aligned}\overline{P}_2^H(\lambda) = {} & -310.1064\cos\lambda - 0.2054\sin\lambda \\ & + 2258.2044\cos^2\lambda + 0.0166\cos\lambda\sin\lambda + 2313.3841\sin^2\lambda,\end{aligned} \tag{4.45c}$$

$$\begin{aligned}\overline{P}_3^H(\lambda) = {} & 1656.7767\cos\lambda + 0.7250\sin\lambda \\ & - 8498.6068\cos^2\lambda - 0.0478\cos\lambda\sin\lambda - 8935.6487\sin^2\lambda \\ & - 39.4232\cos^3\lambda - 0.0745\sin^3\lambda.\end{aligned} \tag{4.45d}$$

Here we give a very brief explanation about the form of $\overline{P}_2^H(\lambda)$ and $\overline{P}_3^H(\lambda)$. Formally, $\overline{P}_2^H(\lambda)$ should be:

$$\overline{P}_2^H(\lambda) = \mathscr{A} + \mathscr{B}\cos\lambda + \mathscr{C}\sin\lambda + \mathscr{D}\cos^2\lambda + \mathscr{E}\cos\lambda\sin\lambda + \mathscr{F}\sin^2\lambda. \tag{4.46}$$

However, let's take a look at the following example:

$$\begin{aligned}\mathfrak{A} = \mathbf{5} + \mathbf{1}\cos^2\lambda + \mathbf{2}\sin^2\lambda = \left[\mathbf{4} + \left(\mathbf{1}\cos^2\lambda + \mathbf{1}\sin^2\lambda\right)\right] + \mathbf{1}\cos^2\lambda + \mathbf{2}\sin^2\lambda &= \mathbf{4} + \mathbf{2}\cos^2\lambda + \mathbf{3}\sin^2\lambda && (4.47a) \\ &= \mathbf{3} + \mathbf{3}\cos^2\lambda + \mathbf{4}\sin^2\lambda && (4.47b) \\ &= -\mathbf{2} + \mathbf{8}\cos^2\lambda + \mathbf{9}\sin^2\lambda && (4.47c) \\ &= \frac{\mathbf{1}}{\mathbf{3}} + \frac{\mathbf{17}}{\mathbf{3}}\cos^2\lambda + \frac{\mathbf{20}}{\mathbf{3}}\sin^2\lambda && (4.47d) \\ &= \dots && (4.47e)\end{aligned}$$

For the same quantity $\mathfrak{A} = \mathscr{A} + \mathscr{D}\cos^2\lambda + \mathscr{F}\sin^2\lambda$, there are infinitely many triplets $(\mathscr{A}, \mathscr{D}, \mathscr{F})$ which give exactly the same result. This comes from the fact that the coefficients $\mathscr{D}$ and $\mathscr{F}$ are not completely independent, they do depend on the constant $\mathscr{A}$, because of the trigonometric property $\cos^2\lambda + \sin^2\lambda = 1$. So now coming back with the formal $\overline{P}_2^H(\lambda)$. We redo the mentioned process in section 4.2.6.2 to compute the six coefficients, to obtain result of the polynomial $\overline{P}_2^H(\lambda)$. But when it comes to solving the system of linear equations, we can never solve for $\mathscr{A}$, $\mathscr{D}$ and $\mathscr{F}$ with the explained reason above. Instead, $\mathscr{A}$ can be chosen freely, $\mathscr{D}$ and $\mathscr{F}$ will be suitably chosen depending on $\mathscr{A}$. The other three coefficients $\mathscr{B}$, $\mathscr{C}$, $\mathscr{E}$ can be solved easily, Thus, to reduce the computation work, we decide that $\mathscr{A} = 0$ at the beginning, and consider $\overline{P}_2^H(\lambda)$ only in the form:

$$\overline{P}_2^H(\lambda) = \mathscr{B}\cos\lambda + \mathscr{C}\sin\lambda + \mathscr{D}\cos^2\lambda + \mathscr{E}\cos\lambda\sin\lambda + \mathscr{F}\sin^2\lambda. \tag{4.48}$$

The reason is that the less coefficients to compute, the less linear equations in the system to look at, which leads to the less computation work.

The same thing happens with $\overline{P}_3^H(\lambda)$, it formally is:

$$\begin{aligned}\overline{P}_3^H(\lambda) = {} & \mathscr{A} + \mathscr{B}\cos\lambda + \mathscr{C}\sin\lambda + \mathscr{D}\cos^2\lambda + \mathscr{E}\cos\lambda\sin\lambda + \mathscr{F}\sin^2\lambda && (4.49) \\ & + \mathscr{G}\cos^3\lambda + \mathscr{H}\cos^2\lambda\sin\lambda + \mathscr{I}\cos\lambda\sin^2\lambda + \mathscr{J}\sin^3\lambda. && (4.50)\end{aligned}$$

(We are sorry to use the same notations of the coefficients as in the formula of $\overline{P}_2^H(\lambda)$, but it should not cause any problem of confusion.) However, with the same idea as above, we can reduce this form and rewritten it as:

$$\begin{aligned}\overline{P}_3^H(\lambda) &= \mathscr{A} + \mathscr{B}\cos\lambda + \mathscr{C}\sin\lambda + \mathscr{D}\cos^2\lambda + \mathscr{E}\cos\lambda\sin\lambda + \mathscr{F}\sin^2\lambda && (4.51) \\ &\quad + \mathscr{G}\cos^3\lambda + \mathscr{H}\cos^2\lambda\sin\lambda + \mathscr{I}\cos\lambda\sin^2\lambda + \mathscr{J}\sin^3\lambda && (4.52) \\ &= \mathscr{A}\left(\cos^2\lambda + \sin^2\lambda\right) + \mathscr{B}\cos\lambda + \mathscr{C}\sin\lambda + \mathscr{D}\cos^2\lambda + \mathscr{E}\cos\lambda\sin\lambda + \mathscr{F}\sin^2\lambda && (4.53) \\ &\quad + \mathscr{G}\cos^3\lambda + \mathscr{H}\left(1 - \sin^2\lambda\right)\sin\lambda + \mathscr{I}\cos\lambda\left(1 - \cos^2\lambda\right) + \mathscr{J}\sin^3\lambda && (4.54) \\ &= (\mathscr{B} + \mathscr{I})\cos\lambda + (\mathscr{C} + \mathscr{H})\sin\lambda + (\mathscr{A} + \mathscr{D})\cos^2\lambda + \mathscr{E}\cos\lambda\sin\lambda + (\mathscr{A} + \mathscr{F})\sin^2\lambda && (4.55) \\ &\quad + (\mathscr{G} - \mathscr{I})\cos^3\lambda + (\mathscr{J} - \mathscr{H})\sin^3\lambda. && (4.56)\end{aligned}$$

And this explains why we obtain this form in the result of $\overline{P}_3^H(\lambda)$, because we did choose to use this form right at the beginning to reduce the computation work.

4.2.10 Playing with *CBCC13*

The feeling about *CBCC13* at the end of section 4.2.8 keeps motivating us to seek for other DCCs in different particular geometry contexts, which are special cases of *CBCC13* geometry. The work is to use the definitions (4.34b), (4.35) and to apply *CBCC13* (4.36) in each geometry context to see if there exists some interesting DCCs. It sounds quite ambiguous, so let's dive directly into some precise cases. Sections 4.2.10.1, 4.2.10.2 and 4.2.10.3 respectively shows the DCCs extracted from *CBCC13* in the geometry contexts with elliptic, linear, parabolic source trajectories and horizontal detector.

4.2.10.1 Elliptic source trajectory

In this geometry, the source is assumed to move along an ellipse $(x_1/R_1)^2 + (x_2/R_2)^2 = 1$ on the trajectory plane $x_3 = 0$, which can be parameterized as $\tilde{\mathbf{s}}_\lambda = (R_1 \cos\lambda, R_2 \sin\lambda, 0)$ with $R_1, R_2 > 0$ and $\lambda \in [0, 2\pi)$. The horizontal detector is still at distance T from the trajectory plane, but now the two standard axes u and w on the detector respectively have the same directions as:

$$\tilde{\beta}_\lambda = \frac{1}{\delta(\lambda)} (-R_2 \sin\lambda, R_1 \cos\lambda, 0) \quad \text{and} \quad \tilde{\alpha}_\lambda = \frac{1}{\delta(\lambda)} (R_1 \cos\lambda, R_2 \sin\lambda, 0), \tag{4.57}$$

where $\delta(\lambda) = \sqrt{R_1^2 \cos^2\lambda + R_2^2 \sin^2\lambda}$. We define the weighted cone-beam projection of function f on the horizontal detector with the source moving along an ellipse as the following:

$$\begin{aligned}
&p_\lambda^{H,\text{ ellipse}}(u, w) \\
&= \int_0^\infty f\left(\tilde{\mathbf{s}}_\lambda + t\left(u\tilde{\beta}_\lambda + w\tilde{\alpha}_\lambda + T\vec{e}_3 - \tilde{\mathbf{s}}_\lambda\right)\right) dt &\text{(4.58a)}\\
&= \int_0^\infty f\left(\tilde{\mathbf{s}}_\lambda + t\left(\left(\frac{-R_2 u \sin\lambda + R_1 w \cos\lambda}{\delta(\lambda)}, \frac{R_1 u \cos\lambda + R_2 w \sin\lambda}{\delta(\lambda)}, T\right) - (R_1 \cos\lambda, R_2 \sin\lambda, 0)\right)\right) dt. &\text{(4.58b)}
\end{aligned}$$

Comparing this to the definition (4.34b) of the general projection on the horizontal detector in *CBCC13* geometry, we can see that:

$$p_\lambda^{H,\text{ ellipse}}(u, w) = g^H\left(R_1 \cos\lambda, R_2 \sin\lambda, \frac{-R_2 u \sin\lambda + R_1 w \cos\lambda}{\delta(\lambda)}, \frac{R_1 u \cos\lambda + R_2 w \sin\lambda}{\delta(\lambda)}\right). \tag{4.59}$$

So if we define the moment in the form $M_n^{H,\text{ ellipse}}(\lambda) = \iint p_\lambda^{H,\text{ ellipse}}(u, w)\, u^n du dw$, then by the definition (4.35):

$$\begin{aligned}
M_n^{H,\text{ ellipse}}(\lambda) &= \iint g^H\left(R_1 \cos\lambda, R_2 \sin\lambda, \frac{-R_2 u \sin\lambda + R_1 w \cos\lambda}{\delta(\lambda)}, \frac{R_1 u \cos\lambda + R_2 w \sin\lambda}{\delta(\lambda)}\right) u^n du dw &\text{(4.60a)}\\
&= \iint g^H(R_1 \cos\lambda, R_2 \sin\lambda, x_1, x_2) \left(\frac{-R_2 x_1 \sin\lambda + R_1 x_2 \cos\lambda}{\delta(\lambda)}\right)^n dx_1 dx_2 &\text{(4.60b)}\\
&= \iint g^H(R_1 \cos\lambda, R_2 \sin\lambda, x_1, x_2) \left(x_1\left(\frac{-R_2 \sin\lambda}{\delta(\lambda)}\right) + x_2\left(\frac{R_1 \cos\lambda}{\delta(\lambda)}\right)\right)^n dx_1 dx_2 &\text{(4.60c)}\\
&= J_n^H\left(R_1 \cos\lambda, R_2 \sin\lambda, \frac{-R_2 \sin\lambda}{\delta(\lambda)}, \frac{R_1 \cos\lambda}{\delta(\lambda)}\right). &\text{(4.60d)}
\end{aligned}$$

Here we have changed the variables:

$$x_1 = \frac{-R_2 u \sin\lambda + R_1 w \cos\lambda}{\delta(\lambda)}, \quad x_2 = \frac{R_1 u \cos\lambda + R_2 w \sin\lambda}{\delta(\lambda)}, \tag{4.61}$$

then conversely:

$$u = \frac{-R_2 x_1 \sin\lambda + R_1 x_2 \cos\lambda}{\delta(\lambda)}, \quad w = \frac{R_1 x_1 \cos\lambda + R_2 x_2 \sin\lambda}{\delta(\lambda)}, \tag{4.62}$$

and $dudw = dx_1dx_2$. Next, using *CBCC13* (4.36) and the same technique as section 4.2.8, we obtain:

$$\begin{aligned}
M_n^{H,\text{ ellipse}}(\lambda) &= J_n^H\left(R_1\cos\lambda, R_2\sin\lambda, \frac{-R_2\sin\lambda}{\delta(\lambda)}, \frac{R_1\cos\lambda}{\delta(\lambda)}\right) && \text{(4.63a)}\\
&= K_n^H\left(\frac{-R_2\sin\lambda}{\delta(\lambda)}, \frac{R_1\cos\lambda}{\delta(\lambda)}, -R_1\cos\lambda\left(\frac{-R_2\sin\lambda}{\delta(\lambda)}\right) - R_2\sin\lambda\left(\frac{R_1\cos\lambda}{\delta(\lambda)}\right)\right) && \text{(4.63b)}\\
&= K_n^H\left(\frac{-R_2\sin\lambda}{\delta(\lambda)}, \frac{R_1\cos\lambda}{\delta(\lambda)}, 0\right) && \text{(4.63c)}\\
&= \sum_{i+j+k=n} C_{i,j,k}^H\left(\frac{-R_2\sin\lambda}{\delta(\lambda)}\right)^i\left(\frac{R_1\cos\lambda}{\delta(\lambda)}\right)^j 0^k && \text{(4.63d)}\\
&= \sum_{\substack{k=0\\ i+j=n}} C_{i,j,0}^H\left(\frac{-R_2\sin\lambda}{\delta(\lambda)}\right)^i\left(\frac{R_1\cos\lambda}{\delta(\lambda)}\right)^j && \text{(4.63e)}\\
&= \frac{1}{\delta^n(\lambda)}\sum_{i+j=n} C_{i,j,0}^H R_2^i R_1^j\left(-\sin\lambda\right)^i\left(\cos\lambda\right)^j. && \text{(4.63f)}
\end{aligned}$$

This means if we define the adjusted moment

$$\widetilde{M}_n^H(\lambda) = \delta^n(\lambda)\, M_n^{H,\text{ ellipse}}(\lambda) = \sqrt{R_1^2\cos^2\lambda + R_2^2\sin^2\lambda}^{\,n}\, M_n^{H,\text{ ellipse}}(\lambda), \tag{4.64}$$

then $\widetilde{M}_n^H(\lambda)$ is a homogeneous polynomial in $\cos\lambda$ and $\sin\lambda$ of degree n. Now the DCC in this geometry can be stated as:

If $p_\lambda^{H,\text{ ellipse}}(u,w)$ is the weighted cone-beam projection of some real-valued function f (whose support is compact) on the horizontal detector with the source moving along an ellipse $(x_1/R_1)^2 + (x_2/R_2)^2 = 1$ on the plane $x_3 = 0$, for all $\lambda \in [0, 2\pi)$, then the adjusted moment:

$$\widetilde{M}_n^H(\lambda) = \sqrt{R_1^2\cos^2\lambda + R_2^2\sin^2\lambda}^{\,n} \iint p_\lambda^{H,\text{ ellipse}}(u,w)\, u^n\, dudw, \tag{4.65}$$

is a homogeneous polynomial in $\cos\lambda$ and $\sin\lambda$ of degree n for all non-negative integer n.

Numerical simulations The information of the object and the horizontal detector is the same as section 4.2.6, but now the source is moving along the ellipse: $(x_1/2)^2 + x_2^2 = 1$ on the trajectory plane $x_3 = 0$. Figure 4.7 shows us the raw moments $M_n^{H,\text{ ellipse}}(\lambda)$ and figure 4.8 shows us the adjusted moment $\widetilde{M}_n^H(\lambda)$. The nearest homogeneous polynomial fitting the data of the adjusted moments $\widetilde{M}_n^H(\lambda)$ are:

$$\begin{aligned}
Q_0^{H,\text{ ellipse}}(\lambda) &= 269.769253, && \text{(4.66a)}\\
Q_1^{H,\text{ ellipse}}(\lambda) &= 0.096025\cos\lambda - 54.687581\sin\lambda, && \text{(4.66b)}\\
Q_2^{H,\text{ ellipse}}(\lambda) &= 673.400521\cos^2\lambda + 0.034210\cos\lambda\sin\lambda + 113.233219\sin^2\lambda, && \text{(4.66c)}\\
Q_3^{H,\text{ ellipse}}(\lambda) &= 0.185858\cos^3\lambda - 421.744008\cos^2\lambda\sin\lambda + 0.100347\cos\lambda\sin^2\lambda - 66.215520\sin^3\lambda. && \text{(4.66d)}
\end{aligned}$$

4.2.10.2 Linear source trajectory

Now we assume that the source is moving along a line $x_2 = E_1x_1 + E_0$ on the trajectory plane $x_3 = 0$. The x-ray source location is parameterized as $\tilde{\mathbf{s}}_\lambda = (\lambda, E_1\lambda + E_0, 0)$. In this geometry, we fix the detector, meaning it is not allowed to rotate, or the two standard axes of the horizontal detector are x_1 and x_2. This also means we are staying exactly in the world of *CBCC13* geometry. The weighted cone-beam projection of function f on the horizontal detector is now defined as:

$$p_\lambda^{H,\text{ line}}(x_1,x_2) = g^H(\lambda, E_1\lambda + E_0, x_1, x_2) = \int_0^\infty f\left(\tilde{\mathbf{s}}_\lambda + t\left((x_1,x_2,T) - (\lambda, E_1\lambda + E_0, 0)\right)\right)dt. \tag{4.67}$$

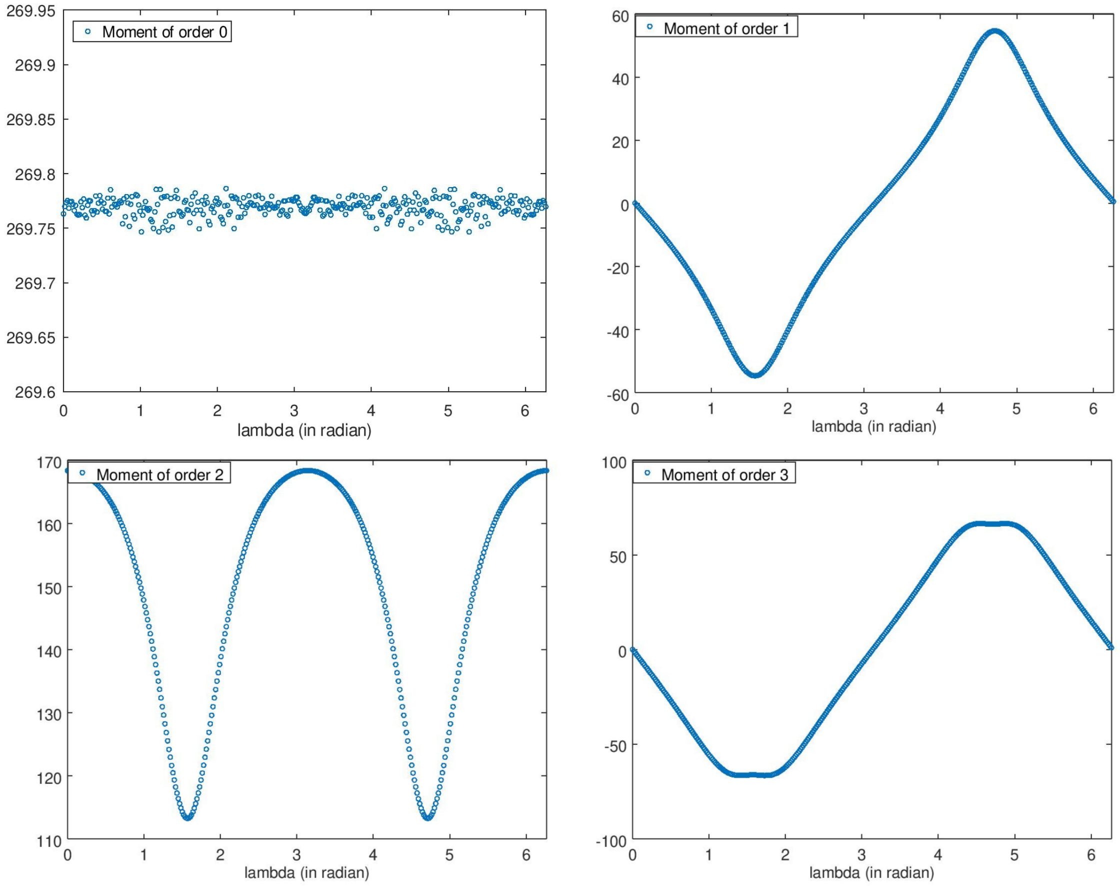

Figure 4.7: Raw moments $M_n^{H,\text{ ellipse}}(\lambda)$ of orders 0 (top-left), 1 (top-right), 2 (bottom-left), 3 (bottom-right) of the weighted cone-beam projections on the horizontal detector, where the source is moving along an ellipse $(x_1/2)^2 + x_2^2 = 1$ on the trajectory plane $x_3 = 0$.

Then by the definition (4.35), we can define the moment as:

$$
\begin{aligned}
M_{n,A,B}^{H,\text{ line}}(\lambda) &= J_n^H(\lambda, E_1\lambda + E_0, A, B) && (4.68a)\\
&= \iint g^H(\lambda, E_1\lambda + E_0, x_1, x_2)(Ax_1 + Bx_2)^n \, dx_1 dx_2 && (4.68b)\\
&= \iint p_\lambda^{H,\text{ line}}(x_1, x_2)(Ax_1 + Bx_2)^n \, dx_1 dx_2, && (4.68c)
\end{aligned}
$$

where A and B are two arbitrary real numbers. Using *CBCC13* (4.36), we can see that:

$$
\begin{aligned}
M_{n,A,B}^{H,\text{ line}}(\lambda) &= J_n^H(\lambda, E_1\lambda + E_0, A, B) && (4.69a)\\
&= K_n^H(A, B, -A\lambda - B(E_1\lambda + E_0)) && (4.69b)\\
&= K_n^H(A, B, -(A + BE_1)\lambda - BE_0) && (4.69c)\\
&= \sum_{i+j+k=n} C_{i,j,k}^H A^i B^j (-1)^k \left[(A + BE_1)\lambda + BE_0\right]^k, && (4.69d)
\end{aligned}
$$

which is a polynomial in λ of degree n, if $A + BE_1 \neq 0$. Thus we obtain a DCC in this case:

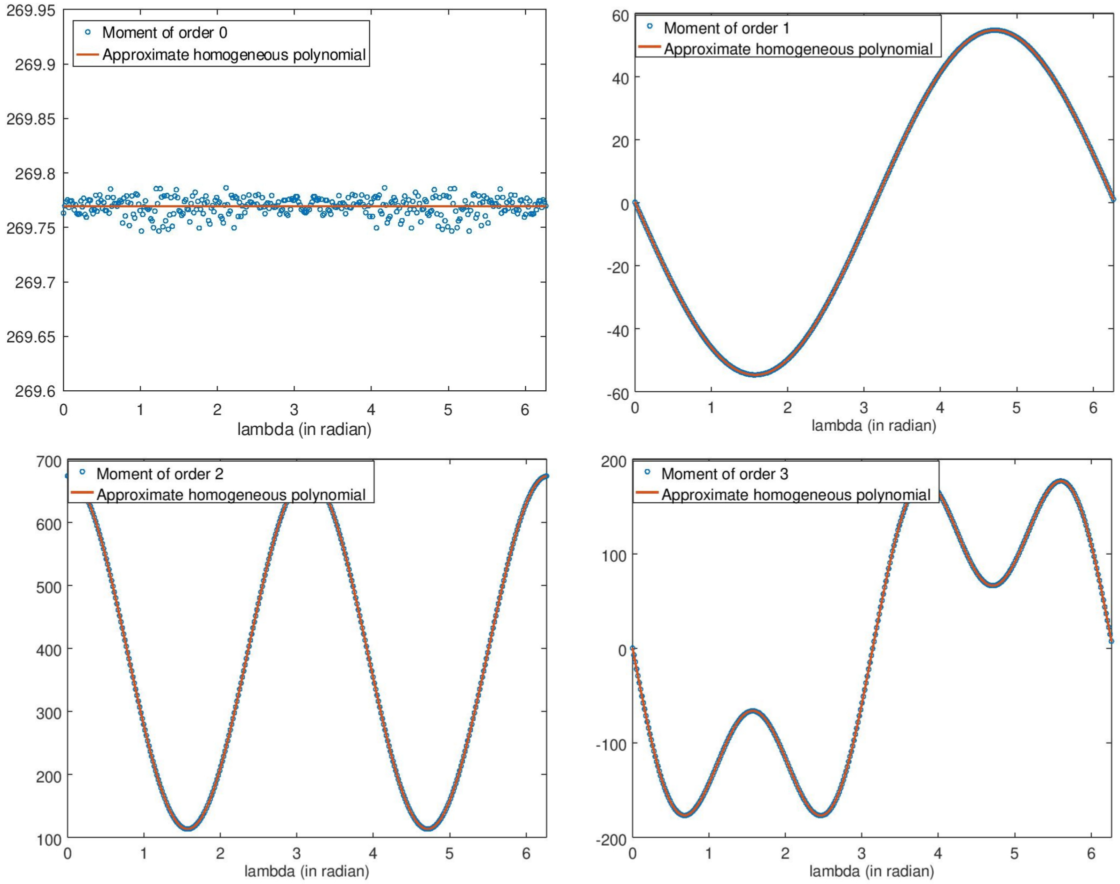

Figure 4.8: Adjusted moments $\widetilde{M}_n^H(\lambda)$ (computed by formula (4.65)) of orders 0 (top-left), 1 (top-right), 2 (bottom-left), 3 (bottom-right) of the weighted cone-beam projections on the horizontal detector, where the source is moving along an ellipse $(x_1/2)^2 + x_2^2 = 1$ on the trajectory plane $x_3 = 0$.

If $p_\lambda^{H,\text{ line}}(x_1, x_2)$ is the weighted cone-beam projection of some real-valued function f (whose support is compact) on the horizontal detector with the source moving along a line $x_2 = E_1 x_1 + E_0$ on the trajectory plane $x_3 = 0$, for all $\lambda \in \mathbb{R}$, then the moment:

$$M_{n,A,B}^{H,\text{ line}}(\lambda) = \iint p_\lambda^{H,\text{ line}}(x_1, x_2)\,(Ax_1 + Bx_2)^n\, dx_1 dx_2, \quad \text{with} \quad A + BE_1 \neq 0, \tag{4.70}$$

is a polynomial in λ of degree n for all non-negative integer n.

Numerical simulations Now the source is moving along the line $x_2 = (3/2)\,x_1 + 3$ on the trajectory plane $x_3 = 0$; the object and the horizontal detector remains the same as section 4.2.6. We obtain the following results of the moments $M_{n,A,B}^{H,\text{ line}}(\lambda)$ with $n = 0, 1, 2, 3$, $A = 1$ and $B = 3/5$, see figure 4.9. The nearest polynomials in λ fitting the moment data are shown below:

$$Q_0^{H,\text{ line}}(\lambda) = 269.7682, \tag{4.71a}$$

$$Q_1^{H,\text{ line}}(\lambda) = -526.0980\lambda - 443.6710, \tag{4.71b}$$

$$Q_2^{H,\text{ line}}(\lambda) = 1239.0359\lambda^2 + 2111.8163\lambda + 1062.4493, \tag{4.71c}$$

$$Q_3^{H,\text{ line}}(\lambda) = -3322.2266\lambda^3 - 8539.1657\lambda^2 - 8325.6712\lambda - 2944.3829. \tag{4.71d}$$

Comment Instead of a general line on the trajectory plane, if we consider the source moving along x_1-axis, meaning its location is parameterized as $\tilde{\mathbf{s}}_\lambda = (\lambda, 0, 0)$, or $E_1 = E_0 = 0$, then the definition of the weighted projection can be rewritten as:

$$p_{\lambda}^{H,x_1-\text{axis}}(x_1,x_2)=g^H(\lambda,0,x_1,x_2)=\int_0^{\infty} f\left(\tilde{\mathbf{s}}_{\lambda}+t\left((x_1,x_2,T)-(\lambda,0,0)\right)\right)dt. \tag{4.72}$$

And the above DCC will become:

If $p_{\lambda}^{H,x_1-axis}(x_1,x_2)$ is the weighted cone-beam projection of some real-valued function f (whose support is compact) on the horizontal detector with the source moving along x_1-axis, for all $\lambda\in\mathbb{R}$, then the moment:

$$M_{n,A,B}^{H,x_1-axis}(\lambda)=\iint p_{\lambda}^{H,x_1-axis}(x_1,x_2)\left(Ax_1+Bx_2\right)^n dx_1dx_2, \quad \textit{with} \quad A\neq 0, \tag{4.73}$$

is a polynomial in λ of degree n for all non-negative integer n.

In fact, when the source moves along x_1-axis, our considering geometry is similar to the geometry described in chapter 3. If we rename (x_1,x_2,x_3) in the considering geometry by (x_1,x_3,x_2), then the two geometry contexts exactly coincide. In chapter 3, we have dealt with the 3D cone-beam calibration problem with the source moving along x_1-axis, by considering it as a series of many 2D fan-beam calibration problems, then solving each 2D problem and choosing the common solution to obtain the true solution of the 3D problem. We are not discussing again the details of the 3D cone-beam calibration problem, but just to recall, the main tool we used to solve each 2D problem is the moment condition, where the moment had this formula: $\int p_{x_1}(u)\,u^n du$. We just rewrite the same notation as chapter 3. But now in *CBCC13* geometry context, x_1 is in fact λ, because its role is the source-location variable; and u is in fact x_1, because it is the horizontal axis on the detector. Changing the notation, the moment condition

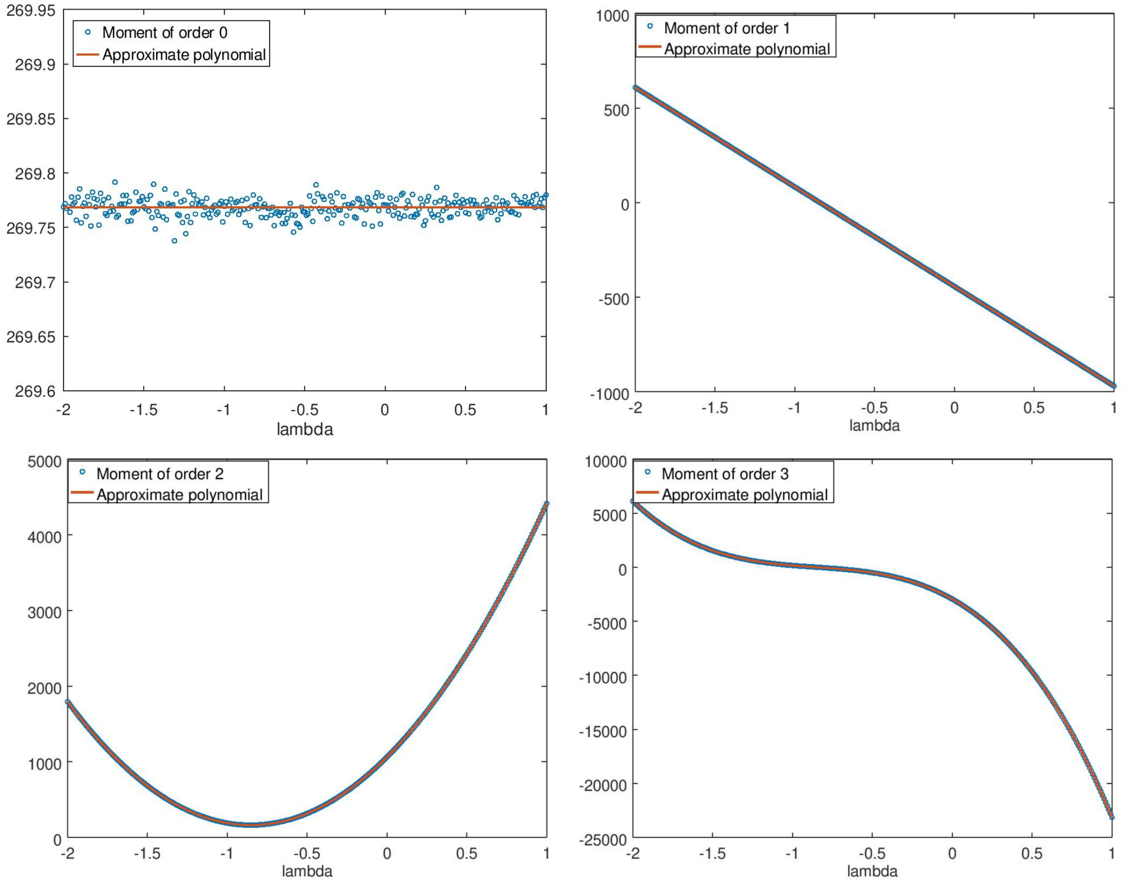

Figure 4.9: Moments $M_{n,A,B}^{H,\text{ line}}(\lambda)$ (with $A=1$, $B=3/5$) of orders 0 (top-left), 1 (top-right), 2 (bottom-left), 3 (bottom-right) of the weighted cone-beam projections on the horizontal detector, where the source is moving along the line $x_2=(3/2)\,x_1+3$ on the trajectory plane $x_3=0$.

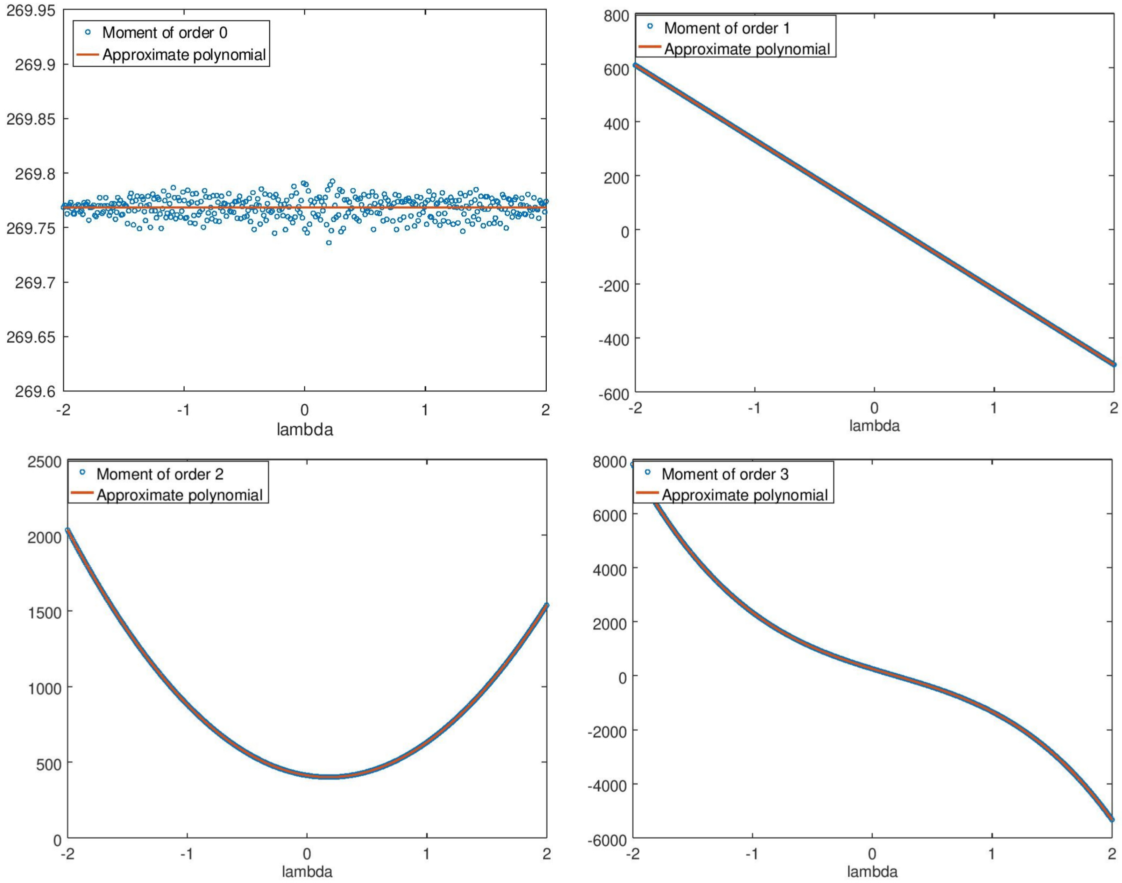

Figure 4.10: Moments $M_{n,A,B}^{H,x_1-\text{axis}}(\lambda)$ (with $A=1$, $B=4/3$) of orders 0 (top-left), 1 (top-right), 2 (bottom-left), 3 (bottom-right) of the weighted cone-beam projections on the horizontal detector, where the source is moving along x_1-axis.

in chapter 3 confirmed that $\int p_\lambda(x_1)\, x_1^n dx_1$ is a homogeneous polynomial in λ of degree n, which help solve the 2D fan-beam calibration problem. Then we can see that the above DCC is a more general version of this moment condition. Precisely, if we consider $M_{n,A,B}^{H,x_1-\text{axis}}(\lambda)$ with $A=1$ and $B=0$, then the above DCC is the 3D version of the moment condition in chapter 3, which can deal directly with the 3D cone-beam projection, while the moment condition in chapter 3 works with the slice of the cone-beam projection.
We can see a small simulation in the case where the source is moving along x_1-axis. Figure 4.10 shows us the moments $M_{n,A,B}^{H,x_1-\text{axis}}(\lambda)$ with $A=1$ and $B=4/3$, since A and B can be chosen arbitrarily under the only constraint that $A \neq 0$. The nearest polynomials in λ fitting the data of the moments are:

$$Q_0^{H,\text{ axis}}(\lambda) = 269.7682, \tag{4.74a}$$
$$Q_1^{H,\text{ axis}}(\lambda) = -276.8502\lambda + 54.7416, \tag{4.74b}$$
$$Q_2^{H,\text{ axis}}(\lambda) = 343.2204\lambda^2 - 124.1715\lambda + 412.5029, \tag{4.74c}$$
$$Q_3^{H,\text{ axis}}(\lambda) = -483.8850\lambda^3 + 248.3903\lambda^2 - 1351.2619\lambda + 253.7662. \tag{4.74d}$$

4.2.10.3 Parabolic source trajectory

This case is quite similar to the case of linear source trajectory. Let's say we have the same object and the same fixed (not rotated) horizontal detector, but now the source is moving along the parabola $x_2 = E_2 x_1^2 + E_1 x_1 + E_0$ on the trajectory plane $x_3 = 0$. The source location is parameterized as $\tilde{\mathbf{s}}_\lambda = \left(\lambda, E_2\lambda^2 + E_1\lambda + E_0, 0\right)$. Similar to the previous section, the weighted cone-beam projection of function f is defined as:

$$p_{\lambda}^{H,\text{ parabola}}(x_1,x_2)=g^H\left(\lambda,E_2\lambda^2+E_1\lambda+E_0,x_1,x_2\right)=\int_0^{\infty}f\left(\tilde{\mathbf{s}}_{\lambda}+t\left((x_1,x_2,T)-\left(\lambda,E_2\lambda^2+E_1\lambda+E_0,0\right)\right)\right)dt. \tag{4.75a}$$

By this definition, if we define the moment as:

$$M_n^{H,\text{ parabola}}(\lambda)=\iint p_{\lambda}^{H,\text{ parabola}}(x_1,x_2)\,x_1^n dx_1dx_2, \tag{4.76}$$

then applying the definition (4.35) and *CBCC13* (4.36), we can see that:

$$\begin{aligned}
&M_n^{H,\text{ parabola}}(\lambda) && =\iint g^H\left(\lambda,E_2\lambda^2+E_1\lambda+E_0,x_1,x_2\right)\left(x_1(1)+x_2(0)\right)^n dx_1dx_2 && (4.77a)\\
&=J_n^H\left(\lambda,E_2\lambda^2+E_1\lambda+E_0,1,0\right) && =K_n^H(1,0,-\lambda) && (4.77b)\\
&=\sum_{i+j+k=n}C_{i,j,k}^H 1^i 0^j(-\lambda)^k && =\sum_{\substack{j=0\\ i+k=n}}C_{i,j,k}^H 1^i 0^j(-\lambda)^k && (4.77c)\\
&=\sum_{i+k=n}C_{i,0,k}^H(-\lambda)^k, && && (4.77d)
\end{aligned}$$

which is a polynomial in λ of degree n (here we have used *CBCC13* (4.36) with $Y_1=1$ and $Y_2=0$). The DCC in this geometry can be stated as:

> *If $p_{\lambda}^{H,\text{ parabola}}(x_1,x_2)$ is the weighted cone-beam projection of some real-valued function f (whose support is compact) on the horizontal detector with the source moving along the parabola $x_2=E_2x_1^2+E_1x_1+E_0$ on the trajectory plane $x_3=0$, for all $\lambda\in\mathbb{R}$, then the moment:*
>
> $$M_n^{H,\text{ parabola}}(\lambda)=\iint p_{\lambda}^{H,\text{ parabola}}(x_1,x_2)\,x_1^n dx_1dx_2, \tag{4.78}$$
>
> *is a polynomial in λ of degree n for all non-negative integer n.*

Numerical simulations In this simulation, the source is moving along the parabola: $x_2=2x_1^2-3$ on the trajectory plane $x_3=0$, other information of the object and the horizontal detector remains the same. Figure 4.11 shows us the moments $M_n^{H,\text{ parabola}}(\lambda)$ of orders 0, 1, 2, 3. The nearest polynomials in λ fitting the moments are:

$$Q_0^{H,\text{ parabol}}(\lambda)=269.7677, \tag{4.79a}$$
$$Q_1^{H,\text{ parabol}}(\lambda)=-276.8787\lambda+54.6910, \tag{4.79b}$$
$$Q_2^{H,\text{ parabol}}(\lambda)=343.1776\lambda^2-124.0396\lambda+113.2253, \tag{4.79c}$$
$$Q_3^{H,\text{ parabol}}(\lambda)=-483.9194\lambda^3+248.1499\lambda^2-374.6056\lambda+66.2218. \tag{4.79d}$$

Comment After this case, we can see that: using *CBCC13* with $Y_1=1$ and $Y_2=0$ can handle more than just the parabolic source trajectory case. Let's say the source is moving along a general trajectory, which can be written as $x_2=\tau(x_1)$ on the plane $x_3=0$, where $\tau(t)$ is a single-variable real function. This means the source location is parameterized as $\tilde{\mathbf{s}}_{\lambda}=(\lambda,\tau(\lambda),0)$. If we work with the fixed horizontal detector (*CBCC13* geometry), the weighted cone-beam projection is defined as:

$$p_{\lambda}^{H,\tau}(x_1,x_2)=g^H(\lambda,\tau(\lambda),x_1,x_2); \tag{4.80}$$

then we will define the moment as:

$$M_n^{H,\tau}(\lambda)=\iint p_{\lambda}^{H,\tau}(x_1,x_2)\,x_1^n dx_1dx_2. \tag{4.81}$$

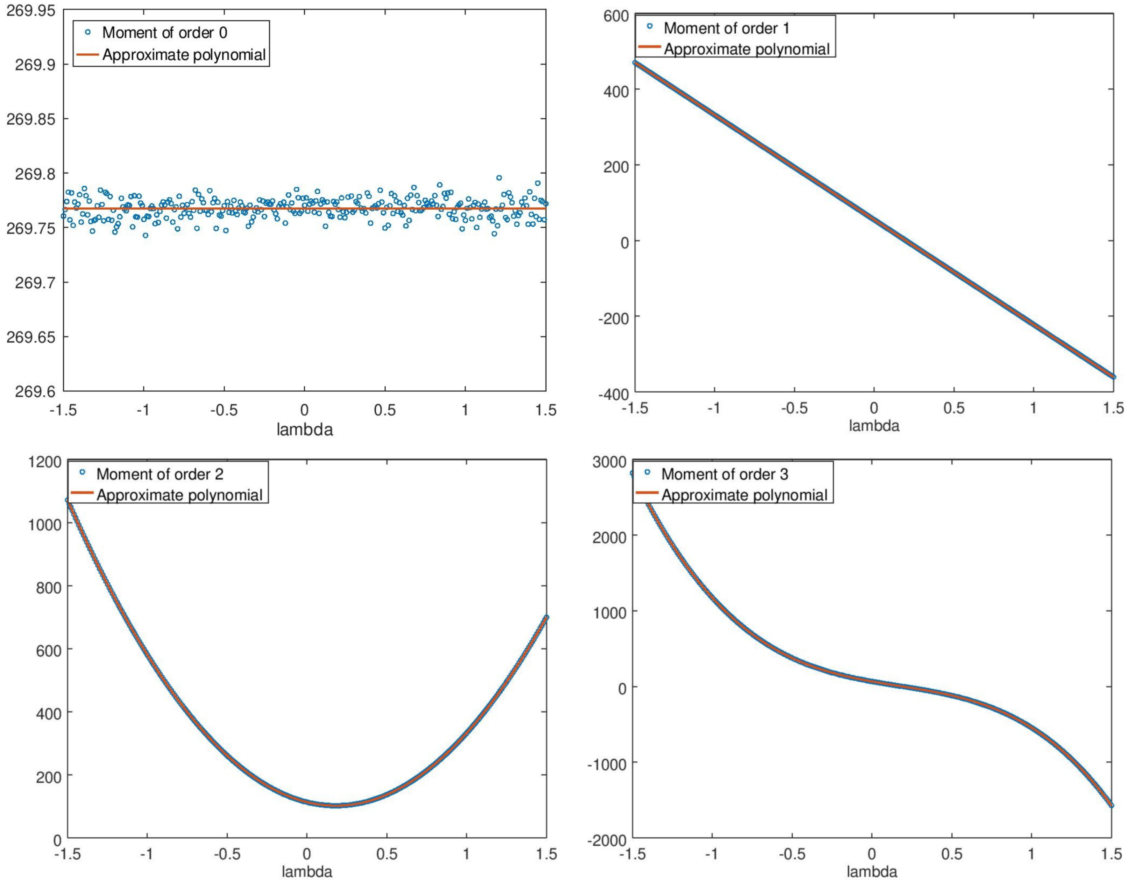

Figure 4.11: Moments $M_n^{H,\text{ parabola}}(\lambda)$ of orders 0 (top-left), 1 (top-right), 2 (bottom-left), 3 (bottom-right) of the weighted cone-beam projections on the horizontal detector, where the source is moving along a parabol $x_2 = 2x_1^2 - 3$ on the trajectory plane $x_3 = 0$.

Similar to the previous case, by the definition (4.35) and *CBCC13* (4.36), this moment can definitely be rewritten:

$$\begin{aligned} M_n^{H,\tau}(\lambda) &= \iint g^H(\lambda, \tau(\lambda), x_1, x_2)\,(x_1(1) + x_2(0))^n\, dx_1 dx_2 && (4.82a)\\ &= J_n^H(\lambda, \tau(\lambda), 1, 0) && (4.82b)\\ &= K_n^H(1, 0, -\lambda) && (4.82c)\\ &= \sum_{i+k=n} C_{i,0,k}^H (-\lambda)^k, && (4.82d) \end{aligned}$$

which is a polynomial in λ of degree n.
So in conclusion, in *CBCC13* geometry, we allow the source to move on a very general trajectory, as long as it is on the plane $x_3 = 0$. If the source trajectory can be represented by $x_2 = \tau(x_1)$, where $\tau(t)$ is an arbitrary single-varible real function, with the weighted projection on the fixed horizontal detector $p_\lambda^{H,\tau}(x_1, x_2) = g^H(\lambda, \tau(\lambda), x_1, x_2)$, we define the moment as $M_n^{H,\tau}(\lambda) = \iint p_\lambda^{H,\tau}(x_1, x_2)\, x_1^n dx_1 dx_2$, then there always exists the DCC:

If $p_\lambda^{H,\tau}(x_1, x_2)$ is the weighted cone-beam projection of some real-valued function f (whose support is compact) on a fixed horizontal detector with the source moving along the curve $x_2 = \tau(x_1)$ on the plane $x_3 = 0$, for all $\lambda \in \mathbb{R}$, then the moment $M_n^{H,\tau}(\lambda)$ is a polynomial in λ of degree n for all non-negative integer n.

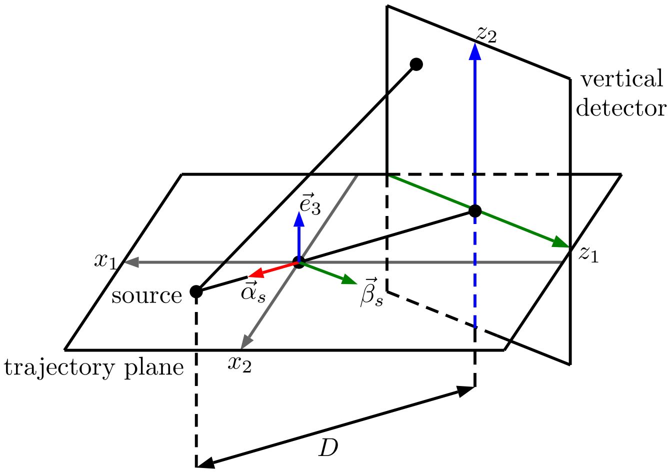

Figure 4.12: *CBCC13Converted* geometry

4.3 *CBCC13Converted*

CBCC13, as shown in the previous sections, is a general CBCC, which can generate many DCCs in many special geometry contexts, by choosing a suitable pair of values of Y_1 and Y_2. In this section, we are going to convert *CBCC13* to obtain its form in the geometry containing the vertical detector. The idea is to obtain a general cone-beam CBCC of the weighted projections in this geometry. A general CBCC can help in geometric calibration, in the sense of obtaining the analytic solutions of the geometric parameters. Sections 4.3.1, 4.3.2 and 4.3.3 show us the whole way to build *CBCC13Converted* from *CBCC13*. Because of being built from *CBCC13*, *CBCC13Converted* is also a full CBCC (necessary and sufficient conditions). Section 4.3.4 gives a direct proof of the necessary condition of *CBCC13Converted* without using the knowledge of *CBCC13*. In section 4.3.5, *CBCC13Converted* is applied in two special geometry contexts with the circular and elliptic source trajectories. Section 4.3.6 concerns the conventional cone-beam projections and the CBCC of these conventional projections constructed from *CBCC13Converted*. In section 4.3.7, we discuss about the suitable position of the object in both cases of geometry contexts with the horizontal and vertical detectors. Section 4.3.8 shows us a way to develop *CBCC13Converted* to a real generalization of *CBCC16*. And the last section 4.3.9 gives a preliminary result in automatic calibration in *CBCC16* geometry context, dealing with the vertical detector and the circular source trajectory, using *CBCC13Converted*.

4.3.1 *CBCC13Converted* geometric context and the weighted cone-beam projection on the vertical detector

CBCC13Converted geometry context is in fact a generalized version of *CBCC16* geometry. In this geometry, the source is assumed to move on the trajectory plane $x_3 = 0$, but no specific trajectory is required. The vertical detector is at distance D away from the source. We assume that D is sufficiently big, such that the source and the vertical detector are always on different sides comparing to the world origin. Moreover, the source location, the world origin and the origin of the detector are also always collinear. The source is now denoted as: $\vec{s} = (s_1, s_2, 0)$. We define:

$$\vec{\alpha}_s = \frac{1}{\|\vec{s}\|}(s_1, s_2, 0), \quad \vec{\beta}_s = \frac{1}{\|\vec{s}\|}(-s_2, s_1, 0) \quad \vec{e}_3 = (0, 0, 1), \tag{4.83}$$

where $\vec{\alpha}_s$ is the unit vector pointing towards the source location and $\vec{\beta}_s$ is obtained by rotating $\vec{\alpha}_s$ 90 degree counter-clockwise. The two standard axes on the vertical detector are z_1 and z_2 axes having the same directions as the unit vectors $\vec{\beta}_s$ and $\vec{e}_3$. For now we continue to assume that the 3D object is strictly above the trajectory plane $x_3 = 0$. Figure 4.12 shows us the geometry. Let $\mathcal{G}^{\mathcal{V}}$ be the projection operator applying on the object f to produce the weighted cone-beam projection on a vertical detector, which is at distance D away from the source position: $g^V = \mathcal{G}^{\mathcal{V}} f$, where the x-ray source is moving on the plane $(x_3 = 0)$ without any specific trajectory, then the projection data is:

$$g^V(s_1, s_2, z_1, z_2) = \mathcal{G}^{\mathcal{V}} f(s_1, s_2, z_1, z_2) = \int_0^{\infty} f\left(\vec{s} + t\left(z_1\vec{\beta}_s + z_2\vec{e}_3 - D\vec{\alpha}_s\right)\right) dt. \tag{4.84}$$

4.3.2 Relationship between the weighted cone-beam projections on the horizontal and vertical detectors (*CBCC13* and *CBCC13Converted* geometry contexts)

The idea is very similar to section 4.2.3. We consider the line connecting the x-ray source and the point (z_1, z_2) on the vertical detector. This line intersects the horizontal detector $x_3 = T$ at one point. Since these three points are collinear, the weighted cone-beam projections on the two detectors relate to each other, because they are both computed at the same direction from the source. Here, the line goes through the source $\vec{s} = (s_1, s_2, 0)$ and parallel to the following vector

$$z_1\vec{\beta}_s + z_2\vec{e}_3 - D\vec{\alpha}_s = z_1\frac{1}{\|\vec{s}\|}\begin{bmatrix}-s_2\\ s_1\\ 0\end{bmatrix} + z_2\begin{bmatrix}0\\0\\1\end{bmatrix} - D\frac{1}{\|\vec{s}\|}\begin{bmatrix}s_1\\ s_2\\ 0\end{bmatrix} = \frac{1}{\|\vec{s}\|}\begin{bmatrix}-z_1s_2 - Ds_1\\ z_1s_1 - Ds_2\\ z_2\|\vec{s}\|\end{bmatrix}, \tag{4.85}$$

so it has the following equation:

$$\frac{x_1 - s_1}{-z_1s_2 - Ds_1} = \frac{x_2 - s_2}{z_1s_1 - Ds_2} = \frac{x_3}{z_2\|\vec{s}\|}. \tag{4.86}$$

The intersection of the above line and the horizontal detector plane $x_3 = T$ is $(\widehat{x}_1, \widehat{x}_2, \widehat{x}_3)$ where:

$$\widehat{x}_1 = s_1 - \frac{T}{z_2\|\vec{s}\|}\left(z_1s_2 + Ds_1\right), \tag{4.87a}$$

$$\widehat{x}_2 = s_2 + \frac{T}{z_2\|\vec{s}\|}\left(z_1s_1 - Ds_2\right), \tag{4.87b}$$

$$\widehat{x}_3 = T. \tag{4.87c}$$

Since the two coordinate axes on the horizontal detector $x_3 = T$ (in *CBCC13* geometry) are in fact the same as the two axes x_1 and x_2 in the standard 3D coordinate system (x_1, x_2, x_3) (this is why we kept the same notations x_1 and x_2), then the intersection $(\widehat{x}_1, \widehat{x}_2, \widehat{x}_3)$ in 3D will be the point $(\overline{x}_1, \overline{x}_2)$ on the horizontal detector, where $\overline{x}_1 = \widehat{x}_1$ and $\overline{x}_2 = \widehat{x}_2$. In other words, (z_1, z_2) on the vertical detector, $(\overline{x}_1, \overline{x}_2)$ on the horizontal detector and the source location are collinear. Then there exists a relationship between $g^V(s_1, s_2, z_1, z_2)$ and $g^H(s_1, s_2, \overline{x}_1, \overline{x}_2)$. We seek out this relationship. By the definitions (4.34b) and (4.84), we can see that:

$$g^H(s_1, s_2, \overline{x}_1, \overline{x}_2)$$

$$= g^H\left(s_1, s_2, s_1 - \frac{T}{z_2\|\vec{s}\|}\left(z_1s_2 + Ds_1\right), s_2 + \frac{T}{z_2\|\vec{s}\|}\left(z_1s_1 - Ds_2\right)\right) \tag{4.88a}$$

$$= \int_0^\infty f\left(\vec{s} + t\left(-\frac{T}{z_2\|\vec{s}\|}\left(z_1s_2 + Ds_1\right), \frac{T}{z_2\|\vec{s}\|}\left(z_1s_1 - Ds_2\right), T\right)\right)dt \tag{4.88b}$$

$$= \int_0^\infty f\left(\vec{s} + t\frac{T}{z_2}\left(z_1\frac{-s_2}{\|\vec{s}\|} - D\frac{s_1}{\|\vec{s}\|}, z_1\frac{s_1}{\|\vec{s}\|} - D\frac{s_2}{\|\vec{s}\|}, z_2\right)\right)dt \tag{4.88c}$$

$$= \int_0^\infty f\left(\vec{s} + t\frac{T}{z_2}\left(z_1\frac{1}{\|\vec{s}\|}\begin{bmatrix}-s_2\\ s_1\\ 0\end{bmatrix} + z_2\begin{bmatrix}0\\0\\1\end{bmatrix} - D\frac{1}{\|\vec{s}\|}\begin{bmatrix}s_1\\ s_2\\ 0\end{bmatrix}\right)\right)dt \tag{4.88d}$$

$$= \int_0^\infty f\left(\vec{s} + t\frac{T}{z_2}\left(z_1\vec{\beta}_s + z_2\vec{e}_3 - D\vec{\alpha}_s\right)\right)dt \tag{4.88e}$$

$$= \int_0^\infty f\left(\vec{s} + t'\left(z_1\vec{\beta}_s + z_2\vec{e}_3 - D\vec{\alpha}_s\right)\right)dt'\frac{z_2}{T} \tag{4.88f}$$

$$= g^V(s_1, s_2, z_1, z_2)\frac{z_2}{T}. \tag{4.88g}$$

Here we have changed the variables $t' = t\dfrac{T}{z_2}$ then $dt' = \dfrac{T}{z_2}dt$. The relationship we obtain is:

$$g^H\left(s_1, s_2, s_1 - \frac{T}{z_2\|\vec{s}\|}\left(z_1s_2 + Ds_1\right), s_2 + \frac{T}{z_2\|\vec{s}\|}\left(z_1s_1 - Ds_2\right)\right) = \frac{z_2}{T}g^V(s_1, s_2, z_1, z_2). \tag{4.89}$$

Now conversely, if we change the variables:

$$x_1 = s_1 - \frac{T}{z_2 \|\vec{s}\|} \left(z_1 s_2 + D s_1 \right), \tag{4.90a}$$

$$x_2 = s_2 + \frac{T}{z_2 \|\vec{s}\|} \left(z_1 s_1 - D s_2 \right). \tag{4.90b}$$

These equations imply:

$$z_1 s_2 + D s_1 = -\frac{z_2 \|\vec{s}\|}{T} \left(x_1 - s_1 \right), \tag{4.91a}$$

$$z_1 s_1 - D s_2 = \frac{z_2 \|\vec{s}\|}{T} \left(x_2 - s_2 \right). \tag{4.91b}$$

Then by some simple calculations, we can compute (z_1, z_2) in terms of (x_1, x_2):

$$z_1 = \frac{D \left(-x_1 s_2 + x_2 s_1 \right)}{\|\vec{s}\|^2 - x_1 s_1 - x_2 s_2}, \tag{4.92a}$$

$$z_2 = \frac{D T \|\vec{s}\|}{\|\vec{s}\|^2 - x_1 s_1 - x_2 s_2}. \tag{4.92b}$$

Thus, the relationship (4.89) can also be rewritten as:

$$g^H \left(s_1, s_2, x_1, x_2 \right) = \frac{D \|\vec{s}\|}{\|\vec{s}\|^2 - x_1 s_1 - x_2 s_2} g^V \left(s_1, s_2, \frac{D \left(-x_1 s_2 + x_2 s_1 \right)}{\|\vec{s}\|^2 - x_1 s_1 - x_2 s_2}, \frac{D T \|\vec{s}\|}{\|\vec{s}\|^2 - x_1 s_1 - x_2 s_2} \right). \tag{4.93}$$

4.3.3 Moment of the weighted cone-beam projections on the vertical detector and *CBCC13Converted*

The moment of the weighted cone-beam projections on the horizontal detector in *CBCC13* geometry was defined as:

$$J_n^H \left(s_1, s_2, Y_1, Y_2 \right) = \iint g^H \left(s_1, s_2, x_1, x_2 \right) \left(x_1 Y_1 + x_2 Y_2 \right)^n dx_1 dx_2, \tag{4.94}$$

see (4.35). Using the relationship (4.93), we explore how the moment $J_n^H \left(s_1, s_2, Y_1, Y_2 \right)$ become in *CBCC13Converted* geometry with the vertical detector:

$$\begin{aligned} & J_n^H \left(s_1, s_2, Y_1, Y_2 \right) \\ & = \iint \frac{D \|\vec{s}\|}{\|\vec{s}\|^2 - x_1 s_1 - x_2 s_2} g^V \left(s_1, s_2, \frac{D \left(-x_1 s_2 + x_2 s_1 \right)}{\|\vec{s}\|^2 - x_1 s_1 - x_2 s_2}, \frac{D T \|\vec{s}\|}{\|\vec{s}\|^2 - x_1 s_1 - x_2 s_2} \right) \left(x_1 Y_1 + x_2 Y_2 \right)^n dx_1 dx_2. \end{aligned} \tag{4.95}$$

The next natural step is to change the variables:

$$z_1 = \frac{D \left(-x_1 s_2 + x_2 s_1 \right)}{\|\vec{s}\|^2 - x_1 s_1 - x_2 s_2}, \quad \text{and} \quad z_2 = \frac{D T \|\vec{s}\|}{\|\vec{s}\|^2 - x_1 s_1 - x_2 s_2}. \tag{4.96}$$

However, in the previous section, we have just obtained these results by changing the variables from (z_1, z_2) to (x_1, x_2) and computing (z_1, z_2) in terms of (x_1, x_2). So this change of variables from (x_1, x_2) to (z_1, z_2) is nothing but just the inverse direction comparing to what we have done in the previous section. Therefore, we already have the formulae of x_1 and x_2 in terms of z_1 and z_2 in equations (4.90a) and (4.90b). From this, we can compute the Jacobian matrix as follows:

$$J = \begin{bmatrix} \dfrac{\partial x_1}{\partial z_1} & \dfrac{\partial x_1}{\partial z_2} \\ \dfrac{\partial x_2}{\partial z_1} & \dfrac{\partial x_2}{\partial z_2} \end{bmatrix} = \begin{bmatrix} \dfrac{-T s_2}{z_2 \|\vec{s}\|} & \dfrac{T \left(z_1 s_2 + D s_1 \right)}{z_2^2 \|\vec{s}\|} \\ \dfrac{T s_1}{z_2 \|\vec{s}\|} & -\dfrac{T \left(z_1 s_1 - D s_2 \right)}{z_2^2 \|\vec{s}\|} \end{bmatrix}, \tag{4.97a}$$

$$\det J = \frac{T^2 \left(z_1 s_1 s_2 - D s_2^2 \right)}{z_2^3 \|\vec{s}\|^2} - \frac{T^2 \left(z_1 s_1 s_2 + D s_1^2 \right)}{z_2^3 \|\vec{s}\|^2} = \frac{-D T^2 \left(s_1^2 + s_2^2 \right)}{z_2^3 \|\vec{s}\|^2} = \frac{-D T^2 \|\vec{s}\|^2}{z_2^3 \|\vec{s}\|^2} = \frac{-D T^2}{z_2^3}. \tag{4.97b}$$

Thus we obtain: $dx_1 dx_2 = \frac{DT^2}{z_2^3} dz_1 dz_2$. Then the above integral becomes:

$$\begin{aligned}
&J_n^H(s_1, s_2, Y_1, Y_2) \\
&= \iint \frac{z_2}{T} g^V(s_1, s_2, z_1, z_2) \left[\left(s_1 - \frac{T}{z_2 \|\vec{s}\|}(z_1 s_2 + D s_1)\right) Y_1 + \left(s_2 + \frac{T}{z_2 \|\vec{s}\|}(z_1 s_1 - D s_2)\right) Y_2\right]^n \frac{DT^2}{z_2^3} dz_1 dz_2 && \text{(4.98a)} \\
&= DT \iint g^V(s_1, s_2, z_1, z_2) \left[\left(s_1 - \frac{T}{z_2 \|\vec{s}\|}(z_1 s_2 + D s_1)\right) Y_1 + \left(s_2 + \frac{T}{z_2 \|\vec{s}\|}(z_1 s_1 - D s_2)\right) Y_2\right]^n \frac{dz_1 dz_2}{z_2^2} && \text{(4.98b)} \\
&= DT \iint g^V(s_1, s_2, z_1, z_2) \left[(s_1 Y_1 + s_2 Y_2) + \left(-\frac{T}{z_2 \|\vec{s}\|}(z_1 s_2 + D s_1)\right) Y_1 + \left(\frac{T}{z_2 \|\vec{s}\|}(z_1 s_1 - D s_2)\right) Y_2\right]^n \frac{dz_1 dz_2}{z_2^2} && \text{(4.98c)} \\
&= DT \iint g^V(s_1, s_2, z_1, z_2) \left[(s_1 Y_1 + s_2 Y_2) + \left(\frac{Tz_1}{z_2} \frac{-s_2}{\|\vec{s}\|} - \frac{DT}{z_2} \frac{s_1}{\|\vec{s}\|}\right) Y_1 + \left(\frac{Tz_1}{z_2} \frac{s_1}{\|\vec{s}\|} - \frac{DT}{z_2} \frac{s_2}{\|\vec{s}\|}\right) Y_2\right]^n \frac{dz_1 dz_2}{z_2^2} && \text{(4.98d)} \\
&= DT \iint g^V(s_1, s_2, z_1, z_2) \left[(s_1 Y_1 + s_2 Y_2) + \left(\frac{Tz_1}{z_2} \vec{\beta}_s - \frac{DT}{z_2} \vec{\alpha}_s\right) \cdot (Y_1, Y_2, 0)\right]^n \frac{dz_1 dz_2}{z_2^2}. && \text{(4.98e)}
\end{aligned}$$

The last equality is obtained by substituting the definitions of $\vec{\alpha}_s$ and $\vec{\beta}_s$. We continue to use the binomial theorem:

$$\left[(s_1 Y_1 + s_2 Y_2) + \left(\frac{Tz_1}{z_2} \vec{\beta}_s - \frac{DT}{z_2} \vec{\alpha}_s\right) \cdot (Y_1, Y_2, 0)\right]^n = \sum_{l=0}^{n} \binom{n}{l} (s_1 Y_1 + s_2 Y_2)^{n-l} \left[\left(\frac{Tz_1}{z_2} \vec{\beta}_s - \frac{DT}{z_2} \vec{\alpha}_s\right) \cdot (Y_1, Y_2, 0)\right]^l. \tag{4.99}$$

Then the above integral becomes:

$$\begin{aligned}
&J_n^H(s_1, s_2, Y_1, Y_2) \\
&= DT \iint g^V(s_1, s_2, z_1, z_2) \left[\sum_{l=0}^{n} \binom{n}{l} (s_1 Y_1 + s_2 Y_2)^{n-l} \left[\left(\frac{Tz_1}{z_2} \vec{\beta}_s - \frac{DT}{z_2} \vec{\alpha}_s\right) \cdot (Y_1, Y_2, 0)\right]^l\right] \frac{dz_1 dz_2}{z_2^2} && \text{(4.100a)} \\
&= DT \sum_{l=0}^{n} \binom{n}{l} (s_1 Y_1 + s_2 Y_2)^{n-l} \iint g^V(s_1, s_2, z_1, z_2) \left[\left(\frac{Tz_1}{z_2} \vec{\beta}_s - \frac{DT}{z_2} \vec{\alpha}_s\right) \cdot (Y_1, Y_2, 0)\right]^l \frac{dz_1 dz_2}{z_2^2} && \text{(4.100b)} \\
&= DT \sum_{l=0}^{n} \binom{n}{l} (-1)^{n-l} (-s_1 Y_1 - s_2 Y_2)^{n-l} \iint g^V(s_1, s_2, z_1, z_2) \left[\frac{T}{z_2} \left(z_1 \vec{\beta}_s - D \vec{\alpha}_s\right) \cdot (Y_1, Y_2, 0)\right]^l \frac{dz_1 dz_2}{z_2^2} && \text{(4.100c)} \\
&= DT \sum_{l=0}^{n} \binom{n}{l} T^l (-1)^{n-l} (-s_1 Y_1 - s_2 Y_2)^{n-l} \iint g^V(s_1, s_2, z_1, z_2) \left[\left(z_1 \vec{\beta}_s - D \vec{\alpha}_s\right) \cdot (Y_1, Y_2, 0)\right]^l \frac{dz_1 dz_2}{z_2^{l+2}} && \text{(4.100d)} \\
&= DT \sum_{l=0}^{n} \binom{n}{l} T^l (-1)^{n-l} (-s_1 Y_1 - s_2 Y_2)^{n-l} I_l, && \text{(4.100e)}
\end{aligned}$$

where

$$I_l = \iint g^V(s_1, s_2, z_1, z_2) \left[\left(z_1 \vec{\beta}_s - D \vec{\alpha}_s\right) \cdot (Y_1, Y_2, 0)\right]^l \frac{dz_1 dz_2}{z_2^{l+2}}. \tag{4.101}$$

At this stage, we re-perform one special technique, which has been used in the paper [Clackdoyle and Desbat, 2013]. From the knowledge of *CBCC13*, we know that:

$$J_n^H(s_1, s_2, Y_1, Y_2) = K_n^H(Y_1, Y_2, -s_1 Y_1 - s_2 Y_2) = \sum_{i+j+k=n} C_{i,j,k}^H Y_1^i Y_2^j (-s_1 Y_1 - s_2 Y_2)^k. \tag{4.102}$$

$J_n^H(s_1, s_2, Y_1, Y_2)$ is a homogeneous polynomial in Y_1, Y_2 and $-s_1 Y_1 - s_2 Y_2$ of degree n, meaning each term of $J_n^H(s_1, s_2, Y_1, Y_2)$ has degree n in total. Now from (4.100e), for each value of l, there has already existed the term $(-s_1 Y_1 - s_2 Y_2)$ of degree $n - l$. Thus in order to make every term of $J_n^H(s_1, s_2, Y_1, Y_2)$ have degree n in total, the integral I_l must be a homogeneous polynomial in Y_1, Y_2 and $(-s_1Y_1 - s_2Y_2)$ of degree l, for every value of l. If we rename the double integral I_l, and define the moment of the weighted cone-beam projection on the vertical detector (with no specific source trajectory) as:

$$J_n^V(s_1, s_2, Y_1, Y_2) = \iint g^V(s_1, s_2, z_1, z_2)\left[\left(z_1\vec{\beta}_s - D\vec{\alpha}_s\right)\cdot(Y_1, Y_2, 0)\right]^n \frac{dz_1dz_2}{z_2^{n+2}}, \tag{4.103}$$

then the above statement confirm that:

$$J_n^V(s_1, s_2, Y_1, Y_2) = K_n^V(Y_1, Y_2, -s_1Y_1 - s_2Y_2), \tag{4.104}$$

where $K_n^V(Y_1, Y_2, Y_3) = \sum_{i+j+k=n} C_{i,j,k}^V Y_1^i Y_2^j Y_3^k$ is a three-variable homogeneous polynomial. Hence we finally obtain our *CBCC13Converted* as follows:

> *g^V is in the range of $\mathcal{G}^\mathcal{V}$: $g^V = \mathcal{G}^\mathcal{V} f$ for some f (which is a compactly supported real function, whose support is strictly above the plane $x_3 = 0$), if and only if for all $(s_1, s_2) \in \mathbb{R}^2$, $g^V(s_1, s_2, \cdot, \cdot)$ has compact support in $\mathbb{R}\times\mathbb{R}^+$ and:*
>
> $$J_n^V(s_1, s_2, Y_1, Y_2) = K_n^V(Y_1, Y_2, -s_1Y_1 - s_2Y_2), \quad \forall n = 0, 1, 2, \dots, \tag{4.105}$$
>
> *where $K_n^V(Y_1, Y_2, Y_3) = \sum_{i+j+k=n} C_{i,j,k}^V Y_1^i Y_2^j Y_3^k$ is a homogeneous polynomial in three variables Y_1, Y_2, Y_3 of degree n.*

Comments

CBCC13Converted is created from *CBCC13* or it is in fact the form of *CBCC13* in the geometry with the vertical detector, so it has some properties as *CBCC13*:

- *CBCC13Converted* is a full CBCC: both necessary and sufficient condition.
- *CBCC13Converted* is general: substituting suitable pair of values of Y_1 and Y_2 will generate many new DCCs in different geometry contexts.

4.3.4 Direct proof of the necessary direction of *CBCC13Converted*

At some point, there may be a chance that we only need the necessary direction of *CBCC13Converted*. This direction of the condition can also be proven directly from the definitions, without using *CBCC13*. This can be a shortcut, in comparison to walking all the paths to construct *CBCC13Converted* from *CBCC13*, in the case we do not really need the whole full CBCC. And again, sacrificing the background knowledge means paying back by a lot of computations.

Assuming we have the definitions of the projection (4.84) and the moment (4.103), we are going to prove that $J_n^V(s_1, s_2, Y_1, Y_2)$ is the intersection when slicing the plane $Y_3 = -s_1Y_1 - s_2Y_2$ through the three-variable homogeneous polynomial $K_n^V(Y_1, Y_2, Y_3)$. By the definitions, we can see that:

$$J_n^V(s_1, s_2, Y_1, Y_2) = \iint g^V(s_1, s_2, z_1, z_2)\left[\left(z_1\vec{\beta}_s - D\vec{\alpha}_s\right)\cdot(Y_1, Y_2, 0)\right]^n \frac{dz_1dz_2}{z_2^{n+2}} \tag{4.106a}$$

$$= \iint\int_0^\infty f\left(\vec{s} + t\left(z_1\vec{\beta}_s + z_2\vec{e}_3 - D\vec{\alpha}_s\right)\right)\left[\left(z_1\vec{\beta}_s - D\vec{\alpha}_s\right)\cdot(Y_1, Y_2, 0)\right]^n \frac{dtdz_1dz_2}{z_2^{n+2}}. \tag{4.106b}$$

As usual, we change the variables: $\vec{x} = \vec{s} + t\left(z_1\vec{\beta}_s + z_2\vec{e}_3 - D\vec{\alpha}_s\right)$, or more precisely:

$$x_1 = s_1 + t\frac{-z_1s_2 - Ds_1}{\|\vec{s}\|}, \tag{4.107a}$$

$$x_2 = s_2 + t\frac{z_1s_1 - Ds_2}{\|\vec{s}\|}, \tag{4.107b}$$

$$x_3 = tz_2. \tag{4.107c}$$

Conversely, we can compute (t, z_1, z_2) in terms of (x_1, x_2, x_3):

$$t = \frac{x_3}{z_2}, \tag{4.108a}$$

$$-z_1 s_2 - D s_1 = \frac{\|\vec{s}\| (x_1 - s_1)}{t}, \tag{4.108b}$$

$$z_1 s_1 - D s_2 = \frac{\|\vec{s}\| (x_2 - s_2)}{t}. \tag{4.108c}$$

Since $t = x_3/z_2$, the two last equations become:

$$-z_1 s_2 - D s_1 = \frac{\|\vec{s}\| z_2 (x_1 - s_1)}{x_3}, \tag{4.109a}$$

$$z_1 s_1 - D s_2 = \frac{\|\vec{s}\| z_2 (x_2 - s_2)}{x_3}. \tag{4.109b}$$

By the familiar technique of multiplying the suitable values on each equation and summing together, we obtain:

$$z_1 \left(s_1^2 + s_2^2\right) = \frac{\|\vec{s}\| z_2 (-x_1 s_2 + s_1 s_2)}{x_3} + \frac{\|\vec{s}\| z_2 (x_2 s_1 - s_1 s_2)}{x_3} = \frac{\|\vec{s}\| z_2 (-x_1 s_2 + x_2 s_1)}{x_3}, \tag{4.110a}$$

$$D \left(s_1^2 + s_2^2\right) = \frac{\|\vec{s}\| z_2 \left(-x_1 s_1 + s_1^2\right)}{x_3} + \frac{\|\vec{s}\| z_2 \left(-x_2 s_2 + s_2^2\right)}{x_3} = \frac{\|\vec{s}\| z_2 \left(-x_1 s_1 - x_2 s_2 + s_1^2 + s_2^2\right)}{x_3}. \tag{4.110b}$$

From (4.110b), we can compute:

$$z_2 = \frac{D \left(s_1^2 + s_2^2\right) x_3}{\|\vec{s}\| (-x_1 s_1 - x_2 s_2 + s_1^2 + s_2^2)} = \frac{D \|\vec{s}\|^2 x_3}{\|\vec{s}\| \left(-x_1 s_1 - x_2 s_2 + \|\vec{s}\|^2\right)} = \frac{D \|\vec{s}\| x_3}{\|\vec{s}\|^2 - x_1 s_1 - x_2 s_2} \tag{4.111}$$

Then from (4.110a):

$$z_1 = \frac{\|\vec{s}\| z_2 (-x_1 s_2 + x_2 s_1)}{x_3 (s_1^2 + s_2^2)} = \frac{\|\vec{s}\| (-x_1 s_2 + x_2 s_1)}{x_3 \|\vec{s}\|^2} \frac{D \|\vec{s}\| x_3}{\|\vec{s}\|^2 - x_1 s_1 - x_2 s_2} = \frac{D (-x_1 s_2 + x_2 s_1)}{\|\vec{s}\|^2 - x_1 s_1 - x_2 s_2}. \tag{4.112}$$

And from (4.108a):

$$t = \frac{x_3}{z_2} = x_3 \frac{\|\vec{s}\|^2 - x_1 s_1 - x_2 s_2}{D \|\vec{s}\| x_3} = \frac{\|\vec{s}\|^2 - x_1 s_1 - x_2 s_2}{D \|\vec{s}\|}. \tag{4.113}$$

Moreover, from (4.107), we can also compute the Jacobian matrix as follows:

$$J = \begin{bmatrix} \frac{\partial x_1}{\partial t} & \frac{\partial x_1}{\partial z_1} & \frac{\partial x_1}{\partial z_2} \\ \frac{\partial x_2}{\partial t} & \frac{\partial x_2}{\partial z_1} & \frac{\partial x_2}{\partial z_2} \\ \frac{\partial x_3}{\partial t} & \frac{\partial x_3}{\partial z_1} & \frac{\partial x_3}{\partial z_2} \end{bmatrix} = \begin{bmatrix} \frac{-z_1 s_2 - D s_1}{\|\vec{s}\|} & \frac{-t s_2}{\|\vec{s}\|} & 0 \\ \frac{z_1 s_1 - D s_2}{\|\vec{s}\|} & \frac{t s_1}{\|\vec{s}\|} & 0 \\ z_2 & 0 & t \end{bmatrix}, \tag{4.114a}$$

$$\det J = \frac{-z_1 s_2 - D s_1}{\|\vec{s}\|} \frac{t^2 s_1}{\|\vec{s}\|} + \frac{z_1 s_1 - D s_2}{\|\vec{s}\|} \frac{t^2 s_2}{\|\vec{s}\|} \tag{4.114b}$$

$$= \frac{t^2}{\|\vec{s}\|^2} \left(-z_1 s_1 s_2 - D s_1^2 + z_1 s_1 s_2 - D s_2^2\right) \tag{4.114c}$$

$$= \frac{-D t^2}{\|\vec{s}\|^2} \left(s_1^2 + s_2^2\right) \tag{4.114d}$$

$$= -D t^2. \tag{4.114e}$$

This means $d\vec{x} = dx_1 dx_2 dx_3 = D t^2 dt dz_1 dz_2$. Or conversely, using the above formula of t in terms of (x_1, x_2, x_3):

$$dt dz_1 dz_2 = \frac{1}{D} \frac{D^2 \|\vec{s}\|^2}{\left(\|\vec{s}\|^2 - x_1 s_1 - x_2 s_2\right)^2} d\vec{x} = \frac{D \|\vec{s}\|^2}{\left(\|\vec{s}\|^2 - x_1 s_1 - x_2 s_2\right)^2} d\vec{x}. \tag{4.115}$$

From all of these materials and the condition that the support of the object is compact, we are ready to change the variables of the triple integral in the formula of the moment $J_n^V(s_1, s_2, Y_1, Y_2)$ as follows:

$$\begin{aligned}
&J_n^V(s_1, s_2, Y_1, Y_2)\\
&= \iint \int_0^\infty f\left(\vec{s} + t\left(z_1\vec{\beta}_s + z_2\vec{e}_3 - D\vec{\alpha}_s\right)\right)\left[\left(z_1\vec{\beta}_s - D\vec{\alpha}_s\right)\cdot(Y_1, Y_2, 0)\right]^n \frac{dtdz_1dz_2}{z_2^{n+2}}
\end{aligned} \tag{4.116a}$$

$$= \iiint f(\vec{x})\left[\left(\frac{D(-x_1s_2 + x_2s_1)}{\|\vec{s}\|^2 - x_1s_1 - x_2s_2}\vec{\beta}_s - D\vec{\alpha}_s\right)\cdot(Y_1, Y_2, 0)\right]^n \frac{\left(\|\vec{s}\|^2 - x_1s_1 - x_2s_2\right)^{n+2}}{D^{n+2}\|\vec{s}\|^{n+2}x_3^{n+2}} \frac{D\|\vec{s}\|^2}{\left(\|\vec{s}\|^2 - x_1s_1 - x_2s_2\right)^2}d\vec{x} \tag{4.116b}$$

$$= \iiint f(\vec{x})\left[\left(\frac{D(-x_1s_2 + x_2s_1)}{\|\vec{s}\|^2 - x_1s_1 - x_2s_2}\vec{\beta}_s - D\vec{\alpha}_s\right)\cdot(Y_1, Y_2, 0)\right]^n \frac{\left(\|\vec{s}\|^2 - x_1s_1 - x_2s_2\right)^{n}}{D^{n+1}\|\vec{s}\|^{n}x_3^{n+2}}d\vec{x}. \tag{4.116c}$$

For simplicity, we will compute the terms in the square brackets first (in this step, we write the vectors in column form to make it easier to read):

$$\left(\frac{D(-x_1s_2 + x_2s_1)}{\|\vec{s}\|^2 - x_1s_1 - x_2s_2}\vec{\beta}_s - D\vec{\alpha}_s\right)\cdot\begin{bmatrix}Y_1\\Y_2\\0\end{bmatrix}$$

$$= \frac{D}{\|\vec{s}\|^2 - x_1s_1 - x_2s_2}\left[(-x_1s_2 + x_2s_1)\vec{\beta}_s - \left(\|\vec{s}\|^2 - x_1s_1 - x_2s_2\right)\vec{\alpha}_s\right]\cdot\begin{bmatrix}Y_1\\Y_2\\0\end{bmatrix} \tag{4.117a}$$

$$= \frac{D}{\|\vec{s}\|^2 - x_1s_1 - x_2s_2}\left[(-x_1s_2 + x_2s_1)\frac{1}{\|\vec{s}\|}\begin{bmatrix}-s_2\\s_1\\0\end{bmatrix} - \left(\|\vec{s}\|^2 - x_1s_1 - x_2s_2\right)\frac{1}{\|\vec{s}\|}\begin{bmatrix}s_1\\s_2\\0\end{bmatrix}\right]\cdot\begin{bmatrix}Y_1\\Y_2\\0\end{bmatrix} \tag{4.117b}$$

$$= \frac{D}{\|\vec{s}\|\left(\|\vec{s}\|^2 - x_1s_1 - x_2s_2\right)}\left[(-x_1s_2 + x_2s_1)\begin{bmatrix}-s_2\\s_1\\0\end{bmatrix} - \left(\|\vec{s}\|^2 - x_1s_1 - x_2s_2\right)\begin{bmatrix}s_1\\s_2\\0\end{bmatrix}\right]\cdot\begin{bmatrix}Y_1\\Y_2\\0\end{bmatrix}. \tag{4.117c}$$

Here we have substituted the definitions of $\vec{\alpha}_s$ and $\vec{\beta}_s$. By simple computations, we can see that:

$$\left(\frac{D(-x_1s_2 + x_2s_1)}{\|\vec{s}\|^2 - x_1s_1 - x_2s_2}\vec{\beta}_s - D\vec{\alpha}_s\right)\cdot\begin{bmatrix}Y_1\\Y_2\\0\end{bmatrix}$$

$$= \frac{D}{\|\vec{s}\|\left(\|\vec{s}\|^2 - x_1s_1 - x_2s_2\right)}\begin{bmatrix}x_1s_2^2 - x_2s_1s_2 - \|\vec{s}\|^2 s_1 + x_1s_1^2 + x_2s_1s_2\\ -x_1s_1s_2 + x_2s_1^2 - \|\vec{s}\|^2 s_2 + x_1s_1s_2 + x_2s_2^2\\ 0\end{bmatrix}\cdot\begin{bmatrix}Y_1\\Y_2\\0\end{bmatrix} \tag{4.118a}$$

$$= \frac{D}{\|\vec{s}\|\left(\|\vec{s}\|^2 - x_1s_1 - x_2s_2\right)}\begin{bmatrix}x_1\left(s_1^2 + s_2^2\right) - \|\vec{s}\|^2 s_1\\ x_2\left(s_1^2 + s_2^2\right) - \|\vec{s}\|^2 s_2\\ 0\end{bmatrix}\cdot\begin{bmatrix}Y_1\\Y_2\\0\end{bmatrix} \tag{4.118b}$$

$$= \frac{D\|\vec{s}\|^2}{\|\vec{s}\|\left(\|\vec{s}\|^2 - x_1s_1 - x_2s_2\right)}\begin{bmatrix}x_1 - s_1\\x_2 - s_2\\0\end{bmatrix}\cdot\begin{bmatrix}Y_1\\Y_2\\0\end{bmatrix} \tag{4.118c}$$

$$= \frac{D\|\vec{s}\|}{\|\vec{s}\|^2 - x_1s_1 - x_2s_2}\left[(x_1 - s_1)Y_1 + (x_2 - s_2)Y_2\right] \tag{4.118d}$$

$$= \frac{D\|\vec{s}\|}{\|\vec{s}\|^2 - x_1s_1 - x_2s_2}\left[x_1Y_1 + x_2Y_2 + (-s_1Y_1 - s_2Y_2)\right]. \tag{4.118e}$$

Coming back with the triple integral, by the multinomial theorem, we obtain:

$$J_n^V(s_1,s_2,Y_1,Y_2) = \iiint f(\vec{x}) \frac{D^n \|\vec{s}\|^n}{\left(\|\vec{s}\|^2 - x_1s_1 - x_2s_2\right)^n} \left[x_1Y_1 + x_2Y_2 + (-s_1Y_1 - s_2Y_2)\right]^n \frac{\left(\|\vec{s}\|^2 - x_1s_1 - x_2s_2\right)^n}{D^{n+1}\|\vec{s}\|^n x_3^{n+2}} d\vec{x} \tag{4.119a}$$

$$= \iiint f(\vec{x}) \left[x_1Y_1 + x_2Y_2 + (-s_1Y_1 - s_2Y_2)\right]^n \frac{1}{Dx_3^{n+2}} d\vec{x} \tag{4.119b}$$

$$= \iiint f(\vec{x}) \left[\sum_{i+j+k=n} \binom{n}{i,j,k} (x_1Y_1)^i (x_2Y_2)^j (-s_1Y_1 - s_2Y_2)^k\right] \frac{1}{Dx_3^{n+2}} d\vec{x} \tag{4.119c}$$

$$= \sum_{i+j+k=n} \left[\frac{1}{D}\binom{n}{i,j,k} \iiint f(\vec{x}) x_1^i x_2^j \frac{d\vec{x}}{x_3^{n+2}}\right] Y_1^i Y_2^j (-s_1Y_1 - s_2Y_2)^k \tag{4.119d}$$

$$= \sum_{i+j+k=n} C_{i,j,k}^V Y_1^i Y_2^j (-s_1Y_1 - s_2Y_2)^k. \tag{4.119e}$$

This shows $J_n^V(s_1,s_2,Y_1,Y_2)$ becomes a homogeneous polynomial in three variables Y_1, Y_2 and $-s_1Y_1 - s_2Y_2$, where the coefficients $C_{i,j,k}^V$ depends only on f, here $\binom{n}{i,j,k} = (n!)/(i!\ j!\ k!)$. And it completes the necessary direction of *CBCC13Converted*.

Comments

- In the previous section constructing *CBCC13Converted* from *CBCC13*, we only know that the moment of the weighted projections $J_n^V(s_1,s_2,Y_1,Y_2)$ happens to be a slice of an already existed three-variable homogeneous polynomial $K_n^V(Y_1,Y_2,Y_3)$, with the coefficients depending only on f. But until this section, the direct proof gives us the explicit form of this homogeneous polynomial:

  $$K_n^V(Y_1,Y_2,Y_3) = \sum_{i+j+k=n} C_{i,j,k}^V Y_1^i Y_2^j Y_3^k = \sum_{i+j+k=n} \left[\frac{1}{D}\binom{n}{i,j,k} \iiint f(\vec{x}) x_1^i x_2^j \frac{d\vec{x}}{x_3^{n+2}}\right] Y_1^i Y_2^j Y_3^k. \tag{4.120}$$

  The coefficients are clearly shown. Moreover, the three-variable homogeneous polynomial $K_n^H(Y_1,Y_2,Y_3)$ in *CBCC13* geometry has also been shown in the paper [Clackdoyle and Desbat, 2013]. With those explicit homogeneous polynomials, one can also find the relationship between their coefficients to see if they link together, which has not been done in this work.
- The coefficients of $K_n^V(Y_1,Y_2,Y_3)$ depend only on f, which means given some 3D object f, there has already existed the three-variable homogeneous polynomial $K_n^V(Y_1,Y_2,Y_3)$, regardless of the source locations or the projections. On the other hand, if we take the source locations into account, then the projections can be computed from the 3D object f and the moments can be computed from the projections, correspondingly to the source locations. And those moments have to follow the homogeneous polynomial (which existed even before them) by the rule of the CBCC. In this case, one moment is such a slice of the plane $Y_3 = -s_1Y_1 - s_2Y_2$ through the three-variable homogeneous polynomial $K_n^V(Y_1,Y_2,Y_3)$.
- All the DCCs from the beginning of this chapter until now are the projection-form DCCs, because they are the conditions on the moments, which are directly constructed from the projections. In other words, this type of DCCs link together the projections obtained from many source locations. Projection-form DCCs can be useful in geometric calibration. Because in the situation that we know all the projections, but the corresponding geometric parameters are unknown, e.g. the corresponding source locations, then computing the moments directly from the projections and applying these DCCs can generate a lot of crucial information, and help us calibrate the unknown geometric parameters, with the aim of obtaining the analytic estimations of the unknown parameters.

4.3.5 *CBCC13Converted* in some special cases

In this section, we applied *CBCC13Converted* in two special geometry contexts: the circular and elliptic source trajectory. Section 4.3.5.1 is for the circular source trajectory, and it also shows us the link between *CBCC13Converted* and *CBCC16*. Section 4.3.5.2 is for the elliptic source trajectory and we can also find a new DCC for the weighted projections in this geometry context.

4.3.5.1 Circular source trajectory

We know that *CBCC16* geometry is a special case of *CBCC13Converted* geometry. Precisely, in *CBCC13Converted* geometry, if we consider the x-ray source to move along a circle on the trajectory plane $x_3 = 0$, whose center is at the world origin and radius is R, then the source location can be parameterized as $\vec{s} = \vec{s}_\lambda = (R\cos\lambda, R\sin\lambda, 0)$. As a consequence, from the definitions of $\vec{\alpha}_s$ and $\vec{\beta}_s$ in *CBCC13Converted* geometry, we also have:

$$\vec{\alpha}_s = (\cos\lambda, \sin\lambda, 0) = \vec{\alpha}_\lambda, \quad \vec{\beta}_s = (-\sin\lambda, \cos\lambda, 0) = \vec{\beta}_\lambda, \tag{4.121}$$

and we can get back *CBCC16* geometry. Moreover, the definition (4.84) of the weighted projection in *CBCC13Converted* geometry can be rewritten as:

$$g^V(s_1, s_2, z_1, z_2) = g^V(R\cos\lambda, R\sin\lambda, z_1, z_2) = \int_0^\infty f\left(\vec{s}_\lambda + t\left(z_1\vec{\beta}_\lambda + z_2\vec{e}_3 - D\vec{\alpha}_\lambda\right)\right) dt = p_\lambda^V(z_1, z_2). \tag{4.122}$$

Here we just check again with the definition (4.2) of the weighted projection in *CBCC16* geometry, and see that the both definitions coincide. Moreover, by the definition (4.103) of the moment $J_n^V(s_1, s_2, Y_1, Y_2)$, we can see that:

$$\begin{aligned} J_n^V(s_1, s_2, Y_1, Y_2) &= J_n^V(R\cos\lambda, R\sin\lambda, Y_1, Y_2) && \text{(4.123a)} \\ &= \iint g^V(R\cos\lambda, R\sin\lambda, z_1, z_2)\left[\left(z_1\vec{\beta}_\lambda - D\vec{\alpha}_\lambda\right)\cdot(Y_1, Y_2, 0)\right]^n \frac{dz_1 dz_2}{z_2^{n+2}} && \text{(4.123b)} \\ &= \iint p_\lambda^V(z_1, z_2)\left[\left(z_1\vec{\beta}_\lambda - D\vec{\alpha}_\lambda\right)\cdot(Y_1, Y_2, 0)\right]^n \frac{dz_1 dz_2}{z_2^{n+2}}. && \text{(4.123c)} \end{aligned}$$

Then if we choose $Y_1 = -\sin\lambda$ and $Y_2 = \cos\lambda$, which means $(Y_1, Y_2, 0) = (-\sin\lambda, \cos\lambda, 0) = \vec{\beta}_\lambda$, the above integral will become:

$$\begin{aligned} J_n^V(R\cos\lambda, R\sin\lambda, -\sin\lambda, \cos\lambda) &= \iint p_\lambda^V(z_1, z_2)\left[\left(z_1\vec{\beta}_\lambda - D\vec{\alpha}_\lambda\right)\cdot\vec{\beta}_\lambda\right]^n \frac{dz_1 dz_2}{z_2^{n+2}} && \text{(4.124a)} \\ &= \iint p_\lambda^V(z_1, z_2)\frac{z_1^n}{z_2^{n+2}} dz_1 dz_2 && \text{(4.124b)} \\ &= M_n^V(\lambda), && \text{(4.124c)} \end{aligned}$$

because of the definition (4.3) of the moment defined in *CBCC16* geometry. On the other hand, *CBCC13Converted* also says that:

$$\begin{aligned} J_n^V(R\cos\lambda, R\sin\lambda, -\sin\lambda, \cos\lambda) &= K_n^V(-\sin\lambda, \cos\lambda, -R\cos\lambda(-\sin\lambda) - R\sin\lambda\cos\lambda) && \text{(4.125a)} \\ &= K_n^V(-\sin\lambda, \cos\lambda, 0) && \text{(4.125b)} \\ &= \sum_{i+j+k=n} C_{i,j,k}^V(-\sin\lambda)^i(\cos\lambda)^j 0^k && \text{(4.125c)} \\ &= \sum_{\substack{k=0 \\ i+j=n}} C_{i,j,0}^V(-\sin\lambda)^i(\cos\lambda)^j. && \text{(4.125d)} \end{aligned}$$

Then we obtain the fact that:

$$M_n^V(\lambda) = J_n^V(R\cos\lambda, R\sin\lambda, -\sin\lambda, \cos\lambda) = \sum_{i+j=n} C_{i,j,0}^V(-\sin\lambda)^i(\cos\lambda)^j, \tag{4.126}$$

which is a homogeneous polynomial in $\cos\lambda$ and $\sin\lambda$ of degree n. This is *CBCC16*. So we clearly see that, using *CBCC13Converted* with $Y_1 = -\sin\lambda$ and $Y_2 = \cos\lambda$ generates *CBCC16*, which happens the same in the case of *CBCC13* and *CBCC16Converted* geometry contexts.

Numerical simulations Now for the numerical simulations, the modified 3D Shepp-Logan phantom is still considered as our object. The source is moving along the circle $x_1^2 + x_2^2 = (5/2)^2$ on the trajectory plane $x_3 = 0$, the vertical detector is at distance $D = 4.5$ away from the source (such that the source, the world origin and the origin of the detector are always collinear). We can see that this is exactly the same situation as the experiment in *CBCC16* geometry, which has been shown before, see 4.2.6. Thus we hope a similar result to what we have obtained.

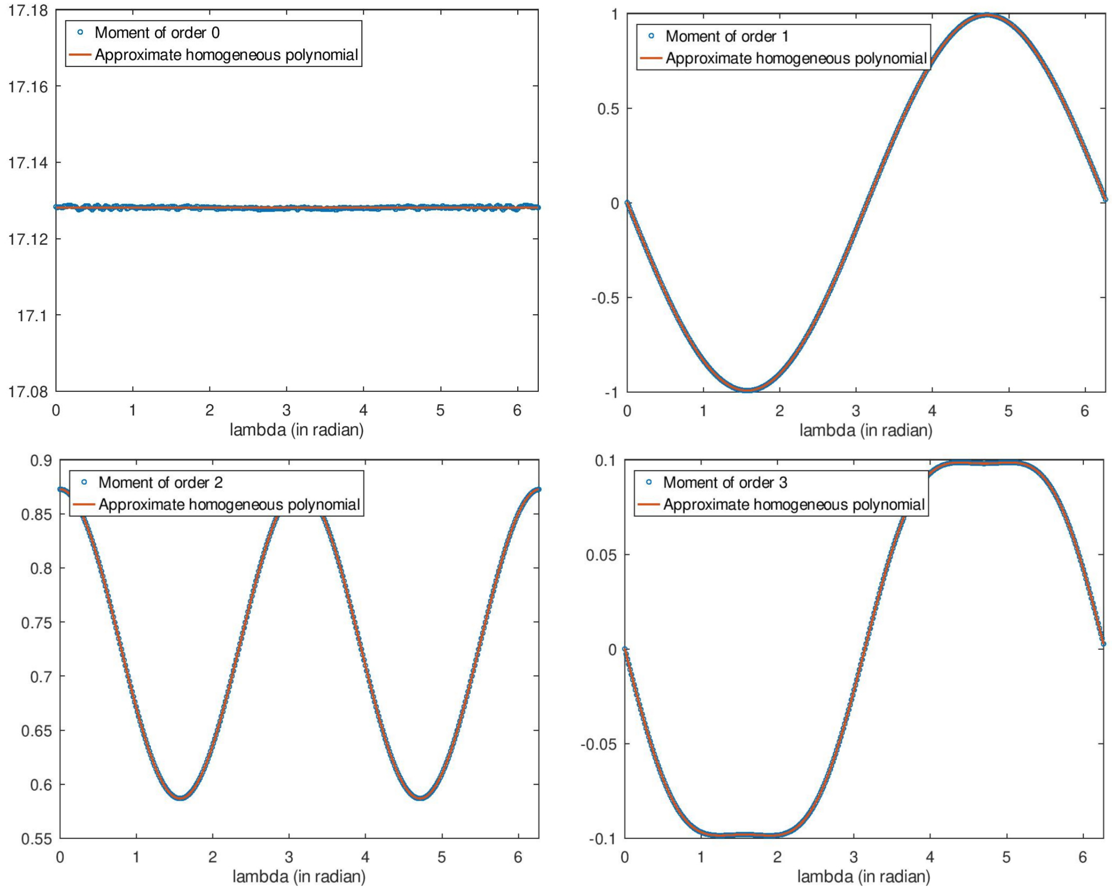

Figure 4.13: Moments $M^V(\lambda)$ of orders 0 (top-left), 1 (top-right), 2 (bottom-left), 3 (bottom-right) of the weighted cone-beam projections on the vertical detector, where the source is moving along the circle $x_1^2 + x_2^2 = (5/2)^2$ on the trajectory plane $x_3 = 0$.

Figure 4.13 shows us the moments $J_n^V(s_1, s_2, Y_1, Y_2)$ (with $s_1 = R\cos\lambda$, $s_2 = R\sin\lambda$, $Y_1 = -\sin\lambda$, $Y_2 = \cos\lambda$) of order $0, 1, 2, 3$. The nearest homogeneous polynomials in $\cos\lambda$ and $\sin\lambda$ fitting the data are the followings:

$$Q_0^{V,\text{ circle}}(\lambda) = 17.1281, \tag{4.127a}$$

$$Q_1^{V,\text{ circle}}(\lambda) = 0.0009\cos\lambda - 0.9919\sin\lambda, \tag{4.127b}$$

$$Q_2^{V,\text{ circle}}(\lambda) = 0.8727\cos^2\lambda + 0.0001\cos\lambda\sin\lambda + 0.5868\sin^2\lambda, \tag{4.127c}$$

$$Q_3^{V,\text{ circle}}(\lambda) = 0.0000\cos^3\lambda - 0.1562\cos^2\lambda\sin\lambda + 0.0001\cos\lambda\sin^2\lambda - 0.0980\sin^3\lambda. \tag{4.127d}$$

The homogeneous polynomials $Q_n^{V,\text{ circle}}(\lambda)$ in (4.127) respectively match $P_n^V(\lambda)$ in (4.29) for $n = 0, 1, 2, 3$.

4.3.5.2 Elliptic source trajectory

Now the source is assumed to move along an ellipse $(x_1/R_1)^2 + (x_2/R_2)^2 = 1$ on the trajectory plane $x_3 = 0$, then its location can be parameterized as $\vec{s} = \tilde{\mathbf{s}}_\lambda = (R_1\cos\lambda, R_2\sin\lambda, 0)$. From this, we can construct the unit vectors as follows:

$$\vec{\alpha}_s = \tilde{\alpha}_\lambda = \frac{1}{\delta(\lambda)}(R_1\cos\lambda, R_2\sin\lambda, 0), \quad \vec{\beta}_s = \tilde{\beta}_\lambda = \frac{1}{\delta(\lambda)}(-R_2\sin\lambda, R_1\cos\lambda, 0), \tag{4.128}$$

where $\delta(\lambda) = \sqrt{R_1^2 \cos^2\lambda + R_2^2 \sin^2\lambda}$. Then by the definitions of the projections in *CBCC13Converted* geometry (4.84) and the corresponding moments (4.103), we can see that:

$$g^V(s_1, s_2, z_1, z_2) = g^V(R_1\cos\lambda, R_2\sin\lambda, z_1, z_2) \tag{4.129a}$$

$$= \int_0^\infty f\left(\tilde{\mathbf{s}}_\lambda + t\left(z_1\tilde{\beta}_\lambda + z_2\vec{e}_3 - D\tilde{\alpha}_\lambda\right)\right) dt, \tag{4.129b}$$

$$J_n^V(s_1, s_2, Y_1, Y_2) = J_n^V(R_1\cos\lambda, R_2\sin\lambda, Y_1, Y_2) \tag{4.129c}$$

$$= \iint g^V(R_1\cos\lambda, R_2\sin\lambda, z_1, z_2)\left[\left(z_1\tilde{\beta}_\lambda - D\tilde{\alpha}_\lambda\right)\cdot(Y_1, Y_2, 0)\right]^n \frac{dz_1 dz_2}{z_2^{n+2}}. \tag{4.129d}$$

In this case, we choose $Y_1 = -R_2\sin\lambda$ and $Y_2 = R_1\cos\lambda$, then $(Y_1, Y_2, 0) = (-R_2\sin\lambda, R_1\cos\lambda, 0) = \delta(\lambda)\tilde{\beta}_\lambda$, thus the above moment becomes:

$$J_n^V(R_1\cos\lambda, R_2\sin\lambda, -R_2\sin\lambda, R_1\cos\lambda) = \iint g^V(R_1\cos\lambda, R_2\sin\lambda, z_1, z_2)\left[\left(z_1\tilde{\beta}_\lambda - D\tilde{\alpha}_\lambda\right)\cdot\left(\delta(\lambda)\tilde{\beta}_\lambda\right)\right]^n \frac{dz_1 dz_2}{z_2^{n+2}} \tag{4.130a}$$

$$= \delta^n(\lambda)\iint g^V(R_1\cos\lambda, R_2\sin\lambda, z_1, z_2)\left[\left(z_1\tilde{\beta}_\lambda - D\tilde{\alpha}_\lambda\right)\cdot\tilde{\beta}_\lambda\right]^n \frac{dz_1 dz_2}{z_2^{n+2}} \tag{4.130b}$$

$$= \delta^n(\lambda)\iint g^V(R_1\cos\lambda, R_2\sin\lambda, z_1, z_2)\frac{z_1^n}{z_2^{n+2}} dz_1 dz_2. \tag{4.130c}$$

And on the other hand, using *CBCC13Converted*:

$$J_n^V(R_1\cos\lambda, R_2\sin\lambda, -R_2\sin\lambda, R_1\cos\lambda)$$

$$= K_n^V(-R_2\sin\lambda, R_1\cos\lambda, -R_1\cos\lambda(-R_2\sin\lambda) - R_2\sin\lambda R_1\cos\lambda) \tag{4.131a}$$

$$= K_n^V(-R_2\sin\lambda, R_1\cos\lambda, 0) \tag{4.131b}$$

$$= \sum_{i+j+k=n} C_{i,j,k}^V(-R_2\sin\lambda)^i(R_1\cos\lambda)^j 0^k \tag{4.131c}$$

$$= \sum_{i+j+k=n} C_{i,j,k}^V(-R_2)^i(R_1)^j(\sin\lambda)^i(\cos\lambda)^j 0^k \tag{4.131d}$$

$$= \sum_{\substack{k=0\\ i+j=n}} C_{i,j,0}^V(-R_2)^i(R_1)^j(\sin\lambda)^i(\cos\lambda)^j, \tag{4.131e}$$

which is a homogeneous polynomial in $\cos\lambda$ and $\sin\lambda$ of degree n.

From these computations, if we define the weighted cone-beam projection of some compactly supported function f on the vertical detector with the source moving along the ellipse $(x_1/R_1)^2 + (x_2/R_2)^2 = 1$ on the trajectory plane $x_3 = 0$ as:

$$p_\lambda^{V,\text{ ellipse}}(u, v) = g^V(R_1\cos\lambda, R_2\sin\lambda, u, v) = \int_0^\infty f\left(\tilde{\mathbf{s}}_\lambda + t\left(u\tilde{\beta}_\lambda + v\vec{e}_3 - D\tilde{\alpha}_\lambda\right)\right) dt, \tag{4.132}$$

and the moments as:

$$M_n^{V,\text{ ellipse}}(\lambda) = \iint p_\lambda^{V,\text{ ellipse}}(u, v)\frac{u^n}{v^{n+2}} du dv \tag{4.133a}$$

$$= \iint g^V(R_1\cos\lambda, R_2\sin\lambda, u, v)\frac{u^n}{v^{n+2}} du dv \tag{4.133b}$$

$$= \frac{J_n^V(R_1\cos\lambda, R_2\sin\lambda, -R_2\sin\lambda, R_1\cos\lambda)}{\delta^n(\lambda)}, \tag{4.133c}$$

then the adjusted moment

$$\widetilde{M}_n^V(\lambda) = \delta^n(\lambda) M_n^{V,\text{ ellipse}}(\lambda) = J_n^V(R_1\cos\lambda, R_2\sin\lambda, -R_2\sin\lambda, R_1\cos\lambda) \tag{4.134}$$

is a homogeneous polynomial in $\cos\lambda$ and $\sin\lambda$ of degree n. We can see that *CBCC13Converted* has just generated a new DCC in this geometry with the elliptic source trajectory:

> *If $p_\lambda^{V,\ ellipse}(u,v)$ is the weighted cone-beam projection of some compactly supported function f on the vertical detector with the source moving along an ellipse $(x_1/R_1)^2 + (x_2/R_2)^2 = 1$ on the plane $x_3 = 0$, for all $\lambda \in [0, 2\pi)$, then the adjusted moment:*
>
> $$\widetilde{M}_n^V(\lambda) = \sqrt{R_1^2\cos^2\lambda + R_2^2\sin^2\lambda}^{\,n} \iint p_\lambda^{V,\ ellipse}(u,v)\,\frac{u^n}{v^{n+2}}dudv, \tag{4.135}$$
>
> *is a homogeneous polynomial in $\cos\lambda$ and $\sin\lambda$ of degree n.*

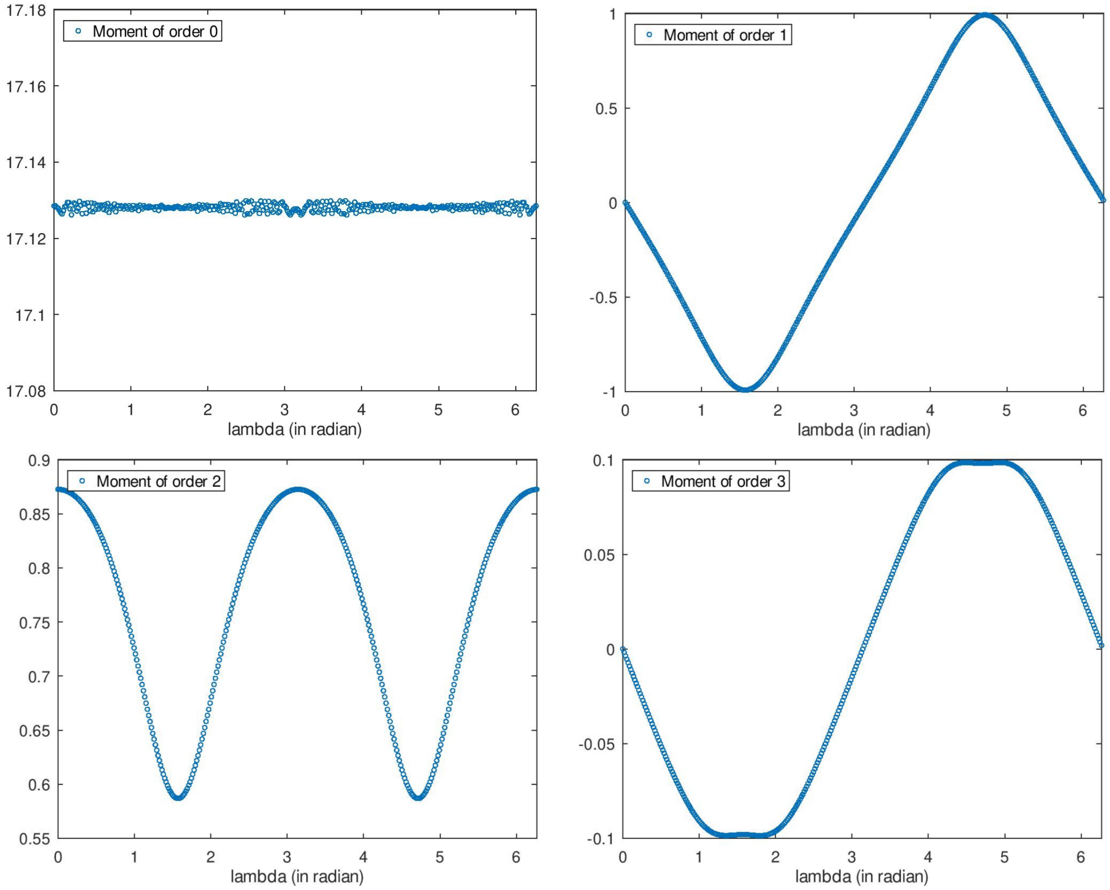

Figure 4.14: Raw moments $M^V(\lambda)$ of orders 0 (top-left), 1 (top-right), 2 (bottom-left), 3 (bottom-right) of the weighted cone-beam projections on the vertical detector, where the source is moving along an ellipse $(x_1/3)^2 + (x_2/2)^2 = 1$ on the trajectory plane $x_3 = 0$.

Numerical simulations In this case, the source is moving on the ellipse $(x_1/3)^2 + (x_2/2)^2 = 1$ on the trajectory plane $x_3 = 0$, the object and the vertical detector remain the same. Figure 4.14 shows us the moments $M_n^{V,\text{ ellipse}}(\lambda)$ of degree $n = 0, 1, 2, 3$ and figure 4.15 shows the adjusted moments $\widetilde{M}_n^V(\lambda)$, which become the homogeneous

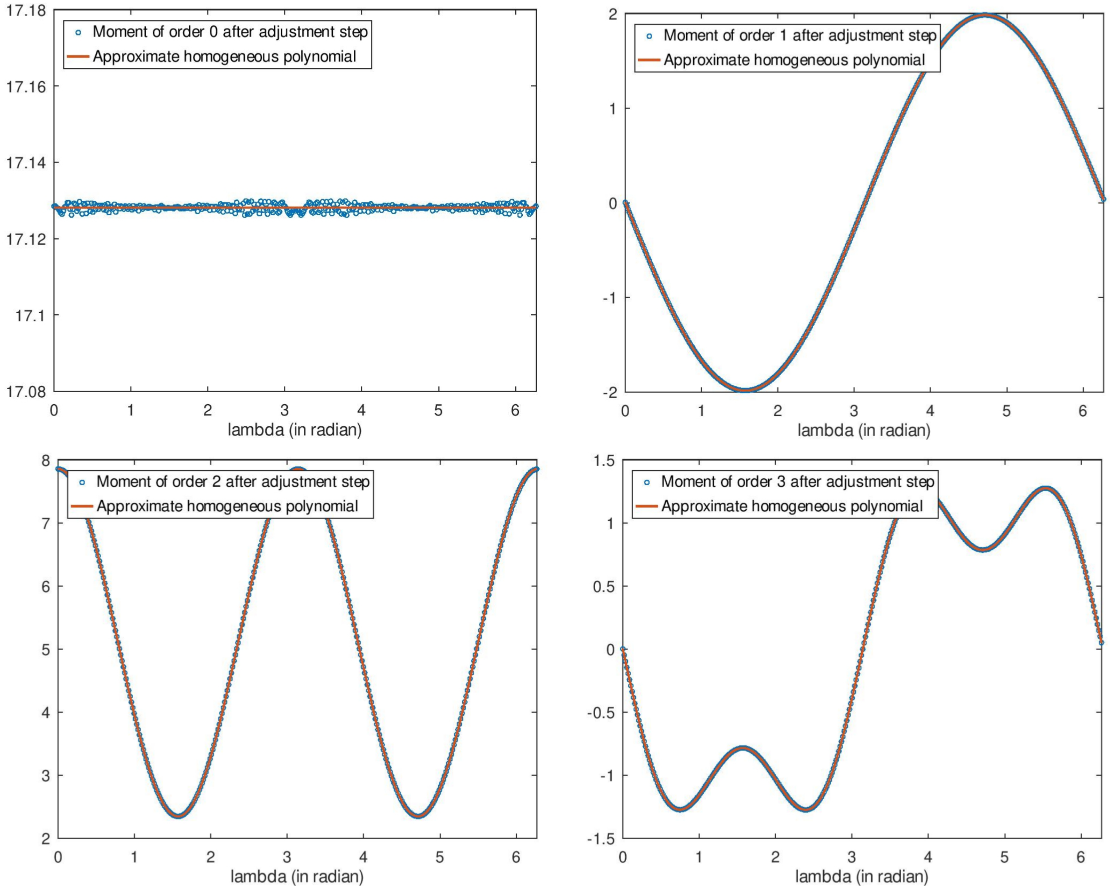

Figure 4.15: Adjusted moments $M^V(\lambda)$ (computed by formula (4.135)) of orders 0 (top-left), 1 (top-right), 2 (bottom-left), 3 (bottom-right) of the weighted cone-beam projections on the vertical detector, where the source is moving along an ellipse $(x_1/3)^2 + (x_2/2)^2 = 1$ on the trajectory plane $x_3 = 0$.

polynomials. More precisely, the approximate homogeneous polynomials in $\cos\lambda$ and $\sin\lambda$ fitting the data are:

$$Q_0^{V,\text{ ellipse}}(\lambda) = 17.1281, \tag{4.136a}$$

$$Q_1^{V,\text{ ellipse}}(\lambda) = 0.0026\cos\lambda - 1.9839\sin\lambda, \tag{4.136b}$$

$$Q_2^{V,\text{ ellipse}}(\lambda) = 7.8539\cos^2\lambda + 0.0001\cos\lambda\sin\lambda + 2.3473\sin^2\lambda, \tag{4.136c}$$

$$Q_3^{V,\text{ ellipse}}(\lambda) = 0.0009\cos^3\lambda - 2.8105\cos^2\lambda\sin\lambda + 0.0003\cos\lambda\sin^2\lambda - 0.7842\sin^3\lambda. \tag{4.136d}$$

4.3.6 The conventional cone-beam projections and their CBCC

From the beginning of this chapter until now, we work with two main geometry contexts, one deals with the vertical detector and one deals with the horizontal detector. We have seen several CBCCs and the links between them. However, without the detector, the cone-beam projection can still be defined theoretically, by the conventional cone-beam projection. Since the discussed weighted projections require certain flat detectors to be defined, the main variables of those functions are the 2D coordinates of the projections on the detectors: (u, v) in *CBCC16* geometry, (u, w) in *CBCC16Converted* geometry, (x_1, x_2) in *CBCC13* geometry and (z_1, z_2) in *CBCC13Converted* geometry. The integration directions are just the vectors connecting the source to those 2D coordinates on the detectors. And these vectors are not unit. On the other hand, the conventional projection can be defined regardless of the detectors, its main variable is the unit vector showing the integration direction. The weighted projections relate to the conventional projection, by normalizing the vector showing the integration directions in the definitions of the weighted projections. In application, the projection we are given is the conventional one. Thus in order to use the CBCCs developed in the previous sections, which are conditions for the weighted projections, we need to know the relationships between the conventional and the weighted projections. Another idea, which is also tempted, is to find the CBCC for even the conventional projections. In fact, this CBCC has been published in the paper [Clackdoyle and Desbat, 2013], which means the CBCC for the conventional projections is constructed from *CBCC13*. As a counterpart, we will also construct the CBCC for the conventional projections from *CBCC13Converted*. We presume that the result will turn out similar to the result in [Clackdoyle and Desbat, 2013]. Section 4.3.6.1 will show us the relations between the conventional cone-beam projection and several weighted projections we consider so far, and section 4.3.6.2 will show us the CBCC of the conventional projections built from *CBCC13Converted*.

4.3.6.1 Relationships of the conventional and the weighted cone-beam projections

Given a 3D funtion f, which has compact support, the conventional cone-beam projection $g^{\text{conv}} = \mathcal{G}^{\text{conv}} f$, computed at the source location $\vec{s}$ and the integration direction $\vec{\xi}$ is defined as folows:

$$g^{\text{conv}}\left(\vec{s}, \vec{\xi}\right) = \int_0^{\infty} f\left(\vec{s} + t\vec{\xi}\right) dt, \quad \forall \vec{\xi} \in \mathbb{S}^2. \tag{4.137}$$

As mentioned above, we can obtain the relationship of the conventional and the weighted projections by normalizing the vector showing the integration direction in the definition of the weighted projections. Precisely, now we are finding the relationship between $g^{\text{conv}}\left(\vec{s}, \vec{\xi}\right)$ and $p_\lambda^H(\lambda)$, which is the weighted projection in *CBCC16* geometry. In the definition (4.2), we can see that the vector showing the integration direction is $\left(u\vec{\beta}_\lambda + v\vec{e}_3 - D\vec{\alpha}_\lambda\right)$ and:

$$\left\| u\vec{\beta}_\lambda + v\vec{e}_3 - D\vec{\alpha}_\lambda \right\|^2 = \left(u\vec{\beta}_\lambda + v\vec{e}_3 - D\vec{\alpha}_\lambda\right) \cdot \left(u\vec{\beta}_\lambda + v\vec{e}_3 - D\vec{\alpha}_\lambda\right) = u^2 + v^2 + D^2, \tag{4.138}$$

since $\vec{\beta}_\lambda$, $\vec{e}_3$, $\vec{\alpha}_\lambda$ are two-by-two perpendicular. The normalized version of this vector is the following unit vector:

$$\vec{\xi}(u,v) = \frac{u\vec{\beta}_\lambda + v\vec{e}_3 - D\vec{\alpha}_\lambda}{\left\| u\vec{\beta}_\lambda + v\vec{e}_3 - D\vec{\alpha}_\lambda \right\|} = \frac{u\vec{\beta}_\lambda + v\vec{e}_3 - D\vec{\alpha}_\lambda}{\sqrt{u^2 + v^2 + D^2}}. \tag{4.139}$$

Then by the definitions (4.2) and (4.137), we know that:

$$\begin{aligned}
p_\lambda^V(u,v) &= \int_0^{\infty} f\left(\vec{s}_\lambda + t\left(u\vec{\beta}_\lambda + v\vec{e}_3 - D\vec{\alpha}_\lambda\right)\right) dt && \text{(4.140a)}\\
&= \int_0^{\infty} f\left(\vec{s}_\lambda + t\sqrt{u^2 + v^2 + D^2}\, \frac{u\vec{\beta}_\lambda + v\vec{e}_3 - D\vec{\alpha}_\lambda}{\sqrt{u^2 + v^2 + D^2}}\right) dt && \text{(4.140b)}\\
&= \int_0^{\infty} f\left(\vec{s}_\lambda + t'\, \frac{u\vec{\beta}_\lambda + v\vec{e}_3 - D\vec{\alpha}_\lambda}{\sqrt{u^2 + v^2 + D^2}}\right) \frac{dt'}{\sqrt{u^2 + v^2 + D^2}} && \text{(4.140c)}\\
&= \int_0^{\infty} f\left(\vec{s}_\lambda + t'\vec{\xi}(u,v)\right) dt' \frac{1}{\sqrt{u^2 + v^2 + D^2}} && \text{(4.140d)}\\
&= g^{\text{conv}}\left(\vec{s}_\lambda, \vec{\xi}(u,v)\right) \frac{1}{\sqrt{u^2 + v^2 + D^2}}. && \text{(4.140e)}
\end{aligned}$$

Here we have changed the variable $t\sqrt{u^2 + v^2 + D^2} = t'$, then $dt = dt'/\sqrt{u^2 + v^2 + D^2}$. Equation (4.140e) is the relationship between the conventional and weighted cone-beam projections, computed in *CBCC16* geometry. Completely similarly, we can also obtain the relationship between the conventional projection and:

- the weighted projection computed in *CBCC16Converted* geometry (see definition (4.5b)):

$$\begin{aligned}
p_\lambda^H(u,w) &= \int_0^{\infty} f\left(\vec{s}_\lambda + t\left(u\vec{\beta}_\lambda + (w - R)\,\vec{\alpha}_\lambda + T\vec{e}_3\right)\right) dt && \text{(4.141a)}\\
&= g^{\text{conv}}\left(\vec{s}_\lambda, \vec{\zeta}(u,w)\right) \frac{1}{\sqrt{u^2 + (w-R)^2 + T^2}}, && \text{(4.141b)}
\end{aligned}$$

$$\vec{\zeta}(u,w) = \frac{u\vec{\beta}_\lambda + (w - R)\,\vec{\alpha}_\lambda + T\vec{e}_3}{\left\| u\vec{\beta}_\lambda + (w - R)\,\vec{\alpha}_\lambda + T\vec{e}_3 \right\|} = \frac{u\vec{\beta}_\lambda + (w - R)\,\vec{\alpha}_\lambda + T\vec{e}_3}{\sqrt{u^2 + (w-R)^2 + T^2}} \in \mathbb{S}^2. \tag{4.141c}$$

- the weighted projection computed in *CBCC13* geometry (see definition (4.34b)):

$$g^{H}\left(s_1,s_2,x_1,x_2\right)=\int_0^{\infty} f\left(\vec{s}+t\left(x_1-s_1,x_2-s_2,T\right)\right)dt \tag{4.142a}$$

$$=g^{\text{conv}}\left(\vec{s},\vec{\gamma}\left(s_1,s_2,x_1,x_2\right)\right)\frac{1}{\sqrt{\left(x_1-s_1\right)^2+\left(x_2-s_2\right)^2+T^2}}, \tag{4.142b}$$

$$\vec{\gamma}\left(s_1,s_2,x_1,x_2\right)=\frac{\left(x_1-s_1,x_2-s_2,T\right)}{\left\|\left(x_1-s_1,x_2-s_2,T\right)\right\|}=\frac{\left(x_1-s_1,x_2-s_2,T\right)}{\sqrt{\left(x_1-s_1\right)^2+\left(x_2-s_2\right)^2+T^2}}\in\mathbb{S}^2. \tag{4.142c}$$

- the weighted projection computed in *CBCC13Converted* geometry (see definition (4.84)):

$$g^{V}\left(s_1,s_2,z_1,z_2\right)=\int_0^{\infty} f\left(\vec{s}+t\left(z_1\vec{\beta}_s+z_2\vec{e}_3-D\vec{\alpha}_s\right)\right)dt \tag{4.143a}$$

$$=g^{\text{conv}}\left(\vec{s},\vec{\eta}\left(s_1,s_2,z_1,z_2\right)\right)\frac{1}{\sqrt{z_1^2+z_2^2+D^2}}, \tag{4.143b}$$

$$\vec{\eta}\left(s_1,s_2,z_1,z_2\right)=\frac{z_1\vec{\beta}_s+z_2\vec{e}_3-D\vec{\alpha}_s}{\left\|z_1\vec{\beta}_s+z_2\vec{e}_3-D\vec{\alpha}_s\right\|}=\frac{z_1\vec{\beta}_s+z_2\vec{e}_3-D\vec{\alpha}_s}{\sqrt{z_1^2+z_2^2+D^2}}\in\mathbb{S}^2. \tag{4.143c}$$

Moreover, from the above relationships, we can recheck the relationships between the weighted cone-beam projections in different geometry contexts, which have been done so far.

- In section 4.2.3, we have already seen the relationship between the weighted projections in *CBCC16Converted* and *CBCC16* geometry contexts:

$$p_{\lambda}^{H}\left(\frac{Tu}{v},R-\frac{DT}{v}\right)=\frac{v}{T}p_{\lambda}^{V}\left(u,v\right), \tag{4.144}$$

  see equation (4.9e). Now using the relationships with the conventional projections in (4.141) and (4.140e), we can see that:

$$\vec{\zeta}\left(\frac{Tu}{v},R-\frac{DT}{v}\right)=\frac{\frac{Tu}{v}\vec{\beta}_{\lambda}-\frac{DT}{v}\vec{\alpha}_{\lambda}+T\vec{e}_3}{\sqrt{\left(\frac{Tu}{v}\right)^2+\left(-\frac{DT}{v}\right)^2+T^2}}=\frac{\frac{T}{v}\left(u\vec{\beta}_{\lambda}+v\vec{e}_3-D\vec{\alpha}_{\lambda}\right)}{\frac{T}{v}\sqrt{u^2+v^2+D^2}}=\vec{\xi}\left(u,v\right), \tag{4.145a}$$

$$p_{\lambda}^{H}\left(\frac{Tu}{v},R-\frac{DT}{v}\right)=g^{\text{conv}}\left(\vec{s}_{\lambda},\vec{\zeta}\left(\frac{Tu}{v},R-\frac{DT}{v}\right)\right)\frac{1}{\sqrt{\left(\frac{Tu}{v}\right)^2+\left(-\frac{DT}{v}\right)^2+T^2}} \tag{4.145b}$$

$$=g^{\text{conv}}\left(\vec{s}_{\lambda},\vec{\xi}\left(u,v\right)\right)\frac{1}{\frac{T}{v}\sqrt{u^2+v^2+D^2}} \tag{4.145c}$$

$$=\frac{v}{T}g^{\text{conv}}\left(\vec{s}_{\lambda},\vec{\xi}\left(u,v\right)\right)\frac{1}{\sqrt{u^2+v^2+D^2}} \tag{4.145d}$$

$$=\frac{v}{T}p_{\lambda}^{V}\left(u,v\right). \tag{4.145e}$$

- Similarly, in section 4.2.8, we saw the relationship between the weighted projections in *CBCC16Converted* and *CBCC13* geometry contexts, in equation (4.37c):

$$p_{\lambda}^{H}\left(u,w\right)=g^{H}\left(R\cos\lambda,R\sin\lambda,-u\sin\lambda+w\cos\lambda,u\cos\lambda+w\sin\lambda\right). \tag{4.146}$$

  From (4.142), we have:

$$\begin{aligned}&\vec{\gamma}\left(R\cos\lambda,R\sin\lambda,-u\sin\lambda+w\cos\lambda,u\cos\lambda+w\sin\lambda\right)\\&=\frac{\left(-u\sin\lambda+\left(w-R\right)\cos\lambda,u\cos\lambda+\left(w-R\right)\sin\lambda,T\right)}{\sqrt{\left(-u\sin\lambda+\left(w-R\right)\cos\lambda\right)^2+\left(u\cos\lambda+\left(w-R\right)\sin\lambda\right)^2+T^2}}=\frac{u\vec{\beta}_{\lambda}+\left(w-R\right)\vec{\alpha}_{\lambda}+T\vec{e}_3}{\sqrt{u^2+\left(w-R\right)^2+T^2}}=\vec{\zeta}\left(u,w\right).\end{aligned} \tag{4.147}$$

Then using the relationships in (4.142) and (4.141) gives us:

$$\begin{aligned}
&g^{H}\left(R\cos\lambda, R\sin\lambda, -u\sin\lambda + w\cos\lambda, u\cos\lambda, +w\sin\lambda\right)\\
&= g^{\mathrm{conv}}\left(\vec{s}_{\lambda}, \vec{\gamma}\left(R\cos\lambda, R\sin\lambda, -u\sin\lambda + w\cos\lambda, u\cos\lambda + w\sin\lambda\right)\right)\times\\
&\quad\times\frac{1}{\sqrt{\left(-u\sin\lambda + (w-R)\cos\lambda\right)^{2} + \left(u\cos\lambda + (w-R)\sin\lambda\right)^{2} + T^{2}}} \qquad (4.148a)\\
&= g^{\mathrm{conv}}\left(\vec{s}_{\lambda}, \vec{\zeta}\,(u,w)\right)\frac{1}{\sqrt{u^{2} + (w-R)^{2} + T^{2}}} \qquad (4.148b)\\
&= p_{\lambda}^{H}(u,w)\,. \qquad (4.148c)
\end{aligned}$$

- In section 4.3.2, the relationship between the weighted projections in *CBCC13* and *CBCC13Converted* has been stated as:

$$g^{H}\left(s_1, s_2, \overline{x}_1, \overline{x}_2\right) = g^{V}\left(s_1, s_2, z_1, z_2\right)\frac{z_2}{T}, \tag{4.149}$$

where:

$$\overline{x}_1 = s_1 - \frac{T}{z_2\left\|\vec{s}\right\|}\left(z_1 s_2 + D s_1\right), \tag{4.150a}$$

$$\overline{x}_2 = s_2 + \frac{T}{z_2\left\|\vec{s}\right\|}\left(z_1 s_1 - D s_2\right). \tag{4.150b}$$

Now from (4.142), we have:

$$\begin{aligned}
\vec{\gamma}\left(s_1, s_2, \overline{x}_1, \overline{x}_2\right) &= \frac{\left(-\frac{T}{z_2\left\|\vec{s}\right\|}\left(z_1 s_2 + D s_1\right), \frac{T}{z_2\left\|\vec{s}\right\|}\left(z_1 s_1 - D s_2\right), T\right)}{\sqrt{\left(-\frac{T}{z_2\left\|\vec{s}\right\|}\left(z_1 s_2 + D s_1\right)\right)^{2} + \left(\frac{T}{z_2\left\|\vec{s}\right\|}\left(z_1 s_1 - D s_2\right)\right)^{2} + T^{2}}} && (4.151a)\\
&= \frac{\frac{T}{z_2}\left(z_1\frac{-s_2}{\left\|\vec{s}\right\|} - D\frac{s_1}{\left\|\vec{s}\right\|}, z_1\frac{s_1}{\left\|\vec{s}\right\|} - D\frac{s_2}{\left\|\vec{s}\right\|}, z_2\right)}{\frac{T}{z_2}\sqrt{\left(z_1\frac{s_2}{\left\|\vec{s}\right\|} + D\frac{s_1}{\left\|\vec{s}\right\|}\right)^{2} + \left(z_1\frac{s_1}{\left\|\vec{s}\right\|} - D\frac{s_2}{\left\|\vec{s}\right\|}\right)^{2} + z_2^{2}}} && (4.151b)\\
&= \frac{\frac{T}{z_2}\left(z_1\vec{\beta}_s + z_2\vec{e}_3 - D\vec{\alpha}_s\right)}{\frac{T}{z_2}\sqrt{z_1^{2} + z_2^{2} + D^{2}}} && (4.151c)\\
&= \vec{\eta}\left(s_1, s_2, z_1, z_2\right), && (4.151d)
\end{aligned}$$

with the notice that $s_1^2 + s_2^2 = \left\|\vec{s}\right\|^2$. Using the relationships with the conventional projection in (4.142) and (4.143), we obtain:

$$\begin{aligned}
&g^{H}\left(s_1, s_2, \overline{x}_1, \overline{x}_2\right)\\
&= g^{\mathrm{conv}}\left(\vec{s}, \vec{\gamma}\left(s_1, s_2, \overline{x}_1, \overline{x}_2\right)\right)\frac{1}{\sqrt{\left(-\frac{T}{z_2\left\|\vec{s}\right\|}\left(z_1 s_2 + D s_1\right)\right)^{2} + \left(\frac{T}{z_2\left\|\vec{s}\right\|}\left(z_1 s_1 - D s_2\right)\right)^{2} + T^{2}}} \qquad (4.152a)\\
&= g^{\mathrm{conv}}\left(\vec{s}, \vec{\eta}\left(s_1, s_2, z_1, z_2\right)\right)\frac{1}{\frac{T}{z_2}\sqrt{z_1^{2} + z_2^{2} + D^{2}}} \qquad (4.152b)\\
&= \frac{z_2}{T}g^{\mathrm{conv}}\left(\vec{s}, \vec{\eta}\left(s_1, s_2, z_1, z_2\right)\right)\frac{1}{\sqrt{z_1^{2} + z_2^{2} + D^{2}}} \qquad (4.152c)\\
&= \frac{z_2}{T}g^{V}\left(s_1, s_2, z_1, z_2\right). \qquad (4.152d)
\end{aligned}$$

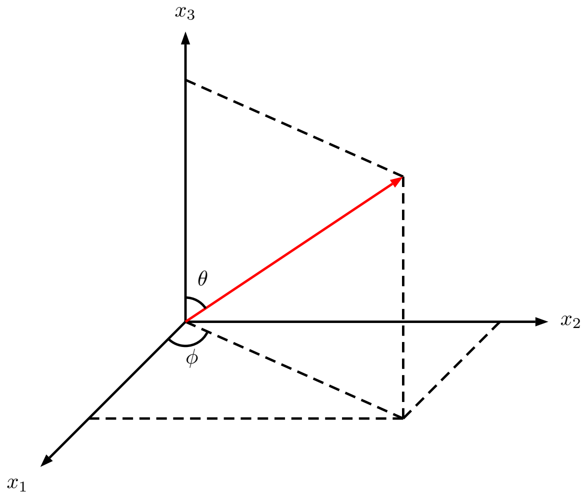

Figure 4.16: Every 3D unit vector can be parameterized by two angular variables (ϕ, θ); the position of the object implies that $(\phi, \theta) \in [0, 2\pi] \times [0, \pi/2]$.

In conclusion, by considering the conventional cone-beam projection as an intermediate function, and using the relationships between it and the weighted cone-beam projections (in many different geometry contexts), we can see how the weighted projections link to each other.

4.3.6.2 CBCC of the conventional cone-beam projections constructed from *CBCC13Converted*

Our aim is to start with *CBCC13Converted*, then to convert the weighted projection in *CBCC13Converted* geometry to the conventional projection, to obtain a new CBCC form, working with the conventional cone-beam projections. Just to remind, the weighted projection and the moment in *CBCC13Converted* geometry context were defined in equations (4.84), (4.103):

$$g^V(s_1, s_2, z_1, z_2) = \int_0^\infty f\left(\vec{s} + t\left(z_1\vec{\beta}_s + z_2\vec{e}_3 - D\vec{\alpha}_s\right)\right) dt, \tag{4.153a}$$

$$J_n^V(s_1, s_2, Y_1, Y_2) = \iint g^V(s_1, s_2, z_1, z_2) \left[\left(z_1\vec{\beta}_s - D\vec{\alpha}_s\right) \cdot (Y_1, Y_2, 0)\right]^n \frac{dz_1 dz_2}{z_2^{n+2}}. \tag{4.153b}$$

One forward step to get closer to the conventional projection is to use the relationship we just obtained in the previous section:

$$g^V(s_1, s_2, z_1, z_2) = g^{\text{conv}}(\vec{s}, \vec{\eta}(s_1, s_2, z_1, z_2)) \frac{1}{\sqrt{z_1^2 + z_2^2 + D^2}}. \tag{4.154}$$

Here $\vec{\eta}(s_1, s_2, z_1, z_2)$ is the unit vector parallel to the vector connecting the source $(s_1, s_2, 0)$ on the trajectory plane and the point (z_1, z_2) on the vertical detector. We have already known that every 3D unit vector can be parameterized by two angular variables ϕ and θ, where ϕ is the angle between x_1-axis and the projection of this unit vector on the trajectory plane $x_3 = 0$, and θ is the angle between x_3-axis and the unit vector. Figure 4.16 gives us an illustration. More precisely, the 3D coordinate of the unit vector in terms of (ϕ, θ) is:

$$\tilde{\eta}(\phi, \theta) = (\cos\phi \sin\theta, \sin\phi \sin\theta, \cos\theta). \tag{4.155}$$

Now we change the variables (z_1, z_2) in the formula of the moment $J_n^V(s_1, s_2, Y_1, Y_2)$ to the angular variables (ϕ, θ). In order to do that, we notice in the previous section $\vec{\eta}(s_1, s_2, z_1, z_2)$ is:

$$\vec{\eta}(s_1, s_2, z_1, z_2) = \frac{z_1\vec{\beta}_s + z_2\vec{e}_3 - D\vec{\alpha}_s}{\sqrt{z_1^2 + z_2^2 + D^2}} = \frac{1}{\|\vec{s}\| \sqrt{z_1^2 + z_2^2 + D^2}} \begin{bmatrix} -z_1 s_2 - D s_1 \\ z_1 s_1 - D s_2 \\ z_2 \|\vec{s}\| \end{bmatrix}. \tag{4.156}$$

Since $\vec{\eta}\left(s_1, s_2, z_1, z_2\right)$ and $\tilde{\eta}\left(\phi, \theta\right)$ are the two different representations of the same unit vector in two different system of variables, thus changing the variables from $\left(z_1, z_2\right)$ to $\left(\phi, \theta\right)$ means setting as follows:

$$\frac{1}{\left\|\vec{s}\right\| \sqrt{z_1^2+z_2^2+D^2}} \begin{bmatrix} -z_1 s_2 - D s_1 \\ z_1 s_1 - D s_2 \\ z_2 \left\|\vec{s}\right\| \end{bmatrix} = \begin{bmatrix} \cos\phi \sin\theta \\ \sin\phi \sin\theta \\ \cos\theta \end{bmatrix}. \tag{4.157}$$

Then we obtain the following system of equations:

$$-z_1 s_2 - D s_1 = \left\|\vec{s}\right\| \sqrt{z_1^2+z_2^2+D^2} \cos\phi \sin\theta, \tag{4.158a}$$

$$z_1 s_1 - D s_2 = \left\|\vec{s}\right\| \sqrt{z_1^2+z_2^2+D^2} \sin\phi \sin\theta, \tag{4.158b}$$

$$z_2 = \sqrt{z_1^2+z_2^2+D^2} \cos\theta. \tag{4.158c}$$

From the first two equations, using the using technique of multiplying the suitable values to each equation and summing together, we obtain:

$$z_1 \left(s_1^2+s_2^2\right) = \left\|\vec{s}\right\| \sqrt{z_1^2+z_2^2+D^2} \sin\theta \left(-s_2 \cos\phi + s_1 \sin\phi\right), \tag{4.159a}$$

$$D \left(s_1^2+s_2^2\right) = \left\|\vec{s}\right\| \sqrt{z_1^2+z_2^2+D^2} \sin\theta \left(-s_1 \cos\phi - s_2 \sin\phi\right). \tag{4.159b}$$

Then we can see that:

$$\sqrt{z_1^2+z_2^2+D^2} = \frac{D\left(s_1^2+s_2^2\right)}{\left\|\vec{s}\right\| \sin\theta \left(-s_1\cos\phi - s_2\sin\phi\right)} = \frac{D\left\|\vec{s}\right\|^2}{\left\|\vec{s}\right\| \sin\theta \left(-s_1\cos\phi - s_2\sin\phi\right)} = \frac{D\left\|\vec{s}\right\|}{-\sin\theta\left(s_1\cos\phi + s_2\sin\phi\right)}. \tag{4.160}$$

Thus from these materials, we obtain:

$$z_2 = \sqrt{z_1^2+z_2^2+D^2}\cos\theta = \frac{D\left\|\vec{s}\right\|}{-\sin\theta\left(s_1\cos\phi+s_2\sin\phi\right)}\cos\theta = \frac{-D\left\|\vec{s}\right\|}{\tan\theta\left(s_1\cos\phi+s_2\sin\phi\right)}, \tag{4.161a}$$

$$z_1 = \frac{\left\|\vec{s}\right\| \sqrt{z_1^2+z_2^2+D^2}\sin\theta\left(-s_2\cos\phi+s_1\sin\phi\right)}{s_1^2+s_2^2} \tag{4.161b}$$

$$= \frac{\left\|\vec{s}\right\|\sin\theta\left(-s_2\cos\phi+s_1\sin\phi\right)}{\left\|\vec{s}\right\|^2} \frac{D\left\|\vec{s}\right\|}{-\sin\theta\left(s_1\cos\phi+s_2\sin\phi\right)} \tag{4.161c}$$

$$= \frac{D\left(-s_1\sin\phi+s_2\cos\phi\right)}{s_1\cos\phi+s_2\sin\phi}. \tag{4.161d}$$

We have completely computed $\left(z_1, z_2\right)$ in terms of $\left(\phi, \theta\right)$.
Now by (4.160), the relationship between the weighted projection in *CBCC13Converted* geometry and the conventional projection can be rewritten as:

$$g^V\left(s_1, s_2, z_1, z_2\right) = g^{\text{conv}}\left(\vec{s}, \vec{\eta}\left(s_1, s_2, z_1, z_2\right)\right) \frac{1}{\sqrt{z_1^2+z_2^2+D^2}} = g^{\text{conv}}\left(\vec{s}, \tilde{\eta}\left(\phi, \theta\right)\right) \frac{-\sin\theta\left(s_1\cos\phi+s_2\sin\phi\right)}{D\left\|\vec{s}\right\|} \tag{4.162}$$

Moveover, we can also compute:

$$\frac{\partial z_1}{\partial \phi} = \frac{D\left(-s_1\cos\phi - s_2\sin\phi\right)\left(s_1\cos\phi + s_2\sin\phi\right) - D\left(-s_1\sin\phi + s_2\cos\phi\right)\left(-s_1\sin\phi + s_2\cos\phi\right)}{\left(s_1\cos\phi + s_2\sin\phi\right)^2}, \tag{4.163a}$$

$$= \frac{-D\left(s_1\cos\phi + s_2\sin\phi\right)^2 - D\left(-s_1\sin\phi + s_2\cos\phi\right)^2}{\left(s_1\cos\phi + s_2\sin\phi\right)^2} \tag{4.163b}$$

$$= \frac{-D\left(s_1^2 + s_2^2\right)}{\left(s_1\cos\phi + s_2\sin\phi\right)^2} \tag{4.163c}$$

$$= \frac{-D\left\|\vec{s}\right\|^2}{\left(s_1\cos\phi + s_2\sin\phi\right)^2}, \tag{4.163d}$$

$$\frac{\partial z_1}{\partial \theta} = 0, \tag{4.163e}$$

$$\frac{\partial z_2}{\partial \theta} = \frac{-D\left\|\vec{s}\right\|}{s_1\cos\phi + s_2\sin\phi}\frac{-1}{\tan^2\theta}\frac{1}{\cos^2\theta} \tag{4.163f}$$

$$= \frac{D\left\|\vec{s}\right\|}{\sin^2\theta\left(s_1\cos\phi + s_2\sin\phi\right)}. \tag{4.163g}$$

Then the determinant of the Jacobian matrix $J = \begin{bmatrix} \frac{\partial z_1}{\partial \phi} & \frac{\partial z_1}{\partial \theta} \\ \frac{\partial z_2}{\partial \phi} & \frac{\partial z_2}{\partial \theta} \end{bmatrix}$ is the following:

$$\det J = \frac{\partial z_1}{\partial \phi}\frac{\partial z_2}{\partial \theta} - \frac{\partial z_1}{\partial \theta}\frac{\partial z_2}{\partial \phi} \tag{4.164a}$$

$$= \frac{-D\left\|\vec{s}\right\|^2}{\left(s_1\cos\phi + s_2\sin\phi\right)^2}\frac{D\left\|\vec{s}\right\|}{\sin^2\theta\left(s_1\cos\phi + s_2\sin\phi\right)} \tag{4.164b}$$

$$= \frac{-D^2\left\|\vec{s}\right\|^3}{\sin^2\theta\left(s_1\cos\phi + s_2\sin\phi\right)^3}. \tag{4.164c}$$

Here $(\partial z_1/\partial\theta) = 0$, so it is not necessary to compute $(\partial z_2/\partial\phi)$. Then this implies:

$$dz_1 dz_2 = \frac{D^2\left\|\vec{s}\right\|^3}{\sin^2\theta\left(s_1\cos\phi + s_2\sin\phi\right)^3} d\phi d\theta. \tag{4.165}$$

We are now ready to change the variables from (z_1, z_2) to (ϕ, θ) in the formula of the moment $J_n^V\left(s_1, s_2, Y_1, Y_2\right)$:

$$J_n^V\left(s_1, s_2, Y_1, Y_2\right)$$

$$= \iint g^V\left(s_1, s_2, z_1, z_2\right)\left[\left(z_1\vec{\beta}_s - D\vec{\alpha}_s\right)\cdot\left(Y_1, Y_2, 0\right)\right]^n \frac{dz_1 dz_2}{z_2^{n+2}} \tag{4.166a}$$

$$= \int_0^{\pi/2}\int_0^{2\pi} g^{\text{conv}}\left(\vec{s}, \tilde{\eta}\left(\phi,\theta\right)\right)\frac{-\sin\theta\left(s_1\cos\phi + s_2\sin\phi\right)}{D\left\|\vec{s}\right\|}\left[\left(\frac{D\left(-s_1\sin\phi + s_2\cos\phi\right)}{s_1\cos\phi + s_2\sin\phi}\vec{\beta}_s - D\vec{\alpha}_s\right)\cdot\left(Y_1, Y_2, 0\right)\right]^n \times$$

$$\times\frac{\tan^{n+2}\theta\left(s_1\cos\phi + s_2\sin\phi\right)^{n+2}}{\left(-1\right)^{n+2}D^{n+2}\left\|\vec{s}\right\|^{n+2}}\frac{D^2\left\|\vec{s}\right\|^3}{\sin^2\theta\left(s_1\cos\phi + s_2\sin\phi\right)^3} d\phi d\theta. \tag{4.166b}$$

The term in the square brackets can be written as:

$$\left(\frac{D\left(-s_1\sin\phi+s_2\cos\phi\right)}{s_1\cos\phi+s_2\sin\phi}\vec{\beta}_s-D\vec{\alpha}_s\right)\cdot\left(Y_1,Y_2,0\right)$$

$$=\frac{D}{s_1\cos\phi+s_2\sin\phi}\left(\left(-s_1\sin\phi+s_2\cos\phi\right)\vec{\beta}_s-\left(s_1\cos\phi+s_2\sin\phi\right)\vec{\alpha}_s\right)\cdot\left(Y_1,Y_2,0\right) \tag{4.167a}$$

$$=\frac{D}{s_1\cos\phi+s_2\sin\phi}\left(\left(-s_1\sin\phi+s_2\cos\phi\right)\frac{1}{\|\vec{s}\|}\begin{bmatrix}-s_2\\ s_1\\ 0\end{bmatrix}-\left(s_1\cos\phi+s_2\sin\phi\right)\frac{1}{\|\vec{s}\|}\begin{bmatrix}s_1\\ s_2\\ 0\end{bmatrix}\right)\cdot\begin{bmatrix}Y_1\\ Y_2\\ 0\end{bmatrix} \tag{4.167b}$$

$$=\frac{D}{\|\vec{s}\|\left(s_1\cos\phi+s_2\sin\phi\right)}\begin{bmatrix}s_1s_2\sin\phi-s_2^2\cos\phi-s_1^2\cos\phi-s_1s_2\sin\phi\\ -s_1^2\sin\phi+s_1s_2\cos\phi-s_1s_2\cos\phi-s_2^2\sin\phi\\ 0\end{bmatrix}\cdot\begin{bmatrix}Y_1\\ Y_2\\ 0\end{bmatrix} \tag{4.167c}$$

$$=\frac{D}{\|\vec{s}\|\left(s_1\cos\phi+s_2\sin\phi\right)}\begin{bmatrix}-\left(s_1^2+s_2^2\right)\cos\phi\\ -\left(s_1^2+s_2^2\right)\sin\phi\\ 0\end{bmatrix}\cdot\begin{bmatrix}Y_1\\ Y_2\\ 0\end{bmatrix} \tag{4.167d}$$

$$=\frac{-D\left\|\vec{s}\right\|^2}{\|\vec{s}\|\left(s_1\cos\phi+s_2\sin\phi\right)}\begin{bmatrix}\cos\phi\\ \sin\phi\\ 0\end{bmatrix}\cdot\begin{bmatrix}Y_1\\ Y_2\\ 0\end{bmatrix} \tag{4.167e}$$

$$=\frac{-D\left\|\vec{s}\right\|}{s_1\cos\phi+s_2\sin\phi}\left(Y_1\cos\phi+Y_2\sin\phi\right). \tag{4.167f}$$

Then the above integral becomes:

$$J_n^V\left(s_1,s_2,Y_1,Y_2\right)$$

$$=\int_0^{\pi/2}\int_0^{2\pi}g^{\text{conv}}\left(\vec{s},\tilde{\eta}\left(\phi,\theta\right)\right)\frac{-\sin\theta\left(s_1\cos\phi+s_2\sin\phi\right)}{D\left\|\vec{s}\right\|}\left[\left(\frac{D\left(-s_1\sin\phi+s_2\cos\phi\right)}{s_1\cos\phi+s_2\sin\phi}\vec{\beta}_s-D\vec{\alpha}_s\right)\cdot\left(Y_1,Y_2,0\right)\right]^n\times$$

$$\times\frac{\tan^{n+2}\theta\left(s_1\cos\phi+s_2\sin\phi\right)^{n+2}}{\left(-1\right)^{n+2}D^{n+2}\left\|\vec{s}\right\|^{n+2}}\frac{D^2\left\|\vec{s}\right\|^3}{\sin^2\theta\left(s_1\cos\phi+s_2\sin\phi\right)^3}d\phi d\theta \tag{4.168a}$$

$$=\int_0^{\pi/2}\int_0^{2\pi}g^{\text{conv}}\left(\vec{s},\tilde{\eta}\left(\phi,\theta\right)\right)\frac{-\sin\theta\left(s_1\cos\phi+s_2\sin\phi\right)}{D\left\|\vec{s}\right\|}\frac{\left(-1\right)^nD^n\left\|\vec{s}\right\|^n}{\left(s_1\cos\phi+s_2\sin\phi\right)^n}\left(Y_1\cos\phi+Y_2\sin\phi\right)^n\times$$

$$\times\frac{\tan^{n+2}\theta\left(s_1\cos\phi+s_2\sin\phi\right)^{n+2}}{\left(-1\right)^{n+2}D^{n+2}\left\|\vec{s}\right\|^{n+2}}\frac{D^2\left\|\vec{s}\right\|^3}{\sin^2\theta\left(s_1\cos\phi+s_2\sin\phi\right)^3}d\phi d\theta \tag{4.168b}$$

$$=\frac{-1}{D}\int_0^{\pi/2}\int_0^{2\pi}g^{\text{conv}}\left(\vec{s},\tilde{\eta}\left(\phi,\theta\right)\right)\left(Y_1\cos\phi+Y_2\sin\phi\right)^n\tan^{n+2}\theta\frac{1}{\sin\theta}d\phi d\theta \tag{4.168c}$$

$$=\frac{-1}{D}\int_0^{\pi/2}\int_0^{2\pi}g^{\text{conv}}\left(\vec{s},\tilde{\eta}\left(\phi,\theta\right)\right)\left(Y_1\cos\phi+Y_2\sin\phi\right)^n\tan^{n+2}\theta\frac{1}{\cos\theta\tan\theta}d\phi d\theta \tag{4.168d}$$

$$=\frac{-1}{D}\int_0^{\pi/2}\int_0^{2\pi}g^{\text{conv}}\left(\vec{s},\tilde{\eta}\left(\phi,\theta\right)\right)\left(Y_1\cos\phi+Y_2\sin\phi\right)^n\frac{\tan^{n+1}\theta}{\cos\theta}d\phi d\theta. \tag{4.168e}$$

On the other hand, *CBCC13Converted* confirms that:

$$J_n^V\left(s_1,s_2,Y_1,Y_2\right)=K_n^V\left(Y_1,Y_2,-s_1Y_1-s_2Y_2\right), \tag{4.169}$$

where $K_n^V\left(Y_1,Y_2,Y_3\right)=\sum_{i+j+k=n}C_{i,j,k}^VY_1^iY_2^jY_3^k$ is a homogeneous polynomial in three variable of degree n. This leads to the following result:

$$\int_0^{\pi/2}\int_0^{2\pi}g^{\text{conv}}\left(\vec{s},\tilde{\eta}\left(\phi,\theta\right)\right)\left(Y_1\cos\phi+Y_2\sin\phi\right)^n\frac{\tan^{n+1}\theta}{\cos\theta}d\phi d\theta=-DJ_n^V\left(s_1,s_2,Y_1,Y_2\right) \tag{4.170a}$$

$$=-DK_n^V\left(Y_1,Y_2,-s_1Y_1-s_2Y_2\right). \tag{4.170b}$$

Thus if we define:

$$J_n^{\text{conv}}\left(\vec{s},Y_1,Y_2\right)=\int_0^{\pi/2}\int_0^{2\pi}g^{\text{conv}}\left(\vec{s},\tilde{\eta}\left(\phi,\theta\right)\right)\left(Y_1\cos\phi+Y_2\sin\phi\right)^n\frac{\tan^{n+1}\theta}{\cos\theta}d\phi d\theta, \tag{4.171a}$$

$$K_n^{\text{conv}}\left(Y_1,Y_2,Y_3\right)=-DK_n^V\left(Y_1,Y_2,Y_3\right), \tag{4.171b}$$

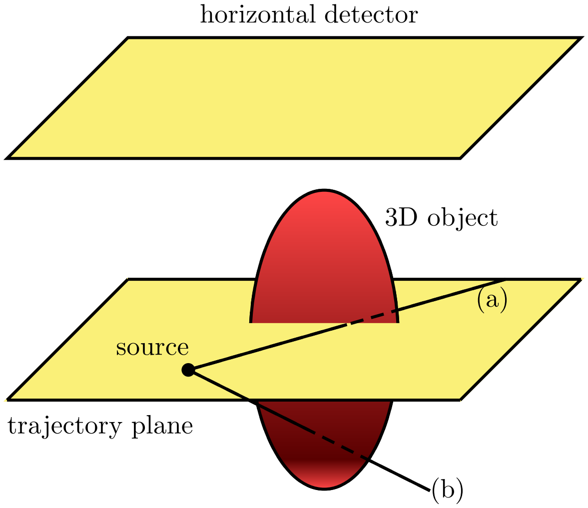

Figure 4.17: The object intersects the trajectory plane and this plane is parallel to the horizontal detector. There are rays connecting the source to the object being parallel to the detector (type (a)), or going away from the detector (type (b)). In both cases, these rays cannot hit the detector, which causes the truncation in the projections.

then we obtain the CBCC of the conventional projections as follows:

g^{conv} is in the range of $\mathcal{G}^{conv}f$: $g^{conv} = \mathcal{G}^{conv}f$ for some f (which is compactly supported real function, whose support is strictly above the plane $x_3 = 0$), if and only if for all $(s_1, s_2) \in \mathbb{R}^2$, $g^{conv}(\vec{s}, \cdot)$ has compact support in the upper unit hemisphere and:

$$J_n^{conv}(\vec{s}, Y_1, Y_2) = K_n^{conv}(Y_1, Y_2, -s_1Y_1 - s_2Y_2), \quad \forall n = 0, 1, 2, \ldots, \tag{4.172}$$

where $K_n^{conv}(Y_1, Y_2, Y_3)$ is a homogeneous polynomial in three variables Y_1, Y_2, Y_3 of degree n.

We can see that the above CBCC is the same as the CBCC for the conventional projections built in the *CBCC13* geometry, see theorem 5 in the paper [Clackdoyle and Desbat, 2013]. The reason is that: in that article, the CBCC for the conventional projections is built from the *CBCC13*. Now in our context, the CBCC we just obtained is built from *CBCC13Converted*, however *CBCC13Converted* is also based on *CBCC13*. Thus they are all connected. In fact, the double integral $\iint dz_1 dz_2$ cannot be changed directly to the integral $\int_0^{\pi/2}\int_0^{2\pi} d\phi d\theta$ without any arguments. But we decide to keep and show it clearly in the following section.

4.3.7 Comments on the position of the 3D object

From the beginning of this chapter, the object always needs to be strictly above the trajectory plane $x_3 = 0$. The reason is quite obvious in the geometry with the horizontal detector $x_3 = T > 0$ (*CBCC16Converted* and *CBCC13* geometry contexts). If the object intersects the trajectory plane, and this plane is parallel to the detector (that is what *horizontal detector* means), then the projections on the detector will be truncated, since the projection values are in fact the integration along the rays starting from the source locations and going towards the detector (here is the ray integral, not the line integral because the integrals in the projection definitions are $\int_0^\infty dt$ on $[0, \infty)$, not over the whole $\mathbb{R}$); but in this situation, even all the rays connecting the source to the (finite) detector cannot sufficiently cover the whole object. There are rays, which connect the source to the object, being parallel to the detector or going away from the detector. These rays are not able to hit the detector and the non-zero integration values on these rays will be missed, which causes the truncation in the projections, see figure 4.17.

In the geometry with the vertical detector (*CBCC16* and *CBCC13Converted* geometry contexts), meaning the detector is perpendicular to the trajectory plane, the formulae of the moments ($M_n^V(\lambda)$ in *CBCC16* geometry, and $J_n^V(s_1, s_2, Y_1, Y_2)$ in *CBCC13Converted* geometry) contain the term $1/\left(v^{n+2}\right)$ or $1/\left(z_2^{n+2}\right)$, which cause the singularity $v = 0$ or $z_2 = 0$. As mentioned in section 4.2.1, this singularity has been handled in *CBCC16* geometry by the paper [Clackdoyle et al., 2016]. But for *CBCC13Converted*, we have done nothing with it yet. That is the reason why we always keep the assumption that the object is strictly above the trajectory plane until now. Moreover, all of the constructions so far are based on the conversion between the geometry contexts. Then it is easy and helpful to keep the object at such a position, that makes all the geometry contexts work. It turns out the object should be strictly above the trajectory plane $x_3 = 0$. In addition to be strictly above the trajectory plane, there is one more hidden assumption on the object, which applies only in the geometry with the vertical detector, that we did not clearly mention yet. For simplicity, let's first assume that we are working with the elliptical-like source trajectory surrounding the world origin (i.e. the circular source trajectory is also counted as a special case); by "surrounding the world origin" we mean the world origin is inside the area of the trajectory. As the above statement, the object needs to be at a position that both geometry contexts (with the vertical and horizontal detectors) work. More precisely, the projections must be available and not truncated on both detectors. In the case with the vertical detector, with the same mechanism as the geometry with the horizontal detector, any rays connecting the source to the object should not be parallel to the vertical detector and must go towards to hit the detector, for all source locations on the trajectory. This means the **o**rthogonal **p**rojection of the **c**onvex **h**ull (OPCH for short) of the object onto the trajectory plane has to be inside the area of the trajectory. For illustration, figure 4.18 shows us two different positions of the object.

- In the top diagram, the OPCH of the object on the trajectory plane is strictly inside the area of the trajectory. So for all the source locations on the trajectory, the rays connecting them to the object go towards hitting the vertical detector. Thus the projections are available and there is no truncation for any source locations.
- On the other hand, in the bottom diagram, the OPCH of the object intersects the trajectory. Then we can see that, there are locations on the source trajectory, at which, there exist rays connecting them to the object, being parallel to the detector (type (a)), or going away from the detector (type (b)). These rays will not hit the vertical detector. So as in the geometry with the horizontal detector, the integration values on these rays will be missed, leading to the truncation in the projections. Similarly, if the OPCH of the object is strictly outside of the trajectory, then there will be source locations, such that all rays connecting them to the object are always in type (b), which go away from the detector. And this leads to the "non-sense" zero-projections, which are the projections with all values are 0 ("non-sense" here means we have no information extracted from these projections).

Thus the additional assumption on the object in the geometry with the vertical detector and an elliptical-like source trajectory surrounding the world origin, is that the orthogonal projection of its convex hull onto the trajectory plane has to be inside the area of the source trajectory.

So until now, with the geometry containing the vertical detector, two crucial conditions on the object to be satisfied are: the "strictly above" and "strictly inside" conditions. As mentioned above, this pair of conditions help determine the suitable position of the object, that makes the system work, but in the case when we have the elliptical-like source trajectory surrounding the world origin. To be more than that, let's consider a general closed convex source trajectory surrounding the world origin, by "closed" we mean that there is no starting-point or end-point on the trajectory. Then the above pair of conditions is still enough to guarantee that the projections and moments are well-defined. More precisely, if we consider the source to move along a general closed convex trajectory surrounding the world origin, if the support of the object is compact and does not intersect the trajectory plane, if the OPCH of the object on the trajectory plane is strictly inside the area of the trajectory and if the distance from the source to the vertical detector is sufficiently large such that the source and the detector are on different side comparing to the world origin for all source locations, then there is no truncation in all projections and no singularity in all moments, and the corresponding CBCC can work properly.

However, if our closed source trajectory is not convex, then the pair of conditions on the object is now not sufficient to determine a suitable position of the object. Figure 4.19 gives us an illustration. Those are the top views of two models, where the objects are initially assumed to be strictly above the trajectory planes, and their OPCHs on the trajectory planes are strictly inside the areas of the trajectories. But in both cases, there exist source locations such that the rays connecting them to the objects cannot hit the vertical detectors, because of the concavity of the trajectories. We show two different situations in figure 4.19 to mention that: the failure is not because of the OPCH of the object being inside a narrow branch of the concave-shape area (as in the top diagram). In the bottom diagram of figure 4.19, although it is not inside any narrow branches, the failure still happens. So it seems that depending on the source trajectory, being or not being inside a narrow branch of the concave-shape trajectory area will cause the failure. However, there is a same point in both models, that is: the OPCH of the object is not sufficiently near the world origin, so the object cannot be in between the source and the detector for all source

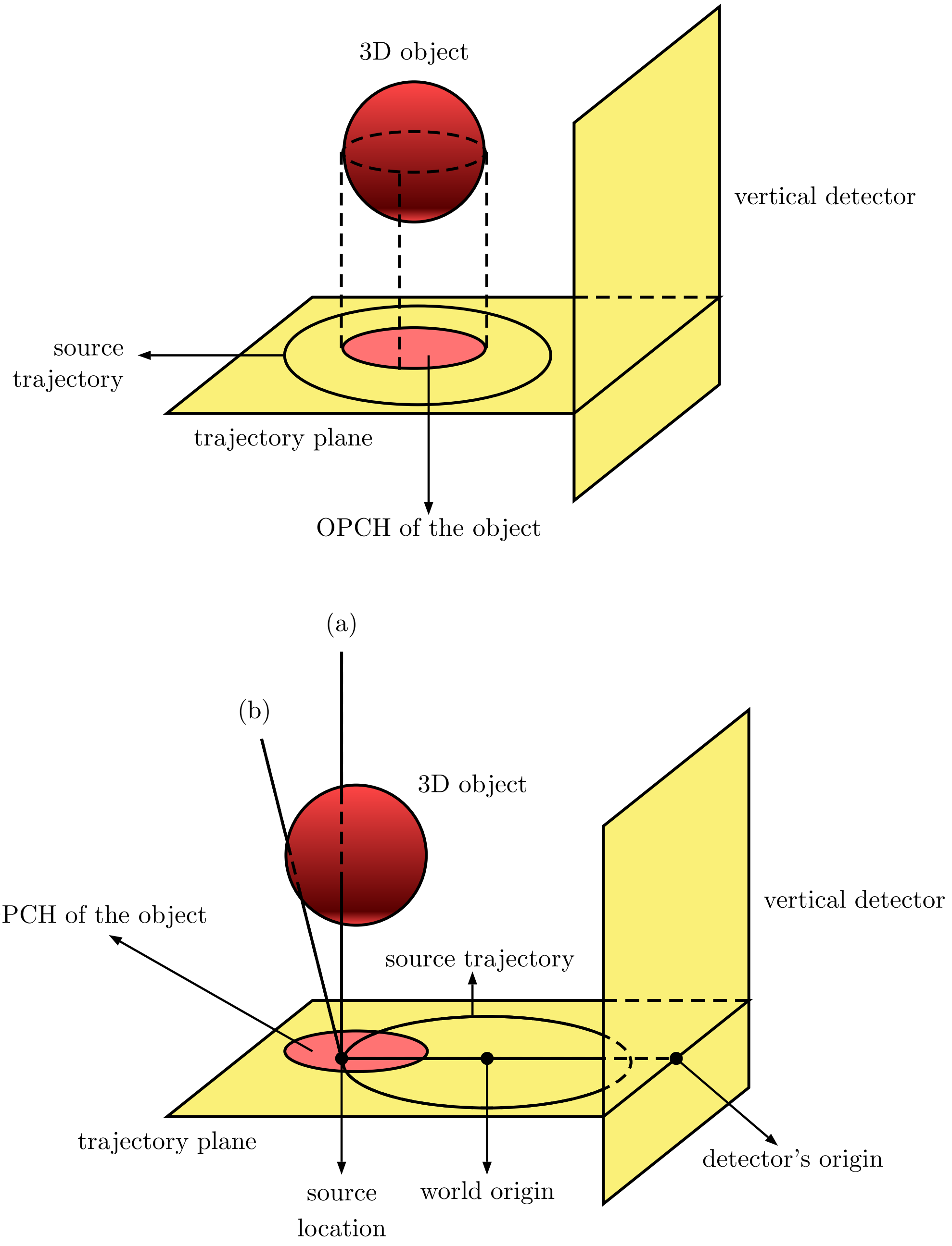

Figure 4.18: Two situations that the object being at two different positions, will or will not cause the truncation in the projections.

locations. Because as known in *CBCC13Converted* geometry, with sufficiently large D (D is the distance from the source to the vertical detector), the source and the vertical detector are always on different sides, comparing to the world origin, then sticking to the world origin and staying strictly inside the trajectory area would help the object be in between the source and the detector for any source locations. Thus for a general closed source trajectory surrounding the world origin, we suggest taking a disk on trajectory plane with the center at the world origin, which is strictly inside or at most tangent (from inside) the source trajectory, then considering the vertical cylinder, which has that disk as its lower base. The area strictly inside this cylinder and strictly above the trajectory plane will be the "safe zone" of the 3D object, because if the object is inside this zone, then it is always in between the source and the vertical detector for all source locations on the trajectory, and its support never intersects the trajectory plane, meaning there is no zero-projection, no truncation in the projections and no singularity in the moments. Figure 4.20 shows us the top view of a model with a general closed source trajectory surrounding the world origin and the orthogonal projection of the corresponding safe zone of the 3D object. There may be other safe positions of

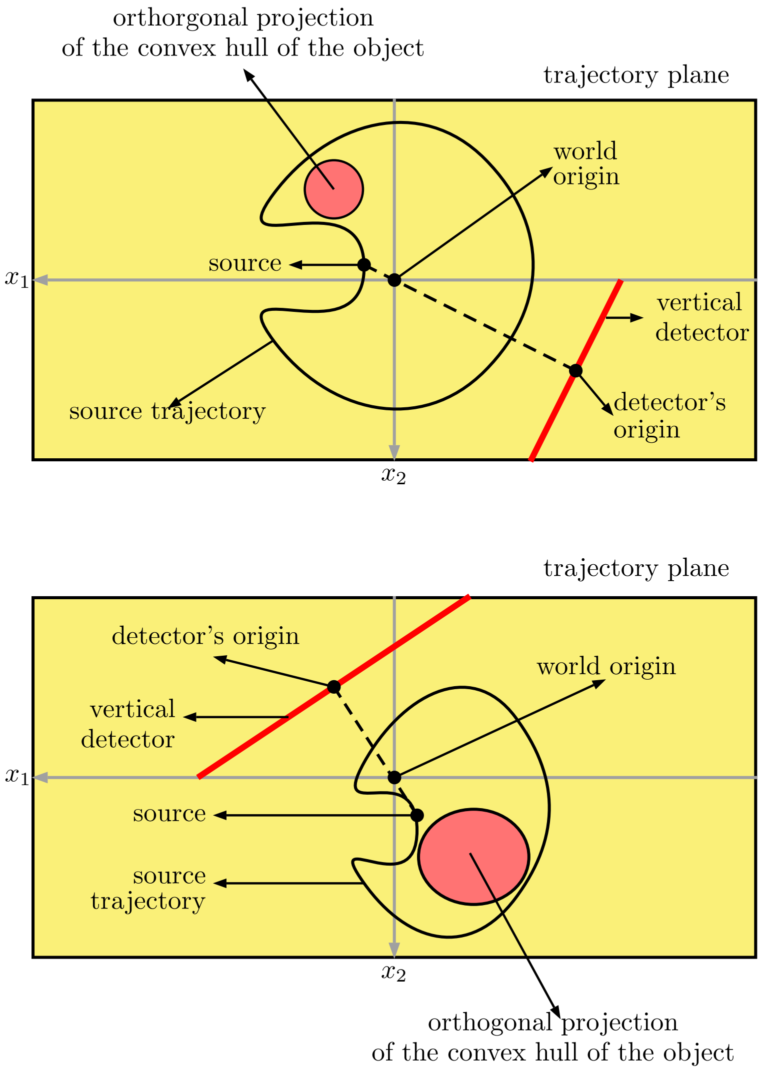

Figure 4.19: Two examples show the fact that the object's position and the source trajectory being not suitable for each other will cause the failure.

the 3D object depending on each particular situation, but our suggestion can probably work for any general closed source trajectory surrounding the world origin. In *CBCC13Converted* geometry, we do not yet develop on the source trajectory as much as in *CBCC13* geometry. We currently stop at the general closed trajectory surrounding the world origin, while in section 4.2.10, *CBCC13* has even been applied on several open trajectories, e.g. linear, parabolic trajectories, in order to obtain new DCCs or to see the relations between *CBCC13* and some old DCCs.

This knowledge on the positions of the object in the geometry with the horizontal and vertical detectors have to be applied respectively in *CBCC16Converted*, *CBCC13* geometry contexts and *CBCC16*, *CBCC13Converted* geometry contexts. Those conditions cannot be absent and are necessary for the process of changing variables in the corresponding geometry contexts. The role of these conditions is also essential during constructing the CBCC of the conventional projections. Let's first consider the condition built from *CBCC13Converted*. We can see that the main idea of the proof is to change the variables from (z_1, z_2) to (ϕ, θ), where ϕ and θ are defined in section 4.3.6.2, see figure 4.16. Normally, in the geometry context with the vertical detector, the integral $\iint dz_1 dz_2$ over the whole $\mathbb{R}^2$ will be changed to $\int_0^\pi \int_{\phi_0}^{\phi_0+\pi} d\phi d\theta$, meaning $(\phi, \theta) \in [\phi_0, \phi_0 + \pi] \times [0, \pi]$ (we will show the explicit the value of ϕ_0 later). Because as shown in figure 4.21, in order to have z_2 moving from $-\infty$ to ∞, θ has to move from 0 to π, the red semi-circle in the figure shows us the range of θ. Similarly, in order to have z_1 moving from $-\infty$ to ∞, we need ϕ to move in a π-range angle, here we say that ϕ is from ϕ_0 to $\phi_0 + \pi$, the semi-circle built from the blue arrows on the trajectory plane shows us the range of ϕ. Thus after the mathematical developments in section 4.3.6.2, the

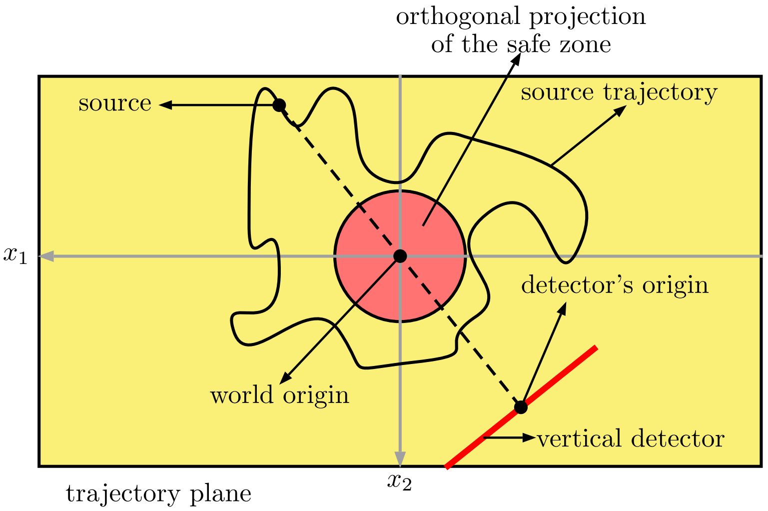

Figure 4.20: Illustration of an ideal position of the object when we have a general source trajectory

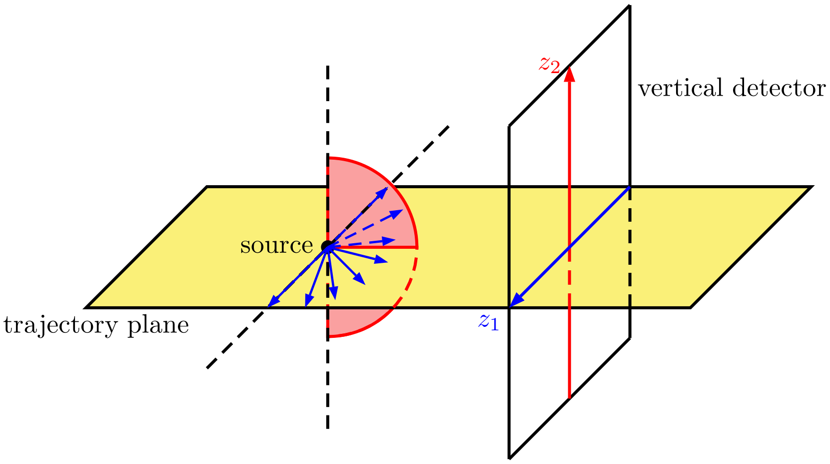

Figure 4.21: Illustration of the range of ϕ and θ when both z_1 and z_2 vary from $-\infty$ to ∞

moment $J_n^V(s_1, s_2, Y_1, Y_2)$ in fact becomes:

$$J_n^V(s_1, s_2, Y_1, Y_2) = \iint g^V(s_1, s_2, z_1, z_2)\left[\left(z_1\vec{\beta}_s - D\vec{\alpha}_s\right)\cdot(Y_1, Y_2, 0)\right]^n \frac{dz_1 dz_2}{z_2^{n+2}} \tag{4.173a}$$

$$= -\frac{1}{D}\int_0^{\pi}\int_{\phi_0}^{\phi_0+\pi} g^{\text{conv}}\left(\vec{s}, \tilde{\eta}(\phi, \theta)\right)(Y_1\cos\phi + Y_2\sin\phi)^n \frac{\tan^{n+1}\theta}{\cos\theta} d\phi d\theta. \tag{4.173b}$$

Now we are going to explain that using the conditions on the object leads the intergral $\int_0^{\pi}\int_{\phi_0}^{\phi_0+\pi} d\phi d\theta$ to the integral $\int_0^{\pi/2}\int_0^{2\pi} d\phi d\theta$, as in the final result we obtain in section 4.3.6.2.

- About θ: We know that the object is strictly above the trajectory plane, so from the figure 4.21, if $\theta \in (\pi/2, \pi]$ then $g^{\text{conv}}(\vec{s}, \tilde{\eta}(\phi, \theta)) = 0$, which means there is no contribution in the above integral if $\theta \in (\pi/2, \pi]$, so it can be rewritten as:

$$J_n^V(s_1, s_2, Y_1, Y_2) = -\frac{1}{D}\int_0^{\pi/2}\int_{\phi_0}^{\phi_0+\pi} g^{\text{conv}}\left(\vec{s}, \tilde{\eta}(\phi, \theta)\right)(Y_1\cos\phi + Y_2\sin\phi)^n \frac{\tan^{n+1}\theta}{\cos\theta} d\phi d\theta \tag{4.174a}$$

$$= -\frac{1}{D}\int_0^{\pi/2}\left[\int_{\phi_0}^{\phi_0+\pi} g^{\text{conv}}\left(\vec{s}, \tilde{\eta}(\phi, \theta)\right)(Y_1\cos\phi + Y_2\sin\phi)^n d\phi\right]\frac{\tan^{n+1}\theta}{\cos\theta} d\theta \tag{4.174b}$$

$$= -\frac{1}{D}\int_0^{\pi/2} L(\vec{s}, Y_1, Y_2, \theta)\frac{\tan^{n+1}\theta}{\cos\theta} d\theta, \tag{4.174c}$$

where

$$L\left(\vec{s}, Y_1, Y_2, \theta\right) = \int_{\phi_0}^{\phi_0+\pi} g^{\text{conv}}\left(\vec{s}, \tilde{\eta}\left(\phi, \theta\right)\right)\left(Y_1 \cos\phi + Y_2 \sin\phi\right)^n d\phi. \tag{4.175}$$

We are considering $L\left(\vec{s}, Y_1, Y_2, \theta\right)$ as a temporary function for convenience. Here we can see that there is a singularity $\cos\theta = 0$, occurring when $\theta = \pi/2$. There is also another singularity $\sin\theta = 0$, occurring when $\theta = 0$, because in the process of the proof in section 4.3.6.2, $\sin\theta$ is on the denominator for a few times. However, thanks to the conditions on the object, these singularities are handled. The support of the object is compact, it does not intersect the trajectory plane, and the object is strictly inside the "safe cylinder" (explained in the previous comments), which means for any source locations, any rays starting from the source and staying in the trajectory plane or being parallel to the corresponding vertical detector, cannot touch the object. Moreover, the conditions on the support of the object lead to the fact that: there exist θ_1 and θ_2 such that: $0 < \theta_1 < \theta_2 < \pi/2$ and:

$$g^{\text{conv}}\left(\vec{s}, \tilde{\eta}\left(\phi, \theta\right)\right) = 0, \quad \forall\theta \in \left[0, \theta_1\right) \cup \left(\theta_2, \pi/2\right]. \tag{4.176}$$

Then the above integral again can be rewritten as:

$$- DJ_n^V\left(s_1, s_2, Y_1, Y_2\right) \tag{4.177a}$$

$$= \int_0^{\pi/2} L\left(\vec{s}, Y_1, Y_2, \theta\right) \frac{\tan^{n+1}\theta}{\cos\theta} d\theta \tag{4.177b}$$

$$= \int_0^{\theta_1} L\left(\vec{s}, Y_1, Y_2, \theta\right) \frac{\tan^{n+1}\theta}{\cos\theta} d\theta + \int_{\theta_1}^{\theta_2} L\left(\vec{s}, Y_1, Y_2, \theta\right) \frac{\tan^{n+1}\theta}{\cos\theta} d\theta + \int_{\theta_2}^{\pi/2} L\left(\vec{s}, Y_1, Y_2, \theta\right) \frac{\tan^{n+1}\theta}{\cos\theta} d\theta \tag{4.177c}$$

$$= \left[\lim_{\epsilon_1 \to 0} \int_{\epsilon_1}^{\theta_1} L\left(\vec{s}, Y_1, Y_2, \theta\right) \frac{\tan^{n+1}\theta}{\cos\theta} d\theta\right] + \int_{\theta_1}^{\theta_2} L\left(\vec{s}, Y_1, Y_2, \theta\right) \frac{\tan^{n+1}\theta}{\cos\theta} d\theta \tag{4.177d}$$

$$+ \left[\lim_{\epsilon_2 \to \pi/2} \int_{\theta_2}^{\epsilon_2} L\left(\vec{s}, Y_1, Y_2, \theta\right) \frac{\tan^{n+1}\theta}{\cos\theta} d\theta\right]. \tag{4.177e}$$

Here we change to the limitations because of the singularities when $\theta = 0$ or $\theta = \pi/2$. Using condition (4.176), we can see that $L\left(\vec{s}, Y_1, Y_2, \theta\right) = 0$ for any $\theta \in \left[0, \theta_1\right) \cup \left(\theta_2, \pi/2\right]$ and this implies the two limitations in fact equal 0 and:

$$-DJ_n^V\left(s_1, s_2, Y_1, Y_2\right) = \int_{\theta_1}^{\theta_2} L\left(\vec{s}, Y_1, Y_2, \theta\right) \frac{\tan^{n+1}\theta}{\cos\theta} d\theta, \tag{4.178}$$

or:

$$J_n^V\left(s_1, s_2, Y_1, Y_2\right) = -\frac{1}{D} \int_0^{\pi/2} \int_{\phi_0}^{\phi_0+\pi} g^{\text{conv}}\left(\vec{s}, \tilde{\eta}\left(\phi, \theta\right)\right)\left(Y_1 \cos\phi + Y_2 \sin\phi\right)^n \frac{\tan^{n+1}\theta}{\cos\theta} d\phi d\theta \tag{4.179a}$$

$$= -\frac{1}{D} \int_{\theta_1}^{\theta_2} \int_{\phi_0}^{\phi_0+\pi} g^{\text{conv}}\left(\vec{s}, \tilde{\eta}\left(\phi, \theta\right)\right)\left(Y_1 \cos\phi + Y_2 \sin\phi\right)^n \frac{\tan^{n+1}\theta}{\cos\theta} d\phi d\theta, \tag{4.179b}$$

where $0 < \theta_1 < \theta_2 < \pi/2$, and this integral does not have any singularities with respect to θ. To summarize this step concerning θ, we have shown that the original integral $\int_0^{\pi} d\theta$ can be rewritten as $\int_0^{\pi/2} d\theta$ because the support of the object is compact and strictly above the trajectory plane, then we have proven that this integral $\int_0^{\pi/2} d\theta$ valids without any singularities because it just equals to $\int_{\theta_1}^{\theta_2} d\theta$ with $0 < \theta_1 < \theta_2 < \pi/2$, again thanks to the conditions on the object.

- <u>About ϕ</u>: As shown in figure 4.21, ϕ needs to move in a π-range angle, where the two bounding rays of the angle together make a parallel line (on the trajectory plane) to the vertical detector. Figure 4.22 is showing us the top view of the model. For any source location on the trajectory, we call $\psi_s \in [0, 2\pi)$ the angle between x_1-axis and the ray connecting the world origin to the source. This angle ψ_s depends on $\vec{s}$ and is defined by the following formulae:

$$\cos\psi_s = \frac{s_1}{\sqrt{s_1^2 + s_2^2}}, \quad \text{and} \quad \sin\psi_s = \frac{s_2}{\sqrt{s_1^2 + s_2^2}}. \tag{4.180}$$

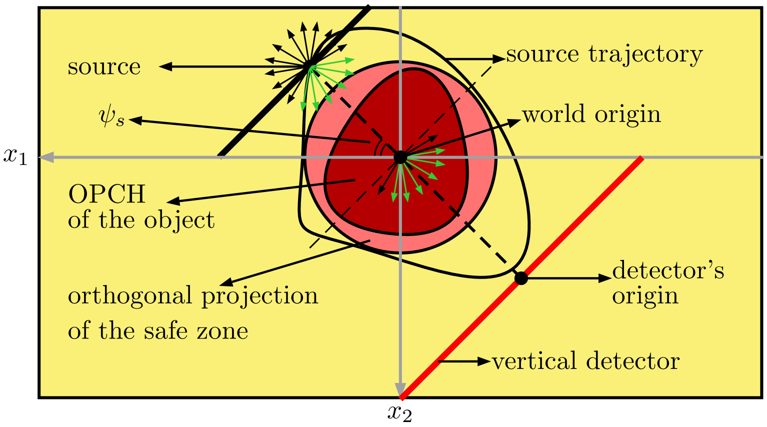

Figure 4.22: Top view of the model showing an illustration of the range of ϕ

Then ϕ will move from $(\phi_0 = \psi_s + \pi/2)$ to $(\phi_0 + \pi = \psi_s + 3\pi/2)$, since the line built from two bounding rays (of the π-range angle of moving of ϕ) is parallel to the vertical detector, and then is perpendicular to the line connecting the world origin to the source, see figure 4.22. Since the support of the object is compact and strictly inside the "safe cylinder", then it does not intersect the plane, which goes through the source location and parallel to the vertical detector. So all the rays starting from the source and staying in this plane cannot touch the object, and we know that these rays have the directions constructed by $\theta \in [0, \pi]$ and $\phi = \phi_0$ or $\phi = \phi_0 + \pi$. This means $g^{\text{conv}}\left(\vec{s}, \tilde{\eta}\left(\phi, \theta\right)\right) = 0$ if $\phi = \phi_0$ or $\phi = \phi_0 + \pi$, or we can say that $\phi = \phi_0$ and $\phi = \phi_0 + \pi$ do not contribute in the integral in the formula of the moment $J_n^V\left(s_1, s_2, Y_1, Y_2\right)$. In fact, $\phi \neq \phi_0$ and $\phi \neq \phi_0 + \pi$ are helpful for the proof in section 4.3.6.2. In that proof, there are a few times the term $(s_1 \cos\phi + s_2 \sin\phi)$ being on the denominator, leading to a singularity $s_1 \cos\phi + s_2 \sin\phi = 0$. This term can be understood as a scalar product of (s_1, s_2) and $(\cos\phi, \sin\phi)$ on the trajectory plane, so it equals 0 when the two vectors (s_1, s_2) and $(\cos\phi, \sin\phi)$ are perpendicular to each other and this only happens when $\phi = \phi_0 = \psi_s + \pi/2$ or $\phi = \phi_0 + \pi = \psi_s + 3\pi/2$, see figure 4.22. Also thanks to the conditions on the support of the object, we can claim that there exist ϕ_1 and ϕ_2 such that: $\phi_0 < \phi_1 < \phi_2 < \phi_0 + \pi$ and:

$$g^{\text{conv}}\left(\vec{s}, \tilde{\eta}\left(\phi, \theta\right)\right) = 0, \quad \forall \phi \in [\phi_0, \phi_1) \cup (\phi_2, \phi_0 + \pi]\,. \tag{4.181}$$

Then using this condition and the same technique of changing the bounds of the integral with respect to ϕ: $\int_{\phi_0}^{\phi_0+\pi} d\phi = \int_{\phi_0}^{\phi_1} d\phi + \int_{\phi_1}^{\phi_2} d\phi + \int_{\phi_2}^{\phi_0+\pi} d\phi$, then passing to the limitations as the above comment concerning θ, we can prove that:

$$-DJ_n^V\left(s_1, s_2, Y_1, Y_2\right) = \int_0^{\pi/2} \int_{\phi_0}^{\phi_0+\pi} g^{\text{conv}}\left(\vec{s}, \tilde{\eta}\left(\phi, \theta\right)\right) \left(Y_1 \cos\phi + Y_2 \sin\phi\right)^n \frac{\tan^{n+1}\theta}{\cos\theta} d\phi d\theta \tag{4.182a}$$

$$= \int_0^{\pi/2} \int_{\phi_1}^{\phi_2} g^{\text{conv}}\left(\vec{s}, \tilde{\eta}\left(\phi, \theta\right)\right) \left(Y_1 \cos\phi + Y_2 \sin\phi\right)^n \frac{\tan^{n+1}\theta}{\cos\theta} d\phi d\theta ., \tag{4.182b}$$

and the integral in equation (4.182b) is well-defined with no singularity. This means we can keep the formula of the integral with respect to ϕ as $\int_{\phi_0}^{\phi_0+\pi} d\phi$ without worrying about the singularity, because the value of this integral in fact coincides with the value of the integral $\int_{\phi_1}^{\phi_2} d\phi$, thanks to the support of the object being compact and strictly inside the "safe cylinder". More than that, also due to these conditions on the support of the object, we can once again extend the bounds of ϕ to $[\phi_0, \phi_0 + 2\pi)$, since $[\phi_0 + \pi, \phi_0 + 2\pi)$ does not contribute in the integral: $g^{\text{conv}}\left(\vec{s}, \tilde{\eta}\left(\phi, \theta\right)\right) = 0$ if $\phi \in [\phi_0 + \pi, \phi_0 + 2\pi)$. Thus the integral in equation (4.182a) can be rewritten as:

$$-DJ_n^V\left(s_1, s_2, Y_1, Y_2\right) = \int_0^{\pi/2} \int_{\phi_0}^{\phi_0+2\pi} g^{\text{conv}}\left(\vec{s}, \tilde{\eta}\left(\phi, \theta\right)\right) \left(Y_1 \cos\phi + Y_2 \sin\phi\right)^n \frac{\tan^{n+1}\theta}{\cos\theta} d\phi d\theta . \tag{4.183}$$

and its value coincides with the integral in equation (4.182b) with no singularity. Now we will prove that the integral with respect to ϕ can also be written as $\int_0^{2\pi} d\phi$. We change the order of integration and set:

$$\overline{L}\left(\vec{s}, Y_1, Y_2, \phi\right) = \int_0^{\pi/2} g^{\text{conv}}\left(\vec{s}, \tilde{\eta}\left(\phi, \theta\right)\right) \left(Y_1 \cos\phi + Y_2 \sin\phi\right)^n \frac{\tan^{n+1}\theta}{\cos\theta} d\theta , \tag{4.184}$$

Then the term $-DJ_n^V(s_1,s_2,Y_1,Y_2)$ will become:

$$-DJ_n^V(s_1,s_2,Y_1,Y_2) \tag{4.185a}$$
$$=\int_{\phi_0}^{\phi_0+2\pi}\overline{L}(\vec{s},Y_1,Y_2,\phi)\,d\phi \tag{4.185b}$$
$$=\int_{\phi_0}^{0}\overline{L}(\vec{s},Y_1,Y_2,\phi)\,d\phi+\int_{0}^{2\pi}\overline{L}(\vec{s},Y_1,Y_2,\phi)\,d\phi+\int_{2\pi}^{\phi_0+2\pi}\overline{L}(\vec{s},Y_1,Y_2,\phi)\,d\phi \tag{4.185c}$$
$$=\int_{\phi_0+2\pi}^{2\pi}\overline{L}(\vec{s},Y_1,Y_2,\phi'-2\pi)\,d\phi'+\int_{0}^{2\pi}\overline{L}(\vec{s},Y_1,Y_2,\phi)\,d\phi+\int_{2\pi}^{\phi_0+2\pi}\overline{L}(\vec{s},Y_1,Y_2,\phi)\,d\phi, \tag{4.185d}$$

here we have changed the variable $\phi'=\phi+2\pi$ in the first integral, then $d\phi'=d\phi$ and ϕ' is from $(\phi_0+2\pi)$ to 2π. Moreover we can see that $\overline{L}(\vec{s},Y_1,Y_2,\phi)$ is in fact a periodic function with respect to ϕ of period 2π, since all the ϕ-dependent terms in the formula of $\overline{L}(\vec{s},Y_1,Y_2,\phi)$ are built from $\cos\phi$ and $\sin\phi$:

$$\tilde{\eta}(\phi+j2\pi,\theta)=\begin{bmatrix}\cos(\phi+j2\pi)\sin\theta\\ \sin(\phi+j2\pi)\sin\theta\\ \cos\theta\end{bmatrix}=\begin{bmatrix}\cos\phi\sin\theta\\ \sin\phi\sin\theta\\ \cos\theta\end{bmatrix}=\tilde{\eta}(\phi,\theta), \tag{4.186a}$$
$$\cos(\phi+k2\pi)=\cos\phi, \tag{4.186b}$$
$$\sin(\phi+l2\pi)=\sin\phi, \tag{4.186c}$$

for any integers j,k,l. Thus we can continue the above calculations as follows:

$$-DJ_n^V(s_1,s_2,Y_1,Y_2) \tag{4.187a}$$
$$=\int_{\phi_0+2\pi}^{2\pi}\overline{L}(\vec{s},Y_1,Y_2,\phi'-2\pi)\,d\phi'+\int_{0}^{2\pi}\overline{L}(\vec{s},Y_1,Y_2,\phi)\,d\phi+\int_{2\pi}^{\phi_0+2\pi}\overline{L}(\vec{s},Y_1,Y_2,\phi)\,d\phi \tag{4.187b}$$
$$=\int_{\phi_0+2\pi}^{2\pi}\overline{L}(\vec{s},Y_1,Y_2,\phi')\,d\phi'+\int_{0}^{2\pi}\overline{L}(\vec{s},Y_1,Y_2,\phi)\,d\phi+\int_{2\pi}^{\phi_0+2\pi}\overline{L}(\vec{s},Y_1,Y_2,\phi)\,d\phi \tag{4.187c}$$
$$=\int_{0}^{2\pi}\overline{L}(\vec{s},Y_1,Y_2,\phi)\,d\phi \tag{4.187d}$$
$$=\int_{0}^{2\pi}\int_{0}^{\pi/2}g^{\text{conv}}(\vec{s},\tilde{\eta}(\phi,\theta))(Y_1\cos\phi+Y_2\sin\phi)^n\frac{\tan^{n+1}\theta}{\cos\theta}d\theta d\phi. \tag{4.187e}$$

Then we obtain the result as in section 4.3.6.2:

$$J_n^V(s_1,s_2,Y_1,Y_2)=-\frac{1}{D}\int_{0}^{\pi/2}\int_{0}^{2\pi}g^{\text{conv}}(\vec{s},\tilde{\eta}(\phi,\theta))(Y_1\cos\phi+Y_2\sin\phi)^n\frac{\tan^{n+1}\theta}{\cos\theta}d\phi d\theta. \tag{4.188}$$

The two final comments we want to make here are the followings:

- The moment of the conventional projections built from *CBCC13* shares the same formula with the one built from *CBCC13Converted*, and has the same singularity $\cos\theta=0$. In the geometry with the horizontal detector, this singularity is handled by the condition that the support of the object is compact and strictly above the trajectory plane. The way to do this is completely similar to what we have done above in *CBCC13Converted* geometry. In the detailed proof changing *CBCC13* to the CBCC of the conventional projections, there is no additional singularity, unlike the proof changing *CBCC13Converted* to the CBCC of the conventional projections (there are a few additional singularities that we need to take care). Anyway, the conditions on the support of the object as we mentioned in the corresponding geometry with the horizontal and vertical detectors are sufficient to build the CBCC of the conventional projections from *CBCC13* and *CBCC13Converted* respectively.

- Since the CBCC of the conventional projections we obtain in section 4.3.6.2 is built from *CBCC13Converted*, and because of the settings *CBCC13Converted* geometry, this CBCC can only be applied on the object having compact support, which is strictly above the trajectory plane and strictly inside the safe cylinder that we have mentioned above; while the CBCC of the conventional projections built from *CBCC13* just require the support of the object to be compact and strictly above the trajectory plane. Thus although the moments in both cases coincide and the two CBCCs share the same statement, the CBCC of the conventional projections built from *CBCC13Converted* seems to be a special case of the one built from *CBCC13*. Anyway, those CBCCs are not the final form of the CBCC for the conventional projections. The CBCC for the conventional projections should not have any requirements on the position of the object. The only requirement on the object is that its support is compact. Because all of the mentioned conditions on the position of the object come from the fact that: the CBCCs of the conventional projections obtained so far are built from some original geometry contexts (*CBCC13* and *CBCC13Converted* geometry contexts) and these corresponding original geometry contexts have detectors, and those detectors are flat. The flat detectors require suitable positions of the object to make the corresponding weighted projections be non-truncated. However, when we really work with the conventional projections, there is no detector. Theoretically, the conventional projections always exist and are non-truncated if the object has compact support. Another “weird” example to also explain why we mention “flat detectors” is that if we still consider the source to move on a finite plane along a general trajectory, and we have a “sphere” detector, which is big enough to contain the finite trajectory plane strictly inside, then the compactly supported object can be anywhere inside that sphere, the weighted projections collected on this sphere detector always exist and are non-truncated. Then building the CBCC of the conventional projections from this geometry context maybe one step towards to obtain the final form of the CBCC for the conventional projections. Here we have no further result than what have been shown, but there are still interesting and considerable things concerning the CBCC for the conventional projections to investigate.

4.3.8 Generalization of *CBCC16*

In this section, we will develop *CBCC13Converted* to a general version of *CBCC16*. As mentioned in the previous section, until now, we still have the singularity $z_2 = 0$ caused by the term $\left(1/z_2^{n+2}\right)$ in the moment $J_n^V\left(s_1, s_2, Y_1, Y_2\right)$ in *CBCC13Converted* geometry, which keeps us having to assume that the support of the object must be strictly above the trajectory plane, while it was handled perfectly in *CBCC16* geometry. In [Clackdoyle et al., 2016], in order to prove the moment $M_n^V(\lambda)$ is a homogeneous polynomial in $\cos\lambda$ and $\sin\lambda$ of degree n allowing the support of the object to intersect the trajectory plane, the authors have defined an intermediate integration of the conventional projection, which can be quickly proven to be a homogeneous polynomial, then this intermediate integration is proven to also equal the original moment. Now, in *CBCC13Converted* geometry, let us redefine again the weighted projections and moments with a different set of notations, to emphasize that: the following projections and moments are computed from the 3D object, which is allowed to intersect the trajectory plane. Precisely, the weighted projections on the vertical detector and the moments are respectively defined as follows:

$$\widehat{g}\left(s_1, s_2, z_1, z_2\right) = \int_0^\infty f\left(\vec{s} + t\left(z_1\vec{\beta}_s + z_2\vec{e}_3 - D\vec{\alpha}_s\right)\right)dt, \quad \text{where } f\left(\cdot,\cdot,x_3\right) \in \mathscr{C}^{n+1}\left(\mathbb{R}\right), \tag{4.189a}$$

$$\widehat{J}_n\left(s_1, s_2, Y_1, Y_2\right) = \iint \widehat{g}\left(s_1, s_2, z_1, z_2\right)\left[\left(z_1\vec{\beta}_s - D\vec{\alpha}_s\right)\cdot\left(Y_1, Y_2, 0\right)\right]^n h_n\left(z_2\right)dz_1dz_2, \tag{4.189b}$$

where $h_n(v)$ is the inverse Fourier transform of $H_n(\nu)$, $h_n(v) = \int H_n(\nu)\, e^{2i\pi\nu v}d\nu$ and:

$$H_n(\nu) = \frac{(-2i\pi)^{n+2}}{2(n+1)!}\left|\nu\right|\nu^n. \tag{4.190}$$

For any $\sigma \in \mathbb{R}$ and $\sigma \neq 0$, we can see that:

$$H_n\left(\frac{\nu}{\sigma}\right) = \frac{(-2i\pi)^{n+2}}{2(n+1)!}\left|\frac{\nu}{\sigma}\right|\left(\frac{\nu}{\sigma}\right)^n = \frac{1}{|\sigma|\,\sigma^n}\frac{(-2i\pi)^{n+2}}{2(n+1)!}\left|\nu\right|\nu^n = \frac{1}{|\sigma|\,\sigma^n}H_n(\nu). \tag{4.191}$$

From this, by a simple change of variables, we can compute:

$$h_n(\sigma v) = \int H_n(\nu)\, e^{2i\pi\nu(\sigma v)}d\nu \qquad = \int H_n(\nu)\, e^{2i\pi(\sigma\nu)v}d\nu \tag{4.192a}$$

$$= \int H_n\left(\frac{\nu'}{\sigma}\right)e^{2i\pi\nu' v}\frac{d\nu'}{|\sigma|} \qquad = \int \frac{1}{|\sigma|\,\sigma^n}H_n\left(\nu'\right)e^{2i\pi\nu' v}\frac{d\nu'}{|\sigma|} \tag{4.192b}$$

$$= \frac{1}{\sigma^{n+2}}\int H_n\left(\nu'\right)e^{2i\pi\nu' v}d\nu' \qquad = \frac{h_n(v)}{\sigma^{n+2}}, \tag{4.192c}$$

$$h_n(v) = \sigma^{n+2}h_n(\sigma v). \tag{4.192d}$$

We obtain these properties for any non-zero real number σ.
Now the generalized CBCC in the geometry with the vertical detector can be stated as:

If $\widehat{g}\left(s_1, s_2, z_1, z_2\right)$ *is the weighted cone-beam projection of some compactly supported function* f*, allowing this support to intersect the trajectory plane, for all* $\left(s_1, s_2\right) \in \mathbb{R}^2$*, where* $f\left(\cdot, \cdot, x_3\right) \in \mathscr{C}^{n+1}\left(\mathbb{R}\right)$ *as defined in equation* (4.189a)*, then:*

$$\widehat{J}_n\left(s_1, s_2, Y_1, Y_2\right) = \widehat{K}_n\left(Y_1, Y_2, -s_1 Y_1 - s_2 Y_2\right), \tag{4.193}$$

where $\widehat{J}_n\left(s_1, s_2, Y_1, Y_2\right)$ *is the moment defined in equation* (4.189b) *and* $\widehat{K}_n\left(Y_1, Y_2, Y_3\right)$ *is a three-variable homogeneous polynomial of degree* n*.*

From the mathematical building blocks in previous sections, we now have in hand two approaches to prove this result: either attacking directly the result (see section 4.3.8.1), or following the beautiful technique presented in the paper [Clackdoyle et al., 2016] (see section 4.3.8.2).

4.3.8.1 Approach 1: attacking directly the result

The idea of this approach is just to reuse the materials in section 4.3.4. Since the moments $J_n^V\left(s_1, s_2, Y_1, Y_2\right)$ and $\widehat{J}_n\left(s_1, s_2, Y_1, Y_2\right)$ are only different because of replacing the term $\left(1/z_1^{n+2}\right)$ by $h_n\left(z_2\right)$, this approach is in fact almost the same as the proof in section 4.3.4. From the definitions (4.189a) and (4.189b), we can see that:

$$\widehat{J}_n\left(s_1, s_2, Y_1, Y_2\right) = \iint \widehat{g}\left(s_1, s_2, z_1, z_2\right) \left[\left(z_1 \vec{\beta}_s - D\vec{\alpha}_s\right) \cdot \left(Y_1, Y_2, 0\right)\right]^n h_n\left(z_2\right) dz_1 dz_2 \tag{4.194a}$$

$$= \iint \int_0^\infty f\left(\vec{s} + t\left(z_1 \vec{\beta}_s + z_2 \vec{e}_3 - D\vec{\alpha}_s\right)\right) \left[\left(z_1 \vec{\beta}_s - D\vec{\alpha}_s\right) \cdot \left(Y_1, Y_2, 0\right)\right]^n h_n\left(z_2\right) dt dz_1 dz_2. \tag{4.194b}$$

We change the variable: $\vec{x} = \vec{s} + t\left(z_1 \vec{\beta}_s + z_2 \vec{e}_3 - D\vec{\alpha}_s\right)$, then from section 4.3.4, the following results have already been obtained:

$$z_1 = \frac{D\left(-x_1 s_2 + x_2 s_1\right)}{\left\|\vec{s}\right\|^2 - x_1 s_1 - x_2 s_2}, \quad z_2 = \frac{D\left\|\vec{s}\right\| x_3}{\left\|\vec{s}\right\|^2 - x_1 s_1 - x_2 s_2}, \quad dt dz_1 dz_2 = \frac{D\left\|\vec{s}\right\|^2}{\left(\left\|\vec{s}\right\|^2 - x_1 s_1 - x_2 s_2\right)^2} d\vec{x}, \tag{4.195a}$$

$$\left(z_1 \vec{\beta}_s - D\vec{\alpha}_s\right) \cdot \left(Y_1, Y_2, 0\right) = \frac{D\left\|\vec{s}\right\|}{\left\|\vec{s}\right\|^2 - x_1 s_1 - x_2 s_2} \left[x_1 Y_1 + x_2 Y_2 + \left(-s_1 Y_1 - s_2 Y_2\right)\right]. \tag{4.195b}$$

Then the above integral can be rewritten as:

$$\widehat{J}_n\left(s_1, s_2, Y_1, Y_2\right) \tag{4.196a}$$

$$= \iint \int_0^\infty f\left(\vec{s} + t\left(z_1 \vec{\beta}_s + z_2 \vec{e}_3 - D\vec{\alpha}_s\right)\right) \left[\left(z_1 \vec{\beta}_s - D\vec{\alpha}_s\right) \cdot \left(Y_1, Y_2, 0\right)\right]^n h_n\left(z_2\right) dt dz_1 dz_2 \tag{4.196b}$$

$$\begin{aligned} &= \iiint f\left(\vec{x}\right) \left[\frac{D\left\|\vec{s}\right\|}{\left\|\vec{s}\right\|^2 - x_1 s_1 - x_2 s_2} \left[x_1 Y_1 + x_2 Y_2 + \left(-s_1 Y_1 - s_2 Y_2\right)\right]\right]^n \times \\ &\qquad \times h_n\left(\frac{D\left\|\vec{s}\right\| x_3}{\left\|\vec{s}\right\|^2 - x_1 s_1 - x_2 s_2}\right) \frac{D\left\|\vec{s}\right\|^2}{\left(\left\|\vec{s}\right\|^2 - x_1 s_1 - x_2 s_2\right)^2} d\vec{x} \end{aligned} \tag{4.196c}$$

$$\begin{aligned} &= \iiint f\left(\vec{x}\right) \frac{D^n \left\|\vec{s}\right\|^n}{\left(\left\|\vec{s}\right\|^2 - x_1 s_1 - x_2 s_2\right)^n} \left[x_1 Y_1 + x_2 Y_2 + \left(-s_1 Y_1 - s_2 Y_2\right)\right]^n \times \\ &\qquad \times \frac{\left(\left\|\vec{s}\right\|^2 - x_1 s_1 - x_2 s_2\right)^{n+2}}{D^{n+2} \left\|\vec{s}\right\|^{n+2}} h_n\left(x_3\right) \frac{D\left\|\vec{s}\right\|^2}{\left(\left\|\vec{s}\right\|^2 - x_1 s_1 - x_2 s_2\right)^2} d\vec{x}. \end{aligned} \tag{4.196d}$$

By simple calculations, we can see that:

$$\widehat{J}_n(s_1,s_2,Y_1,Y_2) = \frac{1}{D}\iiint f(\vec{x})\left[x_1Y_1+x_2Y_2+(-s_1Y_1-s_2Y_2)\right]^n h_n(x_3)\,d\vec{x} \tag{4.197a}$$

$$= \frac{1}{D}\iiint f(\vec{x})\left[\sum_{i+j+k=n}\frac{n!}{i!\,j!\,k!}(x_1Y_1)^i(x_2Y_2)^j(-s_1Y_1-s_2Y_2)^k\right]h_n(x_3)\,d\vec{x} \tag{4.197b}$$

$$= \sum_{i+j+k=n}\left[\frac{1}{D}\frac{n!}{i!\,j!\,k!}\iiint f(\vec{x})\,x_1^ix_2^jh_n(x_3)\,d\vec{x}\right]Y_1^iY_2^j(-s_1Y_1-s_2Y_2)^k \tag{4.197c}$$

$$= \widehat{K}_n(Y_1,Y_2,-s_1Y_1-s_2Y_2), \tag{4.197d}$$

where

$$\widehat{K}_n(Y_1,Y_2,Y_3) = \sum_{i+j+k=n}\left[\frac{1}{D}\frac{n!}{i!\,j!\,k!}\iiint f(\vec{x})\,x_1^ix_2^jh_n(x_3)\,d\vec{x}\right]Y_1^iY_2^jY_3^k, \tag{4.198}$$

is a three-variable homogeneous polynomial of degree n.

4.3.8.2 Approach 2: following the technique in [Clackdoyle et al., 2016]

The idea of the following proof comes directly from the paper [Clackdoyle et al., 2016], although the presentation can be different, it is the same as the proof in [Clackdoyle et al., 2016], with some notation changes to fit the geometry context. We will follow the technique in [Clackdoyle et al., 2016] to define an intermediate integration of the conventional cone-beam projections. In this case, it is:

$$\widetilde{J}_n(\vec{s},Y_1,Y_2) = \iint_{\mathbb{S}^2}\widehat{g}^{\text{conv}}(\vec{s},\vec{\eta})\left[\vec{\eta}\cdot(Y_1,Y_2,0)\right]^n h_n(\vec{\eta}\cdot\vec{e}_3)\,d\vec{\eta}. \tag{4.199}$$

Step 1: Proving $\widehat{J}_n(s_1,s_2,Y_1,Y_2) = (1/D)\,\widetilde{J}_n(\vec{s},Y_1,Y_2)$: We first change the weighted projection in the formula of $\widehat{J}_n(s_1,s_2,Y_1,Y_2)$ to the conventional projection, using the relationship (4.143):

$$\widehat{g}(s_1,s_2,Y_1,Y_2) = \widehat{g}^{\text{conv}}(\vec{s},\vec{\eta}(s_1,s_2,z_1,z_2))\,\frac{1}{\sqrt{z_1^2+z_2^2+D^2}}, \tag{4.200}$$

where

$$\vec{\eta}(s_1,s_2,z_1,z_2) = \frac{z_1\vec{\beta}_s+z_2\vec{e}_3-D\vec{\alpha}_s}{\sqrt{z_1^2+z_2^2+D^2}} = \frac{1}{\|\vec{s}\|\sqrt{z_1^2+z_2^2+D^2}}\begin{bmatrix}-z_1s_2-Ds_1\\ z_1s_1-Ds_2\\ z_2\|\vec{s}\|\end{bmatrix}. \tag{4.201}$$

From this, we also see that:

$$z_1\vec{\beta}_s+z_2\vec{e}_3-D\vec{\alpha}_s = \sqrt{z_1^2+z_2^2+D^2}\;\vec{\eta}(s_1,s_2,z_1,z_2), \tag{4.202a}$$

$$\frac{z_2}{\sqrt{z_1^2+z_2^2+D^2}} = \vec{\eta}(s_1,s_2,z_1,z_2)\cdot\vec{e}_3. \tag{4.202b}$$

Then, also using the property (4.192), we can rewrite the original moment $\widehat{J}_n\left(s_1,s_2,Y_1,Y_2\right)$ as:

$$
\begin{aligned}
&\widehat{J}_n\left(s_1,s_2,Y_1,Y_2\right)\\
&=\iint \widehat{g}\left(s_1,s_2,z_1,z_2\right)\left[\left(z_1\vec{\beta}_s-D\vec{\alpha}_s\right)\cdot\left(Y_1,Y_2,0\right)\right]^n h_n\left(z_2\right)dz_1dz_2 &&\text{(4.203a)}\\
&=\iint \widehat{g}\left(s_1,s_2,z_1,z_2\right)\left[\left(z_1\vec{\beta}_s+z_2\vec{e}_3-D\vec{\alpha}_s\right)\cdot\left(Y_1,Y_2,0\right)\right]^n h_n\left(\sqrt{z_1^2+z_2^2+D^2}\frac{z_2}{\sqrt{z_1^2+z_2^2+D^2}}\right)dz_1dz_2 &&\text{(4.203b)}\\
&=\iint \widehat{g}\left(s_1,s_2,z_1,z_2\right)\times\\
&\quad\times\left[\sqrt{z_1^2+z_2^2+D^2}\,\vec{\eta}\left(s_1,s_2,z_1,z_2\right)\cdot\left(Y_1,Y_2,0\right)\right]^n h_n\left(\sqrt{z_1^2+z_2^2+D^2}\,\vec{\eta}\left(s_1,s_2,z_1,z_2\right)\cdot\vec{e}_3\right)dz_1dz_2 &&\text{(4.203c)}\\
&=\iint \frac{\widehat{g}^{\text{conv}}\left(\vec{s},\vec{\eta}\left(s_1,s_2,z_1,z_2\right)\right)}{\sqrt{z_1^2+z_2^2+D^2}}\times\\
&\quad\times\sqrt{z_1^2+z_2^2+D^2}^{\,n}\left[\vec{\eta}\left(s_1,s_2,z_1,z_2\right)\cdot\left(Y_1,Y_2,0\right)\right]^n\frac{1}{\sqrt{z_1^2+z_2^2+D^2}^{\,n+2}}h_n\left(\vec{\eta}\left(s_1,s_2,z_1,z_2\right)\cdot\vec{e}_3\right)dz_1dz_2 &&\text{(4.203d)}\\
&=\iint \widehat{g}^{\text{conv}}\left(\vec{s},\vec{\eta}\left(s_1,s_2,z_1,z_2\right)\right)\left[\vec{\eta}\left(s_1,s_2,z_1,z_2\right)\cdot\left(Y_1,Y_2,0\right)\right]^n h_n\left(\vec{\eta}\left(s_1,s_2,z_1,z_2\right)\cdot\vec{e}_3\right)\frac{dz_1dz_2}{\sqrt{z_1^2+z_2^2+D^2}^{\,3}}. &&\text{(4.203e)}
\end{aligned}
$$

Now we change $\vec{\eta}\left(s_1,s_2,z_1,z_2\right)$ to a unit vector $\widehat{\eta}\in\mathbb{S}^2$:

$$
\widehat{\eta}=\vec{\eta}\left(s_1,s_2,z_1,z_2\right)==\frac{1}{\|\vec{s}\|\sqrt{z_1^2+z_2^2+D^2}}\begin{bmatrix}-z_1s_2-Ds_1\\ z_1s_1-Ds_2\\ z_2\|\vec{s}\|\end{bmatrix}=\begin{bmatrix}-\|\vec{s}\|^{-1}\left(z_1^2+z_2^2+D^2\right)^{-1/2}\left(z_1s_2+Ds_1\right)\\ \|\vec{s}\|^{-1}\left(z_1^2+z_2^2+D^2\right)^{-1/2}\left(z_1s_1-Ds_2\right)\\ z_2\left(z_1^2+z_2^2+D^2\right)^{-1/2}\end{bmatrix}. \tag{4.204}
$$

Then we also need to change dz_1dz_2 to $d\widehat{\eta}$, and $d\widehat{\eta}$ can be computed in terms of dz_1dz_2 by the formula:

$$
d\widehat{\eta}=\left\|\frac{\partial\widehat{\eta}}{\partial z_1}\times\frac{\partial\widehat{\eta}}{\partial z_2}\right\|. \tag{4.205}
$$

With the above explicit formula of $\widehat{\eta}$, we can compute the partial derivative of $\widehat{\eta}$ with respect to z_1:

$$
\begin{aligned}
\frac{\partial\widehat{\eta}}{\partial z_1}&=\begin{bmatrix}-\|\vec{s}\|^{-1}\left[-\frac{1}{2}\left(z_1^2+z_2^2+D^2\right)^{-3/2}2z_1\left(z_1s_2+Ds_1\right)+\left(z_1^2+z_2^2+D^2\right)^{-1/2}s_2\right]\\ \|\vec{s}\|^{-1}\left[-\frac{1}{2}\left(z_1^2+z_2^2+D^2\right)^{-3/2}2z_1\left(z_1s_1-Ds_2\right)+\left(z_1^2+z_2^2+D^2\right)^{-1/2}s_1\right]\\ z_2\left(-\frac{1}{2}\right)\left(z_1^2+z_2^2+D^2\right)^{-3/2}2z_1\end{bmatrix} &&\text{(4.206a)}\\
&=\|\vec{s}\|^{-1}\left(z_1^2+z_2^2+D^2\right)^{-3/2}\begin{bmatrix}z_1\left(z_1s_2+Ds_1\right)-\left(z_1^2+z_2^2+D^2\right)s_2\\ -z_1\left(z_1s_1-Ds_2\right)+\left(z_1^2+z_2^2+D^2\right)s_1\\ -z_1z_2\|\vec{s}\|\end{bmatrix}. &&\text{(4.206b)}
\end{aligned}
$$

And the partial derivative of $\widehat{\eta}$ with respect to z_2:

$$
\frac{\partial\widehat{\eta}}{\partial z_2}=\begin{bmatrix}-\|\vec{s}\|^{-1}\left(z_1s_2+Ds_1\right)\left(-\frac{1}{2}\right)\left(z_1^2+z_2^2+D^2\right)^{-3/2}2z_2\\ \|\vec{s}\|^{-1}\left(z_1s_1-Ds_2\right)\left(-\frac{1}{2}\right)\left(z_1^2+z_2^2+D^2\right)^{-3/2}2z_2\\ \left(z_1^2+z_2^2+D^2\right)^{-1/2}+z_2\left(-\frac{1}{2}\right)\left(z_1^2+z_2^2+D^2\right)^{-3/2}2z_2\end{bmatrix}=\|\vec{s}\|^{-1}\left(z_1^2+z_2^2+D^2\right)^{-3/2}\begin{bmatrix}z_2\left(z_1s_2+Ds_1\right)\\ -z_2\left(z_1s_1-Ds_2\right)\\ \|\vec{s}\|\left(z_1^2+D^2\right)\end{bmatrix}. \tag{4.207a}
$$

In order to compute $\left\|\frac{\partial\widehat{\eta}}{\partial z_1}\times\frac{\partial\widehat{\eta}}{\partial z_2}\right\|$, we can first compute the cross product of two vectors (the terms on the same row with the same non-black color match together and are ready to be factorized):

$$\begin{bmatrix} z_1\left(z_1s_2+Ds_1\right)-\left(z_1^2+z_2^2+D^2\right)s_2 \\ -z_1\left(z_1s_1-Ds_2\right)+\left(z_1^2+z_2^2+D^2\right)s_1 \\ -z_1z_2\left\|\vec{s}\right\| \end{bmatrix}\times\begin{bmatrix} z_2\left(z_1s_2+Ds_1\right) \\ -z_2\left(z_1s_1-Ds_2\right) \\ \left\|\vec{s}\right\|\left(z_1^2+D^2\right) \end{bmatrix} \tag{4.208a}$$

$$= \begin{bmatrix} -\left\|\vec{s}\right\|z_1\left(z_1^2+D^2\right)\left(z_1s_1-Ds_2\right)+\left\|\vec{s}\right\|s_1\left(z_1^2+D^2\right)\left(z_1^2+z_2^2+D^2\right)-\left\|\vec{s}\right\|z_1z_2^2(z_1s_1-Ds_2) \\ -\left\|\vec{s}\right\|z_1\left(z_1^2+D^2\right)\left(z_1s_2+Ds_1\right)+\left\|\vec{s}\right\|s_2\left(z_1^2+D^2\right)\left(z_1^2+z_2^2+D^2\right)-\left\|\vec{s}\right\|z_1z_2^2(z_1s_2+Ds_1) \\ z_2s_2\left(z_1^2+z_2^2+D^2\right)\left(z_1s_1-Ds_2\right)-z_2s_1\left(z_1^2+z_2^2+D^2\right)\left(z_1s_2+Ds_1\right) \end{bmatrix}, \tag{4.208b}$$

$$= \begin{bmatrix} -\|\vec{s}\|z_1\left(z_1s_1-Ds_2\right)\left(z_1^2+z_2^2+D^2\right)+\|\vec{s}\|s_1\left(z_1^2+D^2\right)\left(z_1^2+z_2^2+D^2\right) \\ -\|\vec{s}\|z_1\left(z_1s_2+Ds_1\right)\left(z_1^2+z_2^2+D^2\right)+\|\vec{s}\|s_2\left(z_1^2+D^2\right)\left(z_1^2+z_2^2+D^2\right) \\ -Dz_2\left(z_1^2+z_2^2+D^2\right)\left(s_1^2+s_2^2\right) \end{bmatrix}, \tag{4.208c}$$

$$= \begin{bmatrix} D\left\|\vec{s}\right\|\left(z_1^2+z_2^2+D^2\right)\left(z_1s_2+Ds_1\right) \\ D\left\|\vec{s}\right\|\left(z_1^2+z_2^2+D^2\right)\left(-z_1s_1+Ds_2\right) \\ -D\left\|\vec{s}\right\|^2z_2\left(z_1^2+z_2^2+D^2\right) \end{bmatrix} \tag{4.208d}$$

$$= D\left\|\vec{s}\right\|\left(z_1^2+z_2^2+D^2\right)\begin{bmatrix} z_1s_2+Ds_1 \\ -z_1s_1+Ds_2 \\ -\left\|\vec{s}\right\|z_2 \end{bmatrix} \tag{4.208e}$$

From these materials, we can compute:

$$\left\|\frac{\partial\widehat{\eta}}{\partial z_1}\times\frac{\partial\widehat{\eta}}{\partial z_2}\right\|$$

$$= \left\|\left\|\vec{s}\right\|^{-2}\left(z_1^2+z_2^2+D^2\right)^{-3}\begin{bmatrix} z_1\left(z_1s_2+Ds_1\right)-\left(z_1^2+z_2^2+D^2\right)s_2 \\ -z_1\left(z_1s_1-Ds_2\right)+\left(z_1^2+z_2^2+D^2\right)s_1 \\ -z_1z_2\left\|\vec{s}\right\| \end{bmatrix}\times\begin{bmatrix} z_2\left(z_1s_2+Ds_1\right) \\ -z_2\left(z_1s_1-Ds_2\right) \\ \left\|\vec{s}\right\|\left(z_1^2+D^2\right) \end{bmatrix}\right\| \tag{4.209a}$$

$$= \left\|\left\|\vec{s}\right\|^{-2}\left(z_1^2+z_2^2+D^2\right)^{-3}D\left\|\vec{s}\right\|\left(z_1^2+z_2^2+D^2\right)\begin{bmatrix} z_1s_2+Ds_1 \\ -z_1s_1+Ds_2 \\ -\left\|\vec{s}\right\|z_2 \end{bmatrix}\right\| \tag{4.209b}$$

$$= D\left\|\vec{s}\right\|^{-1}\left(z_1^2+z_2^2+D^2\right)^{-2}\left\|\begin{bmatrix} z_1s_2+Ds_1 \\ -z_1s_1+Ds_2 \\ -\left\|\vec{s}\right\|z_2 \end{bmatrix}\right\| \tag{4.209c}$$

$$= D\left\|\vec{s}\right\|^{-1}\left(z_1^2+z_2^2+D^2\right)^{-2}\left[\left(z_1s_2+Ds_1\right)^2+\left(-z_1s_1+Ds_2\right)^2+\left\|\vec{s}\right\|^2z_2^2\right]^{1/2} \tag{4.209d}$$

$$= D\left\|\vec{s}\right\|^{-1}\left(z_1^2+z_2^2+D^2\right)^{-2}\left(\left\|\vec{s}\right\|^2z_1^2+\left\|\vec{s}\right\|^2D^2+\left\|\vec{s}\right\|^2z_2^2\right)^{1/2} \tag{4.209e}$$

$$= D\left\|\vec{s}\right\|^{-1}\left(z_1^2+z_2^2+D^2\right)^{-2}\left[\left\|\vec{s}\right\|^2\left(z_1^2+z_2^2+D^2\right)\right]^{1/2} \tag{4.209f}$$

$$= D\left(z_1^2+z_2^2+D^2\right)^{-3/2}. \tag{4.209g}$$

Then $d\widehat{\eta}$ can be written in terms of dz_1dz_2 as:

$$d\widehat{\eta} = \left\| \frac{\partial \widehat{\eta}}{\partial z_1} \times \frac{\partial \widehat{\eta}}{\partial z_2} \right\| dz_1dz_2 = D\left(z_1^2+z_2^2+D^2\right)^{-3/2} dz_1dz_2 = \frac{D}{\sqrt{z_1^2+z_2^2+D^2}^3} dz_1dz_2. \tag{4.210}$$

Thus, the original moment $\widehat{J}_n(s_1, s_2, Y_1, Y_2)$ now becomes:

$$\widehat{J}_n(s_1, s_2, Y_1, Y_2) \tag{4.211a}$$

$$= \frac{1}{D} \iint \widehat{g}^{\text{conv}}(\vec{s}, \vec{\eta}(s_1, s_2, z_1, z_2)) \left[\vec{\eta}(s_1, s_2, z_1, z_2) \cdot (Y_1, Y_2, 0)\right]^n h_n(\vec{\eta}(s_1, s_2, z_1, z_2) \cdot \vec{e}_3) \frac{D}{\sqrt{z_1^2+z_2^2+D^2}^3} dz_1dz_2 \tag{4.211b}$$

$$= \frac{1}{D} \iint_{\mathbb{S}^2} \widehat{g}^{\text{conv}}(\vec{s}, \widehat{\eta}) \left[\widehat{\eta} \cdot (Y_1, Y_2, 0)\right]^n h_n(\widehat{\eta} \cdot \vec{e}_3) d\widehat{\eta} \tag{4.211c}$$

$$= \frac{1}{D} \widetilde{J}_n(\vec{s}, Y_1, Y_2). \tag{4.211d}$$

Step 2: Proving $\widetilde{J}_n(\vec{s}, Y_1, Y_2) = \widehat{K}_n(Y_1, Y_2, -s_1Y_1 - s_2Y_2)$ (here $\widehat{K}_n(Y_1, Y_2, Y_3)$ is a three-variable homogeneous polynomial and we hope its formula coincides with what we obtain in the first approach.)

By the definition (4.199) of the intermediate moment, the definition of the conventional cone-beam projection and the property (4.192) of $h_n(v)$, we can see that:

$$\widetilde{J}_n(\vec{s}, Y_1, Y_2) = \iint_{\mathbb{S}^2} \widehat{g}^{\text{conv}}(\vec{s}, \widehat{\eta}) \left[\widehat{\eta} \cdot (Y_1, Y_2, 0)\right]^n h_n(\widehat{\eta} \cdot \vec{e}_3) d\widehat{\eta} \tag{4.212a}$$

$$= \iint_{\mathbb{S}^2} \int f(\vec{s} + t\widehat{\eta}) \left[\widehat{\eta} \cdot (Y_1, Y_2, 0)\right]^n h_n(\widehat{\eta} \cdot \vec{e}_3) dtd\widehat{\eta} \tag{4.212b}$$

$$= \iint_{\mathbb{S}^2} \int f(\vec{s} + t\widehat{\eta}) \left[t\widehat{\eta} \cdot (Y_1, Y_2, 0)\right]^n t^{-n} h_n(t\widehat{\eta} \cdot \vec{e}_3) t^{n+2} dtd\widehat{\eta} \tag{4.212c}$$

$$= \iint_{\mathbb{S}^2} \int f(\vec{s} + t\widehat{\eta}) \left[t\widehat{\eta} \cdot (Y_1, Y_2, 0)\right]^n h_n(t\widehat{\eta} \cdot \vec{e}_3) t^2 dtd\widehat{\eta}. \tag{4.212d}$$

The obvious next step is to change the variables: $\widetilde{x} = \vec{s} + t\widehat{\eta}$. Here we use a familiar result (which is completely independent of what we are doing, we just use the same notations for simplicity): *for any* $\widehat{\eta} \in \mathbb{S}^2$, $\vec{s} \in \mathbb{R}^3$ *and* $t \in \mathbb{R}$, *if* $\widetilde{x} = \vec{s} + t\widehat{\eta}$, *then* $d\widetilde{x} = t^2dtd\widehat{\eta}$. We can prove this familiar result: any $\widehat{\eta} \in \mathbb{S}^2$ can be parameterized by two angular variables $\phi \in [0, 2\pi)$ and $\theta \in [0, \pi]$, where ϕ and θ are defined as same as in figure 4.16. Now $\widehat{\eta}$ and $\widetilde{x}$ can be rewritten in terms of ϕ and θ as:

$$\widehat{\eta} = \begin{bmatrix} \cos\phi\sin\theta \\ \sin\phi\sin\theta \\ \cos\theta \end{bmatrix} \quad \text{and} \quad \widetilde{x} = \begin{bmatrix} s_1 + t\cos\phi\sin\theta \\ s_2 + t\sin\phi\sin\theta \\ s_3 + t\cos\theta \end{bmatrix} \tag{4.213}$$

Then by the formula mentioned in approach 1:

$$d\widehat{\eta} = \left\| \frac{\partial \widehat{\eta}}{\partial \phi} \times \frac{\partial \widehat{\eta}}{\partial \theta} \right\| d\phi d\theta \tag{4.214a}$$

$$= \left\| \begin{bmatrix} -\sin\phi\sin\theta \\ \cos\phi\sin\theta \\ 0 \end{bmatrix} \times \begin{bmatrix} \cos\phi\cos\theta \\ \sin\phi\cos\theta \\ -\sin\theta \end{bmatrix} \right\| d\phi d\theta \tag{4.214b}$$

$$= \left\| \begin{bmatrix} -\cos\phi\sin^2\theta \\ -\sin\phi\sin^2\theta \\ -\sin^2\phi\cos\theta\sin\theta - \cos^2\phi\cos\theta\sin\theta \end{bmatrix} \right\| d\phi d\theta \tag{4.214c}$$

$$= \left\| \begin{bmatrix} -\cos\phi\sin^2\theta \\ -\sin\phi\sin^2\theta \\ -\cos\theta\sin\theta \end{bmatrix} \right\| d\phi d\theta \tag{4.214d}$$

$$= \left(\cos^2\phi\sin^4\theta + \sin^2\phi\sin^4\theta + \cos^2\theta\sin^2\theta\right)^{1/2} d\phi d\theta \tag{4.214e}$$

$$= \left(\sin^4\theta + \cos^2\theta\sin^2\theta\right)^{1/2} d\phi d\theta \tag{4.214f}$$

$$= \sin\theta d\phi d\theta. \tag{4.214g}$$

And from the formula of $\widetilde{x}$, we can compute the Jacobian matrix:

$$J = \begin{bmatrix} \dfrac{\partial x_1}{\partial t} & \dfrac{\partial x_1}{\partial \phi} & \dfrac{\partial x_1}{\partial \theta} \\ \dfrac{\partial x_2}{\partial t} & \dfrac{\partial x_2}{\partial \phi} & \dfrac{\partial x_2}{\partial \theta} \\ \dfrac{\partial x_3}{\partial t} & \dfrac{\partial x_3}{\partial \phi} & \dfrac{\partial x_3}{\partial \theta} \end{bmatrix} = \begin{bmatrix} \cos\phi\sin\theta & -t\sin\phi\sin\theta & t\cos\phi\cos\theta \\ \sin\phi\sin\theta & t\cos\phi\sin\theta & t\sin\phi\cos\theta \\ \cos\theta & 0 & -t\sin\theta \end{bmatrix}, \tag{4.215a}$$

$$\det J = -t^2\cos^2\phi\sin^3\theta - t^2\sin^2\phi\cos^2\theta\sin\theta - t^2\cos^2\phi\cos^2\theta\sin\theta - t^2\sin^2\phi\sin^3\theta \tag{4.215b}$$

$$= -t^2\sin^3\theta - t^2\cos^2\theta\sin\theta \tag{4.215c}$$

$$= -t^2\sin\theta. \tag{4.215d}$$

Then we obtain:

$$d\widetilde{x} = t^2\sin\theta d\phi d\theta = t^2 d\widehat{\eta}. \tag{4.216}$$

Coming back with our problem, changing the variable $\widetilde{x} = \vec{s} + t\widehat{\eta}$ leads to $d\widetilde{x} = t^2 dt d\widehat{\eta}$. Then the intermediate integration can be rewritten as:

$$\widetilde{J}_n(\vec{s}, Y_1, Y_2) = \iint_{\mathbb{S}^2} \int f(\vec{s} + t\widehat{\eta}) \left[t\widehat{\eta} \cdot (Y_1, Y_2, 0)\right]^n h_n(t\widehat{\eta} \cdot \vec{e}_3)\, t^2 dt d\widehat{\eta} \tag{4.217a}$$

$$= \iiint f(\widetilde{x}) \left[(\widetilde{x} - \vec{s}) \cdot (Y_1, Y_2, 0)\right]^n h_n((\widetilde{x} - \vec{s}) \cdot \vec{e}_3)\, d\widetilde{x} \tag{4.217b}$$

$$= \iiint f(\widetilde{x}) \left[x_1Y_1 + x_2Y_2 + (-s_1Y_1 - s_2Y_2)\right]^n h_n(\widetilde{x} \cdot \vec{e}_3)\, d\widetilde{x} \tag{4.217c}$$

$$= \iiint f(\widetilde{x}) \left[\sum_{k=0}^{n} \frac{n!}{i!\, j!\, k!} (x_1Y_1)^i (x_2Y_2)^j (-s_1Y_1 - s_2Y_2)^k\right] h_n(x_3)\, d\widetilde{x} \tag{4.217d}$$

$$= \sum_{k=0}^{n} \left[\frac{n!}{i!\, j!\, k!} \iiint f(\widetilde{x})\, x_1^i x_2^j h_n(x_3)\, d\widetilde{x}\right] Y_1^i Y_2^j (-s_1Y_1 - s_2Y_2)^k, \tag{4.217e}$$

here $\vec{s} \cdot \vec{e}_3 = 0$ since $\vec{s} = (s_1, s_2, 0)$ and $\vec{e}_3 = (0, 0, 1)$.
Thus from equations (4.211d) and (4.217e), we obtain:

$$\widehat{J}_n(s_1, s_2, Y_1, Y_2) = \frac{1}{D}\widetilde{J}_n(\vec{s}, Y_1, Y_2) \tag{4.218a}$$

$$= \sum_{k=0}^{n} \left[\frac{1}{D}\frac{n!}{i!\, j!\, k!} \iiint f(\widetilde{x})\, x_1^i x_2^j h_n(x_3)\, d\widetilde{x}\right] Y_1^i Y_2^j (-s_1Y_1 - s_2Y_2)^k \tag{4.218b}$$

$$= \widehat{K}_n(Y_1, Y_2, -s_1Y_1 - s_2Y_2), \tag{4.218c}$$

where $\widehat{K}_n(Y_1, Y_2, Y_3)$ is a three-variable homogeneous polynomial, which has the same formula as what we obtain in approach 1. And this completes the proof.

4.3.9 Calibration in 3D cone-beam geometry with circular source trajectory

From the built CBCCs in the previous sections, we obtain the following preliminary geometry calibration result in *CBCC16* geometry:
Let the x-ray source move along a circle, whose center is at the world origin and radius is R; let the vertical detector (the detector perpendicular to the trajectory plane) be not shifted or tilted or rotated, and always be at distance D from the source for all source locations on the trajectory. Assuming that R and D are known, where D is sufficiently large that the source and the detector are always on different side comparing to the world origin. The 3D object is supposed to be strictly above the trajectory plane with its OPCH being inside the circular trajectory area, and the projections are assumed to have no truncation. With all of these materials, our only aim is to calibrate the corresponding source location of each given projection directly from the projections.
The result we obtain so far is that: if we know exactly two corresponding source locations of two known projections,

which are on the circular trajectory and not symmetrical through the world origin, then we can calibrate the source location of any other given projection. The method is to use *CBCC13Converted* to derive two different types of CBCCs, and to end up solving a system of linear equations. Our desire is to obtain an analytic method or analytic solutions of the source locations. The result is not completely done, but we still obtain some considerable clues to get further.
Mathematically, the source locations on a circular trajectory are parameterized by the radius $R > 0$ and the view angles $\lambda \in [0, 2\pi)$. Since R is assumed to be known, then calibrating the source locations means solving for λ. As mentioned in section 4.3.5.1, the weighted projection $g^V(s_1, s_2, z_1, z_2)$ on the vertical detector in *CBCC13Converted* geometry definitely coincide with the weighted projection $p^V_\lambda(z_1, z_2)$ in *CBCC16* geometry (see definitions (4.2) and (4.84)), if we consider the source to move along a circle, since $\vec{s} = (s_1, s_2, 0) = (R\cos\lambda, R\sin\lambda, 0) = \vec{s}_\lambda$ and $\vec{\alpha}_s = \vec{\alpha}_\lambda$, $\vec{\beta}_s = \vec{\beta}_\lambda$.

$$g^V(s_1, s_2, z_1, z_2) = \int_0^\infty f\left(\vec{s} + t\left(z_1\vec{\beta}_s + z_2\vec{e}_3 - D\vec{\alpha}_s\right)\right)dt = \int_0^\infty f\left(\vec{s}_\lambda + t\left(z_1\vec{\beta}_\lambda + z_2\vec{e}_3 - D\vec{\alpha}_\lambda\right)\right)dt = p^V_\lambda(z_1, z_2) \tag{4.219}$$

In *CBCC16* geometry, we already had a set of CBCC, which concerns the moment $M^V_n(\lambda) = \iint p^V_\lambda(z_1, z_2)\frac{z_1^n}{z_2^{n+2}}dz_1dz_2$, see definition (4.3). In fact, as shown in section 4.3.5.1, this moment can be extracted from the *CBCC13Converted* geometry, by substituting $(Y_1, Y_2, 0) = (-\sin\lambda, \cos\lambda, 0) = \vec{\beta}_\lambda$ in the definition (4.103) of $J^V(s_1, s_2, Y_1, Y_2)$ with $s_1 = R\cos\lambda$ and $s_2 = R\sin\lambda$:

$$J^V_n(R\cos\lambda, R\sin\lambda, -\sin\lambda, \cos\lambda) = \iint g^V(R\cos\lambda, R\sin\lambda, z_1, z_2)\left[\left(z_1\vec{\beta}_\lambda - D\vec{\alpha}_\lambda\right)\cdot\vec{\beta}_\lambda\right]^n\frac{dz_1dz_2}{z_2^{n+2}} \tag{4.220a}$$

$$= \iint p^V_\lambda(z_1, z_2)\frac{z_1^n}{z_2^{n+2}}dz_1dz_2 \tag{4.220b}$$

$$= M^V_n(\lambda). \tag{4.220c}$$

Moreover, using *CBCC13Converted* of order 1 with $Y_1 = -\sin\lambda$ and $Y_2 = \cos\lambda$, we can see that:

$$M^V_1(\lambda) = J^V_1(R\cos\lambda, R\sin\lambda, -\sin\lambda, \cos\lambda) \tag{4.221a}$$

$$= K^V_1(-\sin\lambda, \cos\lambda, -R\cos\lambda(-\sin\lambda) - R\sin\lambda\cos\lambda) \tag{4.221b}$$

$$= K^V_1(-\sin\lambda, \cos\lambda, 0) \tag{4.221c}$$

$$= \sum_{i+j+k=n} C^V_{i,j,k}(-\sin\lambda)^i(\cos\lambda)^j 0^k \tag{4.221d}$$

$$= \sum_{\substack{k=0\\ i+j=n}} C^V_{i,j,0}(-\sin\lambda)^i(\cos\lambda)^j \tag{4.221e}$$

$$= -C^V_{1,0,0}\sin\lambda + C^V_{0,1,0}\cos\lambda. \tag{4.221f}$$

Then we get a first-order equation of $\cos\lambda$ and $\sin\lambda$.

$$-C^V_{1,0,0}\sin\lambda + C^V_{0,1,0}\cos\lambda = M^V_1(\lambda). \tag{4.222}$$

Now we will find another first-order equation of $\cos\lambda$ and $\sin\lambda$, by deriving a new CBCC in *CBCC16* geometry from *CBCC13Converted*. Using again the definition (4.103) of the moment $J^V_n(s_1, s_2, Y_1, Y_2)$ with $s_1 = R\cos\lambda$, $s_2 = R\sin\lambda$, and $(Y_1, Y_2, 0) = (\cos\lambda, \sin\lambda, 0) = \vec{\alpha}_\lambda$, we obtain:

$$J^V_n(R\cos\lambda, R\sin\lambda, \cos\lambda, \sin\lambda) = \iint g^V(R\cos\lambda, R\sin\lambda, z_1, z_2)\left[\left(z_1\vec{\beta}_\lambda - D\vec{\alpha}_\lambda\right)\cdot\vec{\alpha}_\lambda\right]^n\frac{dz_1dz_2}{z_2^{n+2}} \tag{4.223a}$$

$$= (-D)^n\iint p^V_\lambda(z_1, z_2)\frac{1}{z_2^{n+2}}dz_1dz_2. \tag{4.223b}$$

We then define a new type of moments in *CBCC16* geometry:

$$\overline{M}^V_n(\lambda) = \iint p^V_\lambda(z_1, z_2)\frac{1}{z_2^{n+2}}dz_1dz_2. \tag{4.224}$$

After that, using *CBCC13Converted* of order 1 with $Y_1 = \cos\lambda$ and $Y_2 = \sin\lambda$, we can obtain:

$$\begin{aligned}
-D\overline{M}_1^V(\lambda) &= J_1^V(R\cos\lambda, R\sin\lambda, \cos\lambda, \sin\lambda) && \text{(4.225a)}\\
&= K_1^V(\cos\lambda, \sin\lambda, -R\cos\lambda\cos\lambda - R\sin\lambda\sin\lambda) && \text{(4.225b)}\\
&= K_1^V\left(\cos\lambda, \sin\lambda, -R\left(\cos^2\lambda + \sin^2\lambda\right)\right) && \text{(4.225c)}\\
&= K_1^V(\cos\lambda, \sin\lambda, -R) && \text{(4.225d)}\\
&= \sum_{i+j+k=n} C_{i,j,k}^V(\cos\lambda)^i(\sin\lambda)^j(-R)^k && \text{(4.225e)}\\
&= C_{1,0,0}^V\cos\lambda + C_{0,1,0}^V\sin\lambda - RC_{0,0,1}^V && \text{(4.225f)}
\end{aligned}$$

And we rewrite this as another first-order equation of $\cos\lambda$ and $\sin\lambda$.

$$C_{1,0,0}^V\cos\lambda + C_{0,1,0}^V\sin\lambda = RC_{0,0,1}^V - D\overline{M}_1^V(\lambda). \tag{4.226}$$

From equations (4.222) and (4.226), we get the following system of equations for all $\lambda \in [0, 2\pi)$:

$$\begin{cases}
-C_{1,0,0}^V\sin\lambda + C_{0,1,0}^V\cos\lambda = M_1^V(\lambda), & \text{(4.227a)}\\
C_{0,1,0}^V\sin\lambda + C_{1,0,0}^V\cos\lambda = RC_{0,0,1}^V - D\overline{M}_1^V(\lambda). & \text{(4.227b)}
\end{cases}$$

In this system of equations, the moments $M_1^V(\lambda)$ and $\overline{M}_1^V(\lambda)$ can be computed directly from the projections, then in order to solve λ, we need to find the coefficients $C_{1,0,0}^V$, $C_{0,1,0}^V$ and $C_{0,0,1}^V$. As in the assumptions, let's say we know exactly two source locations and their corresponding weighted projections, and these two source locations are not symmetrical through the world origin on the circular trajectory, this means we know two view angles $\lambda_1, \lambda_2 \in [0, 2\pi)$, such that:

$$\begin{cases}
\lambda_1 \neq \lambda_2, & \text{(4.228a)}\\
|\lambda_1 - \lambda_2| \neq \pi. & \text{(4.228b)}
\end{cases}$$

Substituting λ by λ_1 and λ_2 respectively in equation (4.227a), we obtain the following system of equations:

$$\begin{cases}
-C_{1,0,0}^V\sin\lambda_1 + C_{0,1,0}^V\cos\lambda_1 = M_1^V(\lambda_1), & \text{(4.229a)}\\
-C_{1,0,0}^V\sin\lambda_2 + C_{0,1,0}^V\cos\lambda_2 = M_1^V(\lambda_2). & \text{(4.229b)}
\end{cases}$$

Since we are finding $C_{1,0,0}^V$ and $C_{0,1,0}^V$, knowing λ_1 and λ_2, so in this system of equations the coefficients are $(-\sin\lambda_1)$, $\cos\lambda_1$, $(-\sin\lambda_2)$, $\cos\lambda_2$ and the unknowns are $C_{1,0,0}^V$ and $C_{0,1,0}^V$. We can see that:

$$\det\begin{bmatrix}-\sin\lambda_1 & \cos\lambda_1\\ -\sin\lambda_2 & \cos\lambda_2\end{bmatrix} = -\sin\lambda_1\cos\lambda_2 + \sin\lambda_2\cos\lambda_1 = \sin(\lambda_2 - \lambda_1) \neq 0. \tag{4.230}$$

$\sin(\lambda_2 - \lambda_1) \neq 0$ is because of the fact that $\lambda_1, \lambda_2 \in [0, 2\pi)$ satisfying the condition (4.228). Since $\lambda_1, \lambda_2 \in [0, 2\pi)$ means $-2\pi < \lambda_2 - \lambda_1 < 2\pi$, and $\lambda_2 - \lambda_1 \notin \{-\pi, 0, \pi\}$ due to the condition (4.228), then $\sin(\lambda_2 - \lambda_1) \neq 0$. Then from this, we can solve for $C_{1,0,0}^V$ and $C_{0,1,0}^V$ in the system (4.229).

$$C_{1,0,0}^V = \frac{\det\begin{bmatrix}M_1^V(\lambda_1) & \cos\lambda_1\\ M_1^V(\lambda_2) & \cos\lambda_2\end{bmatrix}}{\det\begin{bmatrix}-\sin\lambda_1 & \cos\lambda_1\\ -\sin\lambda_2 & \cos\lambda_2\end{bmatrix}} = \frac{M_1^V(\lambda_1)\cos\lambda_2 - M_1^V(\lambda_2)\cos\lambda_1}{\sin(\lambda_2 - \lambda_1)}, \tag{4.231a}$$

$$C_{0,1,0}^V = \frac{\det\begin{bmatrix}-\sin\lambda_1 & M_1^V(\lambda_1)\\ -\sin\lambda_2 & M_1^V(\lambda_2)\end{bmatrix}}{\det\begin{bmatrix}-\sin\lambda_1 & \cos\lambda_1\\ -\sin\lambda_2 & \cos\lambda_2\end{bmatrix}} = \frac{-M_1^V(\lambda_2)\sin\lambda_1 + M_1^V(\lambda_1)\sin\lambda_2}{\sin(\lambda_2 - \lambda_1)}. \tag{4.231b}$$

With these values of $C_{1,0,0}^V$ and $C_{0,1,0}^V$, from equation (4.227b), we can also compute $C_{0,0,1}^V$ by replacing λ by λ_1:

$$C_{0,0,1}^V = \frac{1}{R}\left(C_{0,1,0}^V\sin\lambda_1 + C_{1,0,0}^V\cos\lambda_1 + D\overline{M}_1^V(\lambda_1)\right). \tag{4.232}$$

Coming back with the system of equations (4.227), all of the coefficients $C^V_{1,0,0}$, $C^V_{0,1,0}$ and $C^V_{0,0,1}$ are computed from λ_1 and λ_2, the unknowns now are $\sin\lambda$ and $\cos\lambda$, we can see that if:

$$\det\begin{bmatrix} -C^V_{1,0,0} & C^V_{0,1,0} \\ C^V_{0,1,0} & C^V_{1,0,0} \end{bmatrix} = -\left(C^V_{1,0,0}\right)^2 - \left(C^V_{0,1,0}\right)^2 \neq 0, \tag{4.233}$$

then we obtain unique solution of $(\sin\lambda, \cos\lambda)$ as follows:

$$\sin\lambda = \frac{\det\begin{bmatrix} M^V_1(\lambda) & C^V_{0,1,0} \\ RC^V_{0,0,1} - D\overline{M}^V_1(\lambda) & C^V_{1,0,0} \end{bmatrix}}{\det\begin{bmatrix} -C^V_{1,0,0} & C^V_{0,1,0} \\ C^V_{0,1,0} & C^V_{1,0,0} \end{bmatrix}} = \frac{C^V_{0,1,0}\left(RC^V_{0,0,1} - D\overline{M}^V_1(\lambda)\right) - C^V_{1,0,0}M^V_1(\lambda)}{\left(C^V_{1,0,0}\right)^2 + \left(C^V_{0,1,0}\right)^2}, \tag{4.234a}$$

$$\cos\lambda = \frac{\det\begin{bmatrix} -C^V_{1,0,0} & M^V_1(\lambda) \\ C^V_{0,1,0} & RC^V_{0,0,1} - D\overline{M}^V_1(\lambda) \end{bmatrix}}{\det\begin{bmatrix} -C^V_{1,0,0} & C^V_{0,1,0} \\ C^V_{0,1,0} & C^V_{1,0,0} \end{bmatrix}} = \frac{C^V_{1,0,0}\left(RC^V_{0,0,1} - D\overline{M}^V_1(\lambda)\right) + C^V_{0,1,0}M^V_1(\lambda)}{\left(C^V_{1,0,0}\right)^2 + \left(C^V_{0,1,0}\right)^2}. \tag{4.234b}$$

Thus in conclusion, if the data is consistent, if λ_1 and λ_2 follow the assumptions (4.228) and the crucial condition (4.233): $\left(C^V_{1,0,0}\right)^2 + \left(C^V_{0,1,0}\right)^2 \neq 0$ is satisfied, then the solution of λ is unique and defined by equations (4.234), (4.231) and (4.232).

Comments

- The most crucial condition in this method is the condition (4.233), we are just stopping here with no further clues so far. One may check in which situation, the condition holds or in which situation, both coefficients $C^V_{1,0,0}$ and $C^V_{0,1,0}$ equal 0 at the same time. Anyway, with the current result, we are still able to state that if the solution exists, then it is unique and its analytic formula has been explicitly shown.
- One can also find many other DCCs, e.g. going to higher-order moments, to gain new information. The aim is to get rid of the assumption of (must) knowing exactly two source locations to calibrate the others. We want to obtain the geometric parameters completely and only from the projections to make the method truly be automatic calibration.

Conclusions

French version

Tout au long de cette thèse, nous avons eu la chance d'étudier des connaissances en imagerie médicale et de travailler principalement sur les DCC et la calibration géométrique. Nos contributions sont présentées dans trois chapitres: 2, 3 et 4. Comme mentionné au tout début, notre objectif était de dériver de nouvelles DCC et d'essayer de les appliquer à des problèmes de calibration appropriés.

- Dans le chapitre 2, nous avons travaillé avec la géométrie parallèle 3D. Dans le cas général, nous avons dérivé les DCC par paires s'appliquant à deux projections parallèles arbitraires. En fait, cette condition n'était pas nouvelle, mais nous avons obtenu une méthode et une formule analytique pour calibrer explicitement et rapidement la direction de projection inconnue (qui est un vecteur unitaire 3D), si on nous donne trois projections parallèles, dans lesquelles deux directions de projection sont également données à l'avance. Pour le cas dégénéré du problème, nous résolvons un cas particulier, où les deux directions de vue connues sont supposées être perpendiculaires l'une à l'autre. Sur la base de cette hypothèse, nous pouvons dériver une autre DCC dans le plan pour traiter ce cas dégénéré. En fait, la construction de la DCC dans le plan et la méthode présentée dans le cas dégénéré étaient équivalentes à la résolution du problème d'étalonnage 3D en le divisant en de nombreux problèmes d'étalonnage 2D, en résolvant tous les problèmes 2D et en choisissant la solution commune à tous comme solution estimée de la direction de projection inconnue. Dans ce cas, chaque problème d'étalonnage 2D prend en compte une tranche 2D de l'objet 3D et se situe dans un certain plan parmi un groupe de plusieurs plans parallèles.

- C'était la toute première fois que nous avions cette idée. Dans le chapitre 3, nous l'avons recyclée et réutilisée pour traiter la géométrie du faisceau conique avec la trajectoire linéaire de la source. Notre travail a consisté à construire géométriquement de nombreux plans obliques coupant l'objet 3D pour créer des coupes 2D correspondantes sur les plans obliques. Nous avons ensuite converti le problème d'étalonnage du faisceau conique en un ensemble de problèmes d'étalonnage du faisceau en éventail, un sur chaque plan oblique. Nous avons résolu le problème dans lequel nous disposons de quatre projections en éventail et nous connaissons trois positions de la source parmi celles-ci. Nous sommes alors en mesure d'étalonner la position de la source inconnue en utilisant la condition de cohérence du faisceau en éventail d'ordre 2. Pour ce problème, nous avons également donné un modèle physique d'un objet 3D posé sur un tapis roulant, que l'on peut imaginer comme un bagage posé sur un tapis roulant passant par un système de scanner radiologique d'aéroport. Les chapitres 2 et 3 doivent être considérés comme une paire. Dans les deux cas, les méthodes fonctionnent à condition que l'objet 3D satisfassent certaines conditions (très généralement satisfaites). Bien qu'elles soient différentes pour chaque chapitre dans les détails, l'idée principale était que l'objet 3D doit être suffisamment général pour donner de nouvelles informations sur chaque plan (plan parallèle pour le chapitre 2 et plan oblique pour le chapitre 3) contenant le problème de calibration 2D, de sorte que nous obtenions de nouvelles informations sur les solutions, ce qui nous a aidé à obtenir la solution estimée unique pour le problème de calibration 3D correspondant.

- Nous avons étudié en profondeur deux articles : [Clackdoyle and Desbat, 2013] et [Clackdoyle et al., 2016] dans le chapitre 4. Nous avons d'abord essayé de trouver la relation entre les DCC dans ces deux articles, et avons essayé de convertir les DCC de l'un dans le contexte géométrique de l'autre. Nous avons appris que les DCC de [Clackdoyle and Desbat, 2013] peuvent générer de nombreuses DCC dans de nombreuses géométries particulières, même avec une trajectoire de la source très générale. Nous avons obtenu de nouvelles DCC dans plusieurs situations, mais le plus important était les DCC pour les projections pondérées de faisceaux coniques collectées sur un détecteur perpendiculaire au plan contenant la trajectoire de la source (détecteur vertical si le plan de la trajectoire est horizontal), avec une trajectoire générale de la source. Nous avons finalement appliqué ces DCC au problème de calibration de faisceau conique avec une trajectoire de source circulaire, pour estimerer la position de la source sur le cercle. La méthode de calibration n'a pas encore été étudiée dans tous ses détails, mais elle pourrait potentiellement donner une solution unique au problème d'estimation de la position la source avec une formule analytique (par exemple si on on connait trois projections, dont deux avec des positions de source connues et qu'on cherche à identifier la possition de la troisième).

En général, nos résultats sont théoriques. Cependant, certains d'entre eux peuvent constituer un potentiel pour des développements plus directs afin d'être utiles dans des applications réelles.

English version

Throughout the thesis, we have the chance to study Medical Imaging knowledge and mainly work on the DCC and geometric calibration. Our contributions are presented in three chapters: 2, 3 and 4. As mentioned at the very beginning, we aim to derive new DCC and try to apply them into suitable calibration problems.

- In chapter 2, we worked with the 3D parallel geometry. In general case, we derived the pair-wise DCC applying on two arbitrary parallel projections. In fact, this condition was not new, but from this, we obtained a method and an analytic formula to explicitly and quickly calibrate the unknown viewing direction (which is a 3D unit vector), if we were given three parallel projections, in which two viewing directions were also given in advance. For the degenerate case of the problem, we just solved a particular case, where the two known viewing directions were assumed to be perpendicular to each other. Based on this assumption, we can derive another in-plane DCC to deal with this degenerate case. In fact, the construction of the in-plane DCC and the method presented in the degenerate case were equivalent to solving the 3D calibration problem by splitting it into many 2D calibration problems, solving all the 2D problems, and choosing the common solution among all to be the estimated solution of the unknown viewing direction. Here each 2D calibration problem took a 2D slice of the 3D object into account, and was set in one certain plane in a group of many parallel planes.

- That was the very first time we had this idea. In chapter 3, we recycled and reused it to deal with the cone-beam geometry with the linear source trajectory. Our work was to geometrically construct the group of many oblique planes slicing through the 3D object to create the corresponding 2D slices on the oblique planes. We then converted the cone-beam calibration problem into a set of many fan-beam calibration problems, one on each oblique plane, in which we were given four fan-beam projections and we knew three source positions among them, then we were able to calibrate the unknown source position using the fan-beam consistency condition of order 2. We also gave a physical model of some 3D object sitting on the conveyor belt for this problem, which could be imagined as a luggage sitting on a conveyor belt running through a scan system at the airport. Chapter 2 and chapter 3 should be considered as a pair. The most crucial things made the methods in both of them work were the requirements on the 3D object. Although they were different for each chapter in details, the main idea was that the 3D object must be general enough to give new information on each plane (parallel plane for chapter 2 and oblique plane for chapter 3) containing the 2D calibration problem, so that we earned new information on the solutions, which helped us get the unique estimated solution for the corresponding 3D calibration problem.

- In chapter 4, we dug deeply into two articles: [Clackdoyle and Desbat, 2013] and [Clackdoyle et al., 2016]. We first tried to find the relationship between the DCCs in those two papers, and tried to convert this DCC into the other's geometry context. We learned that the DCC in [Clackdoyle and Desbat, 2013] can generate many DCCs in many particular geometry contexts, even with very general source trajectory. We obtained some new DCCs in several situations, but the most significant one was the DCC for weighted cone-beam projections collected on a detector, which was perpendicular to the plane containing the source trajectory (vertical detector if the trajectory plane is horizontal), with general source trajectory. We finally applied it into the cone-beam calibration problem with circular source trajectory, to calibrate the source position on the circle. The method of calibration was not completely studied in every details yet, but it might be potential enough to give unique solution of the source position, with analytic formula, if we were given in advance three projections, and we knew two source positions among them.

In general, our results are theoretical. However, some of them can be potential for more straight-forward developments to be useful in real applications.

Appendix A

Proceedings paper in 2018 NSS/MIC

In this appendix, our proceedings paper [Clackdoyle et al., 2018] in the 2018 IEEE Nuclear Science Symposium and Medical Imaging Conference is provided. This is an early work at the beginning of the thesis, and it is not too relevant to the other contributions of the thesis. It can be considered as a chance for the author to practice creating new DCC, with the main idea is to apply the knowledge in 2D parallel geometry, to work with a new model, where the integrals are taken over concentric circles (instead of lines).

In this paper, we show that the radar operator $\mathfrak{R}$ is the dual operator of the operator in the image reconstruction problem in the scatter imaging model. Thus, in order to study the nullspace of this operator, we need to know about the range of $\mathfrak{R}$, which leads to the work of deriving range conditions or DCCs on the 2D radar projections. Section A.1 describes the geometry and defines the 2D radar projections. Section A.2 presents one of the DCCs being applied on the 2D radar projections.

A.1 2D radar geometry and 2D radar projections

In this model, we work with the 2D plane and the standard coordinate system (x_1, x_2). There is a 2D object f, with compact support, which is assumed to never intersect the x_1-axis. Now the x-ray source is considered to be on the x_1-axis. We use the notation $(x, 0)$ to refer to the position of this x-ray source. It emits radar waves, which are concentric circles (with the common center is the x-ray source's position), passing through the 2D object. For each

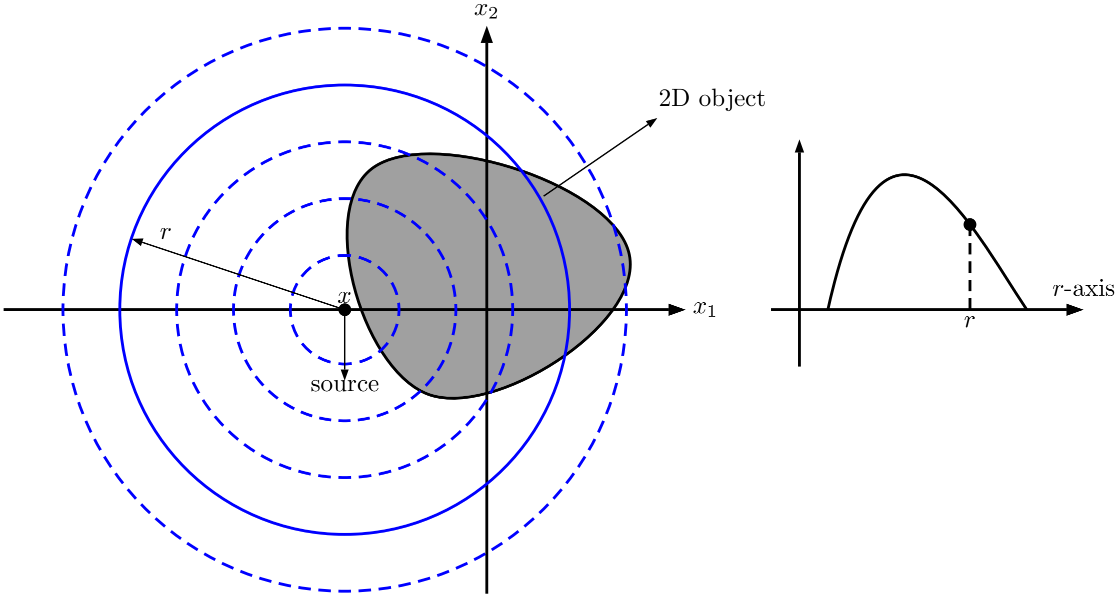

Figure A.1: 2D radar geometry: for each source position $(x, 0)$, the 2D radar projection is a single-variable function, with the variable r being the radius of a certain circle in the radar wave; the data being measured and recorded is the integral over the corresponding circle.

position $(x, 0)$ of the x-ray source on the x_1-axis, we have a projection, which is a single-variable function. This projection records the integral of the 2D object over the concentric circles. The real variable r shows the radius of the considering circle, on which we are computing the corresponding integral. We use the notation $\mathfrak{R}$ to define the radar operator that maps the 2D function f to the set of the integrals over the concentric circles:

$$\mathfrak{R}f\left(x, r\right) = \int_0^{2\pi} f\left(x + r\cos\theta, r\sin\theta\right) d\theta, \quad \forall x \in \mathbb{R}, \forall r \in \left[0, \infty\right). \tag{A.1}$$

Then the 2D radar projection, which corresponds to the source position $(x, 0)$, is defined as follows:

$$\mathfrak{p}_x\left(r\right) = \mathfrak{p}\left(x, r\right) = \mathfrak{R}f\left(x, r\right), \quad \forall r \in \left[0, \infty\right). \tag{A.2}$$

A.2 DCCs for the 2D radar projections

If $\mathfrak{p}$ is in the range of $\mathfrak{R}$: $\mathfrak{p} = \mathfrak{R}f$ for some compactly supported function f, then the moment of order $2n$ defined as follows:

$$M_{2n}^{2D,\ radar}\left(x\right) = \int_0^{\infty} \mathfrak{p}_x\left(r\right) r^{2n+1} dr, \tag{A.3}$$

becomes a polynomial in x of degree (at most) $2n$ (n is a non-negative integer).

As a result, following the idea from the paper [Patch, 2004], we introduce the extension on the projection data:

$$\mathfrak{p}_x\left(r\right) = -\mathfrak{p}_x\left(-r\right), \quad \text{for } r < 0. \tag{A.4}$$

We continue to use the above DCC on the 2D radar projections, and the knowledge about Hermite polynomials (see the book [Abramowitz et al., 1972], pages 773-775 and 785) and the properties of the orthogonal basis (see the book [Szegö, 1939], pages 23-28), we derive the following result:

If $\mathfrak{p}$ is in the range of $\mathfrak{R}$: $\mathfrak{p} = \mathfrak{R}f$ for some compactly supported function f, then the projection data $\mathfrak{p}$ can be written as a series with polynomials as the building blocks:

$$\mathfrak{p}\left(x, r\right) = e^{-r^2} \sum_{j=0}^{\infty} C_{2j+1}\left(x\right) \overline{H}_{2j+1}\left(r\right), \tag{A.5}$$

where $C_{2j+1}\left(x\right)$ is a polynomial in x of degree $2j$, and $\overline{H}_{2j+1}\left(r\right)$ is the normalized Hermite polynomial in r of degree $2j+1$ (with j is a non-negative integer).

Scatter Imaging and Radar: Dual Image Reconstruction Problems

Rolf Clackdoyle, Hung Nguyen, Valérie Perrier, Laurent Desbat

***Abstract*—We are investigating a particular reconstruction problem in the context of coherent scatter imaging. We show the links between this problem and a well-known reconstruction problem in synthetic aperture radar (SAR). Mathematically, the problems are dual to each other. We explore the range conditions of the SAR operator, S, because these conditions are related to the nullspace of the scatter imaging operator S^*. Here we present our preliminary results, and we include simulations and reconstructions for a simple version of the problem.**

I. INTRODUCTION

Imaging of coherently scattered photons in the x-ray energy range has been of potential medical interest for some time, due to the improved contrast of bodily tissues compared to conventional primary-photon imaging [1]. Professor Johns and co-workers at Carleton University in Canada have been developing projection imaging with scattered photons (rather than CT) [2][3]. Figure 1 illustrates the basic concept. When x-rays pass through a small sample, the primary beam is attenuated due to photoelectric effects, to Compton scattered photons, and to coherently scattered photons. The coherent scatter is strongly forward peaked, so it can be readily detected as a pattern of rings centered at the target of the primary beam. The radius of each ring corresponds to a fixed scattering angle, and, ideally, the signal is constant along each ring. This 2D function is called a radial function since it depends only on the radius of the ring (in this simplified description). The radial functions are of interest because their patterns are related to the material of the sample and provide much stronger contrast differences for several biological materials than direct x-ray imaging does.

There are other groups actively studying the coherent scatter imaging problem [4][5][6][7], but their approaches differ considerably from the geometry described here. In their latest developments, Johns *et al* measure an extended object by simultaneously applying several parallel monochromatic x-ray beams through the object. In this case, the radial functions are superimposed on the detector and must be 'disentangled' to separate the individual radial functions corresponding to each x-ray pencil beam. This work is described in [8] where five parallel pencil beams were arranged in a horizontal plane, in the manner illustrated in Figure 2.

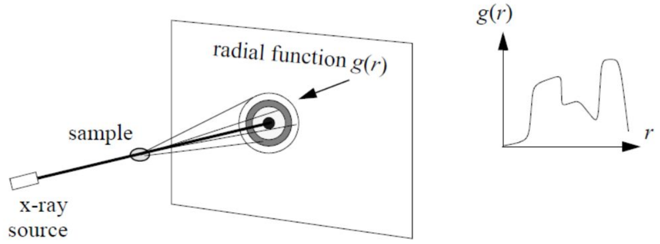

Fig. 1. Measuring coherent scatter. A pencil beam of x-rays interacts with the sample and the scattered rays form rings on the detector, with each ring corresponding to a certain scattering angle at the sample. The pattern of rings depends on the physical characteristics of the sample.

Here we consider the mathematical situation where a parallel pencil beam of x-rays occurs for each point along the x-axis. The problem is to extract (reconstruct) the individual radial functions from the 2D image of superimposed radial functions.

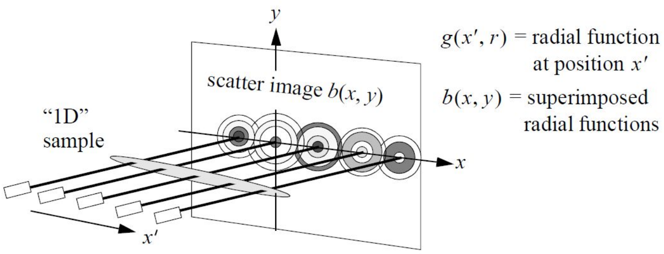

Fig. 2. Parallel data collection. Here, five pencil beams of x-rays are simultaneously passed through the extended sample to generate five radial functions. The radial functions are superimposed on the detector and need to be separated into individual radial functions using a reconstruction method.

The coherent scatter imaging problem is related to a reconstruction problem in synthetic aperture radar (SAR). In a highly simplified description of SAR, an airplane flies in a straight line at a constant altitude, as illustrated in Figure 3. Radar signals emitted from the airplane are bounced back from the ground, and captured according to arrival times. Each time point corresponds to a signal integrated over a circle on the ground centered directly underneath the airplane.

The SAR image reconstruction problem resembles that of classical tomography. The projections consist of integrals over circles instead of along straight lines. A projection can be considered a collection of such integrals for circles with a

This work was partially supported by the labex PERSYVAL-Lab (ANR-11-LABX-0025-01) funded by the French program *Investissement d'Avenir*.

R. Clackdoyle, H. Nguyen, and L. Desbat are all with the TIMC-IMAG laboratory (CNRS UMR 5525), Université Grenoble Alpes, Grenoble, France. V. Perrier is with the Grenoble Insitute of Technology (Grenoble INP), Grenoble, France.

Corresponding author: Rolf Clackdoyle, e-mail: rolf.clackdoyle@univ-grenoble-alpes.fr

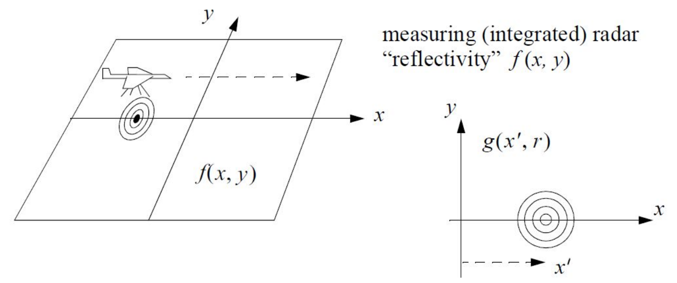

Fig. 3. The radar imaging problem. The ground features are probed by the radar pulses from the airplane. Circular projections of the "reflectivity" are measured.

common centre. A single projection measurement is therefore a radial function, because it only depends on the radius of the circle. Note that **radial functions are the measurements in the SAR problem**, whereas **for coherent scatter imaging, the radial functions are the unknown**, sought quantity. Image reconstruction for SAR has been understood for some time (see, e.g. [9]), and has the familiar features of (i) a slice theorem, (ii) filtered-backprojection (FBP) reconstruction, (iii) backprojection-filtering reconstruction.

II. MATHEMATICAL DESCRIPTIONS

A. Coherent scatter imaging model

For the coherent scatter imaging problem, we let $b(x, y)$ represent the "scatter image", which is the intensity of the measurements on the detector. The vertical axis is y and we assume that the centers of the circles lie along the x-axis. We use g for the radial functions and let $g(x', r)$ be the intensity of the ring of radius r whose center is at location (x', r). We assume and infinite number of pencil beams, one for each point on the x-axis. The measurements consist of the superposition of these radial functions and we use the operator S^* to represent this superposition. So $b = S^*g$ where

$$S^*g\,(x, y) = \int_{-\infty}^{\infty} g(x', r)\big|_{r=\sqrt{(x-x')^2+y^2}}\, dx'. \tag{1}$$

The objective is to reconstruct g from measurements b.

B. SAR model

For the SAR image reconstruction problem we let $f(x, y)$ represent the terrain which is scanned by radar by the airplane flying directly above the x-axis. We assume the measured radar signal at an instant of time is the integrated value of f for all points at equal distance to the airplane, thus a circle of radius r centered at $(x', 0)$, so the measurements are radial functions. We use S to represent this measurement process, hence $g = Sf$ where

$$Sf\,(x', r) = \int_0^{2\pi} f(x' + r\cos\phi, r\sin\phi)\, d\phi. \tag{2}$$

The objective is to reconstruct f from SAR data $g = Sf$.

Note that if f is odd in y (i.e. $f(x, -y) = -f(x, y)$) then it is invisible in the sense that $Sf = 0$. It is therefore assumed that f is even in y, or, equivalently, that only the even part of f can be reconstructed.

C. SAR image reconstruction

The backprojection of g performs the usual "smearing" of the radial functions into the original domain and can be written as

$$b(x, y) = \int_{-\infty}^{\infty} g(x', r)\big|_{r=\sqrt{(x-x')^2+y^2}}\, dx' \tag{3}$$

which is identical to (1), so we can safely use the symbol S^* to represent the backprojection operator in the SAR context.

The SAR slice theorem is

$$\widehat{f}(k_x, k_y) = \widetilde{g}\Big(k_x, \sqrt{k_x^2 + k_y^2}\Big)\, \frac{|k_y|}{2}. \tag{4}$$

As will be evident below, the "slices" are vertical lines in the 2D Fourier space. Here, $\widehat{f}$ is the usual 2D Fourier transform of f, $\widehat{f}(k_x, k_y) = \int\int f(x, y)\, \exp(-2\pi i(k_x x + k_y y))\, dx\, dy$, and $\widetilde{g}$ is the Fourier-Hankel transform of g (Fourier of the first variable, Hankel of the second variable):

$$\widetilde{g}(k_x, \rho) = \int_{-\infty}^{\infty}\int_0^{\infty} g(x, r)\, e^{-2\pi i k_x x}\, J(r\rho)\, r\, dr\, dx \tag{5}$$

where $J(t) = \int_0^{2\pi} e^{2\pi i t \sin\phi}\, d\phi$ is (a scalar multiple of) the Bessel function of order zero.

Re-expressed, the slice theorem is

$$\widetilde{g}(k_x, \rho) = \frac{2}{\sqrt{\rho^2 - k_x^2}} \begin{cases} \widehat{f}(k_x, \sqrt{\rho^2 - k_x^2}) & \text{if } \rho > |k_x| \\ 0 & \text{otherwise} \end{cases} \tag{6}$$

and we more clearly see that there is a relationship in the Fourier domain between vertical slices $\widehat{f}(k_x, \cdot)$ of the sought quantity f, and vertical slices $\widetilde{g}(k_x, \cdot)$ of the Fourier-Hankel transform of the measurements g.

A filtered-backprojection (FBP) reconstruction algorithm for f_{FBP} can be formulated as the backprojection, (1), of "filtered" projections g_{F}:

$$f_{\text{FBP}}(x, y) = S^* g_{\text{F}}(x, y) = \int_{-\infty}^{\infty} g_{\text{F}}(x', \sqrt{(x - x')^2 + y^2})\, dx \tag{7}$$

$$\widetilde{g_{\text{F}}}(k_x, \rho) = \widetilde{g}(k_x, \rho)\, \frac{\sqrt{\rho^2 - k_x^2}}{2} \tag{8}$$

where $\sqrt{\rho^2 - k_x^2}$ is understood to be zero for $|k_x| < \rho$.

Reconstruction by filtering after backprojection is also possible, via

$$\widehat{f}(k_x, k_y) = \widehat{b}(k_x, k_y)\, \frac{|k_y|}{2} \tag{9}$$

All of these results (in section II.C) have been known for some time. Furthermore, they have all been put on a rigorous mathematical foundation [9].

III. IMAGE RECONSTRUCTION FOR COHERENT SCATTER

We report here on our preliminary investigations to invert S^* in order to perform reconstruction for the coherent scatter problem, i.e. to find g from $b = S^*g$.

A. Duality

For the scatter imaging problem, $b = S^* g$, we anticipate for physical reasons, that the backprojection process, symbolized by $(S^*)^*$ would consist of creating and superimposing radial functions from the scatter image $b(x, y)$:

$$(S^*)^* b\,(x', r) = \int_0^{2\pi} b(x' + r\cos\phi, r\sin\phi)\, d\phi \tag{10}$$

To verify this formula mathematically, we consider the usual definition of backprojection, the adjoint of the forward operator. Here the forward operator is S^* so we define the adjoint, $(S^*)^*$, by $\langle S^* g\,, b\rangle_1 = \langle g\,, (S^*)^* b\rangle_2$. The inner products are defined, as expected, by

$$\begin{aligned} \langle b_1\,, b_2\rangle_1 &= \int_{-\infty}^{\infty}\int_{-\infty}^{\infty} b_1(x, y)\, b_2(x, y)\, dx\, dy \\ \langle g_1\,, g_2\rangle_2 &= \int\int_0^{\infty} g_1(x', r)\, g_2(x', r)\, r\, dr\, dx'. \end{aligned} \tag{11}$$

Using these inner products, and the definition of S^*, we obtain

$$\begin{aligned} &\langle S^* g\,, b\rangle_1 = \int\int S^* g(x, y)\, b(x, y)\, dx, dy \\ &= \int\int\int g(x', \sqrt{(x - x')^2 + y^2})\, b(x, y)\, dx'\, dx\, dy \\ &= \int\int\int g(x', \sqrt{\bar{x}^2 + y^2})\, b(\bar{x} + x', y)\, d\bar{x}\, dy\, dx' \\ &= \int\int_0^{\infty}\int_0^{2\pi} g(x', r)\, b(r\cos\phi + x', r\sin\phi)\, d\phi\, r\, dr\, dx' \\ &= \int\int_0^{\infty} g(x', r)\, \Big[\int_0^{2\pi} b(r\cos\phi + x', r\sin\phi)\, d\phi\Big]\, r\, dr\, dx' \\ &= \int\int_0^{\infty} g(x', r)\, \big[(S^*)^* b\,(x', r)\big]\, r\, dr\, dx' \\ &= \langle g\,, (S^*)^* b\rangle_2 \end{aligned} \tag{12}$$

by which we see that $(S^*)^* b$ is indeed given by equation (10). (Note: in (12) and elsewhere, all integrals are evaluated from $-\infty$ to $+\infty$ unless otherwise indicated.)

We have already noted that S^*, the forward model for the coherent scatter problem, is the same as the backprojection operator for the SAR problem. We have now also shown that $(S^*)^*$, the backprojection operator for the coherent scatter problem is the same as the forward model, S for the SAR problem. In other words, $(S^*)^* = S$ and the duality between the two problems is complete: the forward model of one problem corresponds to the backprojection of the other.

Inversion of S^* (to reconstruct g, the coherent scatter radial function) now looks easy, since we know from SAR formulas how to invert S. In short, we expect $(S^*)^{-1} = (S^{-1})^*$. However, the naive procedure to take measurements b, then obtain f using SAR reconstruction (see equation (10) for example), and subsequently calculate $g = Sf$ as a method to reconstruct g will **fail**, in general. The difficulty is that the unknown radial functions g might not be of the form Sf for some f, i.e. the correct g might not be in the range of S. The problem is that the operator S is not onto (not surjective), and is subject to range conditions, also known as "data consistency conditions" as will be discussed in more detail in Section III.B below. The original coherent scatter radial functions g are under no such constraints.

On the other hand, Section II.C gives explicit reconstruction formulas, demonstrating that S is one-to-one (injective). Strictly speaking, S does not have a true inverse; it only has a *left* inverse, say S^L. [ASIDE: The Radon transform has this same characteristic: the Radon inversion formula is a left inverse.] Now letting the identity operator be I, we have $I = S^L S$ and $I = I^* = (S^L S)^* = S^*(S^L)^*$ which shows that S^* has a right inverse, namely $(S^*)^R = (S^L)^*$. Therefore the coherent scatter operator S^* is onto, but not one-to-one. We conclude that unique solutions of $b = S^* g$ for g are not possible.

The nullspace of the operator S^* exactly characterizes the non-uniqueness of the coherent scatter reconstruction problem, so it is essential to obtain a complete description of it. This nullspace is closely linked to the range conditions on S: if $q(x', r)$ is in the nullspace of S^* then $S^* q = 0$, and for all function $b(x, y)$, we have $0 = \langle b\,, S^* q\rangle_1 = \langle (S^*)^* b\,, q\rangle_2 = \langle Sb\,, q\rangle_2$ so q is a range condition on the operator S, and conversely. (In finite dimensions, the statement is just that the nullspace of a matrix is orthogonal to the column space of its transpose.) We therefore search for a suitable description of the range of S.

B. Range conditions for SAR; nullspace for coherent scatter

We have pursued three approaches to describing the range conditions of S. One approach involves moment conditions and polynomial expressions; another approach considers links to wave equations; and the third approach appeals directly to the slice theorem.

Moment conditions are used in the Helgason-Ludwig conditions for the Radon transform and take the form of certain polynomial expressions. Following this approach [10] we consider $g_{x'}(r) = g(x', r)$ as a projection with index x' and take the $2n$th moment which we call $H_n(x')$. If $g = Sf$ for some f, then

$$\begin{aligned} H_n(x') &= \int_0^{\infty} g_{x'}(r)\, r^{2n+1}\, dr \\ &= \int_0^{\infty}\int_0^{2\pi} f(x' + r\cos\phi, r\sin\phi)\, r^{2n}\, d\phi\, r\, dr \\ &= \int\int f(x' + x, y)\, (x^2 + y^2)^n\, dx\, dy \\ &= \int\int f(x, y)((x - x')^2 + y^2)^n\, dx\, dy \end{aligned} \tag{13}$$

which is a polynomial of degree (at most) $2n$ in x'.

We have taken this approach further and have shown that if $g = Sf$ for some f, then g can be written in terms of polynomials:

$$g(x', r) = e^{-r^2} \sum_{j=0}^{\infty} C_{2j+1}(x')\, h_{2j+1}(r) \tag{14}$$

where $h_{2j+1}(r)$ is the normalized Hermite polynomial of degree $2j+1$, and where $C_{2j+1}(x')$ is a polynomial of degree at most $2j$. Therefore, functions of the form $q_{k,j}(x', r) =$

$e^{-r^2}\,(x')^k\, h_{2j+1}(r)$ with $k > 2j$ are in the orthogonal complement of the range of S, and are therefore in the nullspace of S^*.

In our second approach to examining the range conditions for S, we followed the work of Narayanan and Rakesh [11]. Here a link between the operator S was made with a certain partial differential equation. A necessary and sufficient condition for a function $g(x', r)$ to be in the range of S was given in terms of the following formula. For all $x \in \mathbb{R}$ and all non-zero $y \in \mathbb{R}$,

$$\begin{aligned}\int\!\int_0^\infty \frac{H(r^2+y^2-(x')^2)}{\sqrt{r^2+y^2-(x')^2)}}\, r \left(\frac{1}{2r}\frac{\partial}{\partial r}\right) \frac{F(x+x', r)}{r}\, dr\, dx' \\ = 0 \qquad\qquad (15)\end{aligned}$$

where H is the Heaviside function and F is the function of interest. The function F is related to the solution of the wave equation and satisfies the above equation if and only if it is in the range of the operator U defined by

$$\begin{aligned}Uf\,(x', r) =& \frac{1}{\pi}\, r \left(\frac{1}{2r}\frac{\partial}{\partial r}\right) \times \\ & \int\!\!\int \frac{H(r^2-(x'-x)^2-y^2)}{\sqrt{r^2-(x'-x)^2-y^2}}\, f(x,y)\, dx\, dy \qquad (16)\end{aligned}$$

We have not yet clarified the links to the range of S, but these equations seem to be quite different from the other two approaches.

The third approach to examining range conditions for S appealed directly to the slice theorem, equation (6). There we see that if $g = Sf$ for some f, then $\widetilde{g}$ has the property that $\widetilde{g}(k_x, \rho) = 0$ for $\rho < |k_x|$. These zero values each represent a consistency condition (range condition) for S, and therefore a nullspace element for S^*. To clarify, for any $0 < a < |b|$, define $q_{a,b}(x', r) = J(ar)\, \exp(-2\pi i b x')$. Then, for all f, and letting $g = Sf$,

$$\begin{aligned}\langle f\,, S^* q_{a,b}\rangle_1 &= \langle Sf\,,\, q_{a,b}\rangle_2 \\ &= \int\!\int_0^\infty Sf(x', r)\, q_{a,b}(x', r)\, r\, dr\, dx' \\ &= \int\!\int_0^\infty g(x', r)\, J(ar)\, e^{-2\pi i b x'}\, r\, dr\, dx' \\ &= \widetilde{g}(b, a) \\ &= 0 \qquad \text{(because } a < |b|\text{)} \qquad (17)\end{aligned}$$

Since $\langle f\,, S^* q_{a,b}\rangle_1 = 0$ for all f, we must have $S^* q_{a,b} = 0$ so $q_{a,b}$ is in the nullspace of S^*.

For each pair (a, b) (with $0 < a < |b|$) we thus obtain linearly independent elements of the nullspace. This is the most explicit nullspace description for S^* that we have obtained so far.

At this stage of our investigations, we have not studied the relationships between the nullspace elements found using the three approaches.

C. A tomographic model for coherent scatter

In this section, we present the scatter problem as a true tomography problem, in the sense that the measurements represent integrals over some kind of lines. We can then appeal to known results in tomography theory to extract information about the coherent scatter operator S^*.

We begin by recalling the familiar situation of the 2D Radon transform.

$$p(\phi, s) = \mathscr{R}f\,(\phi, s) = \int f(s\cos\phi - t\sin\phi,\, s\sin\phi + t\cos\phi)\, dt \qquad (18)$$

Here, the integration is over straight lines, and a projection $p(\phi, \cdot)$ consists of integrations over parallel lines.

For the 2D Radon transform, the backprojection is given by

$$\mathscr{R}^* p\,(x, y) = \int_0^\pi p(\phi, s)|_{s = x\cos\phi + y\sin\phi}\, d\phi \qquad (19)$$

The set of points in the (ϕ, s) domain that correspond to the set of lines passing through a fixed (x, y), is a sinusoid. The (ϕ, s) domain is known as a *sinogram*. See figure 4 for an illustration of these concepts.

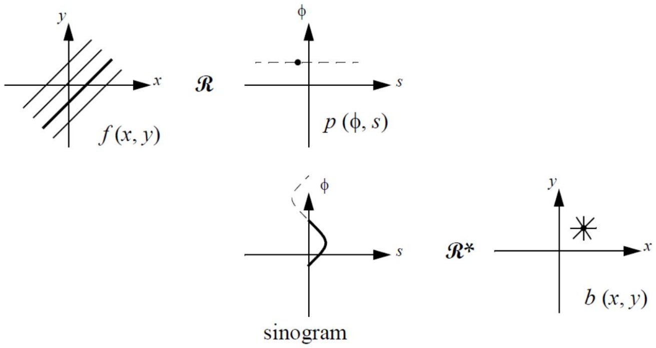

Fig. 4. The Radon transform $\mathscr{R}$ maps integrals over parallel straight lines into the (ϕ, s) domain. The (ϕ, s) domain is called a sinogram because backprojection $\mathscr{R}^* p\,(x, y)$ at the single point (x, y) corresponds to summing over a sinusoid in (ϕ, s).

Turning now to the SAR transform S, and observing the analogy with the 2D Radon transform, if $g(x', r) = Sf\,(x', r)$ (equation (2)) the integrations now take place of circles. Here, a projection, $g(x', \cdot)$ is a collection of concentric circles. Now, recalling the SAR backprojection from equation (3),

$$S^* g\,(x, y) = \int_{-\infty}^{\infty} g(x', r)|_{r = \sqrt{(x-x')^2 + y^2}}\, dx' \qquad (20)$$

and we observe that the set of points in the (x', r) domain that correspond to the set of circles (with centers on the x axis) passing through a fixed (x, y) is an hyperbola. The equation of the hyperbola is $r^2 = (x - x')^2 + y^2$; note that (x, y) is fixed and the hyperbola variables are x' and r. We could call the (x', r) domain a *hyperbologram*. See figure 5.

Finally, we consider S^* as the forward operator for the coherent scatter problem. In this case, the sought functions are radial functions, in the (x', r) domain. A single point $b(x, y)$ in the measurement domain corresponds to contributions from circles that intersect the point (x, y). Thus (repeating equation (1)),

$$S^* g\,(x, y) = \int_{-\infty}^{\infty} g(x', \sqrt{(x-x')^2 + y^2})\, dx' \qquad (21)$$

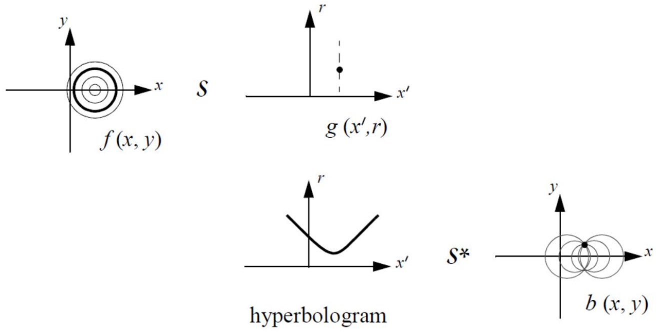

Fig. 5. The SAR transform S maps integrals over concentric circles into the (x', r) domain. The (x', r) domain could be called a hyperbologram because backprojection $S^* g\,(x, y)$ at the single point (x, y) corresponds to summing over a hyperbola in (x', r).

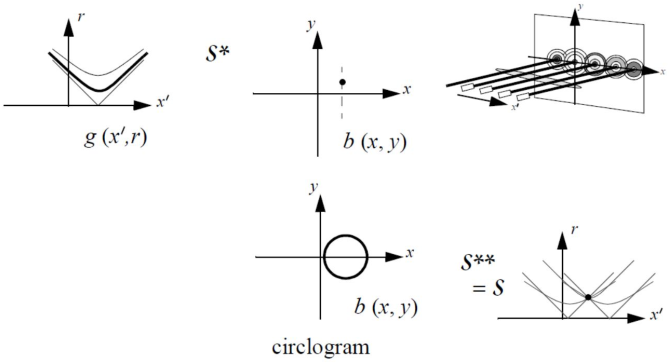

Fig. 6. The coherent scatter transform S^* maps integrals over hyperbolas into the (x, y) domain. The upper right insert is a reminder of the physical system showing superimposed circles. Each point $b(x, y)$ in the scatter image is the result of an integration over a hyperbola in the domain of the radial functions. Here, the (x, y) domain could be referred to as a circlogram because backprojection $S^{**} b\,(x', r)$ at the single location (x', r) corresponds to integrating over a circle in (x, y).

can be seen as integrating along hyperbolas in the (x', r) domain. Projections $b(x, \cdot)$ are now indexed by the x variable, and each projection specifies a collection of hyperbolas with a common center at $x' = x$.

Now, backprojection in this context can be regarded conventionally, as superimposing successive backprojections of individual projections. To see this, we reformulate the backprojection formula, equation (10). We would like to see the integral taken over the projection index x. To this end, we perform a change of integration variables from ϕ to x by $x = x' + r\cos\phi$. (Also, we shorten $(S^*)^*$ to S^{**}.)

$$\begin{aligned} S^{**} b\,(x', r) &= \int_0^{2\pi} b(x' + r\cos\phi, r\sin\phi)\, d\phi \\ &= 2\int_{x'-r}^{x'+r} b(x, y)\big|_{y=\sqrt{r^2-(x-x')^2}}\; J\, dx \qquad (22) \end{aligned}$$

We observe that $y = \sqrt{r^2 - (x - x')^2}$ is indeed the equation of the (semi-) circle in the measurement domain (x, y). We recall that $b(x, y) = b(x, -y)$ so the factor of 2 arises from the reflection in y; the integral adds the upper semi-circle twice, which is equivalent to integrating once over the whole circle. The Jacobian term $J = 1/\sqrt{r^2 - (x - x')^2}$ is present to ensure uniform integration over the circle when parametrizing by x. The measurement domain could (perhaps at a stretch) be called a *circlogram.*

Figure 6 illustrates the representation of the coherent scatter model as a tomography problem.

Viewing S^* as a tomographic operator brings new insights. The integration lines in the (x', r) domain (of radial functions) are hyperbolas of the form $\{(x', r) \mid r^2 - y^2 = (x' - x)^2,\ r \geq 0\}$ where x and y are parameters. These hyperbolas are all aysmptotic to the lines $r = |x' - x|$ and therefore no part of these integration lines are steeper than 45 degrees (the absolute slope $|m|$ never exceeds one).

Using such hyperbolas to probe a function $g(x', r)$ is reminiscent of conventional limited-angle (2D, parallel) tomography with integration lines never within 45 degrees of the vertical. It is well-known that a large wedge-shape missing region in the 2D Fourier domain arises, and that reconstruction artifacts are inevitable. We can anticipate this same behavior for the coherent scatter operator S^* which is not providing any more information than the limited-angle parallel-beam case. This analysis also suggests that the nullspace of the S^* operator is substantial.

Limited-angle tomography usually implies that there are directions of very poor resolution, and only very low sampling in these directions are required. Fortunately, for the coherent scatter problem, the direction of poor resolution is in x' and the high resolution direction is r. The x' direction is under user control, because the spacing of the x-ray pencil beams can be adjusted to match the reconstruction capability of the system.

IV. COMPUTER SIMULATIONS

We have conducted some preliminary numerical experiments. For an artificially simple radial function g_{true}, we simulated (ideal) data $b_{\text{data}} = S^* g_{\text{true}}$. From b_{data} we performed numerical reconstructions to estimate g_{true}, using both an ML-EM algorithm, and a conjugate gradient method. Figure 7 illustrates the results. Both algorithms implicitly enforced compactness of the iterates g_k. Note that seven pencil beams were simulated. After 100 iterations, both algorithms had performed reasonable reconstructions, of roughly comparable visual quality. An ML-EM method was reported in [12], for five pencil beams of real data.

V. DISCUSSION AND CONCLUSIONS

We have described a novel image reconstruction problem arising in the context of coherent scatter imaging. We identified that this problem is mathematically dual to the SAR problem of reconstructing a function from its integrals over circles.

In examining the coherent scatter operator S^*, we appeal heavily to known results on the SAR operator S. We concentrated on obtaining characterizations of the range conditions (consistency conditions) on S because these conditions lead directly to descriptions of the nullspace of S^*. The nullspace tells us what is possible and not possible in principle when reconstructing radial functions in the coherent scatter context.

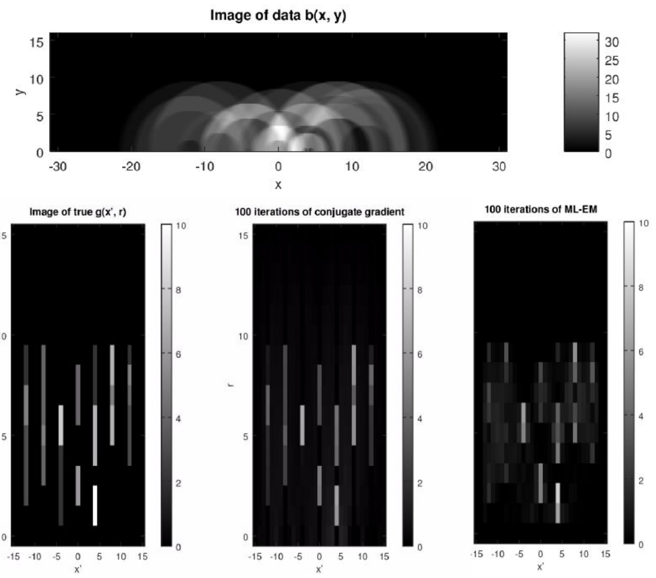

Fig. 7. Top: image of the simulated data $b(x, y)$ from ideal radial functions. Only $y \geq 0$ is shown because $b(x, y)$ is even in y. Bottom left: an image of $g_{\text{true}}(x', r)$ which was defined as piecewise constant in r for 7 discrete values of x'. Bottom middle: 100 iterations of conjugate gradient showing reasonable reconstruction from b_{data} of most of the features of g_{true}. Bottom right: 100 iterations of ML-EM showing different reconstructed features from the conjugate gradient reconstruction.

We obtained descriptions of the nullspace of S^* but in all cases, the descriptions were in terms of functions with unbounded support in x'. In the case of scatter imaging, a bounded extent of the parallel x-ray beams is ensured, so we need to find subspaces of the nullspace for which the support in the x' component is bounded. At this time, we have not pursued this lead.

A consequence of the fact that S is one-to-one (injective) is that S^* must be onto (surjective). In terms of the coherent scatter problem, this means that *any* scatter image $b(x, y)$ is possible, by selecting an appropriate set of radial functions $g(x', r)$. The application of a right inverse $(S^*)^R$ to the desired scatter image b yields $g = (S^*)^R b$ and, taking S^* of both sides of this equation shows that this g indeed produces the required b (i.e. $b = S^* g$). As a small technicality, we have not enforced the physical non-negativity of the radial functions g or the scatter image b, so (without further exploration) there is no assurance that non-negative radial functions g could be found that generate a given non-negative b. These matters concerning the surjectivity of S^* are interesting but probably do not provide useful information on solving the system $b = S^* g$; the non-trivial nullspace of S^* means that different right inverses will give different radial functions g, all of which produce the same scatter image b.

The points made in the previous paragraphs do not take into account the situation of restricting $g(x', r)$ to radial functions which are compact in x'. In particular, it might turn out that the nullspace is trivial under this compactness assumption, which would then imply a left-inverse for S^* that would necessarily match the right inverse to form a true, unique inverse $(S^*)^{-1}$. The model for compact radial functions needs to be studied.

Using the tomographic model of S^*, we observed that the problem appears to correspond to a substantial limited-angle system with only half of the Fourier domain frequencies being measured. Fortunately, the direction of poor resolution is in x' which can be controlled directly by the user by spacing the x-ray pencil beams. It would be useful to use some knowledge of the radial functions (required resolution in r and assumptions on the extent of r) to select some best-possible spacing of the x-ray pencil beams. This approach also remains to be explored.

In summary, we have described a new reconstruction problem in coherent scatter imaging and performed preliminary mathematical investigations. We have identified that there is likely to be nullspace, possibly also in the situation where the domain of the operator S^* is restricted to functions $g(x', r)$ with compact support in x'. Several interesting directions for research in this area have been identified.

REFERENCES

[1] G. Harding, J. Kosanetsky, U. Neitzel "Elastic scatter computed tomography." *Phys. Med. Biol.* 30, 183–186, 1985.

[2] R.J. Leclair and P.C. Johns "A semianalytic model to investigate the potential application of x-ray scatter imaging." *Med. Phys.* 25, 1008–1020, 1998.

[3] B.W. King, K.A. Landheer, P.C. Johns "X-ray coherent scattering form factors of tissues, water and plastics using energy dispersion." *Phys. Med. Biol.* 56, 4377–4397, 2011.

[4] J.R. Spencer, J.E. Carter, C.K. Leung, S.J. McCall, J.A. Greenberg, A.J. Kapadia "Coded aperture coherent scatter spectral imaging for assessment of breast cancers: An ex-vivo demonstration." *Proc. SPIE* 10132, Medical Imaging 2017: Physics of Medical Imaging, 101324K, 2017.

[5] I. Odinaka, J.A. O'Sullivan, D.G. Politte, K.P. MacCabe, Y. Kaganovsky, J.A. Greenberg, M. Lakshmanan, K. Krishnamurthy, A.J. Kapadia, L. Carin, D.J. Brady "Joint System and Algorithm Design for Computationally Efficient Fan Beam Coded Aperture X-Ray Coherent Scatter Imaging." *IEEE Trans. Comp. Imag.* 3, 506–521, 2017.

[6] B. Ghammraoui and L.M. Popescu "Non-invasive classification of breast microcalcifications using x-ray coherent scatter computed tomography." *Phys. Med. Biol.* 62, 1192–1207, 2017.

[7] Z. Zhu and S. Pang "Full three-dimensional direction-dependent X-ray scattering tomography." *Proc. SPIE* 10132, Medical Imaging 2017: Physics of Medical Imaging, 101324M, 2017.

[8] K.A. Landheer and P.C. Johns "Synchrotron-based coherent scatter x-ray projection imaging using an array of monoenergetic pencil beams." *Rev. Sci. Instru.* 83: 095111, 2012.

[9] L.-E. Andersson "On the determination of a function from spherical averages." *SIAM J. Math. Anal.* 19, 214–232, 1988.

[10] S. Patch "Thermoacoustic tomography - consistency conditions and the partial scan problem." *Phys. Med. Biol.* 49, 2305–2315, 2004.

[11] E.K. Narayanan and Rakesh "Spherical means with centers on a hyperplane in even dimensions." *Inv. Prob.* 26, 035014, 2010.

[12] K.A. Landheer and P.C. Johns "Coherent x-ray scatter projection imaging using an array of mono-energetic pencil beams." *Proc. SPIE* 8358, 83581O, 2012.

Appendix B

Proceedings paper in SPIE Medical Imaging 2020

This is our proceedings paper [Nguyen et al., 2020a] in the SPIE Medical Imaging 2020 conference. Chapter 2 presents this work with a few further developments added.

Automatic geometric calibration in 3D parallel geometry

Nguyen, Hung, Clackdoyle, Rolf, Desbat, Laurent

Hung Nguyen, Rolf Clackdoyle, Laurent Desbat, "Automatic geometric calibration in 3D parallel geometry," Proc. SPIE 11312, Medical Imaging 2020: Physics of Medical Imaging, 113123P (16 March 2020); doi: 10.1117/12.2549568

Event: SPIE Medical Imaging, 2020, Houston, Texas, United States

Automatic geometric calibration in 3D parallel geometry

Hung Nguyen[a], Rolf Clackdoyle[a], and Laurent Desbat[a]

[a]Univ. Grenoble Alpes, CNRS, Grenoble INP, TIMC-IMAG, 38000 Grenoble, France

ABSTRACT

This work concerns automatic geometric calibration in 3D parallel geometry. The aim is to develop analytical formulas to identify the view direction and the in-plane angle only from projections of the object. We consider that two view directions are known and treat all others once at a time, repeating the same three-projection procedure. We identify the unknown view direction of the third projection image and the in-plane angles of the three projections.

Keywords: 3D X-ray transform, geometric calibration, data consistency conditions, moments

1. INTRODUCTION

In Medical Imaging and other fields, geometric scanner calibration is vital for accurate image reconstruction. For example, in 3D parallel imaging, each 2D projection image may contain an unknown shift amount and an unknown in-plane rotation. Estimating the view direction, the unknown shift and rotation amount of each projection image is called geometric calibration and is a crucial step before we can reconstruct the 3D object from its projections.

One of the early methods, called the "angular reconstitution", was given by van Heel[1,2] in order to identify the view direction and the unknown rotation, which we call the in-plane angle, of each projection image. His main idea was to use the Fourier-slice theorem. The theorem states that the 2D Fourier transform of a projection image matches a slice through the origin of the 3D Fourier transform of the 3D object. Thus two projection images give us two corresponding slices, and these two slices must have at least one line in common. The "angular reconstitution" method suggested a way to find that common line, and used this information to obtain the relative orientations of the projections.

Singer and Shkolnisky in[3,4] continued the idea of using the Fourier-slice theorem. Using linear algebra techniques, they developed several ways to find the common lines and obtain the geometric parameters of each projection image. Moreover, in[5] Singer *et al* also suggested a voting algorithm to find the common line, with high accuracy, even though their projection images were very noisy.

Using the Fourier-slice theorem and searching for a common line in order to relate two projection images is an application of data consistency conditions (DCCs). In our work, we have created a pairwise DCC. The difference is that instead of using the Fourier transform, we apply the 2D Radon transform to the projections. The "sinogram row-matching procedure" described in the next section allows us to estimate the geometric parameters with direct analytic formulas.

In 2D, the problem of identifying the geometric parameters from parallel projection measurements has been presented in the early work of Basu and Bresler.[6,7] They gave a series of theoretical results, which show that estimates of the view directions and detector shifts can be obtained uniquely from a sufficient number of projection images, from almost any general 2D object. However, analytical formulas for the geometric parameter estimation were not provided. In 3D, there are degenerate geometric configurations where the problem collapses to contiguous 2D problems for which the work of Basu and Bresler is fully relevant.

In this work, we address the problem of geometric self-calibration in the 3D parallel geometry. Our problem: given a collection of 3D parallel projections of some general object, identify the view direction, in-plane angle,

---

Further author information: (If possible send correspondence to H. Nguyen and L. Desbat)
H. Nguyen: E-mail: Hung.Nguyen@univ-grenoble-alpes.fr
L. Desbat: E-mail: Laurent.Desbat@univ-grenoble-alpes.fr

Medical Imaging 2020: Physics of Medical Imaging, edited by Guang-Hong Chen, Hilde Bosmans, Proc. of SPIE
Vol. 11312, 113123P · © 2020 SPIE · CCC code: 1605-7422/20/$21 · doi: 10.1117/12.2549568

and detector shift for each projection. To provide an anchor, we assume two projections to be known. Then we estimate the calibration parameters of all other projections. For simplicity, we present this work for known projections in the $\overline{e}_2$ and $\overline{e}_3$ directions (the y and z view directions). Each subsequent projection is handled independently of the rest.

2. THEORY AND METHODS

2.1 In-plane shift

The shifts are assumed to be corrected already, using standard center of mass techniques obtained from the first order and zero order moments of the projections. For each projection, detector coordinates are shifted so that the origin is the center of mass of the projection.

2.2 The 3D coordinate system and the X-ray transform

We will use the unit vector $\overline{\gamma} = (\gamma_1, \gamma_2, \gamma_3)$ to identify the view direction. Perpendicular to and defined in terms of $\overline{\gamma}$ are two unit vectors $\overline{\alpha}$ and $\overline{\beta}$ in the detector plane. Mathematically, we want $\overline{\alpha}$ and $\overline{\beta}$ to remain unchanged if the view direction $\overline{\gamma}$ changes to $-\overline{\gamma}$. Given a unit vector $\overline{\gamma} = (\gamma_1, \gamma_2, \gamma_3) \in \mathbb{S}^2$, we define

$$\begin{cases} \overline{\alpha} = \dfrac{\operatorname{sgn}(\gamma_3)}{\sqrt{\gamma_1^2 + \gamma_2^2}} \left(-\gamma_2, \gamma_1, 0\right), \\ \overline{\beta} = \dfrac{1}{\sqrt{\gamma_1^2 + \gamma_2^2}} \left(-\gamma_1\gamma_3, -\gamma_2\gamma_3, \gamma_1^2 + \gamma_2^2\right). \end{cases} \tag{1}$$

- If $\gamma_3 = 0$, we define $\overline{\alpha} = \operatorname{sgn}(\gamma_2)(-\gamma_2, \gamma_1, 0)$ and $\overline{\beta} = (0, 0, 1)$.
- If $\gamma_2 = \gamma_3 = 0$, then $\overline{\gamma} = \pm(1, 0, 0)$, we define $\overline{\alpha} = (0, 1, 0)$ and $\overline{\beta} = (0, 0, 1)$ for both cases.
- Finally, if $\gamma_1 = \gamma_2 = 0$, then $\overline{\gamma} = \pm(0, 0, 1)$, we define $\overline{\alpha} = (-1, 0, 0)$ and $\overline{\beta} = (0, -1, 0)$.

From here, our 3D coordinate system is fully defined. With this coordinate system, we define the 3D X-ray transform[8] as follows

$$p_{\overline{\gamma}}(u, v) = X_{\overline{\gamma}} f(u, v) = \int f\left(u\overline{\alpha} + v\overline{\beta} + t\overline{\gamma}\right) dt, \tag{2}$$

where $f \in C^c\left(\mathbb{R}^3\right)$, meaning f is a real-valued continuous function in $\mathbb{R}^3$ with compact support. Note that $p_{\overline{\gamma}}(u, v) = p_{-\overline{\gamma}}(u, v)$.

2.3 Problem statement

In general, we do not know the projection functions $p_{\overline{\gamma}}(u, v)$, because in the above definitions, for each direction $\overline{\gamma}$, we fix a certain pair of $\left(\overline{\alpha}, \overline{\beta}\right)$. However, in reality, we do not know how each corresponding detector has been rotated, which means we do not know the 2D coordinate system of the detector. Therefore, besides the view direction of each projection image being unknown, there is also an unknown in-plane angle. Let ϕ be the in-plane angle on the detector. We define the 2D coordinate system on the detector:

$$\begin{cases} \overline{\alpha}_{\overline{\gamma},\phi} = \cos\phi\overline{\alpha} + \sin\phi\overline{\beta}, \\ \overline{\beta}_{\overline{\gamma},\phi} = -\sin\phi\overline{\alpha} + \cos\phi\overline{\beta}. \end{cases} \tag{3}$$

where ϕ is the angle between $\overline{\alpha}$ and $\overline{\alpha}_{\overline{\gamma},\phi}$. Note that the signs of $\overline{\alpha}_{\overline{\gamma},\phi}$ and $\overline{\beta}_{\overline{\gamma},\phi}$ are reversed when ϕ is increased by π.

From this, let's say for each direction $\overline{\gamma}$, we just know the corresponding measurement on the detector, which is perpendicular to $\overline{\gamma}$

$$m_{\overline{\gamma},\phi}(u, v) = \int f\left(u\overline{\alpha}_{\overline{\gamma},\phi} + v\overline{\beta}_{\overline{\gamma},\phi} + t\overline{\gamma}\right) dt. \tag{4}$$

For simplicity, the problem we are now dealing with is: *Assuming we know* $m_{\overline{\gamma},\phi}$, $m_{\overline{e}_2,\phi_2}$, $m_{\overline{e}_3,\phi_3}$, *where* $\overline{e}_2 = (0, 1, 0)$, $\overline{e}_3 = (0, 0, 1)$. *How can we identify* $\overline{\gamma}$ *and* ϕ, ϕ_2, ϕ_3*?*

We know that $\overline{\alpha}$ and $\overline{\beta}$ are unchanged if $\overline{\gamma}$ becomes $-\overline{\gamma}$, and similarly for $\overline{\alpha}_{\overline{\gamma},\phi}$ and $\overline{\beta}_{\overline{\gamma},\phi}$. We expect the mathematics to generate two solutions $\overline{\gamma}$ and $-\overline{\gamma}$ of opposite sign, because $m_{\overline{\gamma},\phi} = m_{-\overline{\gamma},\phi}$.

2.4 Pairwise Data Consistency Conditions (DCC)

The main strategy is to use a pairwise DCC. The idea of this DCC is based on the relation of the 3D X-ray transform and the 3D Radon transform.

Step 1: Combining definitions of the 3D X-ray transform (2) and the 2D Radon transform, we can see that for any $f \in C^c\left(\mathbb{R}^3\right)$, $\overline{\gamma} \in \mathbb{S}^2$, for an arbitrary angle $\theta \in [0, 2\pi)$

$$\begin{aligned}
R_\theta^2 p_{\overline{\gamma}}(s) &= \int p_{\overline{\gamma}}\left(s\cos\theta - t'\sin\theta, s\sin\theta + t'\cos\theta\right) dt' \\
&= \iint f\left(\left(s\cos\theta - t'\sin\theta\right)\overline{\alpha} + \left(s\sin\theta + t'\cos\theta\right)\overline{\beta} + t\overline{\gamma}\right) dtdt' \\
&= \iint f\left(s\left(\cos\theta\overline{\alpha} + \sin\theta\overline{\beta}\right) + t'\left(-\sin\theta\overline{\alpha} + \cos\theta\overline{\beta}\right) + t\overline{\gamma}\right) dtdt' \\
&= \iint f\left(s\overline{\psi} + t'\overline{\psi}^\perp + t\overline{\gamma}\right) dtdt' \\
&= R_{\overline{\psi}}^3 f(s),
\end{aligned}$$

since the three unit vectors $\left(\overline{\psi}, \overline{\psi}^\perp, \overline{\gamma}\right)$ are perpendicular to each other, where $\overline{\psi} = \cos\theta\overline{\alpha} + \sin\theta\overline{\beta}$ and $\overline{\psi}^\perp = -\sin\theta\overline{\alpha} + \cos\theta\overline{\beta}$. R^2 and R^3 stand for the 2D and 3D Radon transform.

Step 2: From the definition of the measurement (4), the detector 2D coordinate system (3) and the 3D X-ray transform (2), we know that

$$\begin{aligned}
m_{\overline{\gamma},\phi}\left(u, v\right) &= \int f\left(u\left(\cos\phi\overline{\alpha} + \sin\phi\overline{\beta}\right) + v\left(-\sin\phi\overline{\alpha} + \cos\phi\overline{\beta}\right) + t\overline{\gamma}\right) dt \\
&= \int f\left(\left(u\cos\phi - v\sin\phi\right)\overline{\alpha} + \left(u\sin\phi + v\cos\phi\right)\overline{\beta} + t\overline{\gamma}\right) dt \\
&= p_{\overline{\gamma}}\left(u\cos\phi - v\sin\phi, u\sin\phi + v\cos\phi\right).
\end{aligned}$$

Step 3: We apply the 2D Radon transform to the above results. We obtain for all $s \in \mathbb{R}$:

$$\begin{aligned}
&R_\theta^2 m_{\overline{\gamma},\phi}(s) \\
&= \int m_{\overline{\gamma},\phi}\left(s\cos\theta - t'\sin\theta, s\sin\theta + t'\cos\theta\right) dt', \\
&= \int p_{\overline{\gamma}}\left(\left(s\cos\theta - t'\sin\theta\right)\cos\phi - \left(s\sin\theta + t'\cos\theta\right)\sin\phi, \left(s\cos\theta - t'\sin\theta\right)\sin\phi + \left(s\sin\theta + t'\cos\theta\right)\cos\phi\right) dt' \\
&= \int p_{\overline{\gamma}}\left(s\left(\cos\theta\cos\phi - \sin\theta\sin\phi\right) - t'\left(\sin\theta\cos\phi + \cos\theta\sin\phi\right),\right. \\
&\qquad\qquad\left. s\left(\sin\theta\cos\phi + \cos\theta\sin\phi\right) + t'\left(\cos\theta\cos\phi - \sin\theta\sin\phi\right)\right) dt' \\
&= \int p_{\overline{\gamma}}\left(s\cos\left(\theta + \phi\right) - t'\sin\left(\theta + \phi\right), s\sin\left(\theta + \phi\right) + t'\cos\left(\theta + \phi\right)\right) dt' \\
&= R_{\theta+\phi}^2 p_{\overline{\gamma}}\left(s\right).
\end{aligned}$$

Step 4: Finally, combining the results of **step 1** and **step 3**, we obtain for any $f \in C^c\left(\mathbb{R}^3\right)$, $\overline{\gamma} \in \mathbb{S}^2$, for an arbitrary angle $\theta \in [0, 2\pi)$:

$$R_\theta^2 m_{\overline{\gamma},\phi}(s) = R_{\theta+\phi}^2 p_{\overline{\gamma}}(s) = R_{\overline{\Psi}}^3 f(s), \forall s \in \mathbb{R}, \tag{5}$$

where $\overline{\Psi} = \cos\left(\theta + \phi\right)\overline{\alpha} + \sin\left(\theta + \phi\right)\overline{\beta} \in \mathbb{S}^2$.

Then we can create the **Pairwise DCC** as follows:

For two unit directions $\overline{\gamma}$ and $\overline{\gamma}'$, if we can find a suitable pair of angles $(\theta, \theta') \in [0, 2\pi)^2$ such that

$$\cos(\theta + \phi)\,\overline{\alpha} + \sin(\theta + \phi)\,\overline{\beta} = \cos(\theta' + \phi')\,\overline{\alpha}' + \sin(\theta' + \phi')\,\overline{\beta}' \left(= \overline{\Psi}\right), \tag{6}$$

then from (5), we obtain

$$R^2_{\theta} m_{\overline{\gamma},\phi}(s) = R^2_{\theta'} m_{\overline{\gamma}',\phi'}(s) \left(= R^3_{\overline{\Psi}} f(s)\right), \forall s \in \mathbb{R}.$$

We immediately make two important observations.

- By the construction of the pairwise DCC, we can see that $\overline{\Psi}$ here is perpendicular to both $\overline{\gamma}$ and $\overline{\gamma}'$.
- A pair of (θ, θ') satisfying (6) always exists for any given view directions $(\overline{\gamma}, \overline{\gamma}')$ and in-plane angles (ϕ, ϕ'). We just need to take $\overline{\Psi}$ as the normalized cross product of $\overline{\gamma}$ and $\overline{\gamma}'$, then θ can be defined by $\cos(\theta + \phi) = \overline{\Psi} \cdot \overline{\alpha}$ and $\sin(\theta + \phi) = \overline{\Psi} \cdot \overline{\beta}$, and similarly for θ'.

Now we are going to use this DCC in the context where $\overline{\gamma}$ is the unknown direction to be identified and $\overline{\gamma}'$ is the known direction, here in our problem: $\overline{e}_2$ or $\overline{e}_3$.

2.5 Method

We now have three projection measurements $m_{\overline{e}_2,\phi_2}$, $m_{\overline{e}_3,\phi_3}$ and $m_{\overline{\gamma},\phi}$. We note that:

- $\overline{e}_2 = (0, 1, 0)$ yields $\overline{\alpha}_2 = (-1, 0, 0)$ and $\overline{\beta}_2 = (0, 0, 1)$.
- $\overline{e}_3 = (0, 0, 1)$ yields $\overline{\alpha}_3 = (-1, 0, 0)$ and $\overline{\beta}_3 = (0, -1, 0)$.

The first step is to find a suitable pair of $(\theta_{1,2}, \theta_2)$ such that

$$\cos(\theta_{1,2} + \phi)\,\overline{\alpha} + \sin(\theta_{1,2} + \phi)\,\overline{\beta} = \cos(\theta_2 + \phi_2)\,\overline{\alpha}_2 + \sin(\theta_2 + \phi_2)\,\overline{\beta}_2 \left(= \overline{\Psi}_2\right), \tag{7}$$

and $R^2_{\theta_{1,2}} m_{\overline{\gamma},\phi}(s) = R^2_{\theta_2} m_{\overline{e}_2,\phi_2}(s), \forall s \in \mathbb{R}$. More precisely,

$$\begin{aligned}\overline{\Psi}_2 &= \cos(\theta_2 + \phi_2)(-1, 0, 0) + \sin(\theta_2 + \phi_2)(0, 0, 1) \\ &= (-\cos(\theta_2 + \phi_2), 0, \sin(\theta_2 + \phi_2)).\end{aligned}$$

We call this step *the sinograms row-matching procedure*, since from two measurements $m_{\overline{\gamma},\phi}$ and $m_{\overline{e}_2,\phi_2}$, we compute their 2D Radon transforms, which are the sinograms (let's say the horizontal axis of the sinogram is for s and the vertical axis is for θ). Then we will look for a row in the first sinogram and another row in the second sinogram, which perfectly match each other (at least theoretically). These lead to the values of $\theta_{1,2}$ and θ_2 that we are looking for. This procedure will be discussed more precisely in the next section 2.6. Assuming we have done this step and have found $\theta_{1,2}$ and θ_2, then by construction, we know that the unknown direction $\overline{\gamma}$ is perpendicular to $\overline{\Psi}_2 = (-\cos(\theta_2 + \phi_2), 0, \sin(\theta_2 + \phi_2))$.

Repeating this process, we obtain that $\overline{\gamma}$ is also perpendicular to $\overline{\Psi}_3 = (-\cos(\theta_3 + \phi_3), -\sin(\theta_3 + \phi_3), 0)$, where θ_3 is also obtained after performing the sinograms maching row procedure to find a pair $(\theta_{1,3}, \theta_3)$. Thus $\overline{\gamma}$ can be computed as follows

$$\begin{aligned}\overline{\gamma} &= \pm\frac{\overline{\Psi}_2 \times \overline{\Psi}_3}{\left\|\overline{\Psi}_2 \times \overline{\Psi}_3\right\|} \\ &= \pm\frac{(\sin(\theta_2 + \phi_2)\sin(\theta_3 + \phi_3), -\sin(\theta_2 + \phi_2)\cos(\theta_3 + \phi_3), \cos(\theta_2 + \phi_2)\sin(\theta_3 + \phi_3))}{\sqrt{1 - \cos^2(\theta_2 + \phi_2)\cos^2(\theta_3 + \phi_3)}}.\end{aligned}$$

We can see that the explicit solutions of $\overline{\gamma}$ can be found if we know ϕ_2 and ϕ_3. Additionally, the in-plane angle ϕ could also be computed using (7) if ϕ_2 is known.

Therefore the second crucial step is to find ϕ_2 and ϕ_3. We perform again the sinogram row-matching procedure between $m_{\overline{e}_2,\phi_2}$ and $m_{\overline{e}_3,\phi_3}$ and obtain $\theta_{2,3}$ and $\theta_{3,2}$ such that

$$\left(-\cos\left(\theta_{2,3}+\phi_2\right),0,\sin\left(\theta_{2,3}+\phi_2\right)\right)=\left(-\cos\left(\theta_{3,2}+\phi_3\right),-\sin\left(\theta_{3,2}+\phi_3\right),0\right),$$

and $R^2_{\theta_{2,3}}m_{\overline{e}_2,\phi_2}(s)=R^2_{\theta_{3,2}}m_{\overline{e}_3,\phi_3}(s)$. This implies

$$\begin{cases}\cos\left(\theta_{2,3}+\phi_2\right)=\cos\left(\theta_{3,2}+\phi_3\right)\\ \sin\left(\theta_{2,3}+\phi_2\right)=0\\ \sin\left(\theta_{3,2}+\phi_3\right)=0\end{cases}.$$

From this, we obtain $(\phi_2,\phi_3)=(-\theta_{2,3},-\theta_{3,2})$ or $(\phi_2,\phi_3)=(\pi-\theta_{2,3},\pi-\theta_{3,2})$. Although we obtain two solutions for (ϕ_2,ϕ_3), they lead to the same solutions of $\overline{\gamma}$ (two acceptable opposite solutions) and two solutions of the in-plane angle ϕ, which are π-different from each other.

In conclusion, we have successfully identified the view direction $\overline{\gamma}$. And for the in-plane angles (ϕ,ϕ_2,ϕ_3), we obtain two solutions, which are π-different from each other.

2.6 The sinograms row-matching procedure

The sinograms row-matching procedure is performed by computer. We consider two given sinograms as two matrices, with each row representing one value of θ and each column representing one value of s. From the first row of the first matrix, we subtract all rows of the second matrix, then we take the Euclidean norm of each row and obtain a column vector. We save this column vector data in a new matrix, which we call *the Norm of Difference matrix* (NoD). For the second column of the NoD, we take the second row of the first matrix and repeat this process, and so on. The NoD constructed this way is a square matrix, which has size $N_\theta\times N_\theta$, where N_θ is the number of rows of the first or second matrix. We search for the minimum value of the NoD matrix and note its position. This result will show us which row of the first sinogram matches which row of the second sinogram.

The idea of searching for the matching row has appeared in Van Heel's papers.[1,2] Van Heel built a so-called sinogram cross-correlation function, in which he computed the correlation coefficient of two corresponding rows in two sinograms, and then searched for the global maximum value of the function. We compute norm differences instead of cross-correlations because our projections have already been aligned. One can also see reference[5] for a voting algorithm to search for the common line.

2.7 Degenerate case of the problem

The method given in section 2.5 fails if $\left\|\overline{\Psi}_2\times\overline{\Psi}_3\right\|=0$, meaning $\overline{\Psi}_2$ and $\overline{\Psi}_3$ are collinear and $\overline{\gamma}$ is thus in the plane $(\overline{e}_2,\overline{e}_3)$, i.e. $\overline{\gamma}=(0,\gamma_2,\gamma_3)$. Solving this case is equivalent to solving multiple contiguous 2D problems. For this case, we have considered the simple version where the in-plane angles are assumed to be zero in each projection. We define the so-called in-plane moments of order k

$$P^k_{\overline{\gamma}}(u)=\int v^k p_{\overline{\gamma}}(u,v)\,dv. \tag{8}$$

Since $\overline{\gamma}=(0,\gamma_2,\gamma_3)$, applying definition (1), we have

$$\begin{cases}\overline{\alpha}=\dfrac{\operatorname{sgn}(\gamma_3)}{|\gamma_2|}(-\gamma_2,0,0)=\left(-\dfrac{\gamma_2\gamma_3}{|\gamma_2\gamma_3|},0,0\right)\\ \overline{\beta}=\dfrac{1}{|\gamma_2|}\left(0,-\gamma_2\gamma_3,\gamma_2^2\right)\ =\left(0,-\dfrac{\gamma_2\gamma_3}{|\gamma_2|},|\gamma_2|\right)\end{cases}. \tag{9}$$

We remind that (see definition (1))

- If $\overline{\gamma}\equiv\overline{e}_2=(0,1,0)$ then $\overline{\alpha}_2=(-1,0,0)$ and $\overline{\beta}_2=(0,0,1)$.

- If $\overline{\gamma} \equiv \overline{e}_3 = (0,0,1)$ then $\overline{\alpha}_3 = (-1,0,0)$ and $\overline{\beta}_3 = (0,-1,0)$.

Then by the definition of the 3D X-ray transform (2), we know that

$$\begin{cases} p_{\overline{e}_2}(u,v) = \displaystyle\int f\left(u\,(-1,0,0) + v\,(0,0,1) + t\,(0,1,0)\right) dt \quad = \displaystyle\int f\left(-u,t,v\right) dt \\ p_{\overline{e}_3}(u,v) = \displaystyle\int f\left(u\,(-1,0,0) + v\,(0,-1,0) + t\,(0,0,1)\right) dt = \displaystyle\int f\left(-u,-v,t\right) dt \end{cases}. \tag{10}$$

Combining (9) and (2), we can see that

$$\begin{aligned} P^k_{\overline{\gamma}}(u) &= \iint v^k f\left(u\overline{\alpha} + v\overline{\beta} + t\overline{\gamma}\right) dtdv \\ &= \iint v^k f\left(u\left(-\frac{\gamma_2\gamma_3}{|\gamma_2\gamma_3|},0,0\right) + v\left(0,-\frac{\gamma_2\gamma_3}{|\gamma_2|},|\gamma_2|\right) + t\left(0,\gamma_2,\gamma_3\right)\right) dtdv \\ &= \iint v^k f\left(-\frac{u\gamma_2\gamma_3}{|\gamma_2\gamma_3|}, -\frac{v\gamma_2\gamma_3}{|\gamma_2|} + t\gamma_2, v\,|\gamma_2| + t\gamma_3\right) dtdv. \end{aligned} \tag{11}$$

Let $y = -\dfrac{v\gamma_2\gamma_3}{|\gamma_2|} + t\gamma_2$ and $z = v\,|\gamma_2| + t\gamma_3$, we can compute

$$\begin{aligned} -\frac{\gamma_2\gamma_3}{|\gamma_2|}y + |\gamma_2|\,z &= -\frac{\gamma_2\gamma_3}{|\gamma_2|}\left(-\frac{v\gamma_2\gamma_3}{|\gamma_2|} + t\gamma_2\right) + |\gamma_2|\left(v\,|\gamma_2| + t\gamma_3\right) \\ &= v\gamma_3^2 - t\,|\gamma_2|\,\gamma_3 + v\gamma_2^2 + t\,|\gamma_2|\,\gamma_3 \\ &= v\left(\gamma_2^2 + \gamma_3^2\right) \\ &= v, \end{aligned}$$

since $\overline{\gamma} \in \mathbb{S}^2$, and also we have the Jacobian matrix

$$J = \begin{bmatrix} \dfrac{\partial y}{\partial v} & \dfrac{\partial y}{\partial t} \\ \dfrac{\partial z}{\partial v} & \dfrac{\partial z}{\partial t} \end{bmatrix} = \begin{bmatrix} \dfrac{-\gamma_2\gamma_3}{|\gamma_2|} & \gamma_2 \\ |\gamma_2| & \gamma_3 \end{bmatrix},$$

which implies

$$|\det(J)| = \left|-\frac{\gamma_2\gamma_3^2}{|\gamma_2|} - \gamma_2\,|\gamma_2|\right| = \left|-\frac{\gamma_2}{|\gamma_2|}\left(\gamma_3^2 + \gamma_2^2\right)\right| = 1,$$

thus we have $dy\,dz = dt\,dv$. All these materials make the integral in (11) become

$$P^k_{\overline{\gamma}}(u) = \iint \left(-\frac{\gamma_2\gamma_3}{|\gamma_2|}y + |\gamma_2|\,z\right)^k f\left(-\frac{u\gamma_2\gamma_3}{|\gamma_2\gamma_3|}, y, z\right) dydz.$$

Then for $k = 1$ we obtain

$$\begin{aligned} P^1_{\overline{\gamma}}(u) &= \iint \left(-\frac{\gamma_2\gamma_3}{|\gamma_2|}y + |\gamma_2|\,z\right) f\left(-\frac{u\gamma_2\gamma_3}{|\gamma_2\gamma_3|}, y, z\right) dydz \\ &= -\frac{\gamma_2\gamma_3}{|\gamma_2|}\int y\left[\int f\left(-\frac{u\gamma_2\gamma_3}{|\gamma_2\gamma_3|}, y, z\right) dz\right] dy + |\gamma_2|\int z\left[\int f\left(-\frac{u\gamma_2\gamma_3}{|\gamma_2\gamma_3|}, y, z\right) dy\right] dz. \end{aligned}$$

Applying (10) we have

$$\begin{aligned} P^1_{\overline{\gamma}}(u) &= -\frac{\gamma_2\gamma_3}{|\gamma_2|}\int y p_{\overline{e}_3}\left(\frac{u\gamma_2\gamma_3}{|\gamma_2\gamma_3|}, -y\right) dy + |\gamma_2|\int z p_{\overline{e}_2}\left(\frac{u\gamma_2\gamma_3}{|\gamma_2\gamma_3|}, z\right) dz \\ &= \frac{\gamma_2\gamma_3}{|\gamma_2|}\int y p_{\overline{e}_3}\left(\frac{u\gamma_2\gamma_3}{|\gamma_2\gamma_3|}, y\right) dy + |\gamma_2|\int z p_{\overline{e}_2}\left(\frac{u\gamma_2\gamma_3}{|\gamma_2\gamma_3|}, z\right) dz \end{aligned}$$

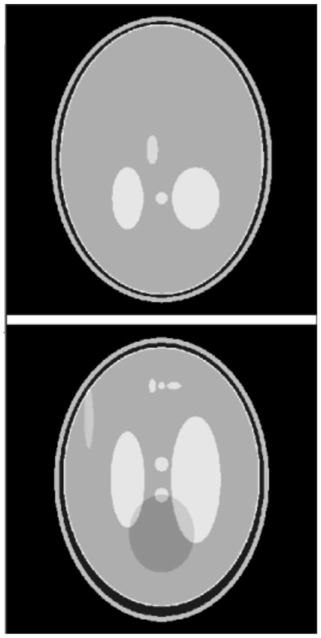

x_{center}	y_{center}	z_{center}	x_0	y_0	z_0
0	0	0	0.72	0.95	0.93
0	0	0	0.69	0.92	0.9
0	-0.0184	0	0.6624	0.874	0.88
0	-0.0184	0	0.6524	0.864	0.87
-0.22	0	-0.25	0.16	0.41	0.21
0.22	0	-0.25	0.11	0.31	0.22
0	0.35	-0,25	0.21	0.25	0.35
0	0.1	-0.25	0.046	0.046	0.046
-0.08	-0.605	-0.25	0.046	0.023	0.02
0.06	-0.605	-0.25	0.023	0.046	0.02
0	-0.1	-0.25	0.046	0.046	0.046
0	-0.605	-0.25	0.023	0.023	0.023
0.06	-0.105	0.0625	0.04	0.056	0.1
0	0.1	0.625	0.056	0.056	0.1
0.47	-0.4	-0.25	0.03	0.2	0.1

Figure 1. Two perpendicular slices through the phantom: $y = -0.125$, $z = -0.25$; and table of centers, axis lengths of the ellipsoids

According to the definition of the in-plane moment (8), we thus obtain the in-plane DCC:

$$P^1_{\overline{\gamma}}(u) = \frac{\gamma_2\gamma_3}{|\gamma_2|} P^1_{\overline{e}_3}\left(\frac{u\gamma_2\gamma_3}{|\gamma_2\gamma_3|}\right) + |\gamma_2|\, P^1_{\overline{e}_2}\left(\frac{u\gamma_2\gamma_3}{|\gamma_2\gamma_3|}\right), \forall u \in \mathbb{R}. \tag{12}$$

In fact, for each real value u, this in-plane DCC (12) is a linear relation of γ_2 and γ_3. From (12) and the fact that $\overline{\gamma} = (0, \gamma_2, \gamma_3)$ is a unit vector, meaning $\gamma_2^2 + \gamma_3^2 = 1$; $\overline{\gamma}$ is then obtained by solving several second-degree equations (with each equation is yielded from one value of u), and then choosing the common solution from many (pairs of) solutions of these second-degree equations.
If the 3D object is completely general, we obtain a unique solution for $\overline{\gamma}$ (as well as $-\overline{\gamma}$). In other situations, such as a perfect cylinder or a cuboid, we obtain at most two solutions for $\overline{\gamma}$, with each solution is a pair of acceptable opposite solutions. Further study is needed for this case of the problem.

3. NUMERICAL SIMULATIONS AND RESULTS

For our computer simulation study, our object was a slightly simplified version of the high-contrast MRI 3D Shepp-Logan phantom.[9] We followed the descriptions in[9] and[10] but removed the inclintion angle of the two oblique ellipsoids. Fig. 1 shows two perpendicular slices through the phantom and a table of centers and half-axis lengths for the 15 component ellipsoids. The respective densities of the ellipsoids were: 0.8, -0.68, 0.86, -0.235, 0.235, 0.235, -0.128, 0.205, 0.205, 0.205, 0.205, 0.205, 0.185, 0.235, 0.105.

For this preliminary numerical experiment, we simulated projections with in-plane rotation angles of zero (assumed known). Using simple numerical integration of the 15 ellipsoid functions, three projections $p_{\overline{e}_2}$, $p_{\overline{e}_3}$, $p_{\overline{\gamma}}$ were simulated of size 513x513 pixels each. We used $\overline{\gamma} = (1/3, -2/3, 2/3)$ as our unknown view direction for the third projection. These three projections are illustrated in fig. 2.

From these three projections as input data, we performed the analytic calibration method. Sinograms of size 360x1025 were generated for each of the three projections (see fig. 3). Sinograms row-matching was performed as described in section 2.6 for projections $p_{\overline{e}_2}$ and $p_{\overline{\gamma}}$ to provide the 3D vector $\overline{\Psi}_2$, and similarly for $p_{\overline{e}_3}$ and $p_{\overline{\gamma}}$ to yield $\overline{\Psi}_3$. The estimate view direction $\overline{\gamma}_{\text{Est1}}$ was calculated by normalizing $\overline{\Psi}_2 \times \overline{\Psi}_3$, to give $\overline{\gamma}_{\text{Est1}} = \pm(0.32603, -0.66847, 0.66847)$. The polar and azimuthal angles of $\overline{\gamma}$ are 48.19^o and -63.43^o; and for $\overline{\gamma}_{\text{Est1}}$ they are 48.05^o and -64.00^o.

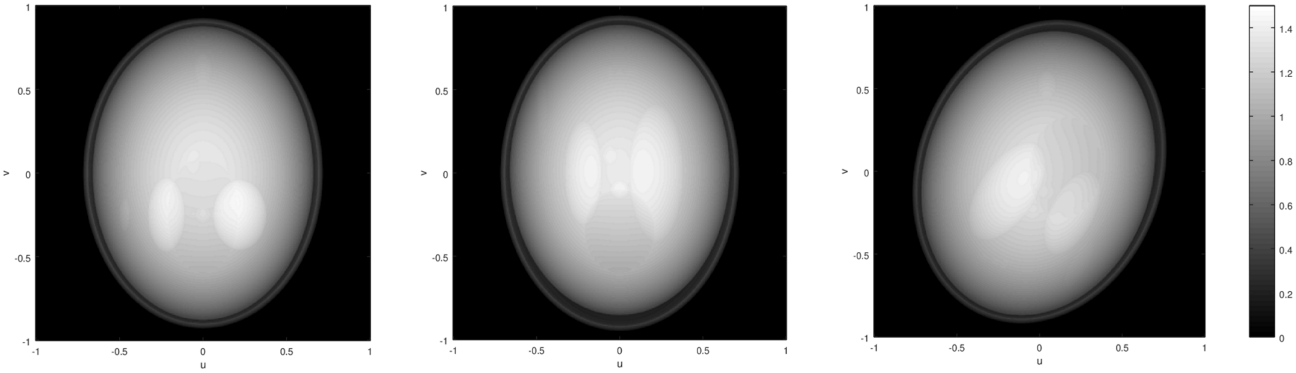

Figure 2. Projection images $p_{\overline{e}_2}$ (left), $p_{\overline{e}_3}$ (middle) and $p_{\overline{\gamma}}$ (right)

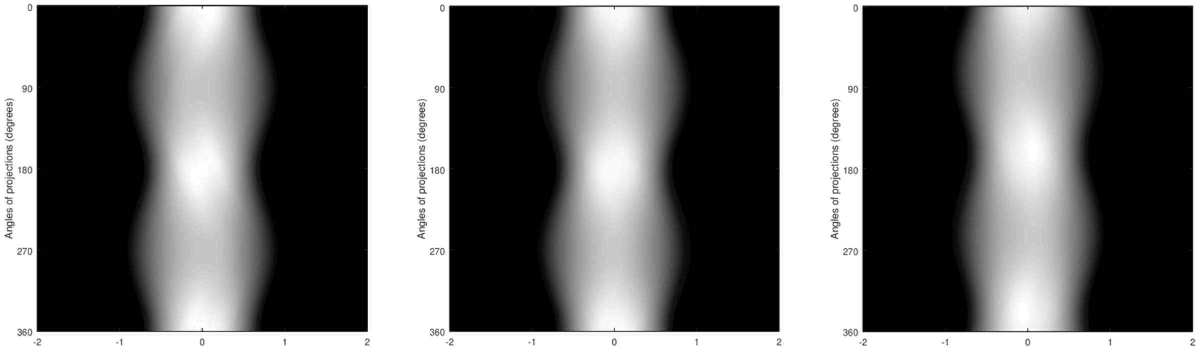

Figure 3. Associated sinograms of $p_{\overline{e}_2}$ (left), $p_{\overline{e}_3}$ (middle) and $p_{\overline{\gamma}}$ (right)

These small errors in the estimated view angle are due to accumulated discretization effects. The angular spacing in the sinograms was $\Delta_\theta = 1^o$, and the row-matching procedure provided $\theta_2 = 206^o$ and $\theta_3 = 26^o$ compared to the true values of $\theta_2 = \pi + \arctan(1/2) \approx 206.565^o$ and $\theta_3 = \arctan(1/2) \approx 26.565^o$. When subsequently applying a refined sinogram sampling in the neighborhood of 206^o for θ_2 and 26^o for θ_3, the new row match was at $\theta_2 = 206.53^o$ and $\theta_3 = 26.56^o$, which yielded $\overline{\gamma}_{\mathrm{Est2}} = \pm(0.33307, -0.66629, 0.66717)$ for polar and azimuthal angles of 48.15^o and -63.44^o. Fig. 4 shows the calculated projections of the Shepp-Logan phantom for $\overline{\gamma}$, $\overline{\gamma}_{\mathrm{Est1}}$ and $\overline{\gamma}_{\mathrm{Est2}}$. This experimental result suggests that just one refinement step in the sinograms row-matching is necessary.

4. DISCUSSIONS AND CONCLUSIONS

For 3D parallel projections, the essential calibration information is the view direction (the normal to the detector plane), the in-plane detector shift, and the in-plane rotation angle. We have described how all these calibration parameters can be obtained directly from the measured projecion of a “production” scan, in an automated way. The principles of the method use data consistency conditions, and assumes two special projections are available whose view directions are known. The method involves a sinogram row-matching step between the unknown projection and the two special projections. The procedure is robust if the image object is general, without special symmetries. We have not completed our analysis of how object symmetries affect uniqueness of the calibration parameter estimates.

The various components of our approach seem to be scattered in the existing literature. Our approach provides a single, comprehensive, mathmatically rigorous proposition. Computer implementation is underway, with preliminary sucessful simulation using the Shepp-Logan and other 3D phantoms.

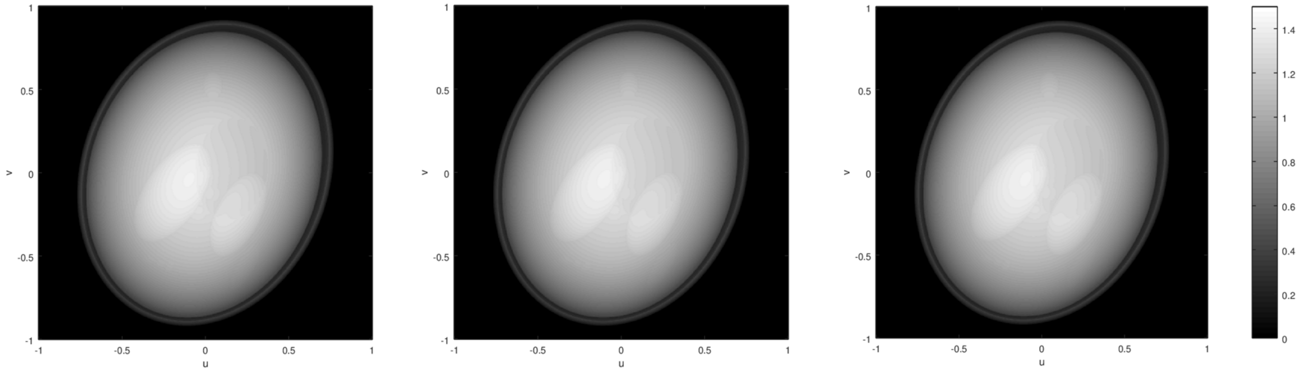

Figure 4. Projections taken at $\overline{\gamma} = (1/3, -2/3, 2/3)$ (left) and two estimate directions $\overline{\gamma}_{\text{Est1}} = (0.32603, -0.66847, 0.66847)$ (middle), $\overline{\gamma}_{\text{Est2}} = (0.33307, -0.66629, 0.66717)$ (right)

ACKNOWLEDGMENTS

This work was supported by the "Fonds unique interministériel" (FUI) and the European Union FEDER in Auvergne Rhône Alpes (3D4Carm project) and by the ANR (ROIdoré project ANR-17-CE19-0006-01).

REFERENCES

[1] Van Heel, M., "Angular reconstitution: a posteriori assignment of projection directions for 3d reconstruction," *Ultramicroscopy* **21**(2), 111–123 (1987).

[2] Van Heel, M., Orlova, E., Harauz, G., Stark, H., Dube, P., Zemlin, F., and Schatz, M., "Angular reconstitution in three-dimensional electron microscopy: historical and theoretical aspects," *Scanning Microscopy* **11**, 195–210 (1997).

[3] Shkolnisky, Y. and Singer, A., "Viewing direction estimation in cryo-em using synchronization," *SIAM journal on imaging sciences* **5**(3), 1088–1110 (2012).

[4] Singer, A. and Shkolnisky, Y., "Three-dimensional structure determination from common lines in cryo-em by eigenvectors and semidefinite programming," *SIAM journal on imaging sciences* **4**(2), 543–572 (2011).

[5] Singer, A., Coifman, R. R., Sigworth, F. J., Chester, D. W., and Shkolnisky, Y., "Detecting consistent common lines in cryo-em by voting," *Journal of structural biology* **169**(3), 312–322 (2010).

[6] Basu, S. and Bresler, Y., "Uniqueness of tomography with unknown view angles," *IEEE Transactions on Image Processing* **9**(6), 1094–1106 (2000).

[7] Basu, S. and Bresler, Y., "Feasibility of tomography with unknown view angles," *IEEE Transactions on Image Processing* **9**(6), 1107–1122 (2000).

[8] Natterer, F., [*The mathematics of computerized tomography*], Wiley (1986).

[9] Gach, H. M., Tanase, C., and Boada, F., "2d & 3d shepp-logan phantom standards for mri," in [*2008 19th International Conference on Systems Engineering*], 521–526, IEEE (2008).

[10] Kak, A. C., Slaney, M., and Wang, G., "Principles of computerized tomographic imaging," *Medical Physics* **29**(1), 107–107 (2002).

Appendix C

Proceedings paper in CT Meeting 2020

This is our proceedings paper [Nguyen et al., 2020b] in the 6th International Conference on Image Formation in X-Ray Computed Tomography. Chapter 3 describes this work with some improvements on the numerical results added.

Automatic geometric calibration in 3D cone-beam geometry with sources on a line

Hung Nguyen, Laurent Desbat and Rolf Clackdoyle.

***Abstract*—In this paper, we consider the geometric calibration problem in 3D cone-beam geometry with sources on a line, as a series of many 2D calibration problems in fan-beam geometry. We give a method to identify the unknown source positions, directly from the projection data, knowing exactly three source positions, even though the detector positions each have unknown offsets. This method works with general objects, meaning they do not have symmetries. We recall two key results for our method: firstly, data consistency conditions for fan-beam geometry with sources on a line and secondly, the link between the center of mass (COM) of the projections and the projections of the COM of a weighted version of the object. We present numerical experiments based on random unit-density balls. These preliminary experiments show that the proposed method solves the source-position self-calibration problem in 3D cone-beam tomography with sources on a line, if three source positions are known.**

I. INTRODUCTION

Geometric calibration has always been of interest in medical imaging, because it is necessary to align the projection images before performing image reconstruction. One idea is to align all projection images according to their centers of mass. In parallel geometry, a well-known result can be stated that: the center of mass of a projection is the projection of the center of mass of the object. We can prove this result by simply considering projection moments or Helgason-Ludwig data consistency consitions (DCCs) of order 0 and 1, see [1], [2], [3]. In [4], Desbat and Clackdoyle produced a very similar result in fan-beam geometry: the center of mass of a fan-beam projection is now the fan-beam projection of the center of mass of a weighted version of the object. Moreover, in fan-beam geometry, if we define the moments of the projections, we can also obtain polynomial-type DCCs. With the same techniques, using the DCCs of order 0 and 1, we can prove the above result of the center of mass.

Projection moments (yielding the Helgason-Ludwig DCCs) have been used by Basu and Bresler for geometric self-calibration in 2D parallel tomography, see [5], [6]. Recent works proposed optimisation methods for geometric self-calibration in 3D cone-beam tomography also by using DCCs, see [7], [8]. In our work, we want to provide analytic formulae based on DCCs for the source positions in cone-beam with sources on a line. The moments and polynomial-type DCCs for fan-beam and cone-beam projections (with the sources on a line or a plane) have been summarized and presented in the context of 2D and 3D geometry in [9]. Furthermore, DCCs for fan-beam projections with the sources on a line have also been carefully studied by Clackdoyle in [10]. He gave two main DCCs for projections, when he considered one fan-beam projection in two different forms: either as an angular ray variable function or as a linear ray variable function. In our paper, we would like to make use of the DCCs for linear ray variable fan-beam projections to deal with the 3D cone-beam geometric calibration problem with the sources on a line. Our aim is to develop an analytic approach to identify the unknown source positions.

Physically, we are considering a horizontal conveyor belt containing our 3D object. It is placed between an x-ray source and a detector. The conveyor belt and the detector are moving together in a certain horizontal direction but at different speeds, to ensure that the projected object remains fairly central on the detector, while the x-ray source is fixed at its own position, see fig. 1. We assume that the detector is sufficiently large, so that none of the projections are truncated. This motion is equivalent to the 3D object being fixed, while the detector and the x-ray source are moving correspondingly to each other in two opposite directions, see fig. 2 (with the motion direction of the detector remaining unchanged compared to the previous model). The x-ray source emits the cone-beam through the 3D object and data are recorded on the detector as the projections. We assume that for some reason, after the first three projections, the system starts losing its track and this leads to the fact that among all of the projections, we only know exactly three relative positions of the x-ray source compared to the 3D object. Thus, we investigate an analytic approach to calibrate all of the others relative positions of the x-ray source.

Our mathematical model considers the 3D object being fixed at a certain location and that an x-ray source is moving along a line, producing a collection of many cone-beam projections of the 3D object, which have been taken on a detector plane parallel to the source line. If we know three source positions corresponding to three acquired projections, then our results claim that we can identify all of the others source positions indeptendently, provided the 3D object is general (with no particular symmetries).

II. 2D MODEL AND BASIC MATERIALS

A. 2D model and definitions

In this section, we recall the classic 2D fan-beam problem with sources on a line. We have the standard 2D coordinate

---

This work was supported by the “Fonds unique interministériel” (FUI) and the European Union FEDER in Auvergne Rhône Alpes (3D4Carm project) and by the ANR (ROIdoré project ANR-17-CE19-0006-01)

H. Nguyen, L. Desbat and R. Clackdoyle are with Univ. Grenoble Alpes, CNRS, Grenoble INP, TIMC-IMAG, 38000 Grenoble, France. e-mail: Hung.Nguyen@univ-grenoble-alpes.fr.

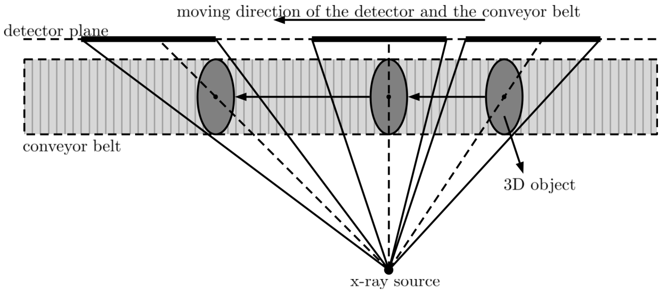

Fig. 1: Top view of the physical model: the x-ray source is fixed, the 3D object and the detector are moving respectively together in the same direction. The detector and conveyor movements are irregular and unknown, and different from each other. But the center of the object projects roughly to the center of the detector at all times, to avoid truncation of the projections.

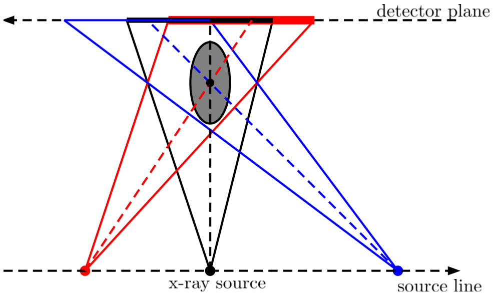

Fig. 2: Top view of the equivalent mathematical model: the 3D object is fixed, the x-ray source and the detector are moving respectively together in opposite directions.

system (x, y). The source is on the x-axis and the detector line is $y = D$ (with D is a positive constant). We call this detector line: the u-axis, which has the origin located at $(0, D)$, see Fig. 3. Our 2D object $f(x, y)$ is between the source line $y = 0$ and the detector line $y = D$.

For each u on detector line, the fan-beam projection with source at $(x, 0)$ is defined as:

$$\begin{aligned} p_x(u) &= \int f\left((x,0) + t\left[(u, D) - (x, 0)\right]\right) dt \\ &= \int f\left(x + tu - tx, tD\right) dt. \qquad (1) \end{aligned}$$

We also define the moment: for the source position $x \in \mathbb{R}$, the moment of projection p_x is: $M_n(p_x, x) = \int p_x(u) u^n du$.

B. Moment conditions (DCCs)

Using the definitions and a simple change of variables, it can be proven (see [10]) that

$$M_n(p_x, x) = \iint \frac{f(y_1, y_2)}{y_2^{n+1}} \left[D y_1 + (y_2 - D)\, x\right]^n dy_1 dy_2.$$

Thus M_n is a polynomial of degree n in x, where x stands for the source position.

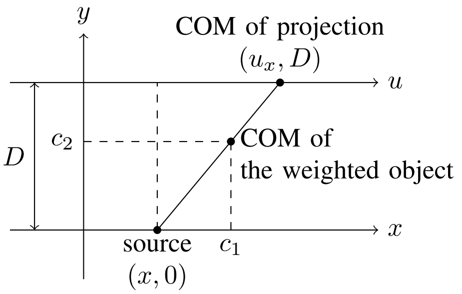

Fig. 3: The COM result can also be proven geometrically by using basic properties of congruent triangles.

C. Center of mass result

We call u_x the position of the center of mass (COM) of the projection associated to source position x. As mentioned in the introduction, using the above moment conditions of order 0 and 1, we can prove that:

$$u_x = x + \frac{D\left(c_1 - x\right)}{c_2}, \qquad (2)$$

with $c_1 = C_{1,0}/C_{0,0}$ and $c_2 = C_{0,1}/C_{0,0}$ where

$$\begin{aligned} C_{0,0} &= \iint \frac{f(x_1, x_2)}{x_2^2} dx_1 dx_2, \\ C_{1,0} &= \iint \frac{f(x_1, x_2)\, x_1}{x_2^2} dx_1 dx_2, \\ C_{0,1} &= \iint \frac{f(x_1, x_2)\, x_2}{x_2^2} dx_1 dx_2. \end{aligned}$$

From the definitions above, (c_1, c_2) is the COM of the weighted object $g(x, y) = f(x, y)/y^2$. Eq. (2) implies that the source $(x, 0)$, the COM of the weighted object (c_1, c_2) and the COM of the projection (u_x, D) are collinear, meaning *the COM of the projection is the fan-beam projection of the COM of the weighted object*. Fig. 3 provides an illustration.

III. FAN-BEAM CALIBRATION PROBLEM AND ALGORITHM

We assume that there exist unknown offsets in the detector positions, and the given data is the raw measurement functions. Our first step is to compute the COM of each raw function; then we shift these functions, so that the COM of each raw function is shifted to the origin of the detector. After this step, we obtain the COM-corrected measurement functions $m_x(u)$. Since $m_x(u)$ is also the corresponding projection to source position x, but has the COM of projection located at the origin of the detector, $m_x(u)$ is related to the theoretical projection $p_x(u)$ (defined at Eq. (1)) by the following formula:

$$m_x(u) = p_x\left(u + u_x\right), \qquad (3)$$

where u_x is position of the COM of projection and is unknown. With the measurements $m_{x_i}(u)$, $i = 1, 2, 3, 4$ and three known source positions x_1, x_2, x_3, we are going to calibrate the unknown position x_4. All other unknown source positions are calibrated the same way.

Solving algorithm

From the four COM-corrected measurements, we compute their moments of order 2:

$$M_2\left(m_x, x\right) = \int m_x(u) u^2 du = \int p_x(u) \left(u - u_x\right)^2 du.$$

Applying the COM result (2), we can show that $M_2\left(m_x, x\right)$ is also a second-degree polynomial in x

$$M_2\left(m_x, x\right) = Ax^2 + Bx + C. \tag{4}$$

Thus if x_1, x_2, x_3 are known and two-by-two different, then we have sufficient information to find the three coefficients A, B, C. Since the unknown source position x_4 must satisfy (4), we end up a second-order equation to solve:

$$Ax_4^2 + Bx_4 + C = M_2\left(m_{x_4}, x_4\right).$$

In conclusion, we obtain at most two possible solutions of the unknown source position for each fan-beam problem.

IV. CONE-BEAM CALIBRATION PROBLEM

We now have a standard 3D coordinate system (x, y, z) and a 3D object F lies between the two planes $y = 0$ and $y = 1$. The x-ray source is moving along the x-axis and the detector plane is $y = 1$. The detector plane has its own origin located at position $(0, 1, 0)$. There are also two standard axes u and v on this plane, which respectively have the same directions as x and z-axis. Then for each point on the detector plane, the cone-beam projection is defined as:

$$\begin{aligned} P_x\left(u, v\right) &= \int F\left(\left(x, 0, 0\right) + t\left[\left(u, 1, v\right) - \left(x, 0, 0\right)\right]\right) dt \\ &= \int F\left(x + tu - tx, t, tv\right) dt. \end{aligned}$$

Fig. 4 illustrates the 3D model being considered.

Given four cone-beam projection images, with three different corresponding source positions known, we will find the other source position.

Solving algorithm

On detector plane, we consider the line $v = v_0$. Since it is parallel to the x-axis there is a plane containing them, which we called the oblique plane $(\Pi_{v_0}) : z = v_0 y$. The origin of (Π_{v_0}) has the same location as the origin of 3D space. The point $(x, y, v_0 y)$ in 3D space will have coordinates $\left(x, y\sqrt{1 + v_0^2}\right)$ on (Π_{v_0}). Assuming (Π_{v_0}) slices through the 3D object, the 2D slice on (Π_{v_0}) is defined as:

$$f_{v_0}\left(x, y\sqrt{1 + v_0^2}\right) = F\left(x, y, v_0 y\right).$$

Combining this and the cone-beam projection definition, we can see that for each point on the line $v = v_0$ on the detector

$$\begin{aligned} P_{x,v_0}(u) = P_x\left(u, v_0\right) &= \int F\left(x + tu - tx, t, v_0 t\right) dt \\ &= \int f_{v_0}\left(x + tu - tx, t\sqrt{1 + v_0^2}\right) dt \\ &= p_x(u)\big|_{D=\sqrt{1+v_0^2}, f=f_{v_0}}, \end{aligned}$$

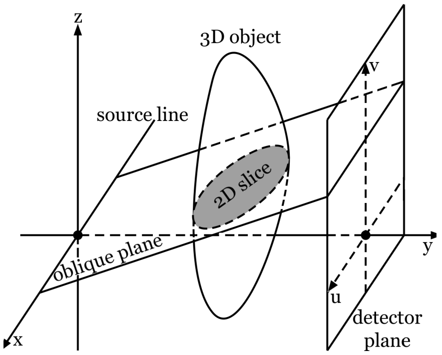

Fig. 4: 3D model in cone-beam geometry

see section II-A. In other words, on (Π_{v_0}), we have exactly the 2D fan-beam calibration problem, where the 2D object f_{v_0} is located between x-axis and the line $y = \sqrt{1 + v_0^2}$.

Therefore, according to section III, each oblique plane (Π_{v_0}) yields at most two possible solutions for the unknown source position. Then N oblique planes being considered will give us roughly N pairs of solutions. If the data are consistent, then these N pairs must have one solution in common, and that common solution is the true solution for the unknown source position. This is our approach to solve a geometric calibration problem in cone-beam with sources on a line; by repeating the same procedure to solve a series of many fan-beam calibration problems and finding the common solution of them.

V. NUMERICAL SIMULATIONS

A. Experiment 1: Testing one random object

The 3D object we considered is the superposition of a set of fifteen unit-density balls, where the centers and radii were selected randomly with a uniform distribution. The centers were in the cube $[-0.2, 0.2] \times [0.4, 0.8] \times [-0.2, 0.2]$ and the radii were in the interval $[0.01, 0.15]$. We define

$$G_i = \begin{cases} 1, \text{if} \left(x - c_x(i)\right)^2 + \left(y - c_y(i)\right)^2 + \left(z - c_z(i)\right)^2 \leq r^2(i) \\ 0, \text{otherwise} \end{cases}$$

with $i = 1, 2, \ldots, 15$, where $(c_x(i), c_y(i), c_z(i))$ and $r(i)$ are the center coordinates and radius of the ith ball. Then the 3D object is $F = \sum_{i=1}^{15} G_i$. Fig. 5 shows 2D slices obtained from four oblique slice planes through the object.

We have developed two main programs, called *simulator* and *solver*. For each oblique plane (Π_{v_0}), *simulator* receives four numbers: the first three numbers are the known source positions, here $x_1 = -0.228$, $x_2 = -0.475$, $x_3 = 0.069$ and the last one $x_4 = 0.312$ is the unknown source position that we need to calibrate. Then it simulates the projections $p_x(u)$ on 1000 equidistant samples of u in $[-2, 2]$ (see Eq. (1)), and shifts them to their COMs to produce the COM-corrected measurements $m_x(u)$ (see Eq. (3)). After that, *solver* receives these measurements and the three known source positions, then estimates the unknown source position. This procedure is repeated for all the oblique planes. We have taken 200 oblique planes of the form $z = v_0 y$, with v_0 from -0.3 to 0.3. After running the whole program, we plot all these pairs of solutions

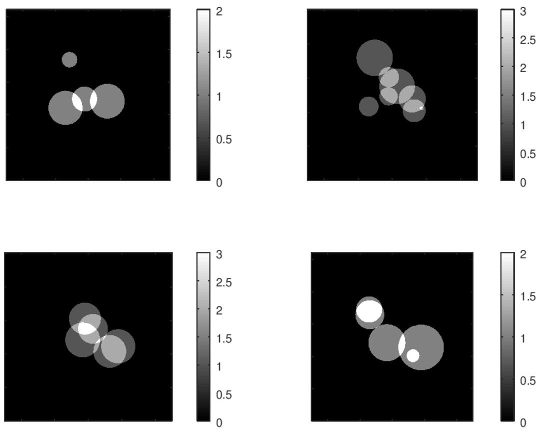

Fig. 5: Four slices of the random object taken from four oblique planes: $z = -0.3y$ (top-left), $z = -0.1y$ (top-right), $z = 0.1y$ (bottom-left) and $z = 0.3y$ (bottom-right)

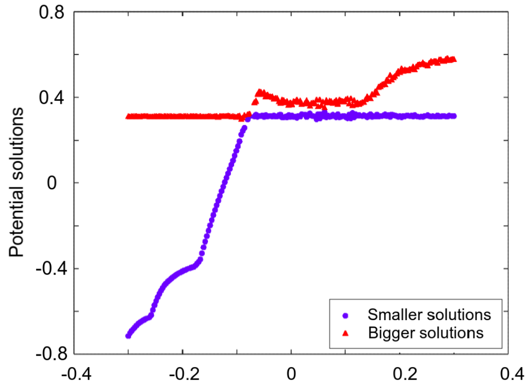

Fig. 6: Solutions on all oblique planes $z = v_0 y$; each value of v_0 (each oblique plane) contain at most two solutions

on a same figure. We presume that there will be a horizontal set of collinear points, where each point is one of each pair of solutions. Fig. 6 shows the result we obtained. Although we can visually identify the correct solution from Fig. 6, we provide the following algorithm to automatically extract the estimated source location.

Computing estimated solution algorithm:

Step 1: We find the minimum solution $x_{\min}$ (the lowest blue point in Fig. 6). We also find the value v_1, where (Π_{v_1}) is the oblique plane containing $x_{\min}$.

Step 2: We find the maximum solution $x_{\max}$ over the other oblique planes: (Π_{v_0}), with $v_0 \neq v_1$. We find v_2 knowing the oblique plane (Π_{v_2}) contains $x_{\max}$.

Step 3: We now have two distinct planes (Π_{v_1}) and (Π_{v_2}). The plane (Π_{v_1}) contains at most two solutions: $x_{\min}$ and $x^{v_1}_{\text{other}}$. The other plane (Π_{v_2}) contains $x_{\max}$ and $x^{v_2}_{\text{other}}$. The points $x_{\min}$ and $x_{\max}$ are different from each other. But there must be two solutions, one on each plane, which are equal or near to each other, because of the fact of the common solution. Thus we compute $H_1 = \left|x_{\max} - x^{v_1}_{\text{other}}\right|, H_2 = \left|x_{\min} - x^{v_2}_{\text{other}}\right|, H_3 = \left|x^{v_1}_{\text{other}} - x^{v_2}_{\text{other}}\right|$ and $H = \min\{H_1, H_2, H_3\}$.

Step 4:

- If $H = H_1$, then $x^{\text{est}} = \left(x_{\max} + x^{v_1}_{\text{other}}\right)/2$.
- If $H = H_2$, then $x^{\text{est}} = \left(x_{\min} + x^{v_2}_{\text{other}}\right)/2$.
- If $H = H_3$, then $x^{\text{est}} = \left(x^{v_1}_{\text{other}} + x^{v_2}_{\text{other}}\right)/2$.

After performing the above algorithm, we obtain the estimated solution $x^{\text{est}} \approx 0.3114$, comparing to the true solution $x^{\text{true}} = 0.312$, with the error $\approx 5.8 \times 10^{-4}$.

B. Experiment 2: Testing 100 random objects

We repeated this test for 100 random objects, where each of them is as the description in experiment 1. We have computed the error vector Err, such that $\text{Err}(i) = x^{\text{est}}(i) - x^{\text{true}}$, $i = 1, 2, \ldots, 100$; and $\text{mean}\,(\text{Err}) = 1/100 \sum_{i=1}^{100} \text{Err}(i) = -3.5 \times 10^{-5}$, is close to 0. We have: $1/100 \sum_{i=1}^{100} |\text{Err}(i)| = 3.8 \times 10^{-3}$, $\sqrt{1/100 \sum_{i=1}^{100} |\text{Err}(i)|^2} = 6.5 \times 10^{-3}$, $\max_i |\text{Err}(i)| = 2.6 \times 10^{-2}$.

VI. DISCUSSIONS AND CONCLUSIONS

We have presented a geometric self-calibration method for cone-beam projections with sources on a line. Assuming three source positions are given, we provide the source position for any new cone-beam projection from the projection data only. The method is based on 2D fan-beam data consistency conditions, more precisely on moments of order 0, 1 and 2. The idea is to consider cone-beam projections with sources on a line as a set of independent fan-beam projections in oblique planes (containing the source line). In this geometry, the moments of order 2 of the fan-beam projections, each centered on its center of mass, is a polynomial of order 2 in the source position variable. Thus the source position is a root of a polynomial of order 2. Thanks to many independent fan-beam projection sets (each contained in an oblique slice) of the cone-beam projections with sources on a line, we can easily identify the common root and thus the source position. We have presented preliminary numerical experiments, including statistics based on 100 phantoms of 15 random ball indicators. They show that this approach solves easily and precisely the source position self-calibration problem in cone-beam projections with sources on a line, provided three source positions are known.

REFERENCES

[1] D. Ludwig, "The radon transform on euclidean space," *Commun. Pure Appl. Math.*, vol. 19, pp. 49–81, 1966.
[2] S. Helgason, *The Radon Transform*. Boston, MA, USA: Birkhaüser, 1980.
[3] F. Natterer, *The Mathematics of Computerized Tomography*. Wiley, 1986.
[4] L. Desbat and R. Clackdoyle, "Calibration and data consistency in parallel and fan-beam linogram geometries," in *IEEE Nuclear Science Symposium and Medical Imaging Conference Proceedings*, 2019. to appear.
[5] S. Basu and Y. Bresler, "Uniqueness of tomography with unknown view angles," *ieeeip*, vol. 9, pp. 1094–1106, 2000.
[6] S. Basu and Y. Bresler, "Feasibility of tomography with unknown view angles," *ieeeip*, vol. 9, pp. 1107–1122, 2000.
[7] A. Aichert, M. Berger, J. Wang, N. Maass, A. Doerfler, J. Hornegger, and A. Maier, "Epipolar consistency in transmission imaging," *IEEE Transactions on Medical Imaging*, vol. 34, pp. 2205–2219, Nov 2015.
[8] J. Lesaint, S. Rit, R. Clackdoyle, and L. Desbat, "Calibration for circular cone-beam ct based on consistency conditions," *IEEE Transaction on Radiation and Plasma Medical Sciences*, vol. 1, no. 6, pp. 517–526, 2017.
[9] R.Clackdoyle, "Data consistency for linograms and planograms," *IEEE Trans Rad Plasma Med*, vol. 4, pp. 288–299, 2018.
[10] R. Clackdoyle, "Necessary and sufficient consistency conditions for fan-beam projections along a line," *IEEE Trans.Nucl.Sci.*, vol. 60, pp. 1560–1569, 2013.

Bibliography

[Abdurahman et al., 2018] Abdurahman, S., Frysch, R., Bismark, R., Melnik, S., Beuing, O., and Rose, G. (2018). Beam hardening correction using cone beam consistency conditions. *IEEE Transactions on Medical Imaging*, 37(10):2266–2277.

[Abramowitz et al., 1972] Abramowitz, M., Stegun, I. A., et al. (1972). *Handbook of mathematical functions: with formulas, graphs, and mathematical tables*, volume 55. National bureau of standards Washington, DC.

[Basu and Bresler, 2000a] Basu, S. and Bresler, Y. (2000a). Feasibility of tomography with unknown view angles. *IEEE Transactions on Image Processing*, 9(6):1107–1122.

[Basu and Bresler, 2000b] Basu, S. and Bresler, Y. (2000b). Uniqueness of tomography with unknown view angles. *IEEE Transactions on Image Processing*, 9(6):1094–1106.

[Carlsson et al., 1994] Carlsson, P. E., Edholm, P. R., and Danielsson, P. E. (1994). The synthesis of a new x-ray picture identical in projection to a previous picture using 3d fourier techniques. *Physics in Medicine and Biology*, 39(3):597–608.

[Clackdoyle, 2013] Clackdoyle, R. (2013). Necessary and sufficient consistency conditions for fanbeam projections along a line. *IEEE Transactions on Nuclear Science*, 60(3):1560–1569.

[Clackdoyle, 2018] Clackdoyle, R. (2018). Data consistency for linograms and planograms. *IEEE Transactions on Radiation and Plasma Medical Sciences*, 2(4):288–299.

[Clackdoyle et al., 2015] Clackdoyle, R., Defrise, M., Desbat, L., and Nuyts, J. (2015). Consistency of fan-beam projections along an arc of a circle. In *Proc. 13th Int. Meeting Fully Three-Dimensional Image Reconstruction Radiol. Nucl. Med.*, pages 253–256.

[Clackdoyle and Desbat, 2013] Clackdoyle, R. and Desbat, L. (2013). Full data consistency conditions for cone-beam projections with sources on a plane. *Physics in Medicine and Biology*, 58(23):8437–8456.

[Clackdoyle and Desbat, 2015] Clackdoyle, R. and Desbat, L. (2015). Data consistency conditions for truncated fanbeam and parallel projections. *Medical Physics*, 42(2):831–845.

[Clackdoyle et al., 2016] Clackdoyle, R., Desbat, L., Lesaint, J., and Rit, S. (2016). Data consistency conditions for cone-beam projections on a circular trajectory. *IEEE Signal Processing Letters*, 23(12):1746–1750.

[Clackdoyle et al., 2018] Clackdoyle, R., Nguyen, H., Perrier, V., and Desbat, L. (2018). Scatter imaging and radar: Dual image reconstruction problems. In *2018 IEEE Nuclear Science Symposium and Medical Imaging Conference Proceedings (NSS/MIC)*, pages 1–6.

[Clackdoyle et al., 2014] Clackdoyle, R., Rit, S., Hoskovec, J., and Desbat, L. (2014). Fanbeam data consistency conditions for applications to motion detection. In *Proc. 3rd Int. Meeting Image Formation X-Ray Comput. Tomography*, pages 324–328.

[Desbat and Clackdoyle, 2019] Desbat, L. and Clackdoyle, R. (2019). Calibration and data consistency in parallel and fan-beam linogram geometries. In *2019 IEEE Nuclear Science Symposium and Medical Imaging Conference (NSS/MIC)*, pages 1–5.

[Gach et al., 2008] Gach, H. M., Tanase, C., and Boada, F. (2008). 2d & 3d shepp-logan phantom standards for mri. In *2008 19th International Conference on Systems Engineering*, pages 521–526.

[Grangeat, 1991] Grangeat, P. (1991). Mathematical framework of cone beam 3d reconstruction via the first derivative of the radon transform. In Herman, G. T., Louis, A. K., and Natterer, F., editors, *Mathematical Methods in Tomography*, pages 66–97, Berlin, Heidelberg. Springer Berlin Heidelberg.

[Helgason, 1980] Helgason, S. (1980). *The Radon Transform.* Boston, MA, USA: Birkhauser.

[Hengyong Yu et al., 2006] Hengyong Yu, Yuchuan Wei, Jiang Hsieh, and Ge Wang (2006). Data consistency based translational motion artifact reduction in fan-beam ct. *IEEE Transactions on Medical Imaging*, 25(6):792–803.

[Kak and Slaney, 1988] Kak, A. C. and Slaney, M. (1988). *Principles of computerized tomographic imaging.* IEEE Press.

[Lesaint, 2018] Lesaint, J. (2018). *Data consistency conditions in X-ray transmission imaging and their application to the self-calibration problem.* Theses, Université Grenoble Alpes.

[Lesaint et al., 2016] Lesaint, J., Clackdoyle, R., Rit, S., and Desbat, L. (2016). Two cone-beam consistency conditions for a circular trajectory. In *Proc. 4th Int. Conf. Image Formation X-Ray Comput. Tomography*, pages 431–434.

[Lesaint et al., 2017] Lesaint, J., Rit, S., Clackdoyle, R., and Desbat, L. (2017). Calibration for circular cone-beam ct based on consistency conditions. *IEEE Transactions on Radiation and Plasma Medical Sciences*, 1(6):517–526.

[Lesaint et al., 2018] Lesaint, J., Rit, S., Clackdoyle, R., Desbat, L., and Noo, F. (2018). Gcc and fbcc for linear tomosynthesis. In *Proceedings of the Fifth International Conference on Image Formation in X-Ray Computed Tomography (CT-Meeting)*, pages 114–118.

[Levine et al., 2010] Levine, M. S., Sidky, E. Y., and Pan, X. (2010). Consistency conditions for cone-beam ct data acquired with a straight-line source trajectory. *Tsinghua Science and Technology*, 15(1):56–61.

[Luo et al., 2020] Luo, S., Zheng, L., Luo, S., Gu, N., and Tang, X. (2020). Data sustained misalignment correction in microscopic cone beam ct via optimization under the grangeat epipolar consistency condition. *Medical physics*, 47(2):498–508.

[Ma et al., 2017] Ma, J., Wu, S., Qi, H., Li, B., Yan, H., Zhou, L., and Xu, Y. (2017). John's equation-based consistency condition and corrupted projection restoration in circular trajectory cone beam ct. *Scientific Reports*, 7(1):1–17.

[Milne-Thomson, 2000] Milne-Thomson, L. M. (2000). *The calculus of finite differences.* American Mathematical Soc.

[Natterer, 2001] Natterer, F. (2001). *The mathematics of computerized tomography.* SIAM.

[Nguyen et al., 2020a] Nguyen, H., Clackdoyle, R., and Desbat, L. (2020a). Automatic geometric calibration in 3d parallel geometry. In *SPIE Medical Imaging 2020: Physics of Medical Imaging*, volume 11312. International Society for Optics and Photonics.

[Nguyen et al., 2020b] Nguyen, H., Desbat, L., and Clackdoyle, R. (2020b). Automatic geometric calibration in 3d cone-beam geometry with sources on a line. In *Sixth international conference on image formation in X-ray computed tomography*, pages 530–533.

[Noo, 1998] Noo, F. (1998). *Méthodes numériques directes de reconstruction d'images tridimensionnelles à partir de projections coniques.* PhD thesis, Université de Liège, Faculté des sciences appliquées.

[Noo et al., 2004] Noo, F., Clackdoyle, R., and Pack, J. D. (2004). A two-step hilbert transform method for 2d image reconstruction. *Physics in Medicine and Biology*, 49(17):3903–3923.

[Patch, 2002a] Patch, S. K. (2002a). Computation of unmeasured third-generation vct views from measured views. *IEEE Transactions on Medical Imaging*, 21(7):801–813.

[Patch, 2002b] Patch, S. K. (2002b). Consistency conditions upon 3d ct data and the wave equation. *Physics in Medicine and Biology*, 47(15):2637–2650.

[Patch, 2004] Patch, S. K. (2004). Thermoacoustic tomography—consistency conditions and the partial scan problem. *Physics in Medicine and Biology*, 49(11):2305–2315.

[Shkolnisky and Singer, 2012] Shkolnisky, Y. and Singer, A. (2012). Viewing direction estimation in cryo-em using synchronization. *SIAM Journal on Imaging Sciences*, 5(3):1088–1110.

[Sidky et al., 2005] Sidky, E. Y., Zou, Y., Xia, D., and Pan, X. (2005). A consistency condition for cone-beam CT with general source trajectories. In Fitzpatrick, J. M. and Reinhardt, J. M., editors, *Medical Imaging 2005: Image Processing*, volume 5747, pages 2042 – 2047. International Society for Optics and Photonics, SPIE.

[Singer et al., 2010] Singer, A., Coifman, R. R., Sigworth, F. J., Chester, D. W., and Shkolnisky, Y. (2010). Detecting consistent common lines in cryo-em by voting. *Journal of Structural Biology*, 169(3):312–322.

[Singer and Shkolnisky, 2011] Singer, A. and Shkolnisky, Y. (2011). Three-dimensional structure determination from common lines in cryo-em by eigenvectors and semidefinite programming. *SIAM Journal on Imaging Sciences*, 4(2):543–572.

[Szegö, 1939] Szegö, G. (1939). *Orthogonal polynomials*, volume 23. American Mathematical Soc.

[Van Heel, 1987] Van Heel, M. (1987). Angular reconstitution: A posteriori assignment of projection directions for 3d reconstruction. *Ultramicroscopy*, 21(2):111–123.

[Van Heel et al., 1997] Van Heel, M., Orlova, E., Harauz, G., Stark, H., Dube, P., Zemlin, F., and Schatz, M. (1997). Angular reconstitution in three-dimensional electron microscopy: historical and theoretical aspects. *Scanning Microscopy*, 11:195–210.

[Yu and Wang, 2007] Yu, H. and Wang, G. (2007). Data consistency based rigid motion artifact reduction in fan-beam ct. *IEEE Transactions on Medical Imaging*, 26(2):249–260.